A Multifunctional MEMS Pressure and Temperature Sensor for Harsh Environment Applications

by

Ali Najafi Sohi

A thesis
presented to the University of Waterloo
in fulfillment of the
thesis requirement for the degree of
Doctor of Philosophy
in
Mechanical Engineering

Waterloo, Ontario, Canada, 2013

©Ali Najafi Sohi 2013

AUTHOR'S DECLARATION

I hereby declare that I am the sole author of this thesis. This is a true copy of the thesis, including any required final revisions, as accepted by my examiners.

I understand that my thesis may be made electronically available to the public.

Abstract

The objective of this thesis was to develop a fast-response multifunctional MEMS (Micro Electro Mechanical Systems) sensor for the simultaneous measurement of in-cylinder pressure and temperature in an internal combustion (IC) engine. In a representative IC engine, the pressure and temperature can reach up to about 1.6 MPa and 580 °C, respectively, at the time of injection during the compression stroke. At the peak of the combustion process, the pressure and temperature near the cylinder wall can go beyond 6 MPa and 1000 °C, respectively. Failure of current membrane-based MEMS pressure sensors operating at high temperatures is mainly caused by cross-sensitivity to temperature, which affects the pressure readout. In addition, the slow thermal response of temperature sensors used for such a dynamic application makes real-time sensing within a combustion engine very challenging. While numerous approaches have been taken to address these issues, no MEMS sensor has yet been reported that can carry out real-time measurements of in-cylinder pressure and temperature.

The operation of the sensor proposed in this Thesis is based on a new non-planar and flexible multifunctional membrane, which responds to both pressure and temperature variations at the same time. The new design draws from standard membrane-based pressure and thermostatic-based temperature MEMS sensing principles to output two capacitance values. A numerical processing scheme uses these values to create a characteristic sensing plot which then serves to decouple the effects of pressure and temperature variations. This sensing scheme eliminates the effect of cross-sensitivity at high temperatures, while providing a short thermal response time. Thermal, mechanical and electrical aspects of the sensor performance were modeled. First, a semi-analytical thermo-mechanical model, based on classic beam theory, was tailored to the shape of the multifunctional membrane to determine the sensor's response to pressure and temperature loading. ANSYS® software was used to verify this semi-analytical model against finite element simulations. Then the model was then used to calculate the capacitive outputs of the multifunctional MEMS sensor subjected to in-cylinder pressure and temperature loading during a complete cycle of operation of a typical IC engine as well as to optimize the sensor specifications.

Several prototypes of the new sensing mechanism fabricated using the PolyMUMPs® foundry process were tested to verify its thermal behavior up to 125 °C. The experiments were performed using a ceramic heater mounted on a probe station with the device connected to a precision LCR-

meter for capacitive readouts. Experimental results show good agreement of the temperature response of the sensor with the ANSYS® finite element simulations. Further simulations of the pressure and temperature response of different configurations of the multifunctional MEMS sensor were carried out. The simulations were performed on an array of 4200 multifunctional devices, each featuring a 0.5 µm thick silicon carbide membrane with an area of 25×25 μm^2, connected in parallel shows that the optimized sensor system can provide an average sensitivity to pressure of up to 1.55 fF/KPa (over a pressure range of 0.1-6 MPa) and an average sensitivity to temperature of about 4.62 fF/°C (over a temperature range of 160-1000 °C) with a chip area of approximately 4.5 mm^2. Assuming that the accompanying electronics can meaningfully measure a minimum capacitance change of 1 fF, this optimized sensor configuration has the potential to sense a minimum pressure change of less than 1 KPa and a minimum temperature change of less than 0.35 °C over the entire working range of the representative IC engine indicated above.

In summary, the new developed multifunctional MEMS sensor is capable of measuring temperature and pressure simultaneously. The unique design of the membrane of the sensor minimizes the effect of cross-sensitivity to temperature of current MEMS pressure sensors and promises a short thermal response time. When materials such as silicon carbide are used for its fabrication, the new sensor may be used for real-time measurement of in-cylinder pressure and temperature in IC engines. Furthermore, a systematic optimization process is utilized to arrive at an optimum sensor design based on both geometry and properties of the sensor fabrication materials. This optimization process can also be used to accommodate other sensor configurations depending on the pressure and temperature ranges being targeted.

Acknowledgements

I would like to thank my supervisors Patricia Nieva and Amir Khajepour for their support throughout my PhD at the University of Waterloo and for helping me set my imagination free to investigate new horizons in MEMS research. Their hardworking has always amazed me and kept me motivated.

I am grateful to my colleagues Mohammad Shavezipur, Phani Madhavi Singaraju, Jeremy Godin and Elena Bassiachvili for their support and suggestions and my friends Keyvan Ahmadi and Ali Emamian who made my life experience in Waterloo so delightful and pleasant. I am also grateful to my MSc supervisor Reza Naghdabadi who shaped my academic life. I feel indebted to him forever.

I would like to acknowledge the funding and financial support provided by the Ontario centers of excellence (OCE), National Science and Engineering Research Council of Canada (NSERC) and the Waterloo Institute of Nanotechnology (WIN) through the WIN Nanotechnology Graduate Student Scholarship as well as the products and services provided by CMC Microsystems that facilitated my research in MEMS area.

Finally, I am thankful for the way in which life has treated me so generously. I hope this Thesis helps make the world a better place to live.

Dedication

This Thesis is dedicated to my loving wife *Farzaneh* whose patience and support made it possible for me to follow this long journey in pursuit of perfection, to my mother *Shohreh* for her endless love and self-sacrifice without which I would never stand here, and to my everlasting hero, my father, *Mahmoud* for all the good things I have acheived in my life by imitating him.

Table of Contents

AUTHOR'S DECLARATION ii
Abstract iii
Acknowledgements v
Dedication vi
Table of Contents vii
List of Figures x
List of Tables xiv
List of Abbreviations xv
List of Symbols xvi
Chapter 1 Introduction 1
1.1 Motivation 1
1.2 Objectives 2
1.3 Organization of thesis 3
Chapter 2 Literature Review 5
2.1 MEMS sensors for harsh environment 6
2.1.1 Definition of harsh environment in the context of this thesis 6
2.1.2 MEMS sensor materials 7
2.1.3 Pressure sensors 15
2.1.4 Temperature sensors 23
2.1.5 Failure of available MEMS sensors in harsh environments 26
2.2 Multifunctional MEMS sensors 27
2.2.1 Discrete approach 27
2.2.2 Integrated approach 29
Chapter 3 Sensor Design 32
3.1 Working conditions 32
3.1.1 Sensor location 32
3.1.2 Working environment 34
3.2 Operational requirements 38
3.2.1 Pressure and temperature working range 38
3.2.2 Sensitivity and resolution 39
3.2.3 Ability to follow the input variation rate 40

3.3 Design of multifunctional membrane 41
3.3.1 Pressure response 42
3.3.2 Temperature response 44
3.3.3 Temperature and pressure combined response 44
3.4 Implementation of capacitance measurement 45
3.5 MEMS sensor 46
Chapter 4 Modeling and Analysis 48
4.1 Thermal modeling 48
4.1.1 Results and optimization 55
4.2 Mechanical modeling 63
4.2.1 Pressure response 65
4.2.2 Temperature response 73
4.2.3 Combined pressure and temperature response 78
4.3 Electrical modeling 82
4.3.1 Fringing effect 83
4.3.2 Connecting multiple sensors in parallel 83
4.3.3 Capacitive output 84
4.3.4 In-cylinder measurement 87
4.4 Sensitivity analysis 87
4.5 Multifunctional sensor design guideline 93
4.6 Effect of fabrication and deviations from design parameters 95
4.6.1 Residual stress in thin films 95
4.6.2 Deviation of dimensions from design parameters 95
Chapter 5 Experiment and Result 98
5.1 PolyMUMPs® microfabrication process 98
5.2 Fabricated devices and results 99
5.2.1 Test devices for material characterization 99
5.2.2 First prototype 101
5.2.3 Second prototype 103
Chapter 6 Concluding Remarks 109
6.1 Conclusion 109
6.2 Contributions of thesis 109

6.2.1 Development of a new membrane for simultaneous measurement of pressure and temperature at one location and a semi-analytical model for the analysis of its response 109
6.2.2 Minimization of the effect of cross-sensitivity to temperature 110
6.2.3 Improved thermal response time 110
6.2.4 Small footprint 111
6.3 Proposed future work 111
6.3.1 Modeling and Optimization 111
6.3.2 Fabrication and packaging 112
6.3.3 Experiments and test setups 113
Appendix A Fabrication process flow 114
Appendix B ANSYS ® APDL codes 118
Appendix C Fringing effect in parallel plate capacitors 149
Appendix D Layouts of PolyMUMPs chips 151
Copyright Permissions 153
Bibliography 156

List of Figures

Figure 2.1. Pressure and temperature ranges as well as characteristic times of some harsh environment applications for which MEMS sensors are being developed 6
Figure 2.2. Thermal conductivity versus temperature for selected MEMS materials 11
Figure 2.3. Specific heat versus temperature for selected MEMS materials 12
Figure 2.4. Elastic modulus versus temperature for selected MEMS materials 13
Figure 2.5. Coefficient of thermal expansion versus temperature for selected MEMS materials 14
Figure 2.6. Schematic of a piezoresistive pressure sensor: (a) top view; (b) side view; (c) piezoresistive strain gauges connected in a Wheatstone bridge configuration 15
Figure 2.7. Schematic of a capacitive MEMS pressure sensor fabricated using surface and bulk micromachining methods. The top electrode is shown deflected under pressure difference 19
Figure 2.8. Schematic of an optical MEMS pressure sensor based on Fabry-Perot interferometry. The depth of the cavity formed between the reflection surfaces changes with pressure difference 21
Figure 2.9. Schematic of the harsh environment multifunctional MEMS sensor proposed by Berkeley Sensor and Actuator Center [113] 28
Figure 2.10. A photo of the harsh environment multifunctional MEMS sensor designed and fabricated by researchers at the University of British Columbia. The capacitive pressure sensor silicon diaphragm and platinum RTD are labeled on the photo [114] (figure used with permission) 28
Figure 2.11. Multifunctinoal MEMS sensor for pressure and temperature measurement; (a) SEM picture of array of microcantilevers, (b) optical measurement system, (c) Contour plot of combined outputs showing viscous damping coefficient as a function of ambient pressure and temperature [118] (figure used with permission) 30

Figure 3.1. IC engine cylinder cross-section view, **(A)**-**(C)** represent the prospective mounting positions for the MEMS sensor and ● marks the characteristic point for temperature measurement . 32
Figure 3.2. MEMS sensor attached to host component with mean bulk temperature T_{bulk}. In the case of in-cylinder MEMS sensor, the host component is either engine block or cylinder head 33
Figure 3.3. Variation of burnt gas temoperature $T_{\infty,1}$ and unburnt gas temoperature $T_{\infty,2}$ (optically measured) with crankshaft angle in an iso-octane powered IC-engine. This figure refers to engine case # 4 in Table 3.1 36

Figure 3.4. Variation of in-cylinder parameters with crankshaft angle in a diesel IC test engine. Directly measured and calculated quantities are shown with ○ and □ symbols, respectively. The primary (hatched section) and secondary working ranges of the sensor are shown in the top panel . 37
Figure 3.5. Rate of variation of in-cylinder (a) pressure and (b) temperature with crankshaft angle in a typical IC engine 41
Figure 3.6. Schematic of multifunctional membrane. The edges of the membrane are fixed 42
Figure 3.7. Multifunctional membrane deformation due to pressure change ΔP 43
Figure 3.8. Multifunctional membrane deformation due to temperature change Δ*T*. The inset highlights the rotation of the membrane around a rotation axis that passes through the step feature 43
Figure 3.9. Multifunctional membrane response to combined pressure and temperature loading 44
Figure 3.10. Schematic of the deformed multifunctional membrane. Two capacitors C_1 and C_2 are formed between the multifunctional membrane and the bottom fixed electrodes. G_1 and G_1 are the initial gaps (prior to membrane deformation) between the electrodes 45
Figure 3.11. Characteristic graph of multifunctional MEMS sensor. One set of inputs (P', T') can be assigned to each pair of outputs (C'_1, C'_2) 46
Figure 3.12. Schematic representation of multifunctional MEMS sensor. For better visualization of sealed cavity and fixed electrodes, half of sensor is shown in this figure 47

Figure 4.1. (a) Array of multifunctional sensor cells connected in parallel, (b) enlarged view of a single cell, (c) exploded views of the sensor cell showing the thermal transfer between different components; Q, *t*, and *T* represent energy, thickness, and temperature, respectively 49
Figure 4.2. Temperature variation rate of a SiC membrane versus CA rotation, i.e. ΔT/ΔCA in (ºC/deg) unit, for different values of t_M and η ($Q_{in} = 25\text{kW/m}^2$, *ω* = 600 rpm) 52
Figure 4.3. Variation of $T_{M,1}$ with in-cylinder temperature $T_{\infty,2}$ for 2 µm $< t_i <$ 5 µm 56
Figure 4.4. Variation of $T_{M,1}$ with in-cylinder temperature $T_{\infty,2}$ for 0.5 µm $< t_M <$ 5 µm 57
Figure 4.5. Variation of $T_{M,1}$ with in-cylinder temperature $T_{\infty,2}$ for different membrane materials . 58
Figure 4.6. Variation of $T_{M,1}$ with in-cylinder temperature $T_{\infty,2}$ for different bonding interfaces 59
Figure 4.7. Variation of $T_{M,1}$ with in-cylinder temperature $T_{\infty,2}$ for different engine speeds 61
Figure 4.8. Variation of temperature of different parts of sensor with in-cylinder temperature $T_{\infty,2}$ 62

Figure 4.9. (a) Multifunctional membrane with built-in boundary condition and the characteristic clamped-clamped beam selected from its middle part; (b) analogous straight clamped-clamped beam attached to extensional and rotational springs at its midspan 64
Figure 4.10. Response of the analogous clamped-clamped beam to (a) both pressure difference ΔP and retaining force F_Z, (b) pressure difference ΔP only, and (c) retaining force F_Z only 66
Figure 4.11. Response of a clamped-clamped beam rigidly supported at its midspan to pressure difference ΔP (corresponding to $k_z = \infty$ in figure 4.10.a) 68
Figure 4.12. Variation of k_z with length and width-to-thickness ratios in an a-SiC multifunctional membrane with a step height-to-thickness ratio of (a) 0.5 or (b) 1 70
Figure 4.13. Variation of ξ_P with length- and width-to-thickness ratios in an a-SiC multifunctional membrane with a step height-to-thickness ratio of (a) 0.5 or (b) 1 72
Figure 4.14. (a) Deformation of a clamped-clamped beam due to temperature increase ΔT, (b) The reaction forces F_T applied by the end supports give rise to an internal bending moment $F_T h$ which is opposed by the torsional moment M_θ from the rotational spring 73
Figure 4.15. Variation of $\bar{\bar{\xi}}_T$ with W/t_M and h/t_M in an a-SiC membrane with $L/t_M = 37.5$ 76
Figure 4.16. Deformation of the multifunctional membrane in (a) *xz*- plane and (b) *yz*-plane for SiC-Si and Ti-Si membrane-substrate systems predicted by the semi-analytical model (solid line with round symbol) and FE simulations (dotted red line) 79
Figure 4.17. Variation of maximum deflection of a 0.5 μm thick a-SiC membrane with length L and width W when subjected to peak in-cylinder pressure and temperature. The region at which the maximum deflection is smaller than the thickness of membrane is contained within dotted line 81
Figure 4.18. Several multifunctional MEMS sensors arrayed in parallel to provide bigger outputs 84
Figure 4.19. (a) C_1 and (b) C_2 predicted by the semi-analytical model (red dotted line) and FE simulation (blue solid line) for the SiC-Si MEMS sensor with dimensions: $L = W = 25$ μm, $h = 0.6$ μm, $t = 0.5$ μm, and $G_1 = G_2 = 0.55$ μm 85
Figure 4.20. Characteristic capacitive output plot for the SiC-Si MEMS sensor with dimensions: $L = W = 25$ μm, $h = 0.6$ μm, $t = 0.5$ μm, and $G_1 = G_2 = 0.55$ μm, calculated by the semi-analytical model. in equation (4.39) 86
Figure 4.21. Capacitive output C_1 of the multifunctional MEMS sensor subjected to in-cylinder pressure P and temperature $T_{\infty,2}$; dimensions of a single MEMS sensor are: $L = W = 25$ μm, $h = 0.6$ μm, $t = 0.5$ μm, and $G_1 = G_2 = 0.55$ μm 88

Figure 4.22. Capacitive output C_2 of the multifunctional MEMS sensor subjected to in-cylinder pressure P and temperature $T_{\infty,2}$; dimensions of a single MEMS sensor are: $L = W = 25$ µm, $h = 0.6$ µm, $t = 0.5$ µm, and $G_1 = G_2 = 0.55$ µm 89
Figure 4.23. (a) S_P in aF/KPa, and (b) S_T in aF/°C for a single multifunctional MEMS sensor 90
Figure 4.24. Sensitivities to (a) pressure and (b) temperature of a SiC-Si multifunctional MEMS sensor when subjected to in-cylinder pressure and temperature loading; The dimensions of the sensor are: $L = W = 25$ µm, $h = 0.6$ µm, $t = 0.5$ µm, and $G_1 = G_2 = 0.55$ µm 91
Figure 4.25. A step-by-step design guideline for multifunctional MEMS sensor (for information on geometrical parameters refer to figure 4.1) 94

Figure 5.1. Bimaterial microcantilevers fabricated using the PolyMUMPs® foundry process and used in this work for material characterization........ 99
Figure 5.2. Optical profile of a gold-polysilicon bimaterial microcantilever 100
Figure 5.3. Clamped-clamped beams fabricated in polysilicon (right) and gold-polysilicon (left) configurations. The inset on top provides a closer isometric look at step feature 102
Figure 5.4. Deformation of a clamped-clamped beam (top) with increased temperature due to Joule heating (right); On the bottom left, the deformation patterns are schematically identified 103
Figure 5.5. Multifunctional membrane (a) before and (b) after the spacers are removed. The membrane is connected to two pads (blue). The bottom electrodes are connected to the other two pads (red). Capacitances C_1 and C_2 are formed between the membrane and the bottom electrodes 104
Figure 5.6. Test setup for capacitive temperature measurements........ 105
Figure 5.7. Capacitive outputs C_1 and C_2 of the device in figure 5.5.b when temperature increases from 25 to 125 °C. The results of high temperature experiments as well as the predictions of FE simulations are shown. The slight difference between the results can be due to etch holes which are not included in the FE model 107
Figure 5.8. Profile of the tested membrane in figure 4.7 at room temperature and 125 °C. The arrows in the bottom panel show the direction of thermally-induced deformation of the membrane 108

List of Tables

Table 2.1. Density of some common MEMS materials 10

Table 3.1. Pressure and temperature at the end of compression and at the peak of combustion strokes in some 4-stroke IC test engines 35

Table 4.1. Working characteristics of different configurations of multifunctional MEMS sensor ... 92

List of Abbreviations

AlN .... Aluminum Nitride
Bi .... Biot number
BTDC .... Before Top Dead Centre (IC engine)
CA .... Crankshaft Angle (IC engine)
Cr .... Chromium
CTE .... Coefficient of Thermal Expansion
CVD .... Chemical Vapor Deposition
GaN .... Gallium Nitride
IC .... Integrated Circuit
IC engine .... Internal Combustion engine
KOH .... Potassium Hydroxide
MEMS .... Micro Electro Mechanical Systems
RF .... Radio Frequency
Si .... Silicon
SiC .... Silicon Carbide
SiCN .... Silicon CarboNitride
Si_3N_4 .... Silicon Nitride
SiO_2 .... Silicon Dioxide
SOI .... Silicon-On-Insulator
TDC .... Top Dead Centre (IC-engine)
Ti .... Titanium

List of Symbols

ΔP .... pressure change
ΔT .... temperature change
E .... Young's modulus, elastic modulus
$\emptyset$ .... heat flux
h .... step height in membrane
h_{th} .... heat transfer coefficient
L .... length of membrane (or cavity)
L_{chip} .... length of substrate chip
v .... poisson's ratio
P .... pressure
Q .... thermal energy
t .... thickness or time (depending on context)
T .... temperature
W .... width of membrane (or cavity)
W_{chip} .... width of substrate chip

Chapter 1
Introduction

Industrial processes, like power generation, can be monitored by measuring their characteristic variables such as pressure and temperature. The efficiency of these processes affects their consumption of valuable resources and the production of pollutants and waste byproducts. The everlasting need for higher efficiencies has led to a huge interest in pushing the working limits of the available measurement technologies even further. To achieve this goal, new sensors are required which can survive the increasing harsh environment conditions found in such applications.

Micro-Electro-Mechanical Systems (MEMS) sensors have received a great interest in recent years because of their potential to precisely measure physical variables in various applications. This, along with their low cost, small foot print, superior reliability, and possibility of integration into an array for multiplexed measurements have made the MEMS sensors a good candidate for measurements in harsh environment applications. The trend for pushing the working limits of industrial processes has created a huge demand for the development of new MEMS sensors which can work appropriately and reliably in extremely harsh conditions. A good example is MEMS sensors sought for combustion monitoring in internal combustion (IC) engines.

1.1 Motivation

The available MEMS technology for pressure and temperature sensing is likely to malfunction in harsh environment applications because of the degradation of the sensor's structural materials and/or the failure of its sensing mechanism(s). While the former shortcoming can be addressed by using stronger materials, the latter one asks for the development of new MEMS sensing mechanisms that can operate in harsh environments with acceptable precision and speed.

MEMS sensors are usually designed single-tasked to measure one parameter at a time. However, they often operate in complex environments at which various parameters change simultaneously. In such environments, one of the major obstacles toward achieving an acceptable operational precision is the cross-sensitivity of the MEMS sensor to undesired parameters. Cross-sensitivity to temperature in MEMS pressure sensor is an example of this problem.

So far, the main solution to the problem of cross-sensitivity to undesired parameters has been using auxiliary sensors for independent measurement of the undesired parameters and then deploying signal

processing schemes to cancel out and compensate for their effects. However, increased size, added cost and the complexity due to the addition of new sensors have hindered successful implementation of this compensation solution in many applications. So, the design of a new MEMS sensor with improved compensation scheme arises as the first motivation for this Thesis.

Additionally, in some harsh environment applications, fast responding sensors are needed to keep up with the rate of temperature variation. Measurement of temperature inside the cylinder of an IC engine is an example of such applications. To carry out in-cylinder temperature measurement, two general approaches have been followed so far: 1) optical based methods and 2) thin film based methods. The first approach enables very fast measurement of temperature; however, it requires relatively bulky components and is not suitable for consumer use outside the laboratory. The second approach has other downsides such as limited life time and relatively moderate response time. This example can be extended to other applications for which fast responding temperature sensors are required but the need has not been fully answered yet. This need for fast responding temperature sensors constitutes the second motivation for this Thesis.

1.2 Objectives

A new MEMS sensor for simultaneous measurement of pressure and temperature inside the cylinder of IC engines is designed in this Thesis. It is called here a multifunctional MEMS sensor since it carries out two measurements. The new sensor addresses the concern of cross-sensitivity to temperature during the measurement of in-cylinder pressure. It also provides a short response time in catching up with the rate of variation of in-cylinder temperature. The new multifunctional MEMS sensor combines membrane-based pressure sensing and bimaterial-based (thermostatic) temperature sensing principles and is designed to specifically achieve the following objectives:

1. Development of a new multifunctional sensing mechanism for simultaneous measurement of pressure and temperature at one location.
2. Improvement of the accuracy of pressure measurement by introducing a new temperature compensation scheme.
3. Improvement of response time for temperature measurement, by taking such measures as minimizing the thermal mass of the sensing body.
4. Small footprint for nonintrusive integration inside the cylinder of IC engine.

5. Compatibility with different measurement techniques like capacitive (implemented in this Thesis) and optical (listed among the future work).

1.3 Organization of thesis

The Thesis is divided into six chapters. Chapter 2 presents a literature review on MEMS sensors for harsh environment applications. It starts by defining a harsh environment in the context of this Thesis and continues by reviewing available harsh environment MEMS materials and available methods for pressure and temperature measurement in such environments. A review of failure mechanisms in available MEMS sensors for harsh environment applications follows. The chapter concludes with a review of current multifunctional MEMS sensing platforms.

In Chapter 3, the operational requirements for the new multifunctional MEMS sensor for IC engines are established and the conceptual design of the sensor is presented. The design evolves around a nonplanar multifunctional membrane whose responses to pressure and temperature variations are inherently different. This difference lays the foundation for and enables decoupling the effects of pressure and temperature variations. The chapter finishes with a section that discusses the integration of capacitive interrogation with the multifunctional membrane.

Chapter 4 presents the modeling and analysis of the sensor's response to different pressure and/or temperature loading cases. It includes both numerical finite element and semi-analytical modeling approaches. The chapter starts with the numerical thermal modeling of the effect of different sensor materials and geometrical parameters. Based on the results of these simulations, appropriate materials and dimensions are selected to achieve the operational requirements set in Chapter 2. Next, based on classic beam theory, a semi-analytical model is developed for the mechanical analysis of the membrane response to pressure and/or temperature loading. This semi-analytical model, which is validated by the finite element simulations, drastically decreases the modeling time. Electrical modeling and sensitivity analysis of the sensor provide capacitive outputs of the sensor at different loading conditions and dimensions. The last section investigates the effects of fabrication errors and deviation from ideal design parameters on the performance of the sensor.

In Chapter 5, experimental results of two groups of fabricated devides are presented. The first group includes test devices designed and fabricated for the determination of the residual stresses of MEMS structural materials. The second group includes proof-of-concept MEMS prototypes made to

qualitatively and quantitatively verify the thermal response mechanism of the new sensor. The test setup used for the experiments is also described in this chapter.

Finally, Chapter 6 concludes the Thesis by listing the main contributions and proposing potential future work trends to continue this research.

Chapter 2
Literature Review

Throughout the physical sciences, measurement is defined as the process of determining the ratio of a physical quantity like pressure to a unit of measurement like Pascal (defined as one newton per square metre). It is usually carried out by a sensor which converts the physical phenomenon (measurand, or input) into a quantity (output) that can be read by an observer or by an instrument. Sensors are an essential part to any industrial application. There are as many sensors as there are different physical quantities to be measured.

In late 1960s, borrowing from the integrated circuit (IC) fabrication technology, the first bulk micromachined silicon wafer was used as a pressure sensor. This led the way for a new category of very small devices later known as Micro-Electro-Mechanical Systems (MEMS). MEMS sensor technology is concerned with highly miniaturized devices (usually less than a few hundreds micrometer in size) that convert physical measurands into electrical signals.

Development of robust MEMS sensors and their utilization in harsh environment applications has recently emerged as one of the most sought for trends in industry. Examples of such applications include down-hole drilling, space missions, and combustion monitoring in automotive industry, to name a few. Various measures have been taken lately to improve the robustness of MEMS sensors, including the development of harsh environment MEMS materials and the design of novel sensing mechanisms for extreme working conditions. Moreover, since accurate measurements are essential in many industries, and considering the fact that all measurements are inherently approximations, a great deal of effort has been put into making the MEMS sensors as accurate as possible. As highlighted in Chapter 1, the cross interference between the effects of desired and undesired measurands (called cross-sensitivity in this Thesis) is a major challenge in many harsh environment applications. To address these problems, the development of new MEMS sensors for harsh environments has recently attracted a lot of interest among both researchers and industry [1, 2].

In the following sections, a review of the main works on sensors for pressure and temperature measurements in harsh environments is presented. It investigates the ongoing research on both MEMS and non-MEMS based competing sensors with a special emphasis on those developed for operation in IC engines. Finally, the current status of multifunctional MEMS sensors is reviewed.

2.1 MEMS sensors for harsh environment

2.1.1 Definition of harsh environment in the context of this thesis

A harsh environment is generally characterized by extreme working conditions such as intense vibrations, radiation, electromagnetic interference, chemically aggressive media, high pressure and most notably high temperature. In the context of this work, we are specifically concerned with harsh environment applicaitons associated with the last two of the aforementioned characteristics. Figure 2.1 reviews the pressure and temperature ranges associated with a handful of such harsh environment

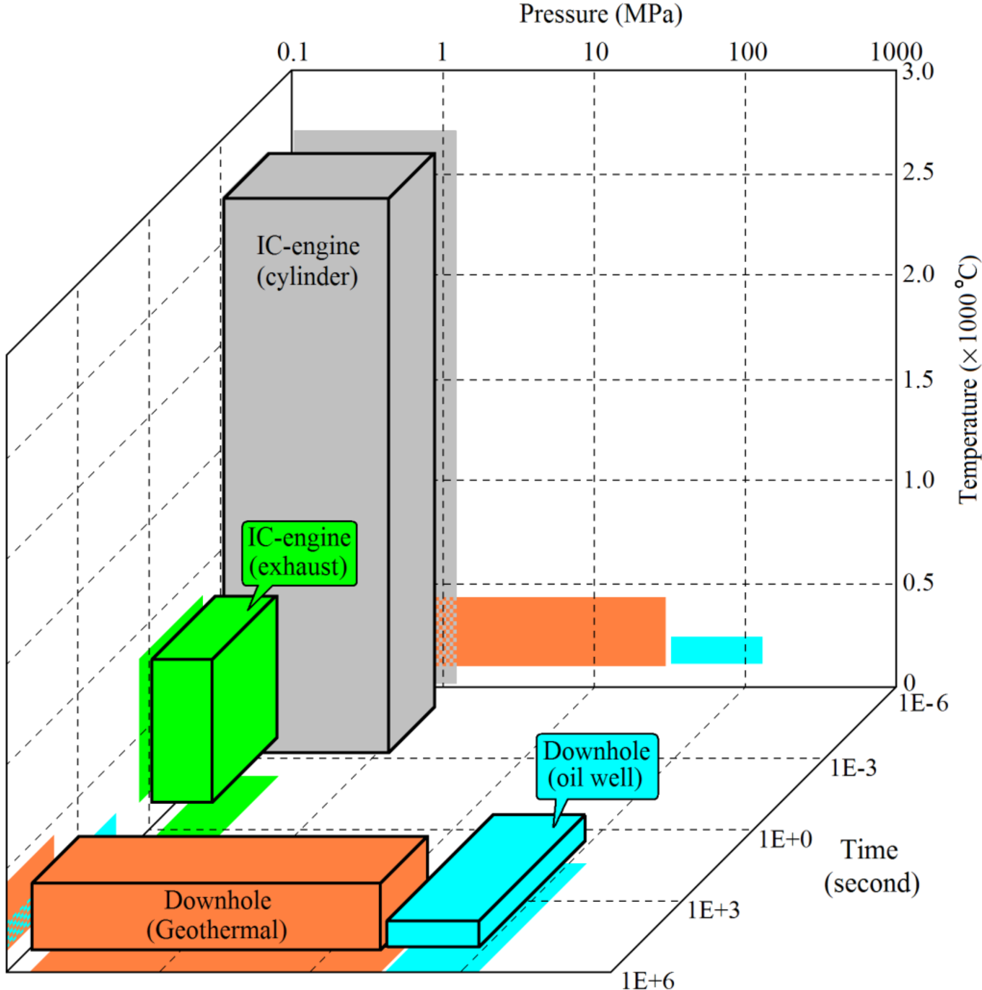

Figure 2.1. Pressure and temperature ranges as well as characteristic times of some harsh environment applications for which MEMS sensors are being developed.

applications. Among the applications represented in Figure 1, those related to IC engine (including both gasoline and diesel powered ones) stand out as highly dynamic and intermittent examples at which pressure and temperature changes occur over very short periods of time (in the order of microsecond or millisecond). Moreover, these applications are associated with some of the highest temperature variations observed among harsh environment applications. On the contrary, for example in downhole applications, pressure and temperature change so slowly that the whole application can be regarded static.

In the automotive industry, the development of reliable sensors for real time monitoring of in-cylinder process conditions is a high demanding research trust. Such sensors can provide unparalleled information to engine control unit in order to minimize fuel consumption and emission level. Successful implementation of in-cylinder sensors includes operation during the various strokes of an IC engine. As a result, such sensors will be exposed to and should survive such harsh conditions as electromagnetic interference (electrical discharge during spark ignition), high pressure and high temperature (during compression and working strokes), and chemically aggressive media (by-products of combustion during the working and exhaust cycles). Additionally, one should notice that in applications such as monitoring of in-cylinder conditions, additional difficulties arise from the fact that such extreme working conditions usually appear in combination with each other.

2.1.2 MEMS sensor materials

The requirement for reliable and robust MEMS sensors for harsh environment applications has initially been answered by pushing the existing MEMS sensor technology to its limit. To do so, many efforts have been put into improving the environmental resistance of MEMS sensors thorough the development and implementation of harsh environment compatible MEMS materials. These materials can be categorized in three main groups: 1) semiconductors such as silicon, aluminum nitride, gallium nitride, diamond and silicon carbide, 2) dielectrics for passivation such as silicon carbonitride, silicon dioxide and silicon nitride, and 3) refractory metals such as titanium, chromium, nickel and tungsten. In the following, the most important MEMS materials and their applications at harsh environment sensors are reviewed.

Silicon (Si)

Silicon is the most commonly used semiconductor in MEMS sensors which can be found in a variety of forms including single crystal substrate (SC-Si), amorphous thin film (a-Si), polycrystalline thin

film (Poly-Si), and single crystalline thin film. From a mechanical point of view, silicon is known to maintain its elastic strength at temperatures up to about 600 °C without showing any noticeable plastic deformation [3]. In terms of electrical properties, silicon-based electronics starts to malfunction at temperatures above 150 °C mainly because of excessive leakage current [4]. By using Silicon on Insulator (SOI) technology, the maximum temperature limit of silicon-based electronics can be further pushed up to 350 °C [5]. So, 350 °C and 600 °C are regarded as the ultimate working temperatures of silicon-based electronics and MEMS mechanical components, respectively.

Aluminum nitride (AlN)

Aluminum nitride is a promising piezoelectric semiconductor for high temperature applications. It maintains its piezoelectric characteristic at temperatures up to 1150 °C [6]. AlN thin films have been successfully deposited/grown in amorphous [7], polycrystalline [8] and single crystal [9, 10] forms on a variety of substrate materials. Recently, single crystal AlN wafers have also been reported [11]. The main shortcoming of AlN in harsh environment applications is that it oxidizes above 800 °C in the presence of oxygen [12].

Gallium nitride (GaN)

Gallium nitride has excellent mechanical and thermal stability as well as inherent piezoelectricity [13]. It is a semiconducting piezomaterial and combines the piezoresistive and piezoelectric behaviors [14]. The main drawback of GaN in harsh environment applications is that it dissociates to gallium oxide and nitrogen at approximately 650 °C in the presence of oxygen [15].

Diamond

Diamond is the hardest material found in nature with superior mechanical strength and thermal conductivity. Single crystal diamond has a room temperature thermal conductivity of 1000 to 2000 $Wm^{-1}K^{-1}$ [16, 17], which makes it the best thermal conductor of any known solid. Although the survival of diamond has been documented at temperatures up to 2200 °C in a hydrogen atmosphere [18], it burns in the presence of oxygen at temperatures above 700 °C which hinders its usage in many harsh environment applications [19].

Silicon Carbide (SiC)

Silicon carbide, the most investigated material for harsh environment applications, is a wide band-gap semiconductor which has been successfully used in the fabrication of high temperature electronics

[20] and MEMS sensors [1]. SiC has been deposited in single crystalline, polycrystalline, and amorphous forms on different substrates [21]. In addition, pure SiC wafers up to four inches in diameter are commercially available [22] and six inches wafers are on the horizon [23]. Among SiC different polytypes, the cubic 3C-SiC and the hexagonal 4H-SiC and 6H-SiC are extensively used in harsh environment MEMS application as structural and high temperature electronic materials, respectively [24]. For high temperature harsh environment application, SiC is known to maintain its outstanding mechanical strength and chemical stability at temperatures in excess of 1000 °C [25, 26].

Silicon carbonitride (SiCN)

Silicon carbonitride typifies a class of amorphous polymer-derived dielectric materials that maintain their mechanical strength and chemical stability at temperatures as high as 1400 °C [27, 28]. SiCN MEMS structures are usually fabricated using liquid polymer polysilazane as a precursor. The fabrication process is rather cheap and simple because the liquid precursor is inexpensive and it is possible to make micro features using only a UV-lithography process [29]. However, realization of small and complex features can not be achieved using a liquid precursor.

Silicon Dioxide (SiO_2)

Silicon Dioxide is commonly used as an intermediate layer to electrically insulate conductive layers from each other. It is also used as a sacrificial layer in wet etching processes. Among the different methods used to deposit SiO_2, wet and dry thermal oxidation have gained a great popularity in MEMS industry, mainly due to the high chemical stability of the resultant oxide layer and its strong adhesion to underneath substance.

Silicon Nitride (Si_3N_4)

Silicon Nitride is widely used as an electrical insulator between conductive layers. It is usually deposition by chemical vapor deposition (CVD) methods. Due to its chemical stability, Si_3N_4 is also used as the masking layer for etching processes.

Titanium (Ti)

Titanium, due to its mechanical toughness and corrosion resistance, has emerged as a potential structural material for the fabrication of MEMS radio frequency (RF) switches for harsh environment applications [30]. In such applications, the native titanium oxide which forms on exposed titanium protects the rest of it from the harsh environment. Moreover, due to its strength at high temperatures

as well as its ability to form conductive alloys with other materials such as nickel and tungsten, titanium is extensively used in the metallization of Ohmic contacts in harsh environment MEMS devices [31].

Chromium (Cr)

Chromium is mostly used in MEMS devices as an adhesion layer between otherwise non bonding materials. It is also used for contact metallization in harsh environment MEMS.

Tungsten (W)

Tungsten is used in the metallization of Ohmic contacts in harsh environment MEMS devices. Thanks to it thermal and phase stability at temperatures up to 2700 °C [32], tungsten alloyed with titanium along with a gold film, following a short annealing step at 1000 °C, is extensively used as a reliable Ohmic contact in SiC MEMS devices for prolonged operation at temperatures up to 300 °C [33, 34].

The densities of the MEMS materials reviewed in this section are given in Table 2.1 and are assumed to be temperature independent.

The remainder of this section reviews the most important temperature dependent properties of these MEMS materials. Figure 2.2 shows how thermal conductivity k of MEMS materials varies with temperature. Among the materials investigated in this figure, diamond possesses the highest thermal conductively of all followed by single crystal SiC (SC-SiC). On the other hand, SiO_2 and Si_3N_4 demonstrate the lowest thermal conductivity which makes them ideal thermal insulators. One general trend observed in Figure 2.2 is the drastic reduction in the thermal conductivities of SiC and Si as their crystalline structure changes from single crystal to amorphous. This is mainly due to the increased phonon scattering on the grain boundaries of the crystalline structures [35].

Table 2.1. Density of some common MEMS materials.

Material	Si	AlN	GaN	Diamond	SiC	
Density (Kg/m^3)	2330	3260	6500	3520	3210	
Material	SiCN	SiO_2	Si_3N_4	Ti	Cr	W
Density (Kg/m^3)	2600	2200	3200	4500	7190	19250

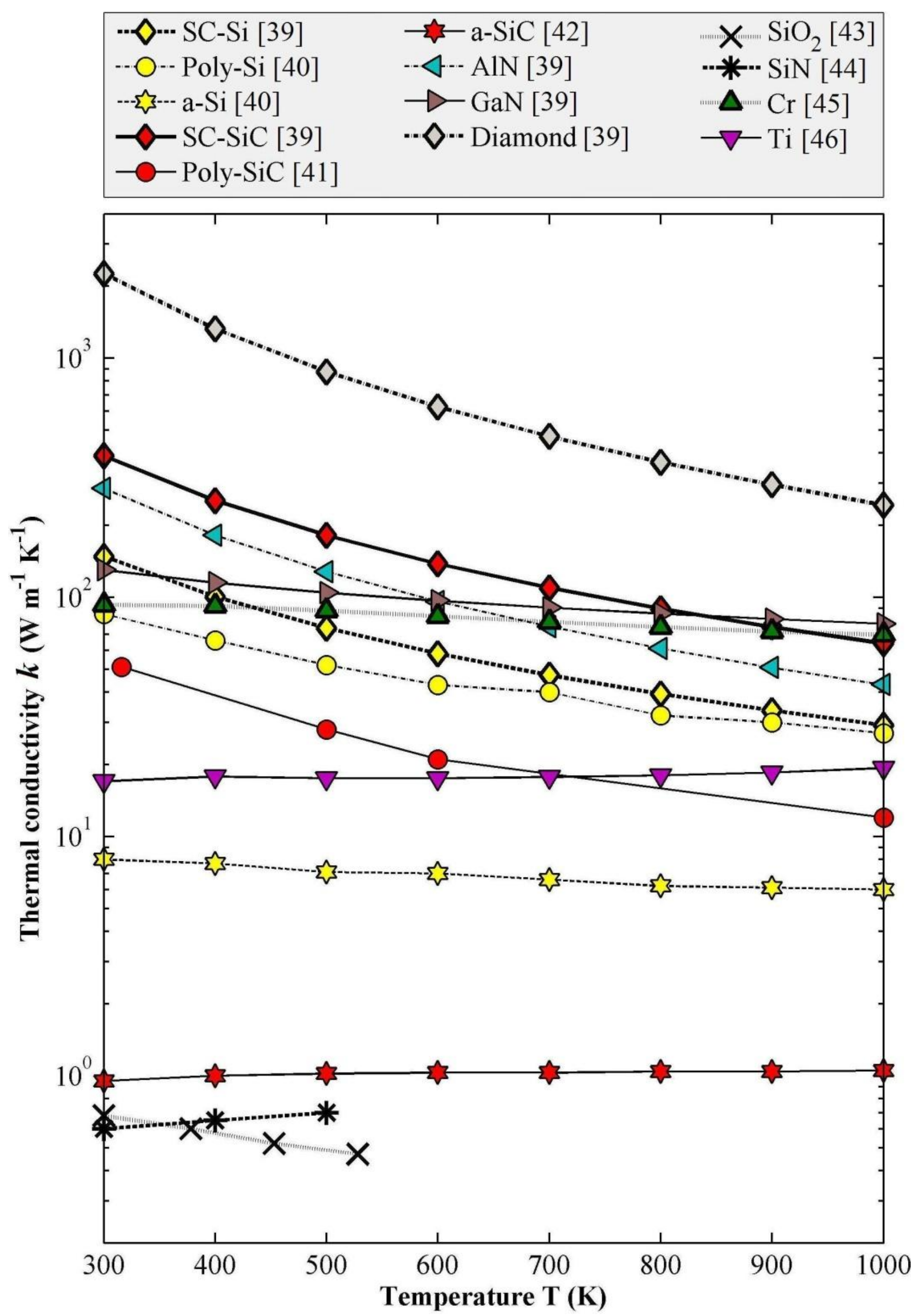

Figure 2.2. Thermal conductivity versus temperature for selected MEMS materials.

Figure 2.3 represents the change in specific heat C of MEMS materials with temperature. Since the specific heat of a material mostly depends on its density, no major difference is observed among the

specific heats of various crystalline structures of materials like Si and SiC [36]. Figures 2.4 and 2.5 show how elastic modulus and coefficient of thermal expansion (CTE) of MEMS materials vary with temperature. Similar to the case of specific heat, no major dependence between the CTE and the

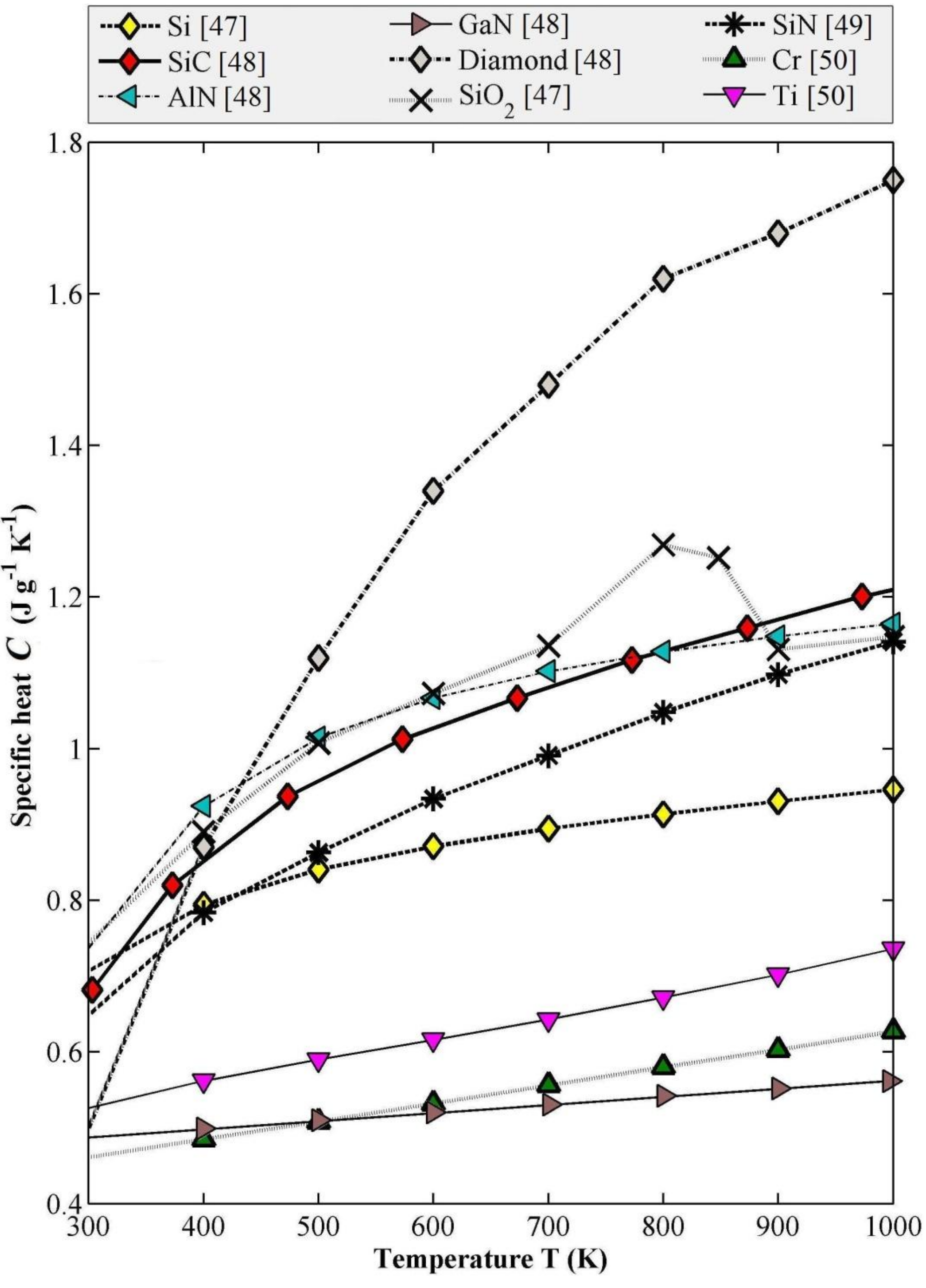

Figure 2.3. Specific heat versus temperature for selected MEMS materials.

crystalline structure of materials is observed. As an anomaly in Figure 2.5, the CTE of SiO_2 is reported as negative [37] which is in agreement with some earlier published data [38].

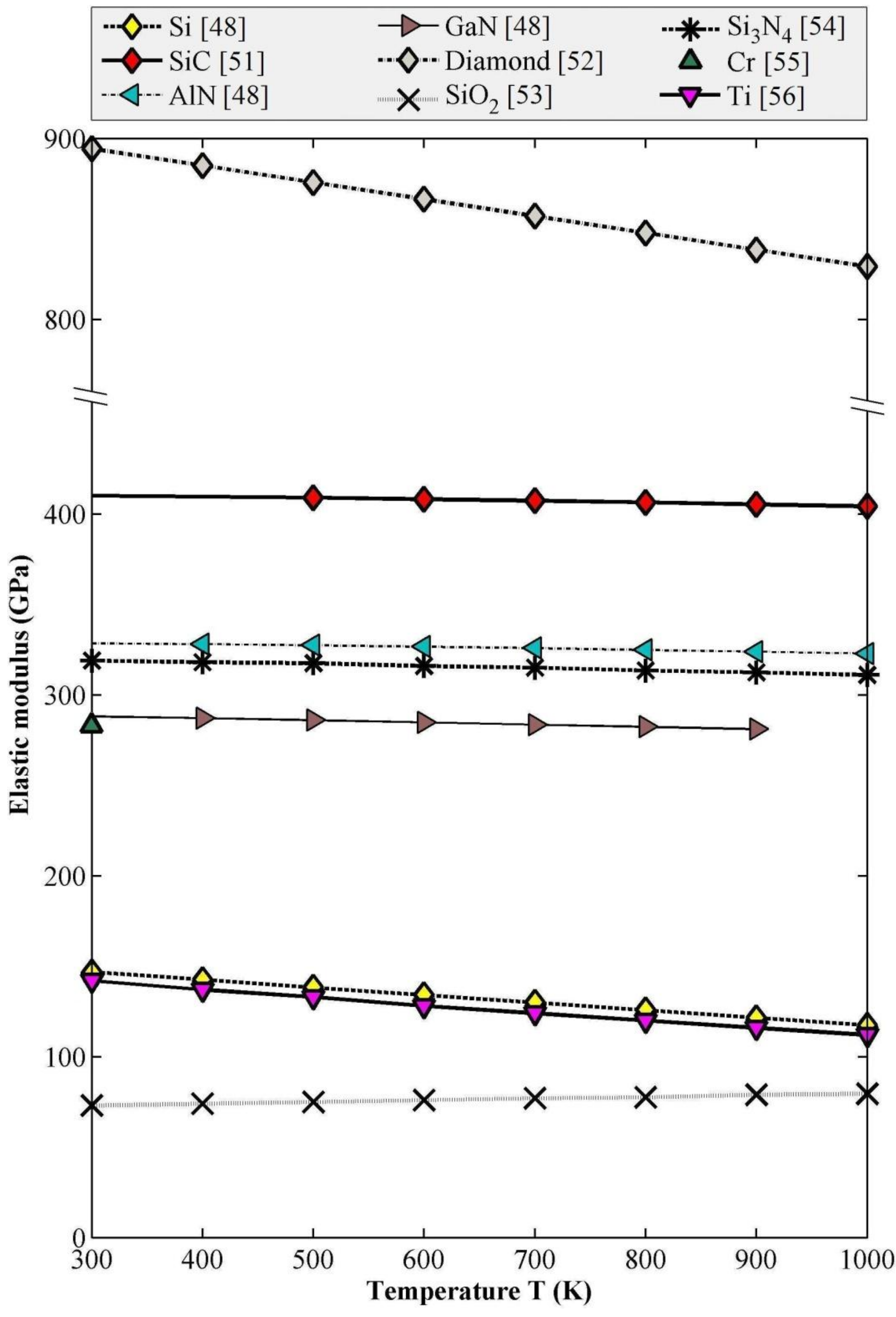

Figure 2.4. Elastic modulus versus temperature for selected MEMS materials.

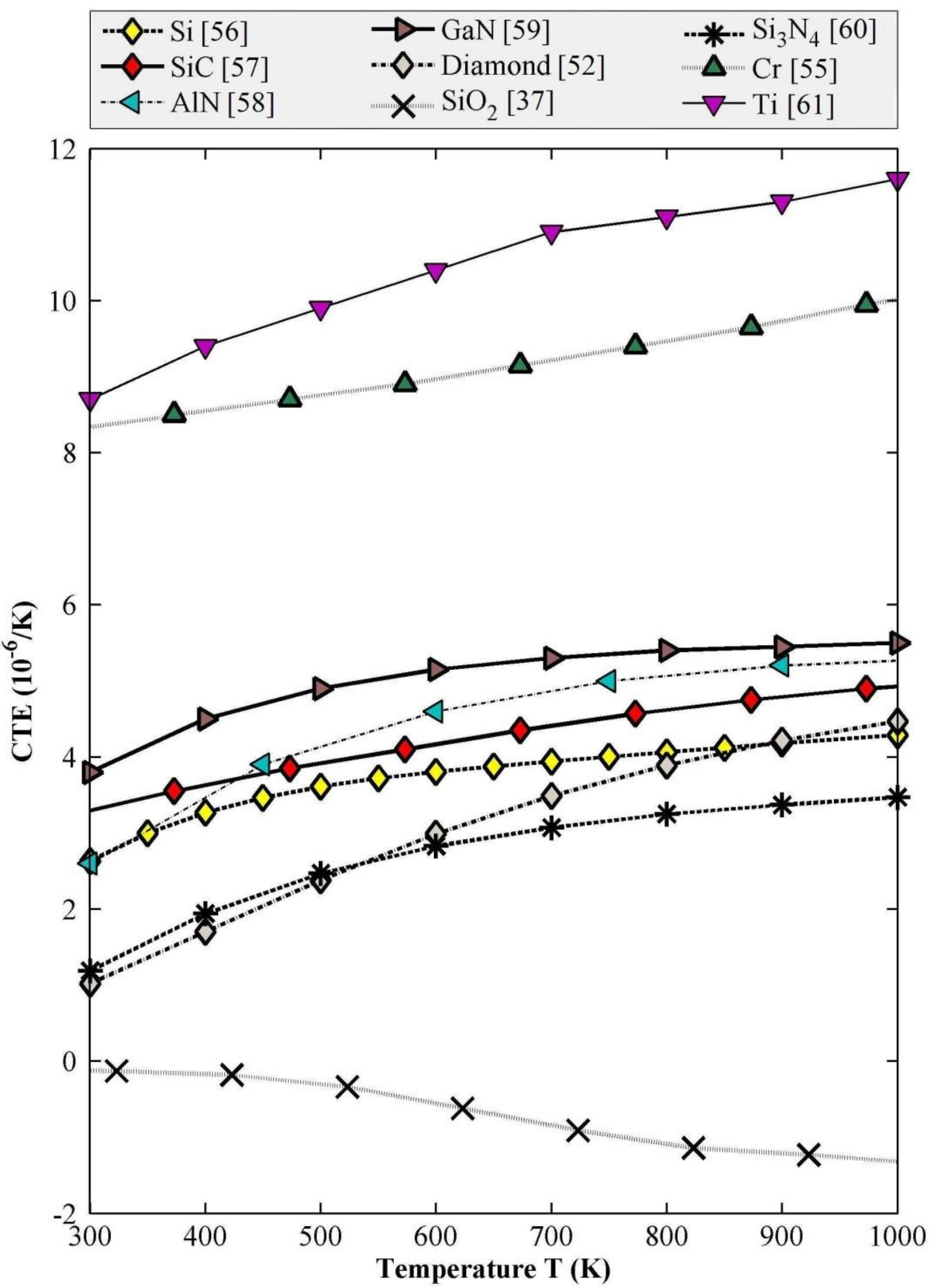

Figure 2.5. Coefficient of thermal expansion versus temperature for selected MEMS materials.

For each of Figures 2.2 to 2.5, the corresponding references from which the data is collected are given in the figure's legend. Throughout this Thesis, wherever needed, the characteristic curves of MEMS material properties reported in this section are extrapolated to cover the temperature range of interest.

2.1.3 Pressure sensors

Pressure sensors are the most extensively investigated MEMS sensors for harsh environment applications. They are designed and fabricated around the idea of utilizing a thin flexible membrane which is made from a resilient material. The membrane serves as the sensing element of the sensor. When there is a pressure difference between its two sides, the membrane deflects. A measurement system is integrated into the sensor which is used to measure the deflection of the membrane under pressure difference. The ultimate output of a MEMS pressure sensor is typically an electrical signal whose amplitude is proportionate to the pressure difference.

Piezoresistive:

A piezoresistive MEMS pressure sensor works based on the change of resistance of a material due to mechanical loading and/or deformation (piezoresistive effect). The change in resistance comes mostly from the physical change of the structure due to deformation [62]. Figure 2.6 schematically shows a

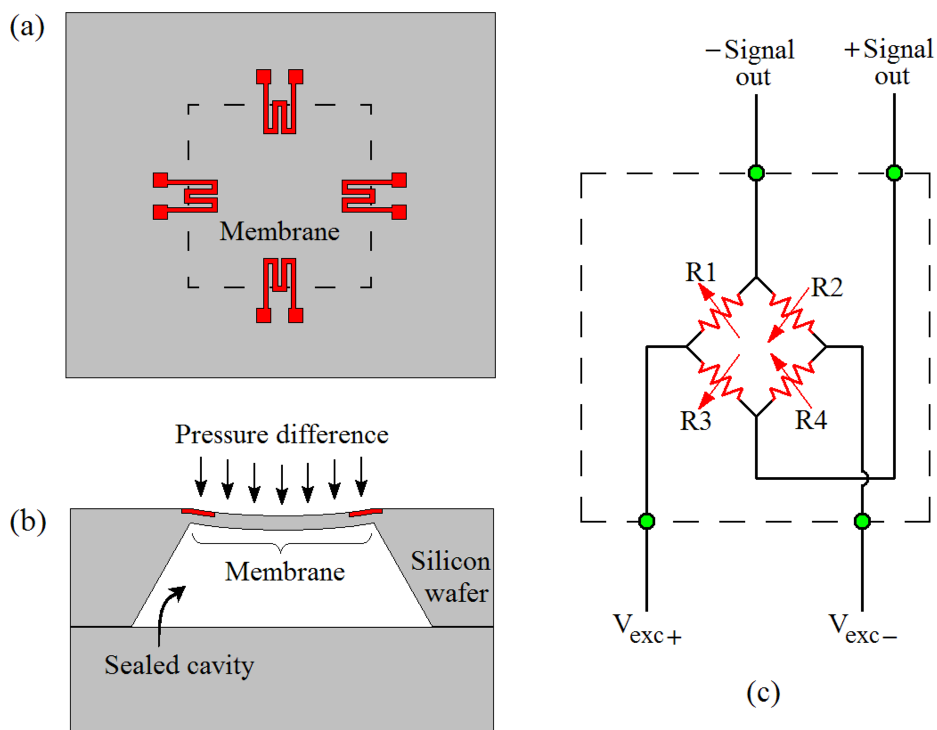

Figure 2.6. Schematic of a piezoresistive pressure sensor: (a) top view; (b) side view; (c) piezoresistive strain gauges connected in a Wheatstone bridge configuration.

piezoresistive MEMS pressure sensor and its equivalent electronics circuit. The Wheatstone bridge configuration is often used for the interface electronics of Piezoresistive MEMS pressure sensors.

In 1954, Smith reported the piezoresistive effect of silicon [63]. The evolution of piezoresistive MEMS pressure sensors started with metallic membrane sensors with bonded silicon piezoresistors, but later crystalline membranes with diffused piezoresistors took over. The first efforts to develop MEMS pressure sensors using piezoresistive micromachined single crystal silicon strain gauges dates back to 1960s. The work by Tufte et al. [64] is one of the earliest of such efforts which reports a MEMS pressure sensor consisting of a single crystal silicon wafer diaphragm having piezoresistive regions formed by localized diffusion of impurities (dopants).

In 1970s, the idea of anisotropically etched silicon membrane was introduced to piezoresistive MEMS pressure sensors which allowed for further miniaturization of the sensors. Samaun et al. [65] used anisotropic potassium hydroxide (KOH) etching of silicon wafer to achieve a single crystal silicon membrane with a thickness of about 5 μm and a diameter of about 500 μm. The sensor achieved a sensitivity of 105 $\mu V\ V^{-1}\ KPa^{-1}$. Utilizing a similar fabrication procedure, Clark and Wise [66] reported a sensitivity of 510 $\mu V\ V^{-1}\ KPa^{-1}$ for a 1 mm^2 square single crystal silicon membrane with a thickness of 10 μm. They also investigated an alternative design of the pressure sensor with a capacitive measurement system and showed that the sensitivity of the capacitive device is approximately an order of magnitude more than that of the piezoresistive one. Furthermore, they showed that the capacitive device is less susceptible to undesired thermal drift effect present in the piezoresistive sensor. So, they concluded that a MEMS pressure sensor with capacitive measurement system is a better candidate for high temperature applications compared to a piezoresistive one.

In 1980s and 1990s, the idea of using MEMS sensors for harsh environment applications started to gain importance in industry. Till this time, the high sensitivity and ease of fabrication of single crystal silicon piezoresistive sensors had led to successful implementation of many MEMS pressure sensors. However, the problem of leakage at high temperatures had limited their applications to temperatures below 150 °C. The leakage occurs at the pn junction that isolates the piezoresistor from the substrate. It can be minimized if an isolating material such as SiO_2 or Si_3N_4 is used between the piezoresistor and the underneath layer. One of the earliest published works on the development of MEMS pressure sensors for high temperature harsh environment applications is that of Petersen et al [67] in which the fabrication of a piezoresistive silicon-based MEMS pressure sensor capable of operation at temperatures between -40 and 250 °C is reported. The sensor was fabricated by a silicon fusion

bonding process. In this process the single crystal silicon piezoresistor elements from one wafer (used as a sacrificial carrier wafer) were bonded to the oxidized surface of a second wafer in which the silicon membrane was anisotropically etched. The intermediate oxide layer electrically isolates the piezoresistors from each other and from the silicon membrane. This guarantees low leakage currents at temperatures as high as 200 °C [68]. The sensor achieved a sensitivity of 145 μV V^{-1} KPa^{-1} and a pressure nonlinearity less than 0.2% for the pressure range of 15 psi (0.1 MPa) to 5000 psi (34 MPa).

To further increase the maximum temperature limit of piezoresistive MEMS pressure sensors, SOI wafers are used instead of silicon wafers. In [69], the piezoresistive properties of polycrystalline silicon and the applicability of SOI wafers for the production of MEMS pressure sensors operating at temperatures up to 200 °C is investigated. Using epitaxial Al_2O_3 films as the isolating material, Chung et al [70] fabricated a high temperature piezoresistive MEMS pressure sensor on hetero-epitaxially grown $Si/Al_2O_3/Si$ SOI wafer. Their device featured a sensitivity of 262 μV V^{-1} KPa^{-1} and worked in the temperature range of -20 to 350 °C with a pressure nonlinearity of 0.18% and a hysteresis of 0.07% for the pressure range of 0 to 93 KPa. Using silicon on sapphire (SOS) substrate, Stuchebnikov [71] reported a piezoresistive a MEMS pressure sensor operating at temperatures up to 350 °C. The sensor measured pressures up to 60 MPa with a pressure nonlinearity less than 0.2% and a hysteresis smaller than of 0.05%.

The problem with using silicon piezoresistors at temperatures above 350 °C is the excessive thermal generation of charge carriers at such high temperatures [72]. Recently, Guo et al [73] demonstrated that by using smart-cut® SOI wafers (featuring a single crystal silicon film less than 0.5 μm in thickness on top of an insulating layer) the maximum operating temperature of a piezoresistive MEMS pressure sensor can be pushed to 600 °C with an acceptable accuracy (below 0.5%) and hysteresis (below 0.1%).

Regarding these efforts, silicon based MEMS technology is already at its maximum temperature limit. Further progress can only be made by using more resilient materials than silicon. For example, [74] reports on the development of a harsh environment MEMS pressure sensor based on piezoresistive effect of boron-doped diamond which works at temperatures up to 250 °C. The membrane of the sensor consists of 5 μm of undoped diamond CVD deposited over a 45 μm silicon membrane with an area of 2×2 mm^2. Boron-doped diamond piezoresistors are deposited and formed on the membrane. The main limitation of diamond piezoresistors at high temperatures is the decrease in their gauge factor with increasing temperature. The highest reported operating temperature for diamond-based

MEMS pressure sensors is 300 °C [75]. To further push the maximum temperature limit of piezoresistive MEMS pressure sensors, SiC has been used extensively. SiC-based piezoresistive MEMS pressure sensors can be categorized into two main groups: 1) SiC-on-silicon devices at which cubic 3C-SiC is deposited on silicon wafer, and 2) SiC-on-SiC devices at which hexagonal 4H- and 6H-SiC are deposited over SiC wafer [76]. The first group can be regarded as a modification to the SOI-based piezoresistive MEMS pressure sensors in that the doped silicon piezoresistive elements are replaced by SiC ones. The membrane and the substrate; however, are still made of single crystal silicon. The limitation on the maximum operational temperature of such devices is due to gradual degradation of silicon mechanical properties at temperatures above 600 °C. This inherent problem is addressed by using the second group devices, i.e. SiC-on-SiC ones. Such all SiC MEMS sensors are investigated for extreme applications such as high-pressure densifiers in jet engines, nuclear power plants, materials processing and space applications.

Piezoresistors are inherently temperature dependent and their output changes with ambient temperature. It is therefore necessary to compensate for this undesired cross-sensitivity to temperature effect. This is usually done by separately measuring the temperature through a second temperature sensor. The two signals are then fed into a signal processing unit which calculates the corrected temperature-independent pressure. This method of compensation is applicable up to the critical temperature at which the resistance value of the piezoresistors drops (around 600 °C for silicon [73]). Substituting piezoresistors with a capacitive measurement system is another method to minimize the temperature sensitivity effect in MEMS pressure sensors. This is because the pressure in a capacitive MEMS pressure sensor is converted to electrical signal by a vacuum capacitor whose dielectric is inherently temperature independent [77].

Capacitive

In a capacitive pressure sensor, a pressure-sensitive membrane is used as the top electrode of a variable capacitor whose bottom electrode is usually fixed to the substrate underneath the membrane. Pressure difference between the two sides deflects the membrane. As a result of this deflection, the gap and the capacitance between the two electrodes change. Figure 2.7 schematically shows a capacitive MEMS pressure sensor which is fabricated using both bulk and surface micromachining methods. A sealed cavity under the electrodes (realized through wafer bonding) provides the reference pressure against which the external pressure is measured. The two electrodes are separated by thin insulator layers.

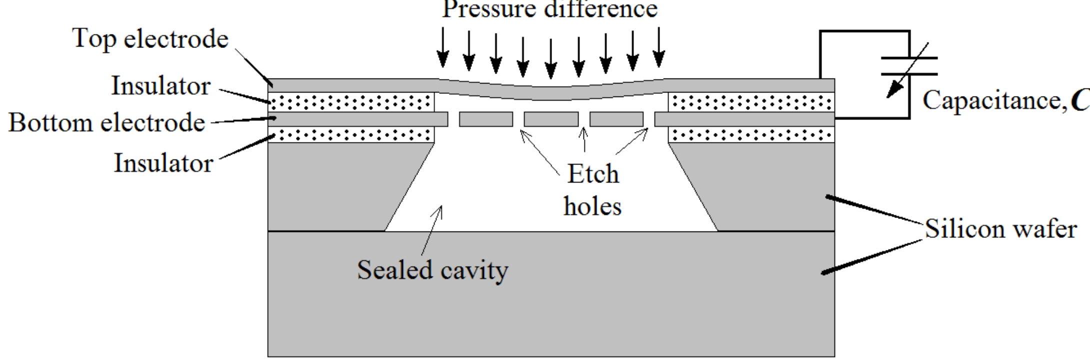

Figure 2.7. Schematic of a capacitive MEMS pressure sensor fabricated using surface and bulk micromachining methods. The top electrode is shown deflected under pressure difference.

Capacitive pressure sensors are advantageous over the piezoresistive ones because they consume less power (the transducer itself consumes no active power), have smaller temperature sensitivity, and are tolerant to contact resistance variations due to temperature change. Moreover, capacitive pressure sensors can achieve higher sensitivities and are less sensitive to environmental variations [78]. In spite of these advantages, excessive signal loss from parasitic capacitances is the major drawback which hindered the development of capacitive MEMS pressure sensors for high temperature applications until on-chip circuitry could be fabricated [79]. However, this solution has its own limitation as the maximum temperature for on-chip signal conditioning circuitry achieved so far is around 500-600 °C, reported by researchers at Case Western Reserve University [80, 1] and NASA Glenn Research Center [20, 81].

The work by Moe et al in 2000 is one of the earliest implementations of silicon-based capacitive MEMS pressure sensor for harsh environment applications [82]. In their work, a pressure sensor for the differential pressure range of 0-100 KPa in oil industry applications was developed. The sensor was fabricated using a triple stack of fusion-bonded silicon wafers. Through bulk micromachining, a bossed membrane with a diameter of 1.8 mm and a minimum thickness of 21 μm was realized. The sensor was successfully tested in temperatures up to 200 °C. To compensate for the ambient temperature variations, a reference capacitor insensitive to the differential pressure and with the same size as the main capacitive pressure sensor was integrated within the design. Having the sensor package filled with oil, the device was reported to achieve a minimum sensitivity of 109 fF KPa^{-1}.

Kasten et al in 2000 reported the fabrication of an array of capacitive MEMS pressure sensors (connected in parallel for bigger capacitive output) based on SOI technology for the measurement of pressures up to 12.6 MPa with ambient temperatures up to 340 °C [77]. To compensate for the parasitic capacitances and the ambient temperature fluctuations, a reference capacitance sensor was added to the design. Distributed over an area of ~ 2 mm^2, an array of 128 circular membranes (60 μm in diameter and 2.5 μm in thickness) achieved a sensitivity of 1.04 fF KPa^{-1} before temperature compensation and 0.91 fF KPa^{-1} after temperature compensation. Later on, they modified the linearity and temperature sensitivity of the sensor by using an on-chip CMOS readout circuit monolithically integrated with the MEMS sensor chip. However, a compromise was made by limiting the new maximum operational temperature of the sensor to 250 °C [83].

Young et al in 2004 reported on a SC-SiC capacitive MEMS pressure sensor. In their sensor, the membrane had a diameter of 400 μm and was realized from a 0.5 μm thick 3C-SiC film epitaxially grown on a silicon substrate [78]. The sensor was used to measure pressures up to 96 KPa in non-contact mode and 332 KPa in contact (touch) mode at temperatures up to 400 °C (limited by the test setup). The average sensitivity the sensor had achieved was around 59 fF KPa^{-1}. Experiments at different temperatures showed that the device had noticeable temperature sensitivity, mostly due to the trapped air inside the sealed cavity and the CTE mismatch between the SiC membrane and the silicon substrate. This necessitated the use of a separate sensor for temperature compensation. In addition, due to the high residual stress in the SiC layer, thicknesses in excess of 0.5 μm could not have been achieved. To solve this problem, replacing the single crystal 3C-SiC film with polycrystalline 3C-SiC was proposed in a follow up work by the same group. However, the modified device still suffered from excessive temperature sensitivity as well as decrease of pressure sensitivity at high temperatures.

In 2008, Chen and Mehregany reported on the successful implementation of an all poly-SiC (membrane and substrate) capacitive MEMS pressure sensor for the measurement of pressure inside the cylinder of an IC engine [1]. In their sensor, the membrane measured 194 μm in diameter and 3 μm in thickness and was equipped with high temperature interface electronics capable of operation at temperatures up to 600 °C. A total of 130 membranes were connected in parallel, over a chip area of ~ 20 mm^2, for amplified capacitive output. Enclosed in a ceramic dual-in-line (DIP) package, the sensor was used to measure static pressures up to around 5 MPa with temperatures up to 574 °C and dynamic pressures up to 0.56 MPa with temperatures up to 150 °C. The dynamic test was carried out

inside a one cylinder test engine running at ω = 750 rpm under partial loads. During the static tests, the sensor achieved a sensitivity of around 1.3 fF KPa^{-1} and a temperature coefficient of 0.05% at the maximum temperature of 574 °C (limited by test setup).

Recently, Jin et al reported on the design and fabrication of a SiC capacitive MEMS sensor for the measurement of pressures up to 4.83 MPa at temperatures as high as 500 °C [84]. The sensor was fabricated in two different configurations: 1) poly-SiC membrane on poly-SiC substrate (SiC-on-SiC, or all SiC), and 2) poly-SiC membrane on silicon substrate (SiC-on-Si). The all SiC and SiC-on-Si configurations (arrays of 260 membranes connected in parallel, each 94 µm in diameter and about 3 µm in thickness) achieved sensitivities of around 0.65 and 0.61 fF KPa^{-1} at room temperature, respectively. No information on temperature coefficient of the sensors was reported in the paper. Moreover, the high temperature experiments reported in this work were carried out in a controlled test chamber with minimum temperature fluctuation.

Optical

Optical pressure sensors are membrane-based sensors whose transduction mechanism is based on optical interferometry. They comprise an optical cavity which is formed between two mirrors: the polished end face of an optical fiber and the bottom side of a pressure-sensitive membrane. The cavity is sealed at a constant reference pressure (ideally vacuum) and any deflection of the membrane due to pressure produces a change in the cavity length which is measured optically. Optical MEMS pressure sensors are inherently immune to electromagnetic interference and can work at very high temperatures since the signal processing can be carried out remotely in a safe environment. Figure 2.8

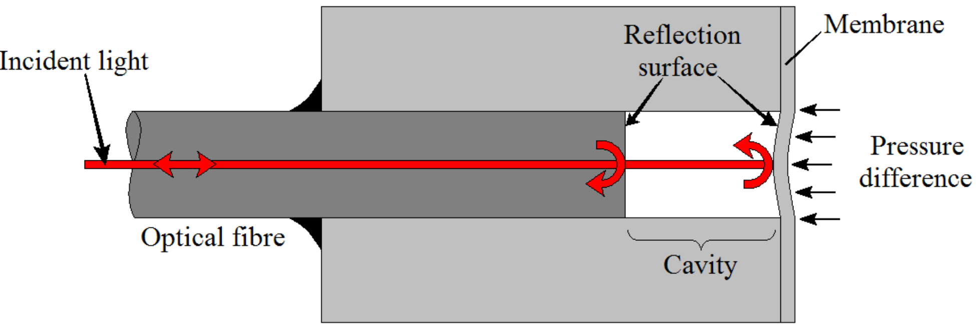

Figure 2.8. Schematic of an optical MEMS pressure sensor based on Fabry-Perot interferometry. The depth of the cavity formed between the reflection surfaces changes with pressure difference.

schematically shows an optical pressure sensor based on Fabry-Perot interferometry. The works by Pulliam et al [85, 86] were among the firsts reporting optical MEMS pressure sensors for harsh environment applications. In these works, hybrid systems based on SiC membrane and sapphire optical fibers were reported. Due to thermal mismatch between the structural materials, these sensors were prone to failure by cracking of the interfaces between their different components [87].

Zhu et al in 2006 reported on an optical MEMS pressure sensor entirely made of fused silica with a maximum working temperature of 710 °C (limited by fused silica creep and fiber dopant diffusion at higher temperatures) and a sensitivity to pressure of 0.22 nm KPa^{-1} [88]. Despite using only one structural material and eliminating the thermal mismatch effect, their sensor showed noticeable temperature sensitivity mainly due to the pressure change of the residual gas trapped inside the cavity with temperature.

In 2009 Ceyssens et al reported on an optical MEMS pressure sensor for the measurement of pressures up to around 0.4 MPa and at temperatures as high as 600 C [89]. The sensor design includes silica optical fiber and amorphous SiO_2/Molybdenum bilayer membrane. Despite the match between the thermal expansions of the sensor's different components and a vacuum-sealed cavity (no residual gas trapped inside), the sensor showed a non-negligible sensitivity to temperature of 0.03% K^{-1}.

Recently, an all-sapphire optical MEMS pressure sensor was reported [90]. The sensor was used for pressure measurement between 0.04 and 1.38 MPa, at room temperature, using white-light interferometry. While no high temperature experiments for the device were reported in the paper, a temperature of 1500 °C was proposed as the maximum functional temperature of the sensor.

Temperature compensation in MEMS pressure sensors

Many MEMS pressure sensors exhibit undesired sensitivity to temperature. In extreme harsh environment applications which are associated with big temperature changes, such as IC engine, this problem is more pronounced. Therefore, some means of temperature compensation are required to be incorporated into the pressure sensor design in order to correct the output signal for temperature effect.

In pressure sensors, two major approaches for temperature compensation are commonly followed. The first approach aims at minimizing the temperature sensitivity through direct modification of the pressure sensor design. Such modifications include for example, fabrication of the sensor from materials with similar CTEs (and ideally from one material) [1, 88], modification of the pressure

sensitive membrane through introduction of corrugation [91-93], or addition of a new material for actively counteracting the temperature effect [94].

The second temperature compensation approach involves measurement of the ambient temperature and cancelling out its effect in the signal processing step. One way of implementing this method was mentioned earlier in the review of the capacitive MEMS pressure sensor by Moe et al [82] at which a reference capacitor insensitive to the measurand (pressure) was integrated within the sensor design to compensate for the ambient temperature variations. The drawbacks of this technique include 1) the need for bigger on-chip property for the reference device, and 2) the undesired inherent difference between the output of the reference device and that of the main sensor (due to differences between their structures). To address these issues, another method is used which involves utilizing a separate temperature sensor to provide supplemental information to the signal processing unit. For the measurements to be as precise as possible, the temperature sensor needs to be as close to the pressure sensor as possible, preferably on the same chip. In IC engine application at which temperature changes happen very quickly and large temperature gradients exist, fast measurement of temperature at the same point where pressure is measured is critical. This implies that the temperature sensor will be exposed to the same harsh environment conditions that the pressure sensor experiences. However, such a fast responding harsh environment temperature sensor has not been reported yet.

2.1.4 Temperature sensors

Temperature measurement in harsh environment applications can be accomplished with a variety of sensors. A brief review of these sensors along with some notes on their applications in harsh environments is provided in this section.

Thermocouple

Thermocouple (TC) consists essentially of two dissimilar electrical conductors joined at one end (called junction). Any change in the temperature of the juncture, with respect to a reference temperature, produces a voltage output roughly proportional to the temperature change. Thermocouples have one of the widest temperature ranges of all available temperature sensor technologies, i.e. -200 to 2300 °C [95]. Ceramic thin film thermocouples have been developed to measure surface temperatures up to 1500 °C [96]. Recently a group of thermocouples with ultrathin junction tips, called surface junction thermocouples have been used in applications in need of fast response time such as heat transfer and surface temperature measurements in IC engine [97, 98].

However, these thermocouples are bulky and their implementation in IC engine requires big holes to be drilled in the cylinder wall [97]. Moreover, their junction gets deteriorated over time (this is why they are sometimes call erodible junction thermocouples) which requires frequent calibration.

Thermostat

A Thermostat is usually formed by bonding strips of two materials with different CTEs together. As a result of temperature change, stress fields develop in the two material layers which cause the whole structure to deform. The deformation is measured and correlated to the temperature change. The maximum working temperature of a thermostat is determined by thermomechanical stability of its structural materials as well as the readout system used to measure its deformation.

Thermistor

Thermistor performance is based on a ceramic material whose resistance varies with temperature. Nagai et al in 1982 demonstrated a thermistor comprising SiC sensing element over alumina substrate with gold- platinum electrodes for measuring temperatures in the range of -20 to 350 °C and with a thermal time constant of 80 sec [99]. Later on, with some modifications, the same group demonstrated a faster SiC thermistor for measuring temperatures as high as 500 °C [100] with a thermal time constant of 1.5 sec. When isolated from harsh environment through encapsulation in a metallic packages (the trade-off would be increased response time), thermistors can measure temperatures as high as 1000 °C, suitable for applications such as automotive exhaust gas temperature sensing [101]. In general, because of their inherent nonlinearity, thermistors are used over narrow temperature ranges, but with high sensitivity.

Resistive temperature detector (RTD)

It is similar to thermistor in performance, but its sensing element is usually made of a metal. In high temperature applications, tungsten and platinum are usually used as the sensing element [102]. RTDs offer good accuracy and linearity over a wider range of temperature than thermistors. Recently, Miyakawa et al has reported on a platinum thin film RTD, coated by CVD deposited SiO_2 and annealed at N_2 atmosphere, for MEMS-based microthruster aerospace applications [103]. Their device has been successfully tested at temperatures up to 1000 °C with good repeatability and small temperature drift, but only for a limited life time of 1 hour.

The major problem with the application of thin film thermistors and RTDs at high temperatures is material degradation in the presence of oxygen [104].

Infrared (IR) sensor

IR sensors (detectors) measure temperature by sensing the thermal radiation emitted by an object. The problem with using IR sensors in harsh environments is that their readout can be easily affected by the surface finish of the object they are aiming at and the presence of dust and particles in the environment. Moreover, these devices are sensitive to the composition of the atmosphere whose temperature they measure.

Other optical temperature sensors

Some other important techniques used for the optical measurement of in-cylinder temperature in IC engines include laser induced fluorescence [105, 106], coherent anti-stokes Raman scattering [107], and Rayleigh scattering [108]. A comprehensive review of these temperature measuring techniques and their drawbacks for in-cylinder operation can be found at reference [109]. One common problem of these techniques is that the optical source is rather bulky and sensitive to temperature. These techniques have proved promising inside laboratories, but their implementation in production IC engines has not succeeded yet.

Another optical sensor recently reported for temperature measurement in harsh environment applications combines Blackbody radiation and laser interferometry [87, 110]. The sensor performs based on the optical signature of a SiC chip in a sintered SiC tube and has been used to measure temperatures as high as 1077 °C. Once more, the bulky components of the sensor have hindered its outside laboratory implementation.

The temperature sensors reviewed in this section can be categorized into two main groups: 1) contact mode devices whose performance is based on conductive and/or convective heat transfer mechanisms and 2) non contact mode devices which work based on thermal radiation. Except for IR sensors, other temperature sensors reviewed in this section belong to the first group. As a general rule for contact mode devices, the smaller they are in size the faster they respond to temperature change. This is because smaller devices have smaller thermal mass as well as larger area-to-volume ratio which facilitates heat transfer. This will be effectively used in Chapter 3 in the design of new multifunctional MEMS sensor.

2.1.5 Failure of available MEMS sensors in harsh environments

Failure of sensing mechanisms due to cross-sensitivity

Cross-sensitivity to undesired parameters, as mentioned in Chapter 1, is a major problem in MEMS sensors working at extreme conditions. One well known example of this problem is the cross-sensitivity to temperature in MEMS pressure sensors which originates from thermal mismatch among the various components of the sensor. Different methods have been deployed so far to address this problem in MEMS pressure sensors, including electronic temperature compensation, selection of materials with similar CTEs, and using corrugated membranes. The electronic temperature compensation schemes are usually accompanied with inherent error which comes from the fact that they are implemented at the pressure sensor's back end where the electronic components are located. In dynamic applications such as IC engine where a considerable temperature gradient may develop through the sensor body, the front end of the sensor (i.e. the pressure sensing membrane) and its back end (where temperature is electronically measured) can experience different temperatures. The selection of materials with similar CTEs could solve the problem of cross-sensitivity only in static applications where a uniform temperature exists. Moreover, it limits the combinations of MEMS materials available for a design. Finally, using corrugated membranes adversely reduces the working pressure range of the pressure sensing membrane. In the new multifunctional MEMS sensor developed in this Thesis, a new method for addressing the problem of temperature cross-sensitivity is proposed.

Degradation of structural materials

The other major problem MEMS sensors encounter in harsh environment applications is the degradation of their structural materials. From a mechanical point of view, MEMS materials lose their elasticity and eventually give way to plastic deformation at high temperatures. Moreover, in a harsh environment application like an IC engine, the cyclic nature of loading could lead to degradation of MEMS materials due to creep. To address these mechanical issues, stronger materials which can survive such harsh environments should be used. In addition to mechanical degradation, the deterioration of electrical properties is also a major concern for the MEMS materials exposed to harsh conditions; examples include redistribution of dopants or reduction of semiconductors bandgap at high temperatures. To solve this problem, wide band gap semiconductor materials or temperature control over the electronics part of the sensor are commonly practiced.

In addition, the degradation of interconnects can also be a limiting factor for harsh environment operation of MEMS sensors, due to diffusion at the material interfaces and changes in the metal/alloy compositions that can lead to non-ohmic contact, for example.

2.2 Multifunctional MEMS sensors

The performance of MEMS sensors in harsh environments faces difficulties due to limited available property area for mounting the sensors, challenging design requirements due to the harsh environments, and demanding computational requirements of orchestrating among multiple MEMS sensors required to simultaneously measure multiple measurands. The solution to these problems is using multifunctional MEMS sensor.

The first approach to implement a multifunctional sensing platform is combining multiple single-tasked MEMS sensors on a single chip (common substrate), called hereafter discrete approach. The result of this approach is a multifunctional chip sensitive to multiple measurands. The second approach, called integrated approach, is based on combining two or more single-tasked MEMS devices into one device which is sensitive to several measurands at the same time. The latter approach results in more complexity compared to the first one; however, on the positive side it enables smaller and more precise MEMS sensors to be realized.

In the following, a review of some recent efforts on developing multifunctional MEMS sensors for harsh environment applications according to the aforementioned categorization is presented. In accordance with the objective of this Thesis, this review mostly focuses on MEMS sensors designed and/or developed for pressure and temperature measurements.

2.2.1 Discrete approach

Berkeley Sensor and Actuator Center (BSAC) at the University of California, Berkeley, in collaboration with researchers from Case Western Reserve University, Ohio, and NASA Glenn Research Center, Ohio, has one of the most prominent research curriculums on multifunctional MEMS sensors for harsh environment applications such as IC engine, geothermal, and power generation. The BSAC efforts on harsh environment MEMS sensors include development of single-tasked MEMS sensors such as SiC resonant strain gauge [111] and SiC resonant tuning fork for accelerometers and pressure sensors [112], high temperature electronics [20], and integration of multiple single-tasked MEMS sensors, along with SiC high temperature electronics, on a single SiC chip for the realization of multifunctional TAPS (Temperature, Acceleration, Pressure and Strain)

sensor (schematically shown in Figure 2.9). The TAPS sensor is supposed to work at temperatures up to 600 °C, pressures up to ~ 7 MPa, High g-shock and corrosive and oxidizing harsh environments [113]; however, no evidence of its completion has been provided yet.

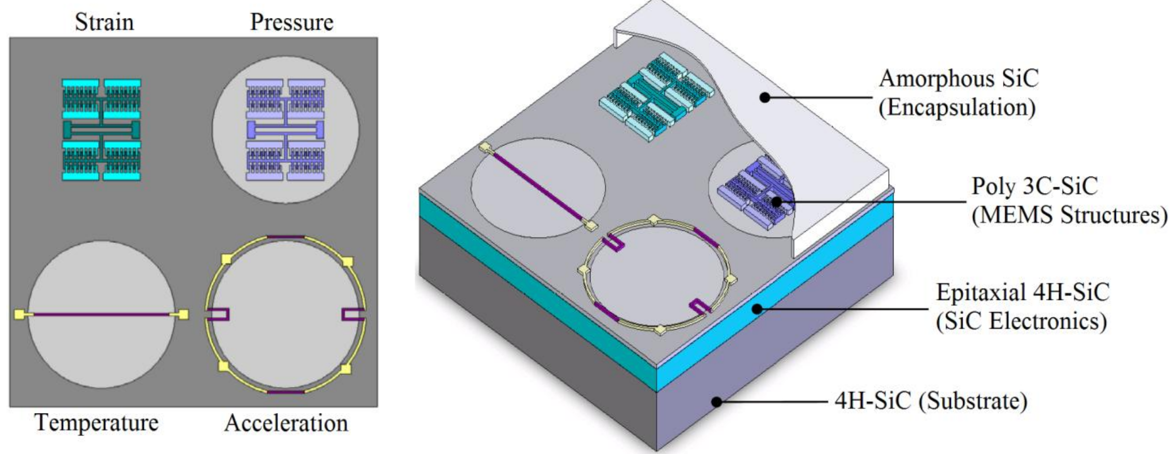

Figure 2.9. Schematic of the harsh environment multifunctional MEMS sensor proposed by Berkeley Sensor and Actuator Center [113].

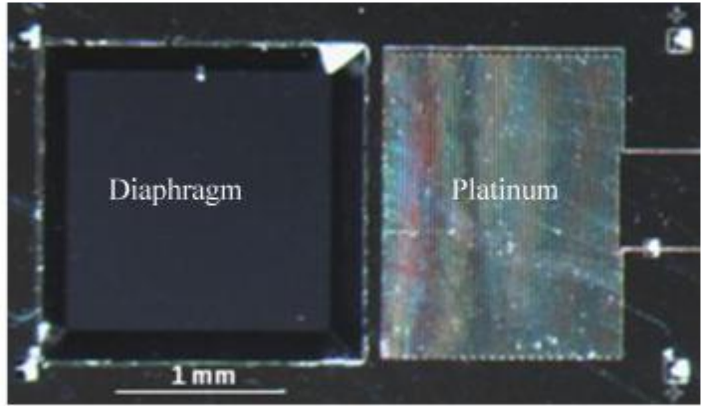

Figure 2.10. A photo of the harsh environment multifunctional MEMS sensor designed and fabricated by researchers at the University of British Columbia. The capacitive pressure sensor silicon diaphragm and platinum RTD are labeled on the photo [114] (figure used with permission).

The research group formed around professor Mu Chiao at the University of British Columbia is another group investigating multifunctional MEMS sensors, based on the distributed approach, for simultaneous measurement of pressure and temperature in harsh environment applications (primarily pulp industry). Its sensor includes a capacitive pressure sensor made by bonding silicon and Pyrex chips using a high temperature bonding adhesive and a platinum thin-film wire RTD patterned on top of the silicon chip [114]. Top view of the sensor is shown in Figure 2.10. To compensate for thermal effects in the capacitive pressure sensor, a second reference pressure sensor with immovable membrane is added to the silicon chip. For protection in harsh environment applications, the final device is embedded into epoxy. The multifunctional sensor has been tested at temperatures up to 170 °C and pressures up to 2 MPa inside an environment test chamber. The maximum error of the sensor was determined as ± 1.74% full-scale output and the average pressure sensitivity was measured as 0.257 fF KPa^{-1}. A piezoresistive version of the device has recently been reported by the same research group which offers a maximum error of ± 0.72% full-scale output and an average pressure sensitivity of 116 μV V^{-1} KPa^{-1} [115].

The distributed approach studied in this section, however, faces difficulties in applications where size matters and/or the measurements need to be carried out at the same location. Moreover, multifunctional sensors designed based on the distributed approach require on-chip electrical connections between their multiple sensing components in addition to and on top of the connection needed to electronics signal processing unit. To address these concerns, the concentrated approach has been pursued through developing new MEMS devices which handle multiple measurements at the same time and location and can be integrated with various measurement techniques such as capacitive and optical.

2.2.2 Integrated approach

The work by Mertens et al [116] was one of the first to investigate the effect of pressure and temperature on the resonance frequency of microcantilevers. The experiments in this work were carried out in atmospheres of helium and dry nitrogen. Based on the results, the authors proposed that in a silicon microcantilever the resonance frequency decreases with temperature increase due to the decrease in Young’s modulus as well as an increase in the length of microcantilever. The authors also showed that the resonance frequency of microcantilevers varies with pressure, mainly due to varying damping effect of ambient atmosphere.

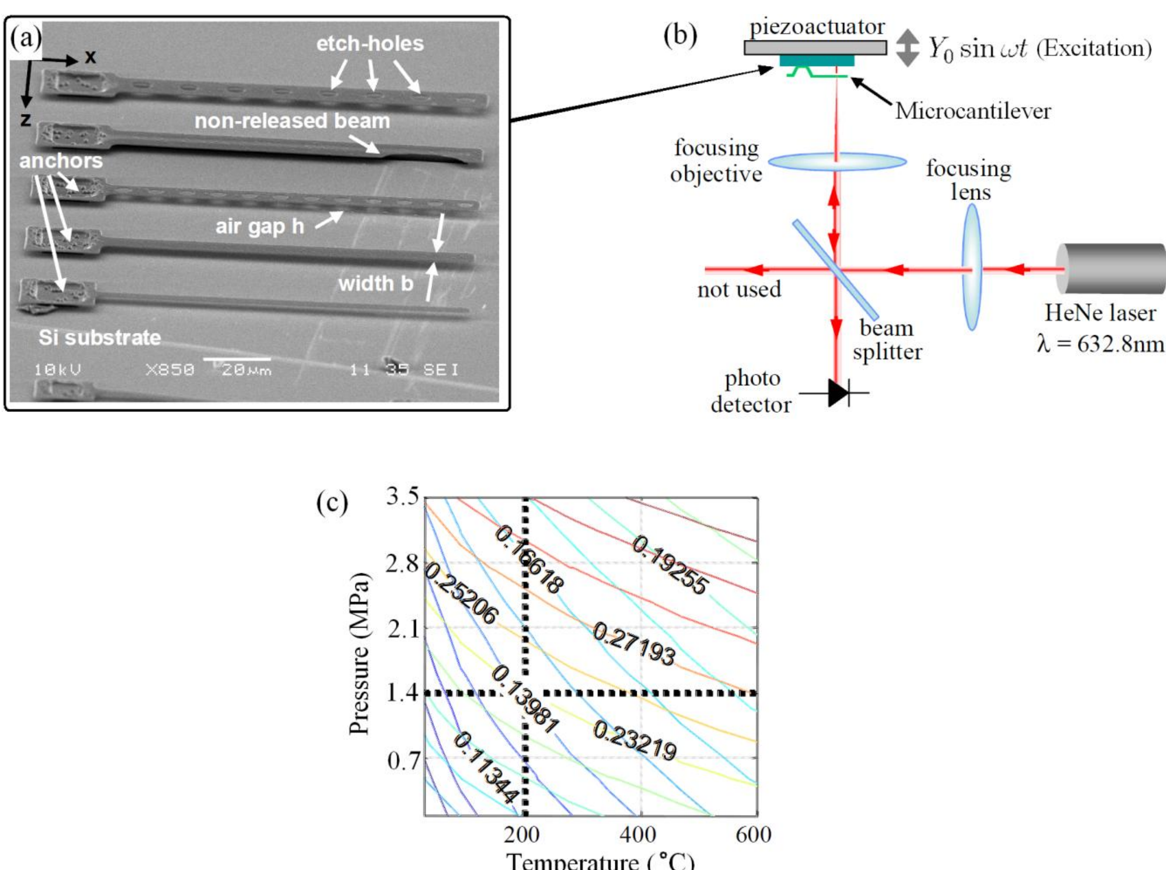

Figure 2.11. Multifunctinoal MEMS sensor for pressure and temperature measurement; (a) SEM picture of array of microcantilevers, (b) optical measurement system, (c) Contour plot of combined outputs showing viscous damping coefficient as a function of ambient pressure and temperature [118] (figure used with permission).

Later on, Sandberg et al showed that for the case of microcantilevers made of thermally grown silicon oxide, the change of dimensions due to thermal expansion has a negligible effect on the shift of resonance frequency of the microcantilevers. They proposed that the temperature dependence of the Young's modulus of silicon oxide is the main reason for the observed frequency shift with temperature [117]. They also studied the resonance frequency of microcantilevers vibrating in a gaseous environment and showed that the resonance frequency decreases with increasing ambient pressure. They suggested that this effect is caused by increase in the effective mass of the microcantilever due to the increased amount of gas molecules moved with the cantilever when it vibrates at higher pressures.

Recently, Nieva et al in 2007 proposed a multifunctional MEMS sensor for the simultaneous measurement of pressure and temperature based on an array of micromachined silicon nitride microcantilevers anchored to silicon substrate (Figure 2.11.a) [118]. Their test setup included a laser source for the characterization of microcantilevers vibration and a piezoelectric actuator for excitation (Figure 2.11.b). The effects of varying temperature and pressure on viscous damping coefficient of air were used to predict the multifunctional output of the sensor (Figure 2.11.c). Based on experimental results, Nieva et al suggested that if two adequately designed microcantilevers are driven at a known displacement and frequency, it is possible to measure and decouple the effect of ambient pressure and temperature. Despite its inherent simplicity and ease of fabrication, their multifunctional MEMS sensor requires a bulky external optical setup as well as a clear optical path for the measurement to be carried out. These requirements, however, make its implementation in harsh environment applications such as IC engine, where particles and combustion products can block the optical path of laser, doubtful. Moreover, since the fragile microcantilever sensing elements are in direct contact with the harsh environment, they are prone to damage.

Chapter 3
Sensor Design

In this chapter, the working conditions inside the cylinder of a typical IC engine are reviewed first. Next, the operational requirements for the new multifunctional MEMS sensor are established. Conceptual design of the sensor which is based on a multifunctional non-planar membrane and a capacitive measurement system is presented next. Finally, a numerical processing scheme for the determination of the pressure and temperature loading based on the capacitive outputs of the sensor is presented.

3.1 Working conditions

3.1.1 Sensor location

Figure 3.1 illustrates the cross-section view of a typical IC engine cylinder. A total of three locations for potential mounting of a MEMS sensor inside the cylinder of an IC engine are identified on this

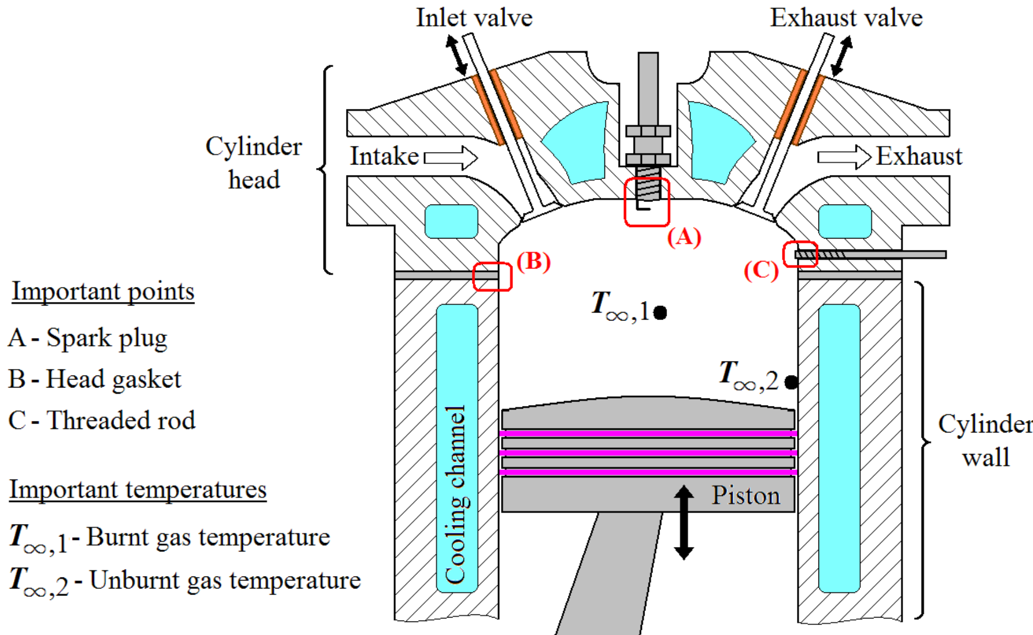

Figure 3.1. IC engine cylinder cross-section view, **(A)**-**(C)** represent the prospective mounting positions for the MEMS sensor and ● marks the characteristic point for temperature measurement.

figure, including (A) spark plug [2, 119], (B) head gasket [120], and (C) threaded rod through the cylinder wall (with the MEMS sensor attached to its end) [1].

The sensor mounting locations identified on Figure 3.1 share the presence of a thermal conductive host for the MEMS sensor which is in thermal equilibrium with the engine body (cylinder head specifically). In a typical IC engine, after warm-up period, the engine body reaches a steady state thermal equilibrium with a mean bulk temperature, T_{bulk}, between 100 °C and 200 °C (127-177 °C [121], 130-180 °C [122], 110-145 °C [123]). The temperature fluctuation over the cylinder interior surface (in contact with combustion products) during the engine combustion stroke is usually smaller than 5 °C [122, 123]. So, it is reasonable to assume that T_{bulk} remains constant throughout engine work period. As a result, all thermally conductive components which are in contact with the cylinder head, such as the spark plug and the threaded rod shown in Figure 3.1, share the same mean temperature as the cylinder head, i.e. T_{bulk}. That said, by properly attaching the sensor to the host component (e.g. by using high-temperature ceramic adhesives such as Ceramabond® family from AREMCO [124] and a similar method as proposed in reference [125]), mean temperature T_{bulk} can be provided to the MEMS sensor's base surface (Figure 3.2). It will be shown in next chapter that maintaining a constant reference temperature on the sensor's base surface is critical to reach a suitable thermal performance. The output signal of the sensor is sent to the engine control unit through a transmission line which is assumed to not affect the thermal performance of the sensor (no noticeable thermal conduction or lost takes place through the transmission line).

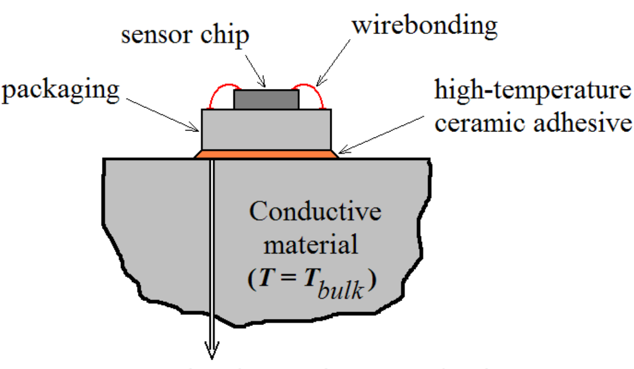

Figure 3.2. MEMS sensor attached to host component with mean bulk temperature T_{bulk}. In the case of in-cylinder MEMS sensor, the host component is either engine block or cylinder head.

3.1.2 Working environment

In a typical IC engine, the air (or air/fuel mixture) drawn into cylinder is usually hotter that the ambient air (e.g. 76-116 °C [123], 90 °C [126]) due to the mechanical work performed on it (for example by a turbocharger) as well as its contact with the hot wall of inlet manifold. To increase the efficiency of the combustion process intercoolers are sometimes used to cool the intake air.

In a naturally aspirated IC engine, the air is drawn into cylinder by the atmospheric pressure acting against a partial vacuum inside the cylinder. For higher volumetric efficiency, turbochargers are sometimes used to force feed the air into cylinder. In such cases, the pressure of the arriving air is slightly higher than the atmospheric pressure. Regardless of such intake pressure variations and considering that the intake pressure is in any case much smaller than the maximum pressure occurring during combustion stroke, in this Thesis it is assumed that the pressure of the arriving air and therefore the pressure inside the cylinder at the start of compression stroke is atmospheric pressure.

After the cylinder is filled and the inlet valves are closed, compression stroke starts. During the compression stroke the average pressure and temperature of cylinder gaseous content increase from their initial values to P_i and T_i at the time of ignition/injection and further to P_{max} and T_{max} at the peak of the combustion stroke. Depending on engine speed, it will take the crankshaft between 4 ms (for a maximum speed of 6500 rpm) to 45 ms (for an idle speed of 600 rpm) to fulfill the compression stroke up to the point of ignition/injection.

Table 3.1 provides more information on the above-mentioned characteristic parameters at several example IC engines. For the HCCI engines reviewed in this table, the end of the compression stroke is determined by finding the point at which the slope of the pressure curve versus crankshaft angle suddenly changes. For the first three cases studied in Table 3.1 (case #1 to #3, shaded rows), the reported temperature is $T_{\infty,2}$ (refer to Figure 3.1) which has been measured with fast responding eroding junction thermocouples. These thermocouples enable a short response time; however, the erosion of their surface junction element by wear continuously changes their response [127] and necessitates frequent calibration. Moreover, the temperature measurements carried out by these thermocouples are approximate and can result in noticeable error (for example, look at the middle panel of Figure 3.4 at which the thermocouple measurement is compared with theoretical prediction. More information can be found in Figure 4.8). For the remaining five IC test engines studied in table 3.1 (case #4 to #8), the reported temperature corresponds to $T_{\infty,1}$ (refer to Figure 3.1), which is either measured by optical methods or theoretically calculated.

Table 3.1. Pressure and temperature at the end of compression and at the peak of combustion strokes in some 4-stroke IC test engines.

<u>IC-engine specifications:</u> (case #) Volume (L) - type (*SI/DI/HCCI*) - # of cylinders -**speed (rpm)**- CR - AFR ; ignition/injection timing - FUEL	Characteristic parameters				Temperature measurement method and location ($T_{\infty,1}$ or $T_{\infty,2}$)	[Ref]
	P_i (MPa)	T_i (°C)	P_{max} (MPa)	T_{max} (°C)		
(1) 0.5-*DI*-1-**1500**-18-NA *; 28° BTDC-DIESEL	1.8	430	6.0	910	thermocouple ($T_{\infty,2}$) **	[128,129]
(2) 0.5-*DI*-1-**2000**-18-NA; 28° BTDC-DIESEL	1.6	584	6.0	1020	thermocouple ($T_{\infty,2}$) §	[97,130]
(3) 0.6-*SI*-1-**600**-8-1.5; 0° BTDC-HYDROGEN	1.5	350	3.7	1500	RTD ($T_{\infty,2}$)	[131]
(4) 0.5-*SI*-1-**1200**-8.3-NA; 30° BTDC-ISO OCTANE	0.27	380	1.4	2630	optical thermometry ($T_{\infty,1}$)	[132]
(5) 1.6-*HCCI*-1-**1000**-17.3-2.7 ₪; 3° BTDC -METHANE	4.8	900	7.5	1700	optical thermometry ($T_{\infty,1}$)	[133]
(6) 7.6-*HCCI*-6-**NA-**22-2; NA- METHANE	6.1	1050	9.7	2100	modeling ($T_{\infty,1}$)	[134]
(7) 3.8-*SI*-6-**1588**-8.25-14.7; 30° BTDC-GASOLINE	2.05	720	4.2	1580	modeling ($T_{\infty,1}$)	[135]
(8) 0.98-*HCCI*-1-**1200**-18-6.7; 0° BTDC-ISO OCTANE	5.0	900	6.5	1240	modeling ($T_{\infty,1}$)	[136]

AFR: air-to-fuel ratio CR: compression ratio BTDC: before top dead center

DI: Direct Injection SI: Spark Ignition HCCI: homogeneous charge compression ignition

* Information not reported in the reference

** The temperatures are directly measured by surface junction eroding thermocouple.

§ The temperatures are calculated using the Newton's law of cooling.

₪ For methane (natural gas) and hydrogen powered engines, AFR is normalized by its stoichiometric value.

During compression stroke, in-cylinder pressure and temperature change gradually due to mechanical work performed. The gaseous content of cylinder is fairly homogenous during compression stroke. So, at any given time during this process the entire cylinder volume can be characterized by a pair of pressure and temperature values. In other words, the pressure and temperature measured by a MEMS sensor during compression stroke can characterize, with a good precision, the entire volume of the cylinder. On the other hand, at the end of compression stroke when ignition/injection takes place the homogeneity inside the cylinder breaks down and a substantial temperature gradient develops [106, 137, 138]. The main reasons for this temperature gradient are the presence of flame front which travels with a speed of 10-20 m/s from its epicenter toward cylinder wall [139] and the formation of thermal boundary layer (also known as unburned gas layer [138]) near cylinder wall [133, 140]. The thickness of thermal boundary layer varies at different locations [138] and can be up to a few millimeters [133, 141].

During working stroke, the temperature of unburnt gas inside the thermal boundary layer ($T_{\infty,2}$ in

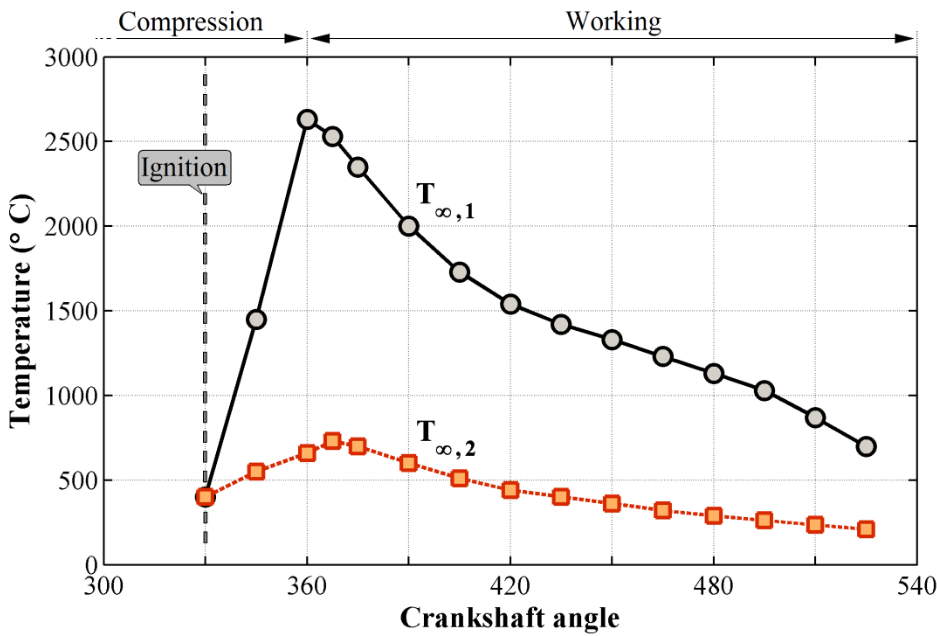

Figure 3.3. Variation of burnt gas temoperature $T_{\infty,1}$ and unburnt gas temoperature $T_{\infty,2}$ (optically measured) with crankshaft angle in an iso-octane powered IC-engine. This figure refers to engine case # 4 in Table 3.1.

Figure 3.1) is noticeably less than that of the mainstream combustion products ($T_{\infty,1}$ in Figure 3.1) [140, 142, 143]. Figure 3.3 shows how $T_{\infty,1}$ and $T_{\infty,2}$ vary with crankshaft angle in an iso-octane powered IC engine (the same engine reported in case # 4, table 3.1). The resulting thermal inhomogeneity lingers on during exhaust stroke as the initial mixing mechanism, i.e. the swirl of the intake air, is disrupted [141]. In other words, following injection/ignition, a single set of pressure and temperature values can no longer characterize the complex situation inside the cylinder.

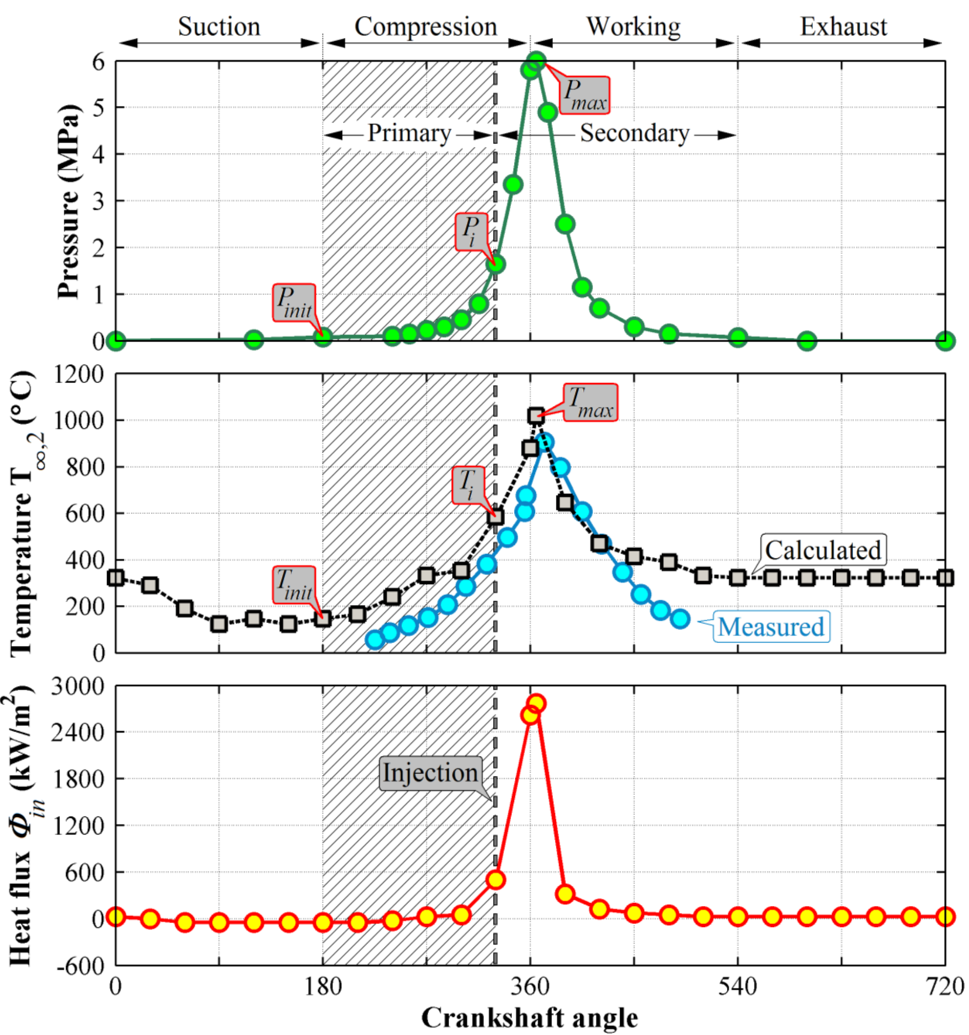

Figure 3.4. Variation of in-cylinder parameters with crankshaft angle in a diesel IC test engine. Directly measured and calculated quantities are shown with ○ and □ symbols, respectively. The primary (hatched section) and secondary working ranges of the sensor are shown in the top panel.

This limits the meaningful working range of any potential sensor developed for the measurement of in-cylinder pressure and temperature, including the multifunctional MEMS sensor developed in this Thesis, to the compression stroke up to the point of injection (or when combustion starts). Figure 3.4 shows how the in-cylinder pressure and temperature vary with crankshaft angle (CA) in an IC engine (the same engine reported in cases # 1 and 2 in Table 3.1). In the middle panel of Figure 3.4, the temperature values directly measured by an erodible junction thermocouple and calculated using the Newton's law of cooling are shown. The calculation of temperature in this figure is based on the assumption that the main mechanism responsible for the heat transfer is thermal conduction. Regardless of the type of IC engine, this assumption is valid up to the point of injection/ignition when the flame initiates and the thermal radiation from the high temperature solid soot particulates emerges [121]. In a diesel IC engine, radiation during working stroke accounts for about 10% to 40% of the total heat transfer from the cylinder while in a gasoline SI engine its share is only about 5 to 10% [121]. The variation of heat flux through the cylinder head with CA is also shown in Figure 3.4 (bottom panel). During the suction and compression strokes ($60° < \mathrm{CA} < 240°$), the heat flux takes negative values which corresponds to reverse heat transfer from hot cylinder head into cooler intake air. Generally speaking, the trends observed in Figure 3.4 can be extended to other IC engines. The data given in Figure 3.4 is used extensively in this Thesis as the reference pressure and temperature loading against which the performance of the designed multifunctional MEMS sensor is characterized. Additionally, the heat flux data given in the bottom panel of Figure 3.4 is widely used in the numerical simulations (appendix B) as the thermal load applied to the sensor.

3.2 Operational requirements

3.2.1 Pressure and temperature working range

The primary operational range of the multifunctional MEMS sensor during which pressure and temperature measurements are carried out covers the compression stroke up to the point of injection ($180° < \mathrm{CA} < 332°$, hatched area in Figure 3.4). During the primary operational range, the in-cylinder pressure and temperature increase from $P_{init} \sim 0.1$ MPa and $T_{init} \sim 125$ ℃ to $P_i \sim 1.5$ MPa and $T_i \sim 580$ ℃, respectively. After injection, as explained before, a considerable temperature gradient develops inside the cylinder which makes the point-wise measurement of temperature irrelevant; however, the in-cylinder pressure still can be meaningfully measured in a point-wise manner. The secondary operational range of the sensor is thus associated with pressure measurement

over the crankshaft angle range of $332° < \mathrm{CA} < 540°$. During the secondary operational range, the in-cylinder pressure and temperature increase from $P_i \sim 1.5$ MPa and $T_i \sim 580$ ℃ to $P_{max} \sim 6$ MPa, and $T_{max} \sim 1000$ ℃, respectively. The secondary range can be further extended to include the exhaust stroke if needed.

3.2.2 Sensitivity and resolution

As the mechanical part of the new MEMS sensor, the multifunctional membrane responds to pressure and temperature variations (the inputs) by adopting a mechanical deformation. The electrical part of the sensor includes two capacitors, formed between the multifunctional membrane and the fixed electrodes underneath, and the onboard electronics for the measurement of these capacitances. The capacitive outputs correlate to the membrane's shape and thus to pressure and temperature inputs.

The sensitivity of a sensor is basically defined as the slope of the output-versus-input characteristic curve. For example, in a capacitive MEMS pressure sensor, the sensitivity to pressure is usually expressed in fF/kPa unit showing how much capacitance change (fF) is observed when a unit pressure change (kPa) occurs. If the sensor's output is not linear with respect to its input, sensitivity should be defined as a local parameter at the corresponding input value. The sensitivity of the multifunctional MEMS sensor depends on the performance of its mechanical and electrical parts. The onboard electronics of the sensor is beyond the scope of this Thesis. So, in order to set and achieve the sensitivity requirements for the sensor we would refer to comparable MEMS devices in literature (which, as will be shown in Chapter 4, will help us determine the minimum area required by the sensor chip). For the case of the multifunctional MEMS sensor, customized definitions for sensitivity to pressure and temperature will be provided in Chapter 4.

The resolution of a sensor refers to the smallest incremental change in the input parameter that can be meaningfully detected in the output signal. In a typical IC engine, the advance/retard setting of ignition/injection is usually carried out with a resolution equal or better than one degree of rotation of crankshaft angle. According to Figure 3.4, around the time of ignition/injection, one degree rotation of CA corresponds to about 80 KPa and 9 °C variation of the in-cylinder pressure and temperature. So, for the multifunctional MEMS sensor to provide precise information for the adjustment of injection/ignition, a pressure resolution better than 80 KPa and a temperature resolution better than 9 °C are required. In this Thesis, it is assumed that the onboard electronics can measure a minimum capacitance change of 1 fF (similar to what the LCR-meter used for the experiments in Chapter 5 provides). This will be used later in Chapter 4 to meet the requirement set here for sensor's resolution.

3.2.3 Ability to follow the input variation rate

In a sensor, response time is the amount of time required for the output to change from its initial value to a new settled value, within a tolerance band of the correct new value, in response to a change in sensor's input. In other words, the response time shows how fast a sensor reacts in response to a variation in its input. A MEMS sensor always includes a mechanical sensing part which transfers the input into a measureable parameter (in our case, pressure and temperature variations are transferred to deformation of a membrane) and an electrical part which converts the secondary measureable parameter into an electrical signal. Each one of these two subsystems requires some time to fulfill its task. In this Thesis, the focus is on the mechanical part; so whenever response time is mentioned the response time associated with the mechanical part is meant.

As will be described shortly, the mechanical part of the new MEMS sensor for in-cylinder pressure and temperature measurement is a multifunctional membrane whose response time relates to the time it needs to undergo a temperature variation (following the in-cylinder temperature variation) and also the time it needs to mechanically respond. The temperature variation part is concerned with 1) convective heat transfer from in-cylinder gaseous content to the membrane, and 2) conductive heat transfer to distribute the input energy throughout the membrane. Though different in nature, these two heat transfer mechanisms are in action at the same time and can not be separated. In Chapter 4, it is shown that thermal conductance in thin films with thicknesses in the order of micrometer is very fast and convective heat transfer is the slower one which determines how fast the sensor performs. A similar argument can be made between the response time due to convective heat transfer to the membrane and that pertained to mechanical deformation. Again, the two processes occur at the same time and the slower one will dominate the total response time of the membrane. Numerical calculations show that for the proposed multifunctional membrane, the total strain energy associated with mechanical deformation is several orders of magnitude smaller than the thermal energy required for temperature change. So, it seems reasonable that we take the heat transfer process as the slower one which dominates the total response time of the mechanical sensing part.

To get some idea about how fast the multifunctional MEMS sensor needs to be for in-cylinder application, Figure 3.5 shows the rates of pressure and temperature variation with crankshaft angle in a typical IC engine (the same engine studied in Figure 3.4). Around the injection time, the rates of pressure and temperature variation are about 80 KPa/deg and 9 °C/deg. Assuming that the variation rates in Figure 3.5 hold true for different engine speeds, for an engine speed of ω = 2000 rpm, the

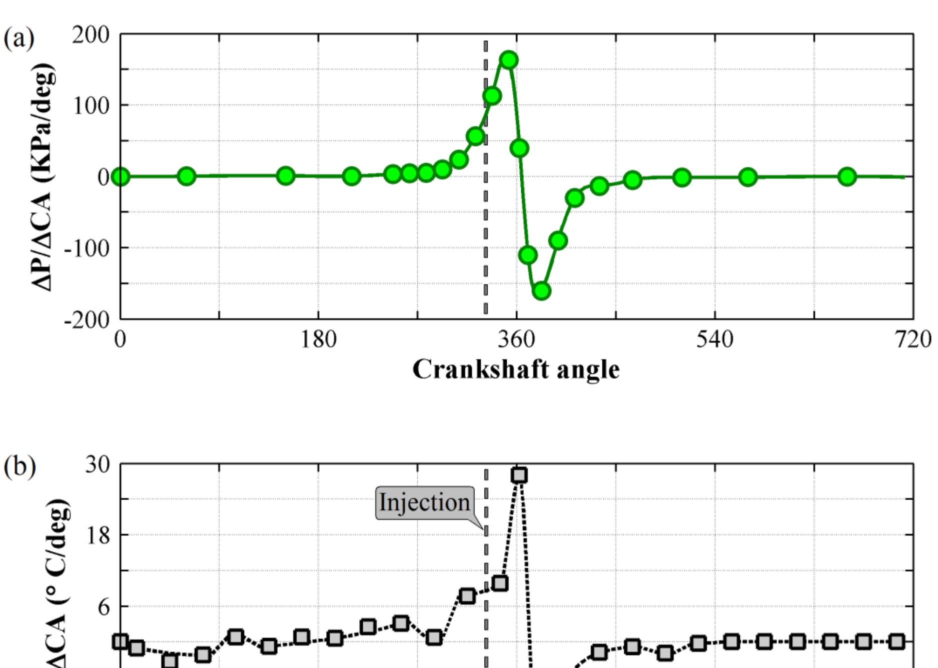

Figure 3.5. Rate of variation of in-cylinder (a) pressure and (b) temperature with crankshaft angle in a typical IC engine.

temperature variation speed at the time of injection ($CA = 332°$) is calculated about 110 °C/ms. This means that the multifunctional membrane should show a temperature variation speed of 110 °C/ms to potentially catch up with the in-cylinder temperature variation trend at $CA = 332°$. In the primary working range of the sensor, this corresponds to the highest temperature variation speed the membrane needs to demonstrate. With the same engine speed of ω = 2000 rpm, the temperature variation speed hits the maximum value of 346 °C/ms at the height of the combustion stroke (equivalent to 28.3 °C/deg around $CA = 360°$ in Figure 3.5).

3.3 Design of multifunctional membrane

Combining the ideas of membrane-based pressure sensing and bimaterial-based temperature sensing, Figure 3.6 schematically presents a multifunctional membrane composed of two planar halves connected through a step feature. The multifunctional membrane is characterized by the lengths

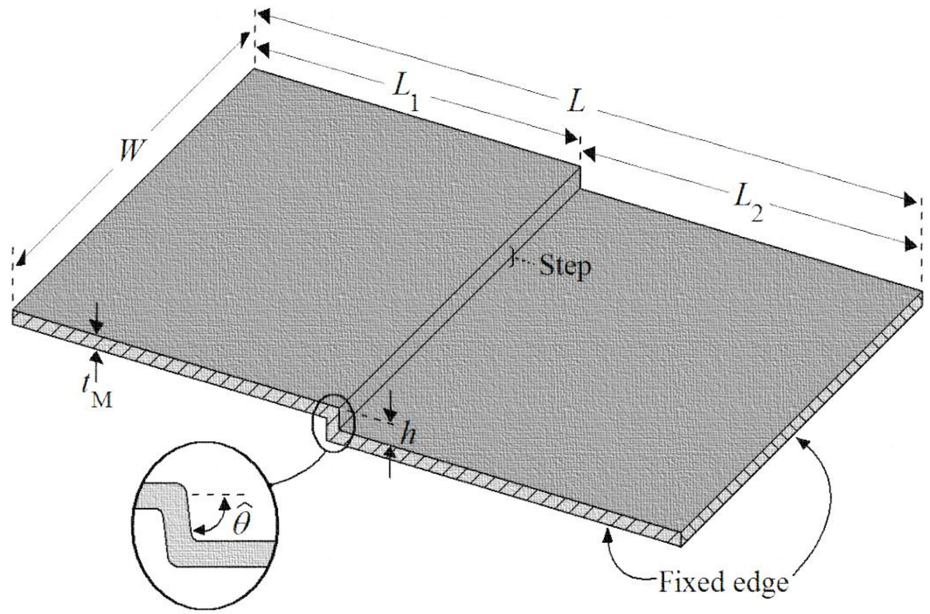

Figure 3.6. Schematic of multifunctional membrane. The edges of the membrane are fixed.

of its halves L_1 (left) and L_2 (right), width W, thickness t_M, and the height of the step feature h. The membrane is fixed on its edges (rigidly anochored to substrate). Below the multifunctional membrane are situated two electrodes, suspended in a vacuum (zero pressure) sealed cavity, which carry out the capacitive measurement (will be described in more detail shortly). The membrane is initially assumed free of any residual stress due to fabrication; however, later in Chapter 4 when the modeling of the membrane is studied this assumption will be partially relaxed and the effect of residual stress will be taken into account. The sensor's response to a temperature increase is based on the assumption that the multifunctional membrane experiences a bigger thermal expansion than the substrate to which it is anchored. The multifunctional membrane's response to pressure increase is a uniform deflection downward analogous to that of other flexible membranes used in MEMS pressure sensors.

3.3.1 Pressure response

When the pressure difference ΔP is applied on the membrane, it deflects downward as depicted in Figure 3.7. The step feature in the membrane functions as a local stiffener and limits the membrane's deflection at its center. As a result, the deformed membrane profile takes a saddle-like shape and the maximum deflection happens at two off-center positions marked by arrows in Figure 3.7.

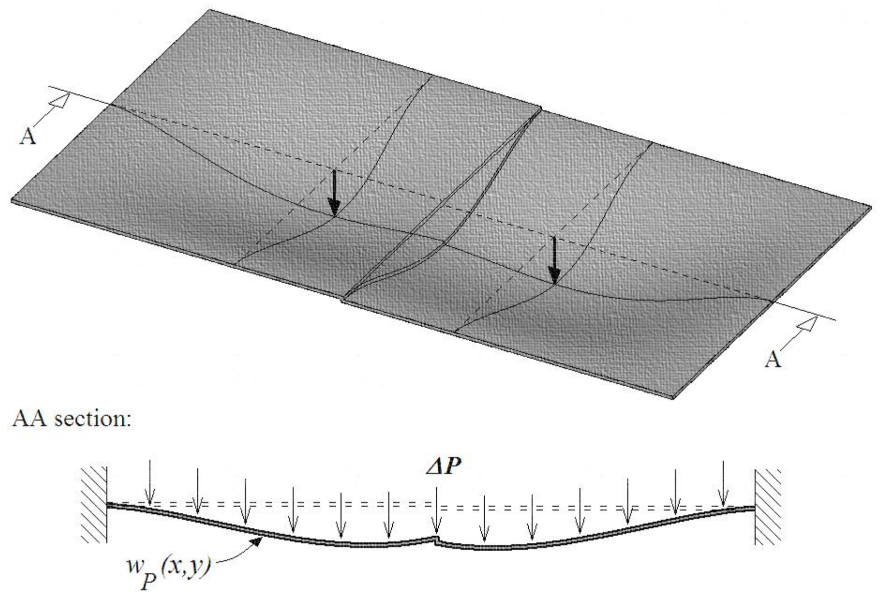

Figure 3.7. Multifunctional membrane deformation due to pressure change Δ*P*.

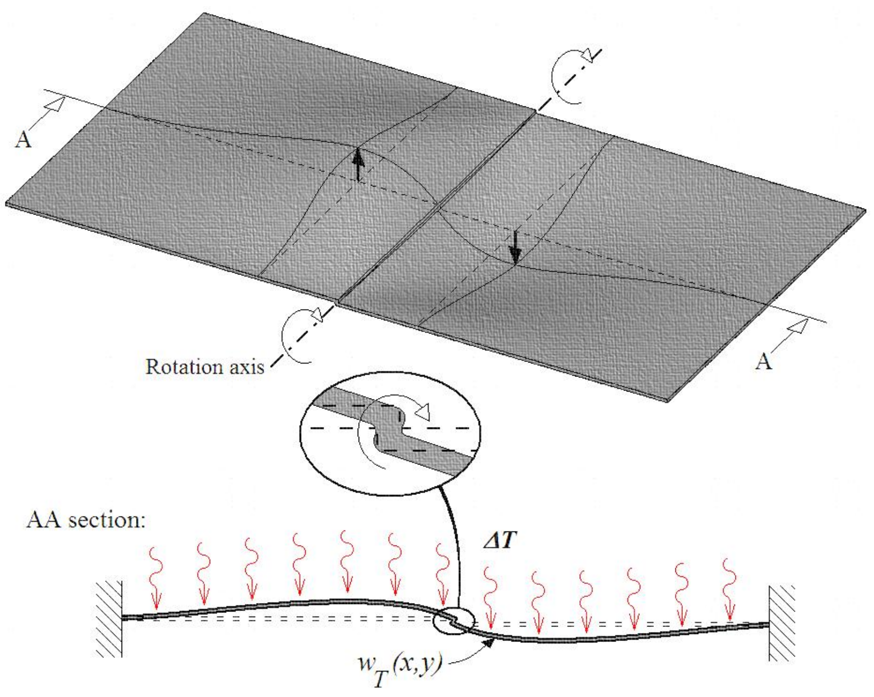

Figure 3.8. Multifunctional membrane deformation due to temperature change Δ*T*. The inset highlights the rotation of the membrane around a rotation axis that passes through the step feature.

3.3.2 Temperature response

When the membrane's temperature increases by ΔT, it demonstrates a bigger thermal expansion than the substrate on top of which it is deposited. Since the membrane's edges are fixed to the substrate, the bigger thermal expansion causes the membrane to deform as schematically depicted in Figure 3.8. The deformation involves both translation and rotation around a rotation axis passing through the step feature. Upon temperature increase, the left side of the membrane deflects upward and the right side deflects downward, with the step feature serving as the rotation axis in between. Such a deformation trend can potentially result in 1) immobility of the center of gravity of the membrane and 2) zero net volume of displaced air over the membrane. These characteristics can be practically used to achieve faster responding devices. In Chapter 4, thermal response of the membrane and the effect of geometrical parameters on it will be investigated in details.

3.3.3 Temperature and pressure combined response

When pressure and temperature simultaneously increase (combined loading), the membrane deformation is more complex than the cases investigated above at which only one parameter changes

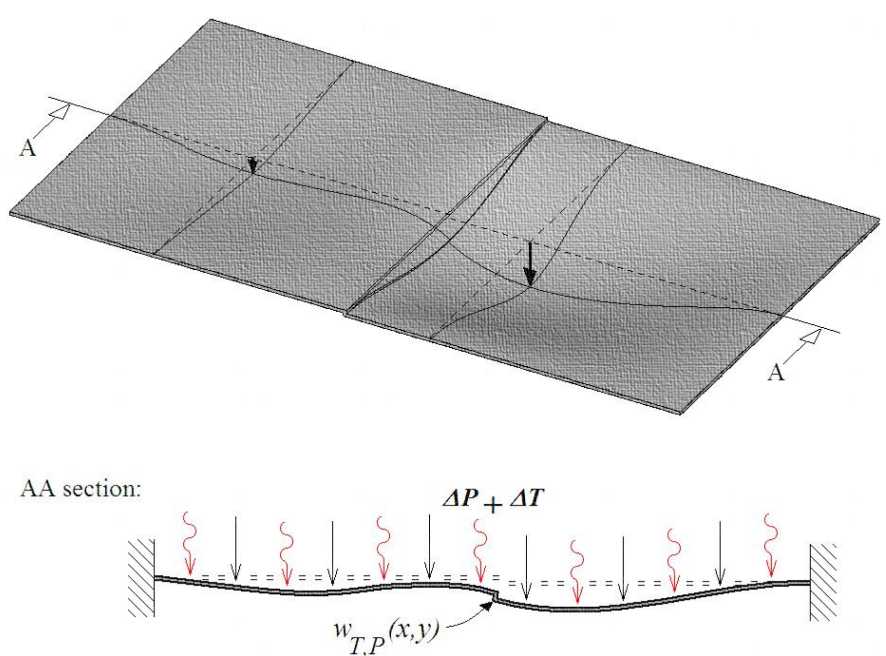

Figure 3.9. Multifunctional membrane response to combined pressure and temperature loading.

at a time. To determine the membrane's deformation when combined loading occurs, the superposition principle can be utilized provided that the deformations are small enough (smaller than the membrane thickness). Consequently, the deformation of each half of the membrane can be regarded as the summation of the deformations it experiences when pressure and temperature loadings are applied separately, as depicted in Figures 3.7 and 3.8. Figure 3.9 schematically shows the deformation due to the combined loading of the multifunctional membrane. On the right half of the membrane, the downward deformations due to pressure and temperature changes agree and add up while on the left half they oppose each other and subtract. In the following section, it will be shown how this unique combination of pressure and temperature induced deformations can be utilized to decouple the effect of and measure the pressure and temperature changes the membrane experiences.

3.4 Implementation of capacitance measurement

The multifunctional sensor design includes two fixed electrodes (referred to as bottom electrodes) situated below the multifunctional membrane. The fixed electrodes form two capacitors C_1 and C_2 with the multifunctional membrane serving as the common electrode (Figure 3.10). The initial gaps (vacuum filled) between the fixed electrodes and the membrane are G_1 and G_2.When pressure and/or temperature change, the membrane deforms and thus the gaps change. This

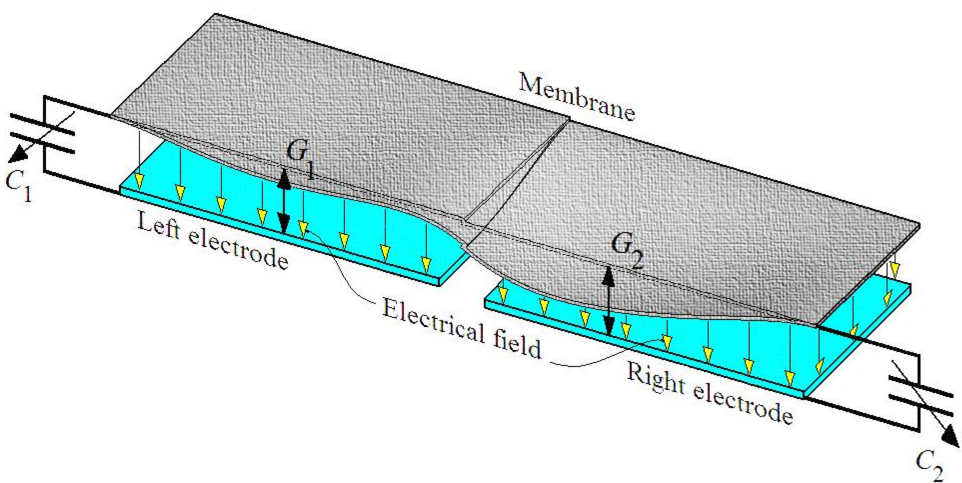

Figure 3.10. Schematic of the deformed multifunctional membrane. Two capacitors C_1 and C_2 are formed between the multifunctional membrane and the bottom fixed electrodes. G_1 and G_1 are the initial gaps (prior to membrane deformation) between the electrodes.

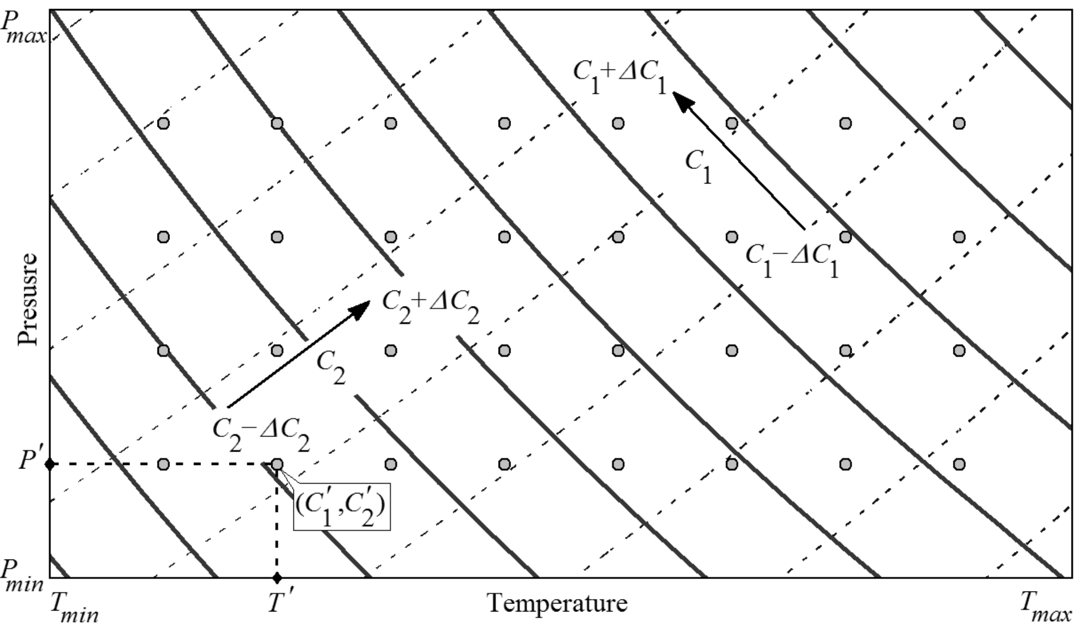

Figure 3.11. Characteristic graph of multifunctional MEMS sensor. One set of inputs (P', T') can be assigned to each pair of outputs (C'_1, C'_2).

results in variations of C_1 and C_2, in line with the deformation of the membrane. For each set of input pressure and temperature values $(\Delta P, \Delta T)$, a unique set of capacitances (C_1, C_2) is measured as the output of the system. The characteristic plot shown in Figure 3.11 represents the relation between the outputs (C_1, C_2) and the inputs $(\Delta P, \Delta T)$ of the multifunctional sensor. The pressure and temperature working ranges of the MEMS sensor are identified on this figure as $(P_{max} - P_{min})$ and $(T_{max} - T_{min})$, respectively. The dotted and the solid lines in Figure 3.11 relate to equal capacitance curves associated with C_1 and C_2, respectively. The characteristic plot of Figure 3.11 enables the electronics part of the sensor to calculate the pressure and temperature loading according to the capacitive outputs. To achieve this, it is only required to find the point (C_1, C_2) in the characteristic plot of the sensor and then determine the corresponding values of P and T. The procedure is shown in Figure 3.11 where (C_1', C_2') is correlated to (P', T').

3.5 MEMS sensor

So far, the design of multifunctional membrane and its integration with capacitive measurement have been addressed. For these components to function as a MEMS sensor, a carrier substrate and a

vacuum sealed cavity under the membrane are also required. Figure 3.12 schematically shows how these components are combined and what the final MEMS sensor looks like. The fabrication process custom designed for this device is described in details in appendix A. In brief, it includes bulk micromachining of silicon substrate to create the cavity (e.g. with DRIE process which creates vertical sidewalls), wet etching of the sacrificial layer to release the fixed electrodes under the multifunctional membrane, and wafer to wafer bonding of the chips (both SiO_2-SiO_2 and Si-Si bonding interfaces are considered).

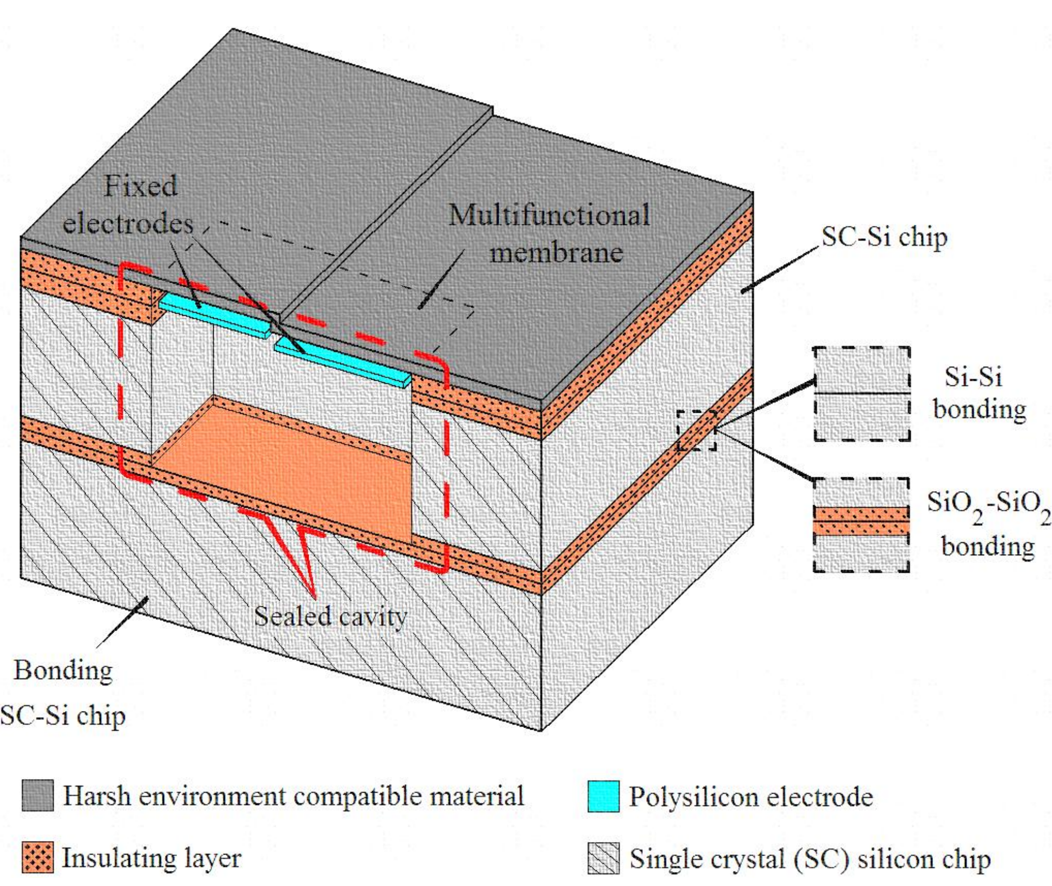

Figure 3.12. Schematic representation of multifunctional MEMS sensor. For better visualization of sealed cavity and fixed electrodes, half of sensor is shown in this figure.

Chapter 4
Modeling and Analysis

In this chapter, different aspects of the modeling and analysis of the multifunctional MEMS sensor are investigated using analytical and numerical approaches. The analytical modeling evolves around the classic beam theory. Modified by introducing some modification factors, the analytical modeling is used in the analysis of the multifunctional membrane. Due to its mixed nature, the analytical modeling is referred to in this Thesis as semi-analytical approach with the distinctive advantage of reduced processing time. Following verification with numerical simulations, the semi-analytical approach is used in the structural and electrical modeling and analysis of the multifunctional MEMS sensor. Moreover, it is used for sensitivity analysis of the sensor. The numerical modeling, on the other hand, relies on finite element (FE) simulations carried out by the commercial FE software ANSYS®. Regarding the type of the modeling, different element types and modules of the software are used in this Thesis with details given in corresponding sections. The ANSYS® software is also used for the transient thermal analysis of the sensor's response to in-cylinder conditions (Figure 3.4).

4.1 Thermal modeling

In this section, convective and conductive heat transfers involved in the thermal performance of the multifunctional MEMS sensor are modeled and analyzed. The results of FE numerical simulations in this section provide useful information on the average temperature and temperature variation of different components of the sensor during its working cycle (the in-cylinder thermal scenario of Figure 3.4 is used in this section as loading). This information is used in the selection of the right structural materials and the optimization of the sensor's dimensions in order to meet the operational requirements set in the section 3.2.

Figure 4.1 provides an insight into the thermal energy trade between the multifunctional MEMS sensor and its surrounding medium. The configuration of the multifunctional MEMS sensor introduced in Figure 3.12 is used in this section. Throughout the thermal modeling section, the presence of the step feature in the multifunctional membrane is ignored and the membrane is simply assumed planar. Moreover, the effect of the fixed bottom electrodes (Figure 3.12) on thermal response of the sensor is ignored in this section, mainly due to their small thermal mass and isolation from the main heat transfer path (Figure 4.1).

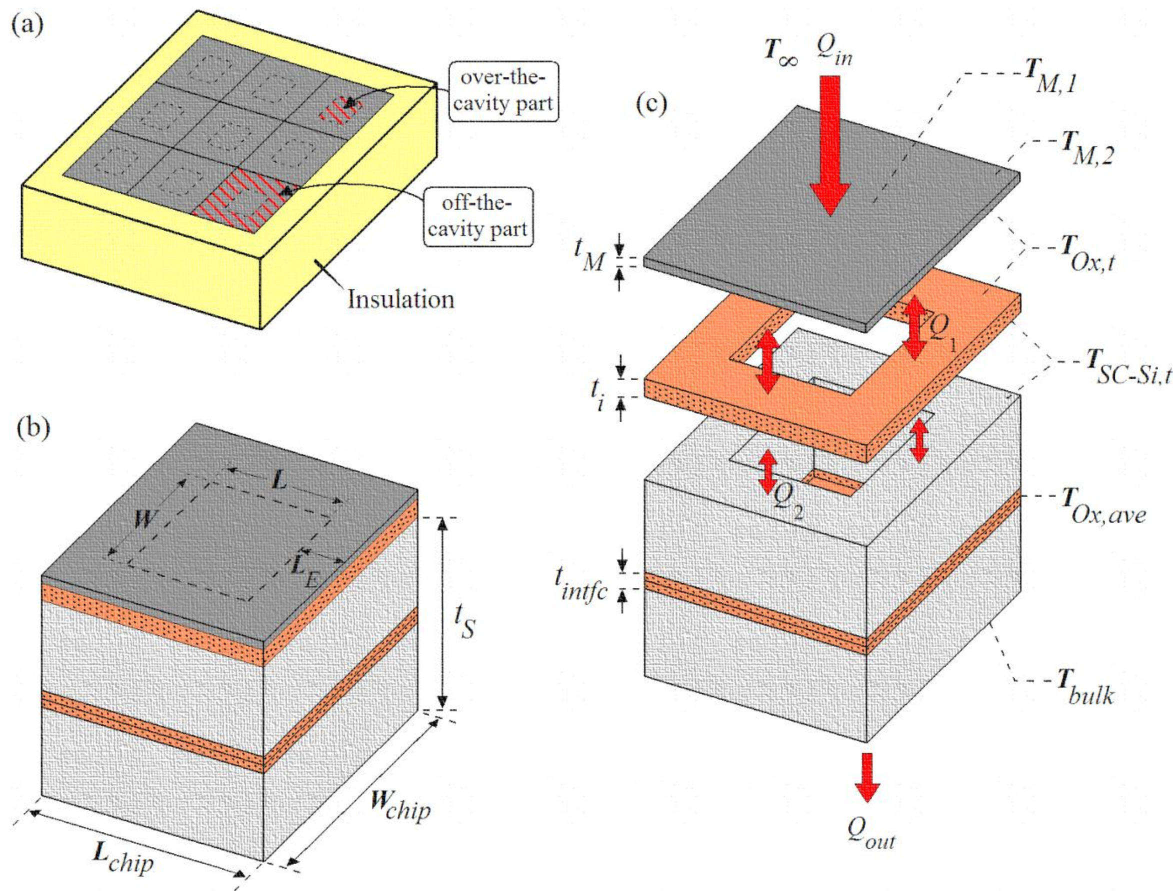

Figure 4.1. (a) Array of multifunctional sensor cells connected in parallel, (b) enlarged view of a single cell, (c) exploded views of the sensor cell showing the thermal transfer between different components; Q, t, and T represent energy, thickness, and temperature, respectively.

As a common practice in capacitive MEMS sensors, in order to get a stronger output signal several devices are usually connected in parallel [1]. This approach is also used in this Thesis, as shown by the array of sensor cells in Figure 4.1.a. Moreover, the sides of the sensor chip are assumed isolated from the in-cylinder harsh environment by a specific packaging. That said, only the top surface of the sensor surface, which happens to include the multifunctional membrane, is in contact with the in-cylinder harsh environment. Furthermore, as will be explained shortly the bottom surface of the sensor is assumed to maintain a reference temperature throughout the sensor work. Taking all these into account, the only path for heat transfer into and from the sensor is through its top and bottom surfaces, respectively.

As the in-cylinder temperature increases during the compression stroke the MEMS sensor absorbs some thermal energy (Q_{in} in Figure 4.1). In this process, convective heat transfer plays the major role in transferring thermal energy from the hot ambient gaseous content ($T = T_{\infty}$) into the sensor cold top surface ($T = T_M$). At the same time that the convective heat transfer works to provide thermal energy into the sensor, conductive heat transfer distributes the arriving thermal energy among the different components of the sensor. The conductive heat transfer inside the sensor is identified in Figure 4.1.c by Q_1 and Q_2, representing the heat transfer between the membrane and the insulation layer and between the insulation layer and the substrate, respectively. Finally, Q_{out} represents the conductive heat transferred from the sensor bottom surface (base) into the underneath material. The important characteristic time-varying temperatures of the different components of the sensor are identified in Figure 4.1 as

- $T_{M,1}$: average temperature of the membrane layer suspended over the cavity,
- $T_{M,2}$: temperature of the top surface of the membrane layer off the cavity,
- $T_{Ox,t}$: temperatures of the top surface of the insulating layers (the same as the temperature of the bottom surface of the membrane layer off the cavity),
- $T_{SC-Si,t}$: temperatures of the top surface of silicon substrate (the same as the temperature of the bottom surface of the insulating layers),
- $T_{Ox,ave}$: average temperature of the bonding SiO_2-SiO_2 interface between the SC-Si chips,
- T_{bulk}: constant reference temperature at sensor's base (the same as the cylinder head temperature after engine warm-up).

Here it is assumed that the temperatures of the adjacent layers on their common surface are equal. Moreover, the membrane is assigned two different temperatures $T_{M,1}$ and $T_{M,2}$ to account for the potential internal heat flow between its over-the-cavity and off-the-cavity parts (the latter can thermally communicate with the underneath insulating layers).

Biot (Bi) number is a dimensionless parameter used in transient heat transfer analysis and is defined as the ratio of the heat transfer resistance inside a body to the heat transfer resistance on its surface. In MEMS devices, owing to small thickness and high thermal conductivity of thin films, the Bi number is usually very small (e.g. Bi numbers as low as 0.01 have been reported for SiC-based devices [144]). A small Bi number suggests that the temperature gradient through the thickness of the corresponding structure is negligible. This allows for assuming that the system behaves like a lumped

one. For the case of multifunctional MEMS sensor, a similar discussion holds true for the over-the-cavity part of the multifunctional membrane. Accordingly, a single temperature value, i.e. $T_{M,1}$, can be used to fully characterize the temperature of that part of the membrane (FE simulation confirms that no noticeable temperature gradient through the thickness of that part of the membrane does exist).

Idealizing the multifunctional membrane as a lumped element with uniform temperature T_M, its thermal behavior can be approximated by the Newton's law of cooling:

$$\frac{dQ_{in}}{dt} = h_{th}A[T_\infty - T_M] \tag{4.1}$$

where h_{th} is the heat transfer coefficient between the multifunctional membrane and the in-cylinder harsh environment and A represents the surface area of the membrane which is in contact with the in-cylinder harsh environment (based on Figure 4.1 equals $L \times W$ for over-the-cavity and $L_{chip} \times W_{chip} - L \times W$ for off-the-cavity part of the membrane). Since T_∞ and T_M vary with time, equation (4.1) can be used to characterize the instantaneous thermal behavior of the system. In the ideal case scenario where the multifunctional membrane is completely isolated from the substrate, all the input energy Q_{in} will be consumed to heat the membrane up (FE simulation shows that the strain energy associated with the deformation of the multifunctional membrane due to thermal loading is several orders of magnitude less than the total input energy). That means no portion of Q_{in} is conducted out or $Q_1 = Q_2 = Q_{out} = 0$ in Figure 4.1. In such a case, the conservation of energy necessitates

$$Q_{in} = mC\Delta T = \rho A t_M C \Delta T \tag{4.2}$$

where ρ and C are the density and the specific heat of the membrane material, respectively, and t_M denotes its thickness. The term $\rho A t_M C$ on the right hand side of equation (4.2) is called the thermal mass of the system.

Heat flux in a thermal system is defined as the rate of the thermal energy passing through a unit surface area on the system boundary. So, for the case of multifunctional membrane, the associated heat flux is expressed as

$$\emptyset_{in} = \frac{Q_{in}}{A\Delta t} \tag{4.3}$$

Combining equations (4.2) and (4.3) gives

$$\emptyset_{in} = \rho t_M C \frac{\Delta T}{\Delta t} \tag{4.4}$$

Holding to the idealization that all the input thermal energy is used to change the temperature of the membrane, equation (4.4) sets an upper limit on the membrane's maximum achievable temperature variation rate, or simply temperature rate. The thermal efficiency of the membrane η is defined as

$$\eta = 1 - \frac{Q_1}{Q_{in}}, \tag{4.5}$$

The thermal efficiency η varies between 0 and 1 and shows how much of the input heat energy is used by the membrane to change its temperature. Alternatively, $1 - \eta$ suggests how much of the input energy is conducted out of the membrane. The ideal thermal scenario mentioned above corresponds to

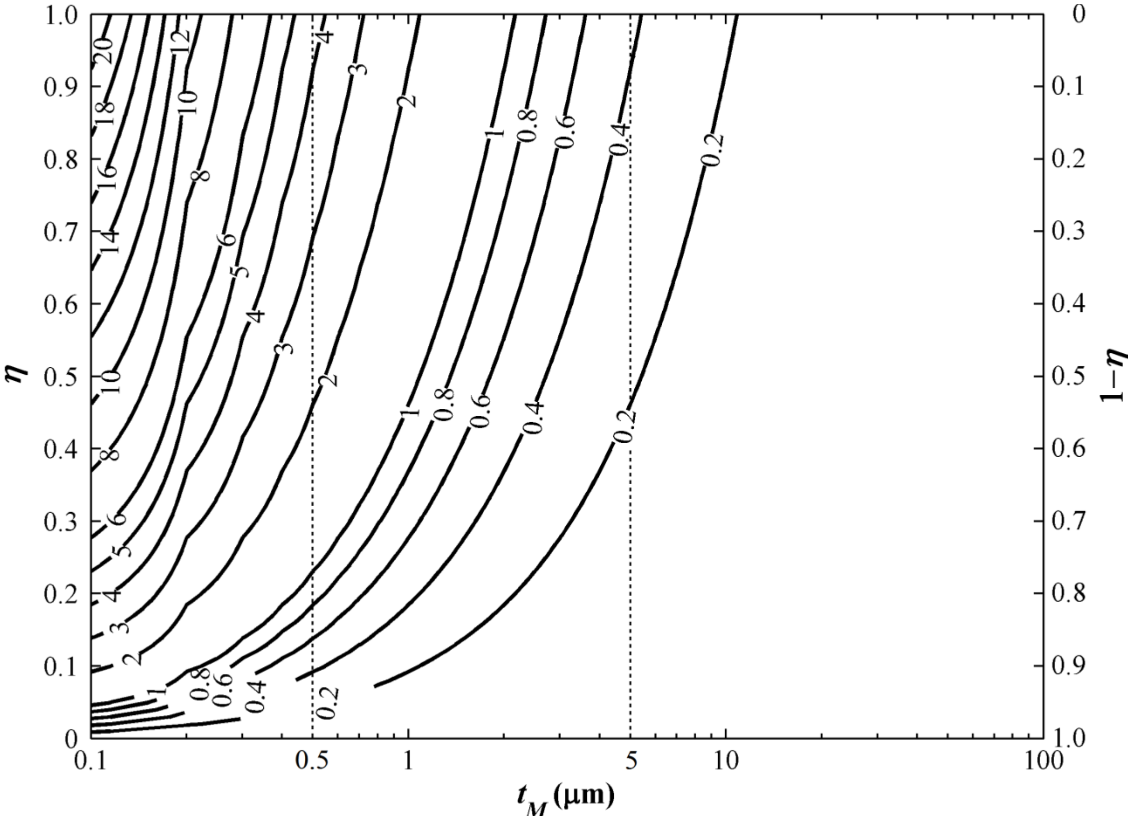

Figure 4.2. Temperature variation rate of a SiC membrane versus CA rotation, i.e. ΔT/ΔCA in (ºC/deg) unit, for different values of t_M and η ($Q_{in} = 25\text{kW/m}^2$, ω = 600 rpm).

$\eta = 1$. Using equations (4.4) and (4.5), Figure 4.2 shows the temperature variation of a SiC membrane versus crankshaft angle rotation, i.e. in (ºC/deg) unit, for various values of η and t_M. The temperature variations in Figure 4.2 are calculated for the case with $Q_{in} = 25\ \mathrm{kw/m^2}$ and the engine speed ω = 600 rpm. In order to develop a better understanding of the effect of the thickness of membrane, a broader thickness range than targeted in this Thesis, i.e. 0.1-100 µm, is analyzed here. According to Figure 4.2, for the ideal case scenario where $\eta = 1$, the maximum temperature rate is around 4.5 ° C/deg for a SiC membrane with $t_M = 0.5$ µm and around 0.4 °C/deg for $t_M = 5$ µm. The results shown in Figure 4.2 can be modified to accommodate other Q_{in} and ω values according to

$$\frac{\Delta T}{\Delta CA} = \frac{\eta \emptyset_{in}}{\rho t_M C} \times \frac{1}{6\omega} \tag{4.6}$$

Equation (4.6) suggests that a high $\emptyset_{in}$ allows for the membrane to experience a bigger temperature variation ΔT. Moreover, it shows that a higher engine speed adversely affects the thermal performance by reducing the time the membrane has to undergo temperature change. Referring to the data in Figure 3.4, the temperature variation rate in a typical IC engine cylinder is about 3 °C/deg at $\mathrm{CA} = 270$ and about 9 °C/deg at the time of injection ($\mathrm{CA} = 332$). The $\emptyset_{in}$ associated with these instances, according to the same figure, are about 25 kW/m^2 and 500 kW/m^2, respectively. Using $\emptyset_{in} = 500\ \mathrm{kW/m^2}$ in equation (4.6), one for example finds that a SiC membrane with $t_M = 0.5$ µm and $\eta = 0.33$ can achieve a maximum temperature variation rate of about 9 °C/deg at the time of injection ($\mathrm{CA} = 332$) with an engine speed of ω = 2000 rpm. Equation (4.4) suggests that for a given input heat flux, the thermal response time (i.e. the time Δt needed for the membrane to undergo a temperature change of ΔT) can be reduced by lowering the thermal mass of the multifunctional membrane. This can be achieved by

- selecting a material with lower density,
- selecting a material with smaller specific heat,
- reducing the thickness of the membrane.

Additionally, as mentioned earlier, the membrane is required to possess a small Bi number. Defining the thermal diffusivity D as the ratio of thermal conductivity to density multiplied by specific heat, i.e. $D = k/(\rho C)$, the above requirements for minimizing the thermal response time of the multifunctional membrane can be combined and summarized into a need for a thin membrane fabricated from a high thermal diffusivity material.

As highlighted in Chapter 2, the successful application of other MEMS materials than SiC in harsh environments is hindered mostly by their chemical instability at high temperatures (diamond burns, AlN oxidizes, and GaN dissociates). So, from a stability point of view SiC stands out as the most promising material for realizing robust harsh environment MEMS. Calculations show that SC-SiC demonstrates the second highest thermal diffusivity after diamond over the temperature range of 300-1000 K, while it also provides a reasonable chemical stability for harsh environment applications. Among the different crystalline variations of SiC, a membrane made in SC-SiC would offer the fastest thermal response time. However, deposition of SC-SiC film is a slow process and requires very high substrate temperatures [145] which make it a formidable task. Moreover, as will be investigated in details shortly, the high thermal conductivity of SC-SiC contributes to two contradicting effects: 1) faster thermal diffusion through the thickness of the multifunctional membrane, and 2) increased thermal flow from the over-the-cavity part of the multifunctional membrane toward its cooler off-the-cavity part which thermally communicates with the underneath insulating layer (Figure 4.1). The latter effect negatively affects the thermal performance of the sensor by increasing the heat flow to the insulating layer. The possible solution to this complex problem is using other crystalline structures of SiC whose deposition process is less demanding and result in films with lower thermal conductivity. To shed more light on the issue the effect of such variations in the material properties of SiC on the thermal performance of the multifunctional membrane will be numerically investigated in the following section.

As mentioned earlier, the ideal thermal scenario for the multifunctional membrane is that no heat transfer occurs between the membrane and the underneath insulation layer and all the input thermal energy Q_{in} is used to increase the temperature of the membrane. But in reality, the heat transfer between the membrane and the insulating layer does exist and its associated heat flux can be expressed as

$$\emptyset_1 = \frac{dQ_1}{A'dt} = k_i \frac{dT}{dz} \tag{4.7}$$

where $A' (= L_{chip} \times W_{chip} - L \times W)$ is the contact area between the membrane and the insulating layer, k_i is the thermal conductivity of the insulating layer material, and z refers to the vertical direction (positive downward). Assuming a linear temperature distribution through the thickness of the insulating layer, equation (4.7) can be rewritten as

$$\emptyset_1 = k_i \frac{T_{Ox,t} - T_{SC-Si,t}}{t_i} \tag{4.8}$$

where t_i represents the thickness of the insulating layer. Equation (4.8) suggests that the undesired conductive heat transfer from the membrane to the insulating layer can be reduced by minimizing the thermal conductivity of the insulating layer and by increasing the thickness of the insulating layer. Moreover, decreasing the contact area between the two layers increases the contact resistance and thus makes the heat transfer harder. Among the different MEMS materials reviewed in Chapter 2, SiO_2 stand outs as the ideal insulating candidate due to its ease of deposition, smaller thermal conductivity compared to the other candidate Si_3N_4, and possibility of its application as the bonding interface material as well. So, SiO_2 is selected in this Thesis for the insulating layer. The effect of the SiO_2 insulating layer thickness on thermal performance of the sensor will be quantitatively investigated in the next section. Moreover, for the sensor substrate material, SC-Si is the default choice due to the maturity and availability of the processing technology. So, the standard thickness of 4- and 6-inch SC-Si wafers, i.e. 525 µm and 700 µm, are used in this Thesis for the substrate chips, i.e. t_S in Figure 4.1.

4.1.1 Results and optimization

In the previous section, the ideal combination of layers/materials for a fast-responding multifunctional MEMS sensor was determined as: a thin SiC layer for multifunctional membrane (to minimize thermal mass while maintaining chemical and physical robustness), a thick insulating SiO_2 layer between the multifunctional membrane and the substrate (to minimize thermal cross-talk between them), and a SC-Si substrate chip.

In this section, the numerical results of thermal simulations using ANSYS® FE software are presented. The thermal models are meshed using SOLID70 which is a 3D thermal element with eight nodes and a single degree of freedom, temperature, at each node. The temperature-dependent properties reviewed in Chapter 2 are used in FE simulations. For thermal boundary conditions, the top surface of the sensor is subjected to the thermal loading (ambient temperature and heat flux) introduced in Figure 3.4. Additionally, a reference temperature, equal to that of the engine body, is applied to the base of the sensor. The ANSYS APDL codes used for the thermal simulations as well as other simulations reported in this Thesis are given in Appendix B.

Thickness of SiO_2 insulating layers (2 μm < t_i < 5 μm)

The effect of the thickness of SiO_2 insulating layer, varying in the range of 2-5 μm, on the thermal response of the multifunctional membrane is studied in Figure 4.3. The specifications of the multifunctional sensor investigated in this figure are $t_M = 5$ μm, $t_S = 1050$ μm (corresponding to the thickness of two bonded 4-inch wafers), $L_{chip} = W_{chip} = 1000$ μm, $L_E = 100$ μm, $\omega = 600$ rpm, poly-SiC as membrane material and $T_{\text{bulk}} = 200$ °C. These dimensions and specifications are used in other FE simulations reported throughout this section unless otherwise stated.

As shown in Figure 4.3, around the time of injection ($\text{CA} = 332$) the thickest SiO_2 layer provides the best thermal response (in terms of $T_{M,1}$ being close to $T_{\infty,2}$). As a general trend in Figure 4.3, during the compression stroke ($180 < \text{CA} < 360$) the difference between the results corresponding to different thicknesses of SiO_2 is relatively small. This suggests that the heating up of the membrane is weakly dependent on SiO_2 thickness. On the other hand, the difference between the results

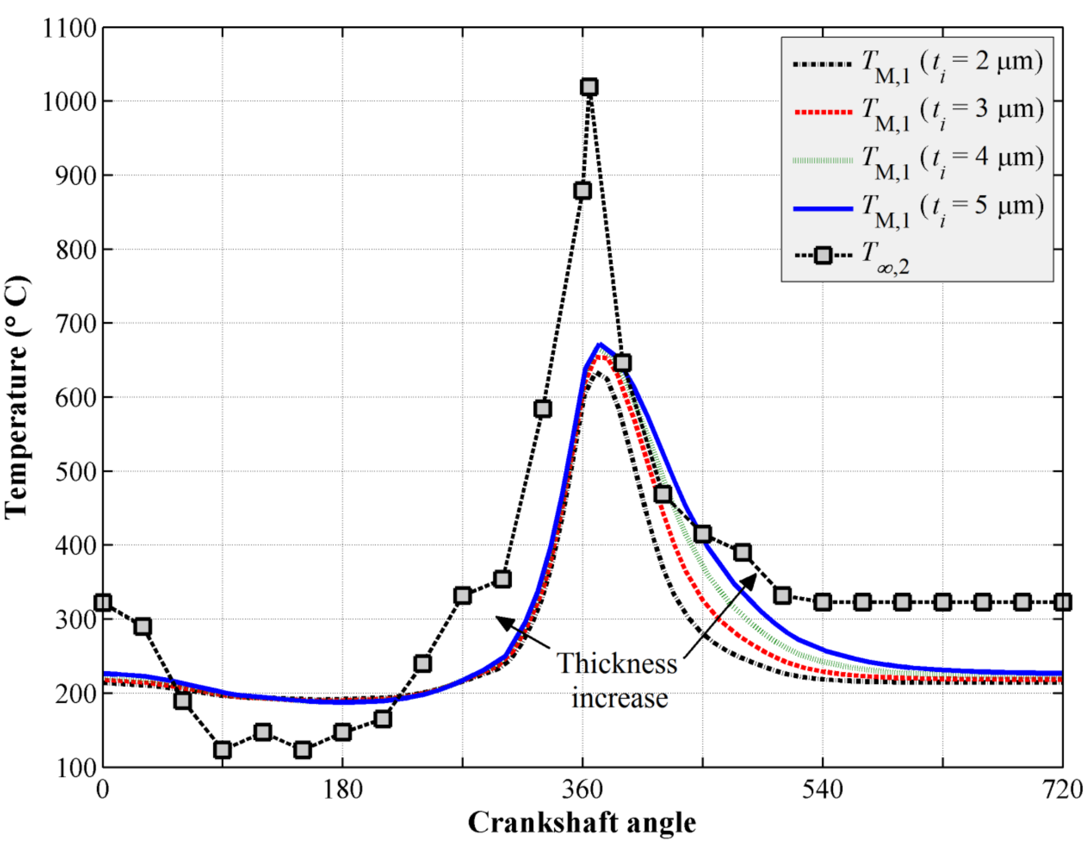

Figure 4.3. Variation of $T_{M,1}$ with in-cylinder temperature $T_{\infty,2}$ for 2 μm < t_i < 5 μm.

corresponding to different thicknesses of SiO_2 during the working stroke ($360 < \mathrm{CA} < 540$), is very noticeable. This is mainly due to the higher thermal resistance and larger heat capacity of the thicker insulating layer which slow down the cooling of the membrane during the working stroke. In summary, the thicker the insulating layer, the better the thermal response of the membrane would be.

Thickness of SiC multifunctional membrane ($0.5\ \mu m < t_M < 5\ \mu m$)

A thinner SiC membrane corresponds to a smaller thermal mass in the system. Since the input heat flux is constant, a thinner membrane translates to a faster thermal response. Figure 4.4 investigates this by providing the results of thermal analyses for different thicknesses of poly-SiC membrane between 0.5 μm and 5 μm. This thickness range more or less covers the typical thickness numbers reported in literature for SiC films at MEMS applications. The results in Figure 4.4 confirm that that the thinnest membrane in the selected thickness range provides the closest match between the

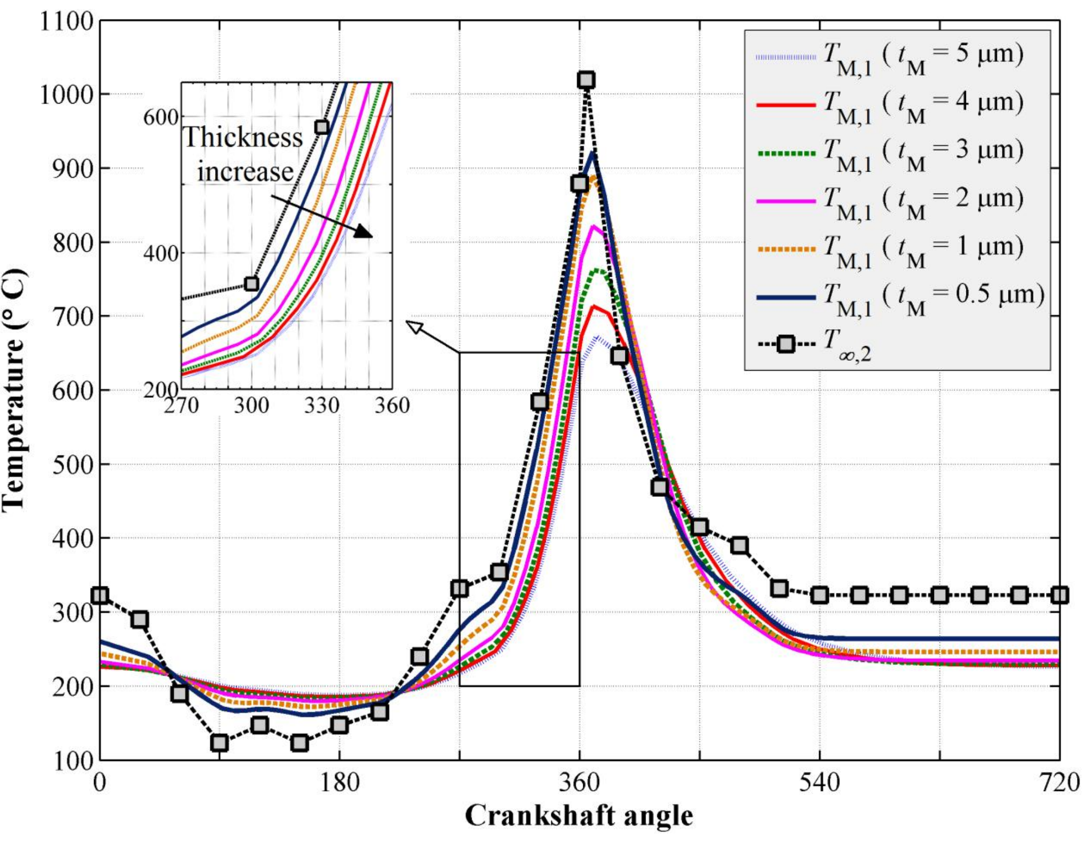

Figure 4.4. Variation of $T_{M,1}$ with in-cylinder temperature $T_{\infty,2}$ for $0.5\ \mu m < t_M < 5\ \mu m$.

membrane response $T_{M,1}$ and the in-cylinder temperature $T_{\infty,2}$. This conclusion is in agreement with the results presented in Figure 4.2.

Multifunctional membrane material (poly-SiC or a-SiC)

Figure 4.5 investigates the effect of the crystalline structure of membrane material on its thermal response when subjected to the in-cylinder thermal loading of Figure 3.4. The results show that the a-SiC membrane does a slightly better job in closely following the in-cylinder temperature variation. The main reason for this promising result is the lower thermal conductivity of a-SiC which reduces the thermal communication between the over-the-cavity and off-the-cavity parts of the membrane. While the thermal conductivity of a-SiC is less than that of Poly-SiC, the small thickness of the a-SiC membrane enables it to achieve a big enough Bi number. This avoids a considerable through-the-

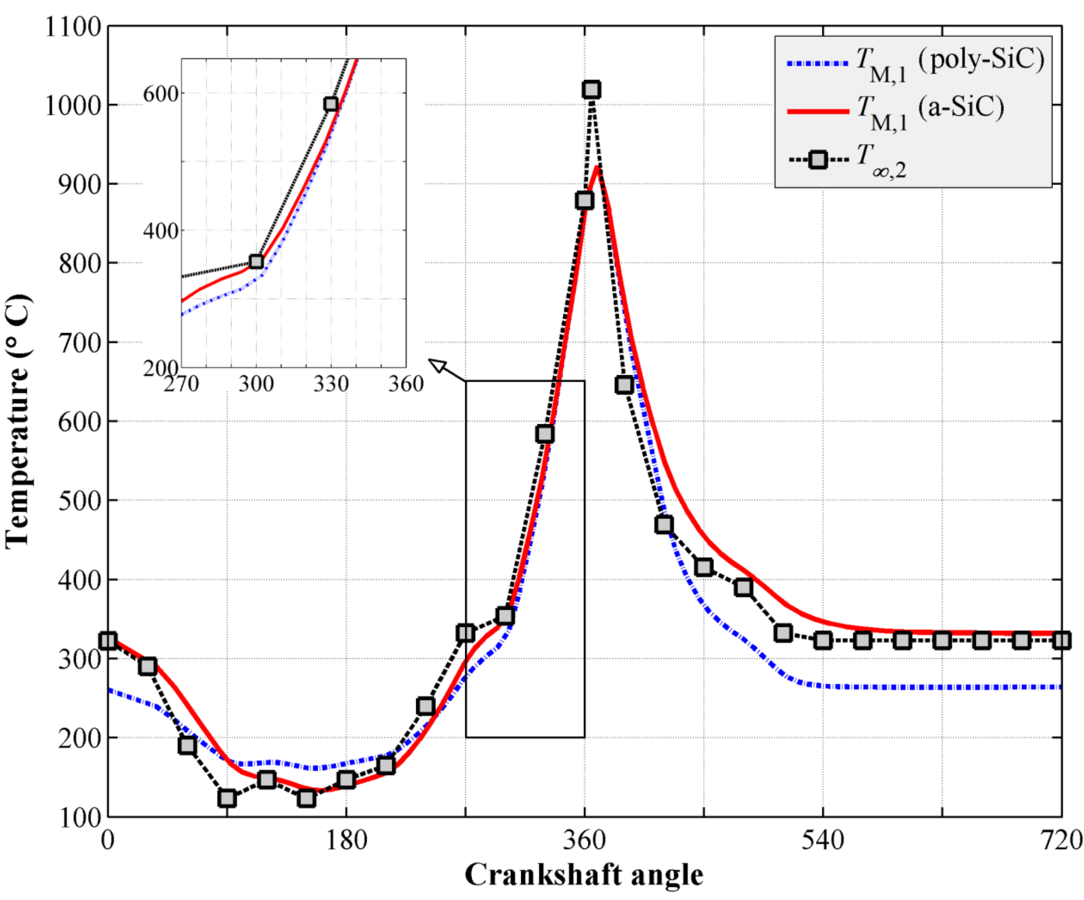

Figure 4.5. Variation of $T_{M,1}$ with in-cylinder temperature $T_{\infty,2}$ for different membrane materials.

thickness temperature gradient develops in the over-the-cavity part of the a-SiC membrane.

Silicon bonding interface (Si-Si or SiO_2-SiO_2)

The other structural characteristic of the sensor studied in this section is the wafer bonding interface featuring Si-Si or SiO_2-SiO_2 contact (Figure 3.12). Figure 4.6 presents the results of two series of FE simulations carried out with and without a 3 μm thick SiO_2 interface layer between the SC-Si chips. The latter scenario resembles the case with Si-Si bonding interface. Based on the results of FE simulations, the difference between the membrane thermal response $T_{M,1}$ predicted for the two interface scenarios is negligible around the injection time ($\mathrm{CA} = 332$) as well as at the height of the combustion stroke ($\mathrm{CA} \sim 365$). On the other hand, during the working stroke the difference between more noticeable and the scenario with the SiO_2-SiO_2 interface results in lower membrane temperature

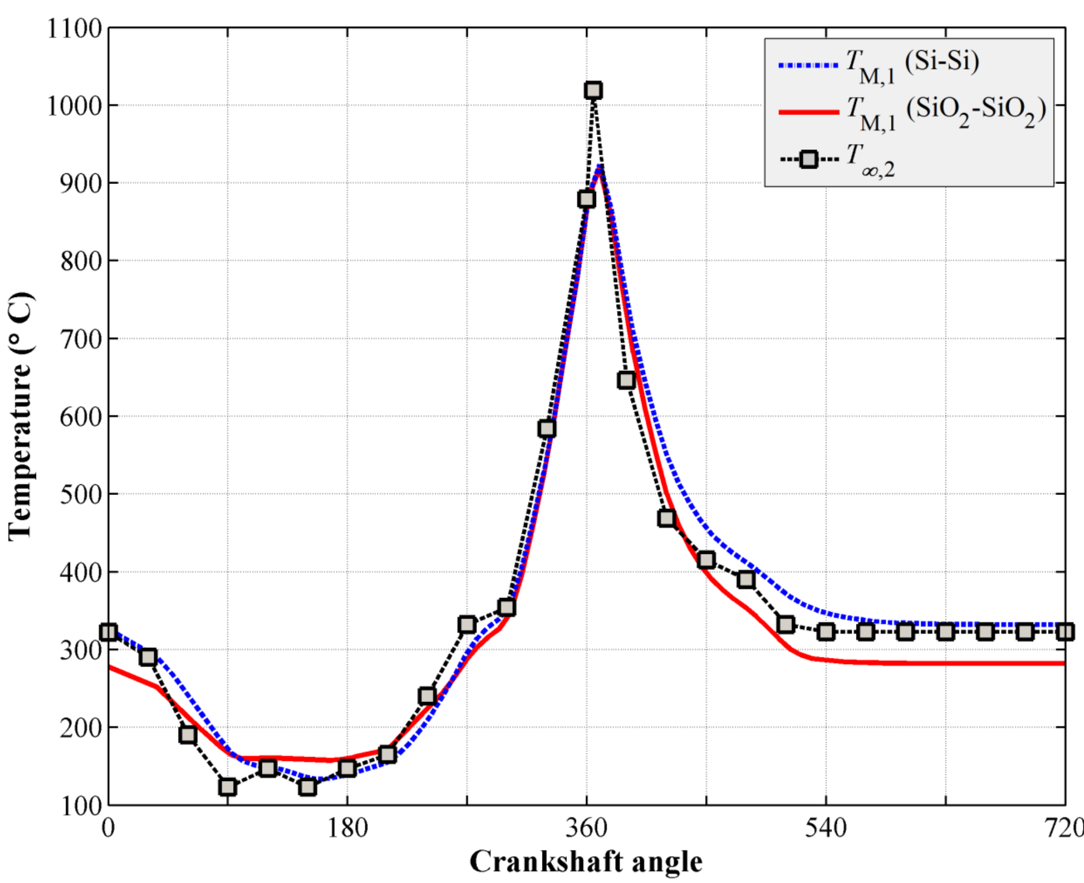

Figure 4.6. Variation of $T_{M,1}$ with in-cylinder temperature $T_{\infty,2}$ for different bonding interfaces.

which gives rise to smaller thermal stresses in the system. Moreover, the SiO_2-SiO_2 wafer bonding is easier to implement in terms of required surface smoothness and bonding temperature.

The width of bonding interface (L_E)

Different widths of the SiO_2- SiO_2 bonding interface (L_E in Figure 4.1) between 20 µm and 200 µm have been used in FE simulations but no noticeable difference in the thermal response of the membrane has been observed. To assure a strong bond between the SC-Si chips, a big bonding interface area is desirable. Here, we assume that a bonding interface width of 150 µm is enough for that purpose.

Thickness of SC-Si substrate

Different thicknesses of the SC-Si substrate chip between 250 µm and 700 µm (inline with typical or thinned 4- and 6-inch wafers available through commercial suppliers such as www.svmi.com and www.universitywafer.com) have been studied; however, no noticeable difference in the thermal response of the membrane has ben observed. So, here we select to continue with 525 µm which is the standard thickness of 4-inch SC-Si wafer. Accordingly, due to wafer bonding, the total thickness of the sensor chip comes to around 1050 µm).

Effect of engine speed (ω)

Engine speed is the important working factor which affects the thermal response of the sensor by changing the time the multifunctional membrane has to undergo temperature variation. As mentioned earlier, at higher engine speeds, the membrane has less time and thus is expected to undergo a smaller temperature change. Figure 4.7 studies this effect by looking at the membrane temperature $T_{M,1}$ variation with CA for different engine speeds between 700 and 4200 rpm. In this figure, the multifunctional membrane is in a-SiC and has a thickness of $t_M = 0.5$ µm.

Throughout the FE simulations in Figure 4.7, it is conservatively assumed that the in-cylinder heat flux and temperature are the same as those given in Figure 3.4 and do not change with $\boldsymbol{\omega}$. Nevertheless, in production IC engines higher engine speeds are usually associated with higher engine loads which in turn drastically increase the in-cylinder heat flux [97]. The increased heat flux would ultimately help the multifunctional membrane demonstrate a better thermal response (closer following of in-cylinder temperature variation) as predicted by equation (4.4).

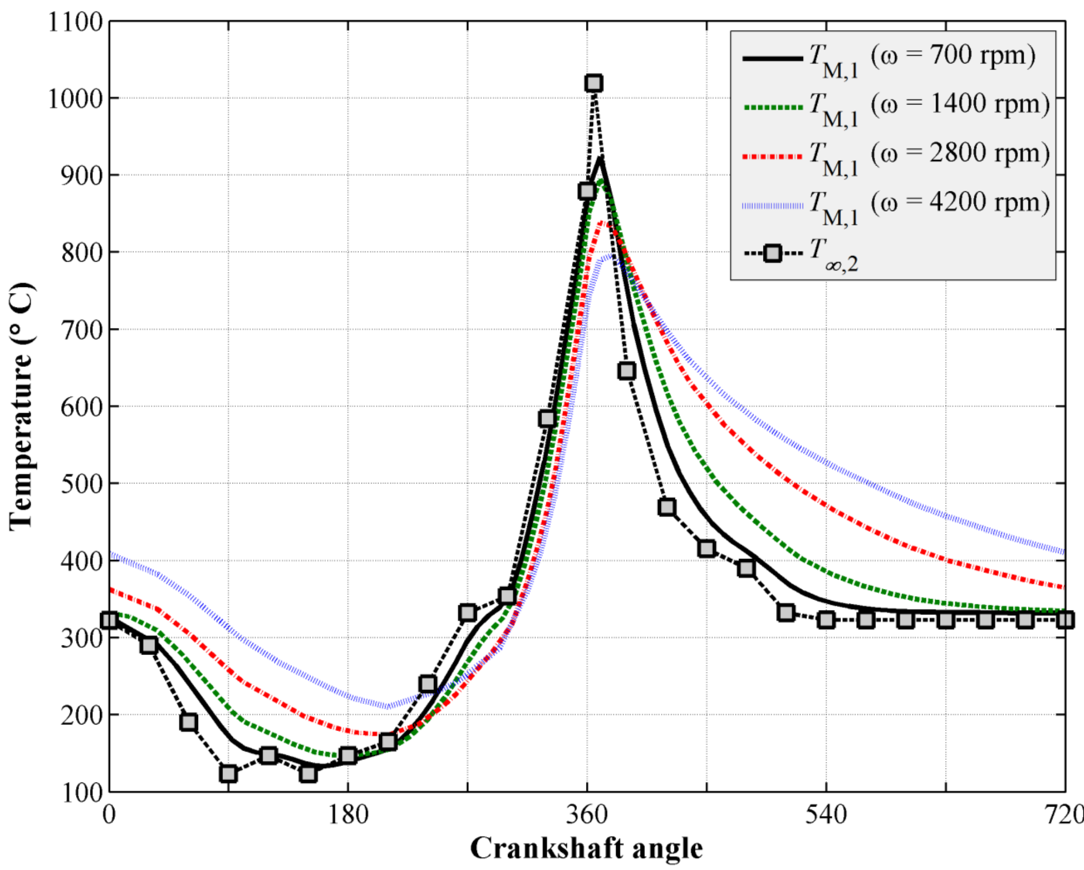

Figure 4.7. Variation of $T_{M,1}$ with in-cylinder temperature $T_{\infty,2}$ for different engine speeds.

Figure 4.8 summarizes the findings so far and shows how the temperatures of different parts of the optimized multifunctional sensor vary with CA for the typical thermal loading of Figure 3.4. The optimized sensor design includes a-SiC membrane ($t_M = 0.5$ µm), SiO_2 insulating ($t_i = 5$ µm) and bonding (thickness = 3 µm) layers, and standard thickness SC-Si chips ($t_{S1} = t_{S2} = 525$ µm). Moreover, the width of the bonding interface is chosen as $L_E = 150$ µm. In the FE simulations, the reference temperature at the base of the sensor is set as $T_{bulk} = 200$ ℃. Based on the results presented in Figure 4.8 some important observations can be made.

The first observation is about the temperature of the off-the-cavity part of the multifunctional membrane $T_{M,2}$ and its variation with CA. The total variation of $T_{M,2}$ for a complete cylinder cycle is about 30 °C which is much less than that of $T_{M,1}$ which is about 750 °C. The reason for this noticeable temperature difference between the over-the-cavity and off-the-cavity parts of the

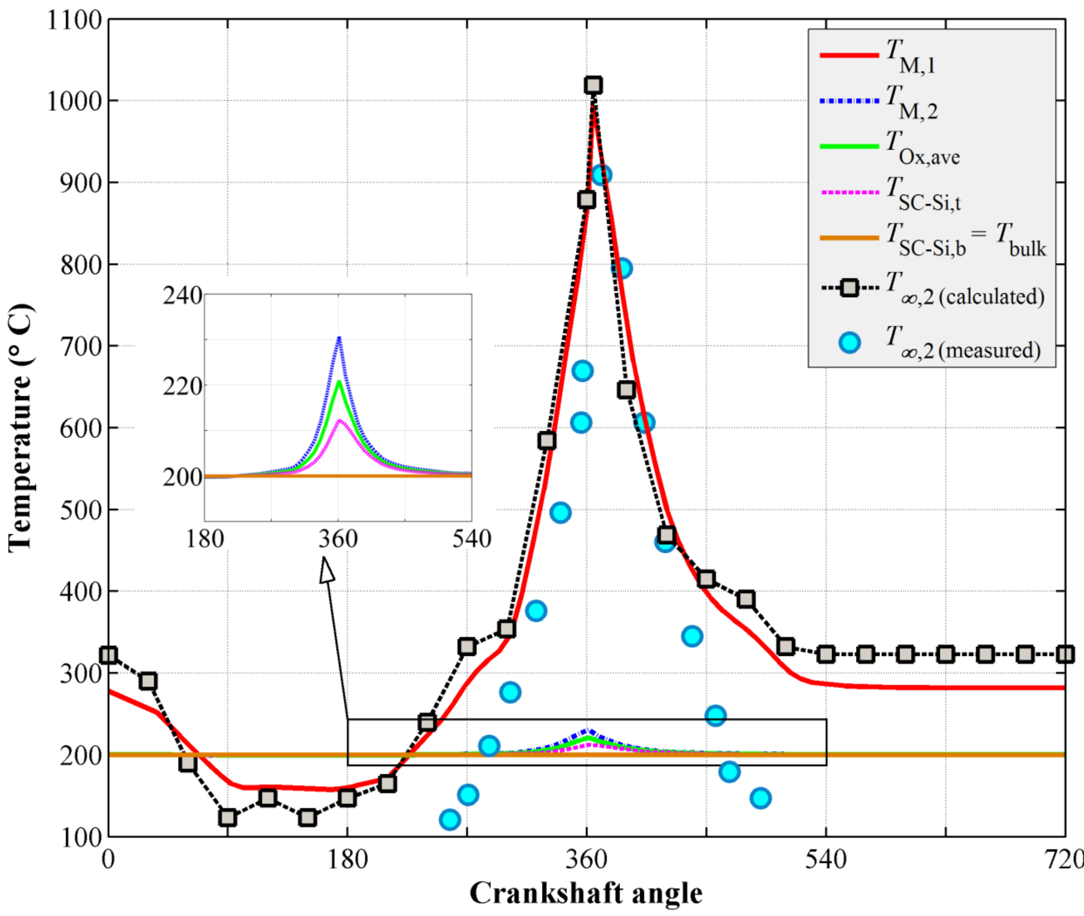

Figure 4.8. Variation of temperature of different parts of sensor with in-cylinder temperature $T_{\infty,2}$.

membrane is the weak thermal conductance of a-SiC from which the membrane is fabricated. By using this material, the thermal communication and heat transfer between the two parts of the membrane is minimized. This allows for the two parts of the membrane to behave almost independently. FE simulation shows that at the time of injection the region between the two parts of the membrane at which the membrane's temperature changes from $T_{M,1}$ to $T_{M,2}$ is less than 100 μm wide. Beyond this region, the over-the-cavity part of the membrane can be considered thermally isolated like an island (the cavity beneath this part is vacuum). Recalling from Figure 4.2 and its ensuing discussion, the over-the-cavity part of the membrane absorbs and keeps almost all of the input heat flux within its structure. In other words, thermal efficiency η in the over-the-cavity part of the membrane is close to 1. On the contrary, the off-the-cavity part of the membrane is in direct

contact with the insulating layer. So, a good portion of the input heat flux into this part is transferred into the underneath layers and ultimately out of the system through the sensor's base.

The second important observation in Figure 4.8 is on the temperature of the SC-Si substrate and its variation with CA. The variation of this temperature is less than 12 °C and mostly occurs in the top SC-Si substrate. A closer look at the FE simulation results suggests that the total temperature variation in the bottom SC-Si substrate is less than 1°C. This is due to: 1) high conductivity of the SC-Si material which quickly conducts the input heat flux out from the sensor's base (Q_{out} in Figure 4.1), and 2) relatively small heat flux reaching the bottom chip. Further FE simulations show that the temperature variation in the SC-Si substrate drastically decreases as the engine speed increases. The multifunctional membrane is actually anchored to the SC-Si substrate. So, it is desirable that the SC-Si substrate maintains its average temperature with a minimum temperature fluctuation. So, by providing the reference temperature T_{bulk} to the sensor's base and also including it in the processing scheme, the sensor would benefit from an almost constant substrate temperature relative to which the membrane temperature will be measured. To summarize the section, the optimized dimensions and materials for the multifunctional MEMS sensor various components are listed below. Among these dimensions, the thickness of substrate (t_S), the thickness of the interface layer (t_{intfc}), and the width of the bonding interface (L_E) can be varied in accordance to fabrication requirements without affecting the thermal performance of the sensor.

- Multifunctional membrane: amorphous SiC, $t_M = 0.5$ µm,
- Insulation layer between the membrane and the substrate: SiO_2, $t_i = 5$ µm,
- substrate: SC-Si, $t_S = 525$ µm (two similar substrates are bonded together),
- Interface layer between the SC-Si substrates: SiO_2, with a thickness of $t_{intfc} = 3$ µm,
- Width of bonding interface: $L_E = 0.5\left(L_{chip} - L\right) = 150$ µm.

4.2 Mechanical modeling

At the core of the multifunctional MEMS sensor is a multifunctional membrane with built-in (fixed) boundary conditions. In this section, a semi-analytical model is developed for the analysis of the multifunctional membrane response to pressure and/or temperature loading. Since an exact analytical solution based on the theory of plates is extremely difficult if not impossible to obtain, we will develop an alternative solution originated from Euler–Bernoulli beam theory and extended to the case of multifunctional membrane. To lay the foundation of the model, some assumptions need to be made

first. Inspired by the analogy between the bending response of a membrane and a clamped-clamped beam, it is assumed here that the response of the multifunctional membrane to pressure and/or temperature loading is similar to that of a clamped-clamped beam cut from its middle and subjected to the same loading. This is schematically shown in

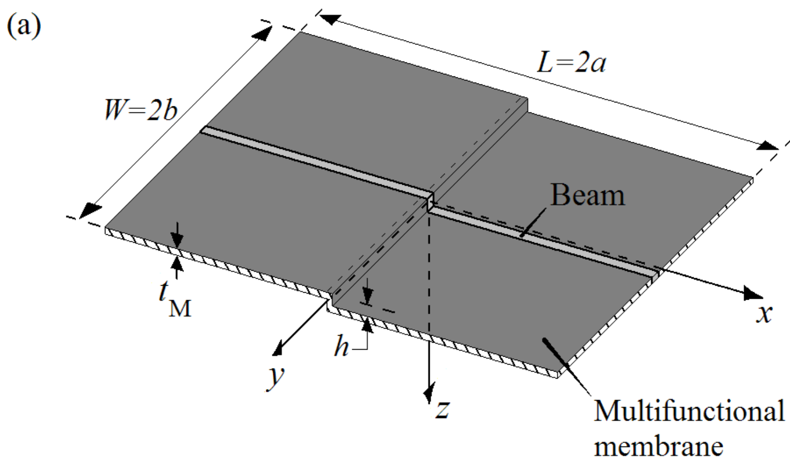

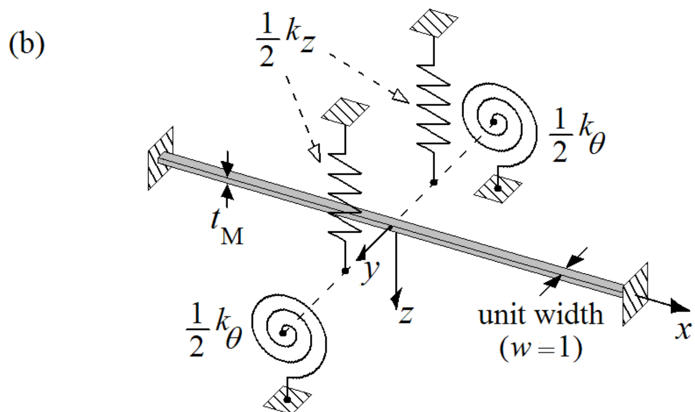

Figure 4.9. (a) Multifunctional membrane with built-in boundary condition and the characteristic clamped-clamped beam selected from its middle part; (b) analogous straight clamped-clamped beam attached to extensional and rotational springs at its midspan.

Figure 4.9.a where the clamped-clamped beam (light color) is selected from the middle part of the membrane (dark color). In line with the previous section, the membrane is represented by its dimension: length (L), width (W), thickness (t_M) and step height (h). In order to assimilate the effect of the step feature, the analogous straight clamped-clamped beam (whose width is equal to 1) is assumed to be supported at its midspan by at-the-moment unknown extensional and rotational springs k_z and k_θ, respectively (Figure 4.9.b). When the analogous beam experiences deformation due to pressure and/or temperature loading, these springs provide counteracting extensional force and/or rotational moment which oppose the beam deformation.

The other assumption made here is that the deflections of the membrane and the clamped-clamped beam are small enough (compared to their thickness) to allow the principle of superposition to be used. The deformation of the membrane due to combined pressure and temperature loading can thus be expressed as

$$z(x,y) = z_P(x,y) + z_T(x,y) \tag{4.1}$$

where z_P and z_T refer to deformations due to pressure and temperature loading, respectively (Figure 3.9). In line with the analogy mentioned earlier and using separation of variables, the pressure and temperature responses on the right hand side of equation (4.1) are assumed to take the forms of

$$\begin{cases} z_P(x,y) = \xi_P z_P(x)\tilde{z}_P(y) & (4.2) \\ \\ z_T(x,y) = \xi_T z_T(x)\tilde{z}_T(y) & (4.3) \end{cases}$$

where ξ_P and ξ_T are unitless amplitude modification factors, $z_P(x)$ and $z_T(x)$ represent the deformation of the clamped-clamped beam due to pressure and temperature loading, respectively, and $\tilde{z}_P(y)$ and $\tilde{z}_T(y)$ expand the deformation of the beam to that of the membrane. Moreover, the deformation given by equations (4.20 and (4.3) should satisfied the membrane boundary conditions.

4.2.1 Pressure response

Figure 4.10 shows the deformation of a clamped-clamped subjected to a pressure change ΔP on its top surface and supported by an extensional spring at its midspan. To utilize the symmetry of the beam, the origin of the coordinate system is selected at its midspan with the *x*-axis extending along its

length to the right. Using the inherent symmetry with respect to the z-axis, the deformation of the right half of the beam $(0 \leq x \leq a)$ is studied first. Using the principle of superposition, the

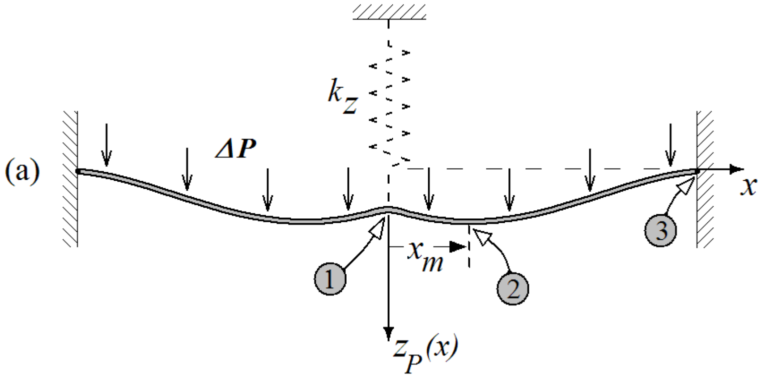

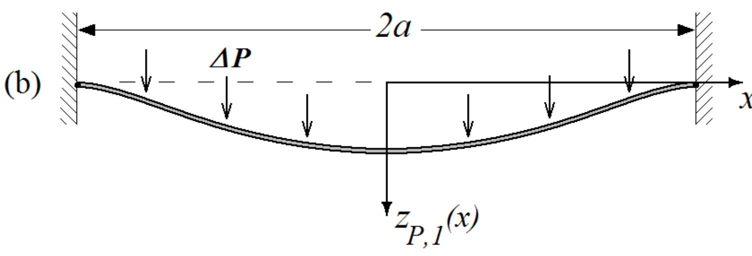

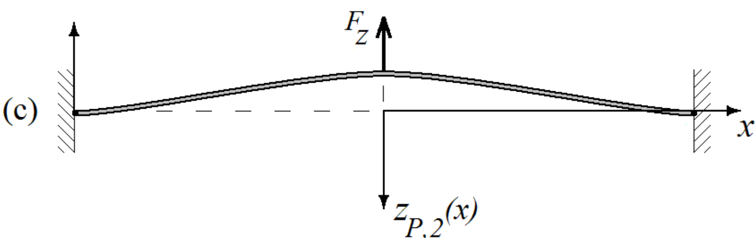

Figure 4.10. Response of the analogous clamped-clamped beam to (a) both pressure difference ΔP and retaining force F_Z, (b) pressure difference ΔP only, and (c) retaining force F_Z only.

deformation of the right half of th ebeam is determined by adding its deformations due to ΔP and concentrated retaining force F_Z, i.e.

$$z_P(x) = z_{P,1}(x) + z_{P,2}(x) \qquad (0 \leq x \leq a) \tag{4.4}$$

The clamped-clamped beam investigated here features a rectangular cross section with a unit width ($w = 1$ as in Figure 4.9). Its bending moment of inertia around the *y*-axis is thus given by

$$I_y = \frac{w{t_M}^3}{12} = \frac{{t_M}^3}{12} \tag{4.5}$$

So, the deformations of the clamped-clamped beam due to pressure difference ΔP (Figure 4.10.b) and concentrated load F_Z (Figure 4.10.c) are approximated, respectively, by [146]

$$z_{P,1}(x) = \frac{\Delta P}{2E^*{t_M}^3}(x^2 - a^2)^2 \tag{4.6}$$

and

$$z_{P,2}(x) = \frac{F_z}{2E^*{t_M}^3}(-2x^3 + 3x^2 a - a^3) \tag{4.7}$$

where $E^* = E \times w$ and $F_z = k_z z_P(0)$. Combining equations (4.4), (4.6) and (4.7), the total deformation of the beam can be expressed as

$$z_P(x) = \frac{\Delta P}{2E^*{t_M}^3}(x^2 - a^2)^2 + \frac{k_z z_P(0)}{2E^*{t_M}^3}(-2x^3 + 3x^2 a - a^3)\,. \tag{4.8}$$

To eliminate $z_P(0)$ from equation (4.8), *x* is set equal to zero which results in

$$z_P(0) = \frac{\Delta P a^4}{2E^*{t_M}^3 + k_z a^3} \tag{4.9}$$

Substituting from equation (4.9) back into (4.8) gives

$$z_P(x) = \frac{\Delta P}{2E^*{t_M}^3}\left[(x^2 - a^2)^2 + \frac{1}{1 + 2E^*{t_M}^3/k_z a^3}(-2ax^3 + 3a^2x^2 - a^4)\right] \tag{4.10}$$

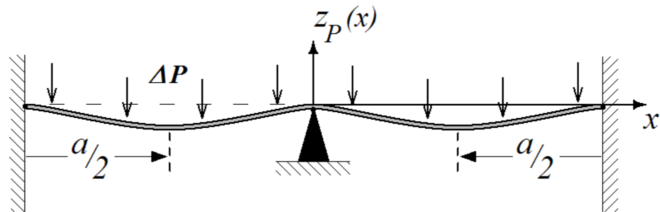

Figure 4.11. Response of a clamped-clamped beam rigidly supported at its midspan to pressure difference ΔP (corresponding to $k_z = \infty$ in Figure 4.10.a).

If $k_z = 0$, equation (4.10) reduces to equation (4.6) of a beam under pressure difference only. On the other hand, if $k_z = \infty$, the problem corresponds to a clamped-clamped beam subjected to a uniform pressure ΔP and rigidly supported at its midspan, as shown in Figure 4.11.

If $k_z = \infty$, equation (4.10) reduces to

$$z_P(x) = \frac{\Delta P}{2E^* {t_M}^3}(x^4 - 2ax^3 + a^2x^2) \tag{4.11}$$

which exhibits three extremum points at $x = (0, a/2, a)$. Equation (4.10) governs the deflection of the right half of the clamped-clamped beam. Due The deformation of the left half of the beam can easily be determined as the mirror image of that of the right half with respect to the *z*-axis. For the general case where $0 < k_z < \infty$, differentiation of $z_P(x)$ given by equation (4.10) with respect to x gives

$$\frac{\partial z_P(x)}{\partial x} = \frac{\Delta P}{2E^* {t_M}^3}\left[4x(x^2 - a^2) - \frac{1}{1 + 2E^* {t_M}^3 / k_z a^3}(6ax^2 - 6a^2x)\right] \tag{4.12}$$

Setting the right hand side of equation (4.12) equal to zero, and recalling that $0 \leq x \leq a$ for the right half of the beam, the following extremum points in the deflection curve are found

$$\begin{cases} x_1 = 0 & (4.13) \\ x_2 = x_m = \dfrac{1.5a}{1 + 2E^* {t_M}^3 / k_z a^3} - a & (4.14) \\ x_3 = a & (4.15) \end{cases}$$

These extremum points are labeled on Figure 4.10.a by their corresponding numbers 1 to 3. While x_1 and x_3 values are constant and trivial (consistent with the boundary condition and the symmetry of the clamped-clamped beam), x_2 depends on k_z. For the extremum point at $x = x_2$ to exist, the $0 < x_2 < a$ condition should be satisfied. After some calculations, this results in

$$k_z > \frac{4E^* {t_M}^3}{a^3} \tag{4.16}$$

Equation (4.16) establishes the requirement for the extremum point 2 in Figure 4.10.a to exist. If equation (4.16) is not satisfied, only two extremum point at $x = 0$ and $x_3 = a$ will appear. In so, the effect of a nonzero k_z reduces to a mere broadening of the deflection curve around its extremum at $x = 0$. In order to determine k_z for a given membrane geometry, the dimensionless parameter η_1 is defined here as

$$\eta_1 = \frac{z_{P,FEM}(0,0)}{z_{P,FEM}(a/2,0)} \tag{4.17}$$

Using equations (4.10) and (4.17), k_z can be determined by (more details on FE code in appendix B)

$$k_z = 32E^* \frac{{t_M}^3}{a^3}\left(\frac{1}{\eta_1} - \frac{9}{16}\right) \tag{4.18}$$

Utilizing the analogy mentioned earlier between the deflection of a multifunctional membrane and the bending response of a clamped-clamped beam, equation (4.18) constitutes the procedure for the determination of k_z from the results of numerical FE simulations. To do so, η_1 is first calculated from the results of FE simulations on the multifunctional membrane. Next, by substituting the values of t and a used in the FE modeling along with the calculated η_1, k_z can be determined from equation (4.18). To study the effect of membrane geometry on k_z, Figure 4.12 shows how k_z changes with length- and width-to-thickness ratios, i.e. L/t_M and W/t_M, of a a-SiC multifunctional membrane for two cases with step height-to-thickness ratio h/t_M equal to 0.5 and 1.

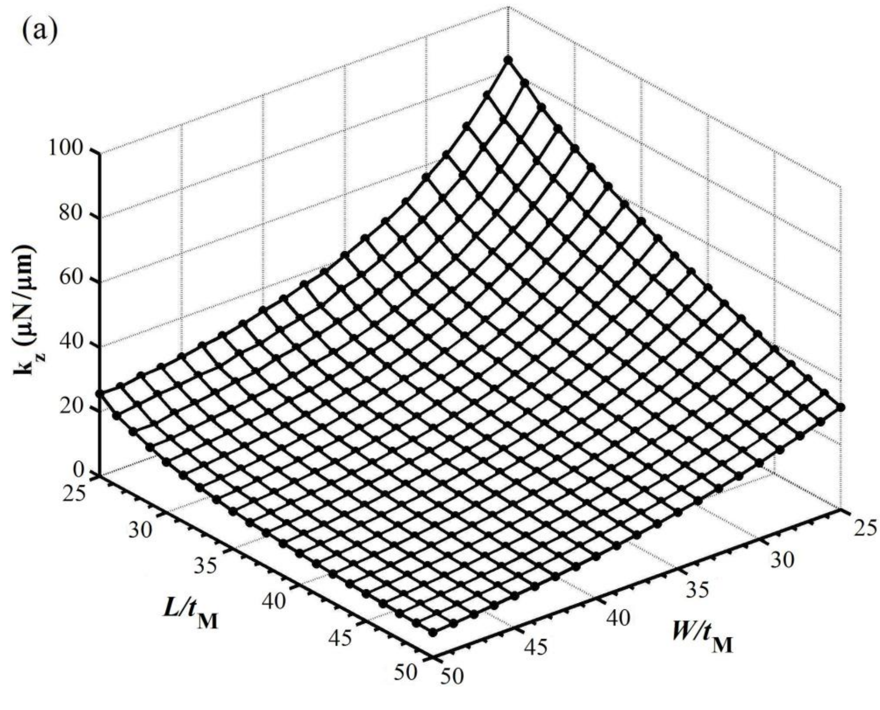

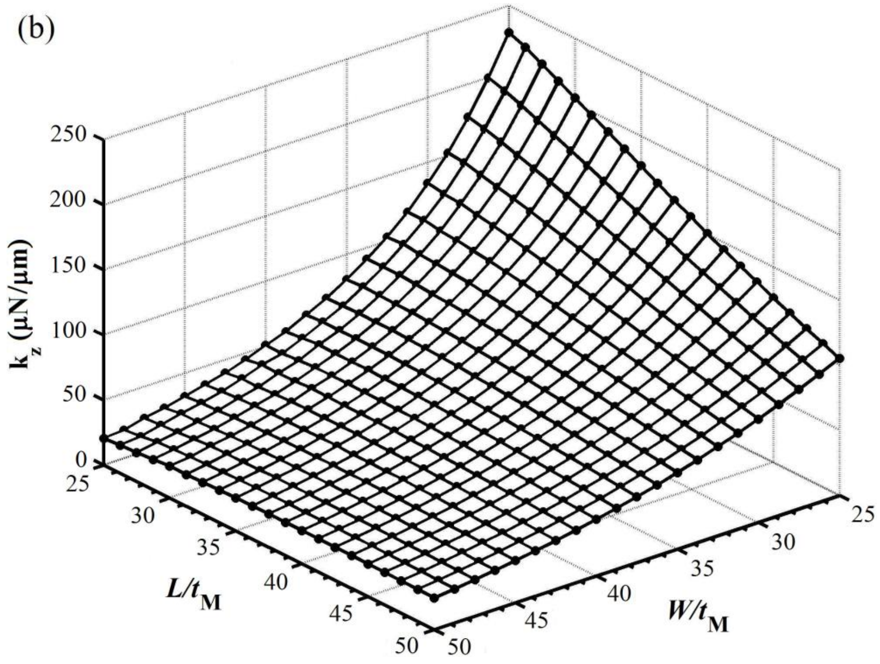

Figure 4.12. Variation of k_z with length and width-to-thickness ratios in an a-SiC multifunctional membrane with a step height-to-thickness ratio of (a) 0.5 or (b) 1.

As a general trend in Figure 4.12, the larger the length- and the width-to-thickness ratios are, the smaller the spring constant k_z will be. In other words, k_z is inversely proportionate to L/t_M and W/t_M. Moreover, a bigger step height-to-thickness ratio contributes to a larger k_z. By knowing the spring constant k_z, the deformation of the clamped-clamped beam under pressure loading ΔP can be fully understood using equation (4.10).

In order to expand the clamped-clamped beam deformation given by equation (4.10) to the case of the multifunctional membrane, $\tilde{z}_P(y)$ in equation (4.2) is introduced as

$$\tilde{z}_P(y) = \left(\frac{y^2}{b^2} - 1\right)^2 \tag{4.19}$$

Equation (4.20) satisfies the fixed-edge boundary condition of the multifunctional membrane at $y = \pm b$ (Figure 4.9.a). Substituting from equations (4.10) and (4.19) into equation (4.2) gives

$$z_P(x,y) = \frac{\xi_P \Delta P}{2E^* {t_M}^3}\left[(x^2 - a^2)^2 + \frac{1}{1 + 2E^* {t_M}^3/k_z a^3}(-2ax^3 + 3a^2x^2 - a^4)\right]\left(\frac{y^2}{b^2} - 1\right)^2 \tag{4.20}$$

The dimensionless amplitude modification factor ξ_P appearing in equation (4.20) compensates for the effect of simplifications and assumptions made so far by scaling the deflection of the analogous clamped-clamped beam for adaptation to the case of multifunctional membrane. ξ_P is numerically calculated as (more details on FE code in appendix B)

$$\xi_P = \frac{z_{P,FEM}(0,0)}{z_P(0)} \tag{4.21}$$

where $z_{P,FEM}(0,0)$ is the deflection at the center of the membrane predicted by FE simulation and $z_P(0)$ is that calculated from equation (4.10). Figure 4.13 shows how ξ_P changes with L/t_M and W/t_M for the same a-SiC multifunctional membrane case investigated in Figure 4.12. The general trend in Figure 4.12 is that ξ_P is inversely proportionate to the membrane's length-to-width aspect ratio L/W. Additionally, except for a small portion of each graph in Figure 4.12 associated with small L/t_M and large W/t_M values, the amplitude modification factor ξ_P is always less than one. This suggests that the beam theory generally predicts a larger deflection for the analogous clamped-clamped beam compared to the multifunctional membrane from which it is taken.

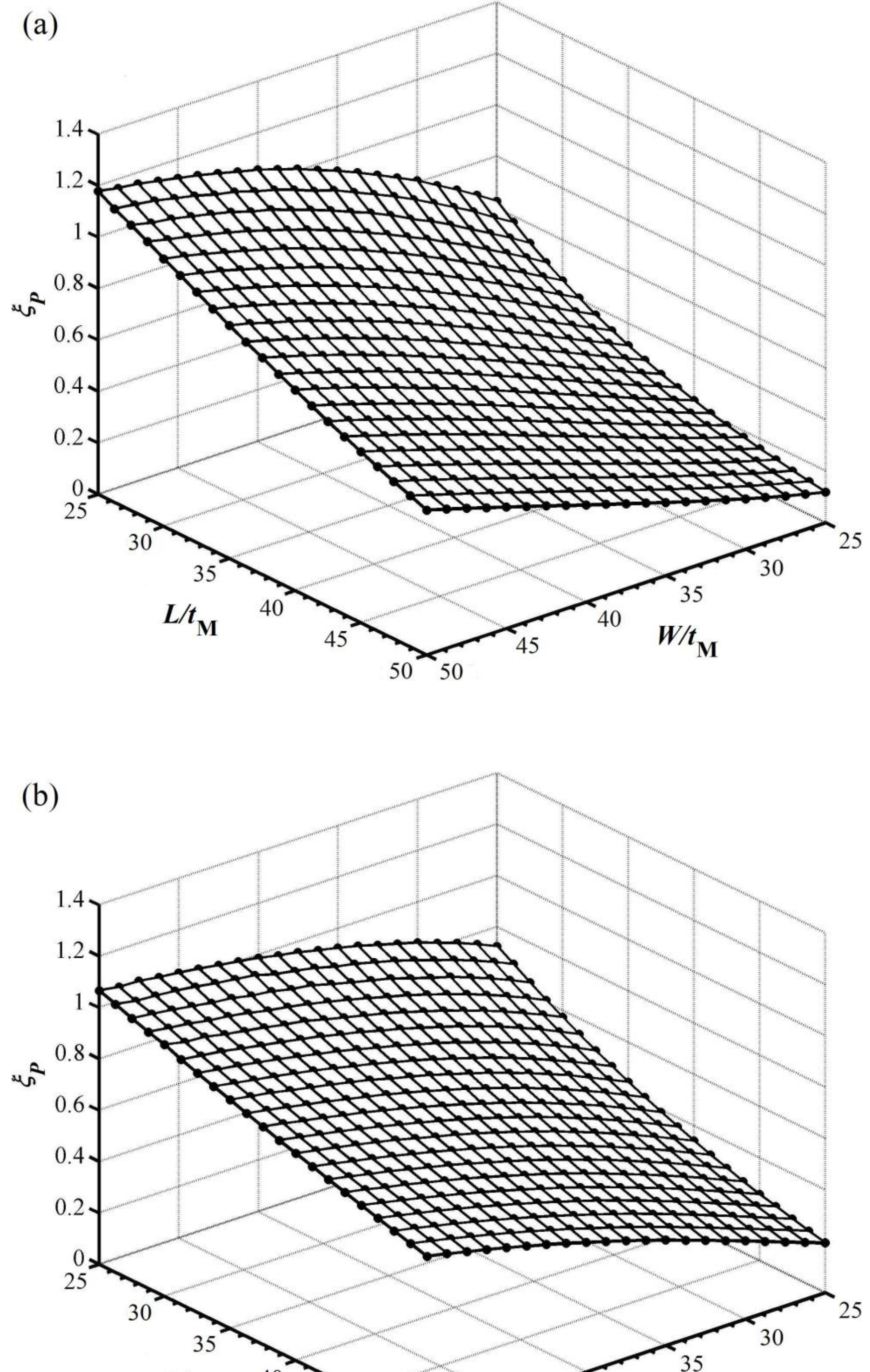

Figure 4.13. Variation of ξ_P with length- and width-to-thickness ratios in an a-SiC multifunctional membrane with a step height-to-thickness ratio of (a) 0.5 or (b) 1.

Finally, substituting the values of k_z and ξ_P extracted from FE simulations into equation (4.20), the three-dimensional deformation profile of the multifunctional membrane subjected to pressure loading ΔP can be determined. In the electrical modeling section, the semi-analytical model of equation (4.20) will be used for the calculation of the capacitive outputs of the sensor.

4.2.2 Temperature response

Figure 4.14 schematically shows the deformation of a clamped-clamped beam (similar to the one represented in Figure 4.9) subjected to a uniform temperature increase ΔT and supported by the torsional spring k_θ at its midspan. The origin of the coordinate system is again selected at the midspan of the beam with the x-axis extending along its length to the right.

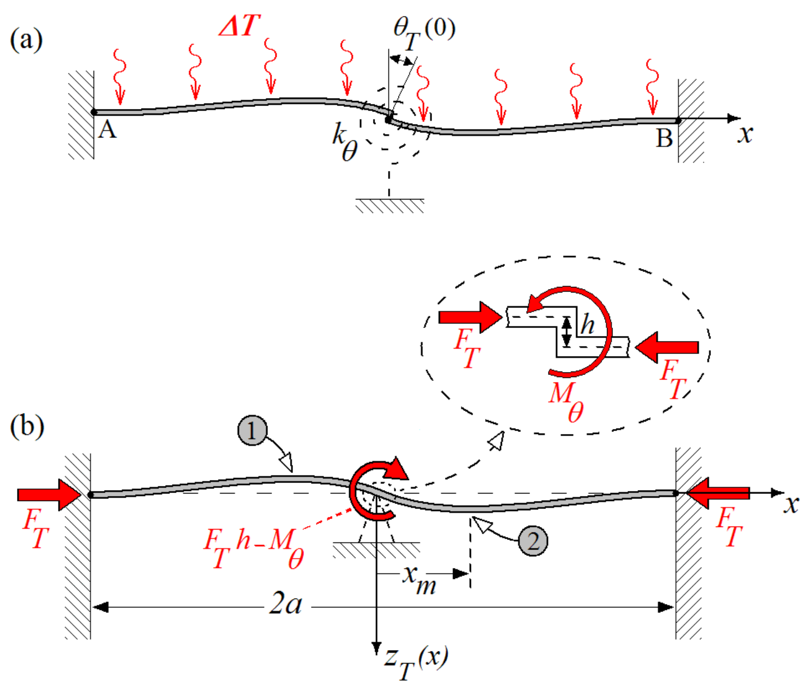

Figure 4.14. (a) Deformation of a clamped-clamped beam due to temperature increase ΔT, (b) The reaction forces F_T applied by the end supports give rise to an internal bending moment $F_T h$ which is opposed by the torsional moment M_θ from the rotational spring.

In previous section it was shown that the contribution of the step feature toward the pressure response of the membrane is an added stiffness which limits the deflection of the membrane around the step

feature. For the case of temperature loading, the contribution of the step feature is more complicated as it provides an internal mechanism which gives rise to a thermal bending moment and deforms the membrane. At the same time, the step feature contributes to the stiffness of the torsional spring which opposes the deformation of the beam.

When the temperature of the beam increases, it tends to expand to accommodate the added length; however, its clamped ends prevent its free expansion by applying an opposing compressive force F_T, as shown in Figure 4.14.b. The compressive force F_T gives rise to a bending moment at the step feature in the middle of the beam whose magnitude is given by

$$M_T \cong F_T h \tag{4.22}$$

This bending moment tends to rotate the clamped-clamped beam around the step feature as shown in Figure 4.14. However, the torsional spring k_θ opposes the deformation of the beam by applying the counteracting torsional moment

$$M_\theta = k_\theta \theta_T(0) \tag{4.23}$$

where $\theta_T(0)$ is the rotation angle of the beam at $x = 0$ determined by

$$\theta_T(0) = z_T{}'(0) = \left. \frac{dz_T(x)}{dx} \right|_{x \to 0} \tag{4.24}$$

The net bending moment applied to the center of the clamed-clamped beam, as shown in Figure 4.14.b, is thus calculated as

$$M = M_T - M_\theta = F_T h - k_\theta z_T{}'(0) \tag{4.25}$$

The deformation of the right half of the clamped-clamped beam subjected to the bending moment M at its midspan can be approximated by [146]

$$z_T(x) = \frac{M}{8aEI_y} x(x-a)^2 = \frac{F_T h - k_\theta z_T{}'(0)}{8aEI_y} x(x-a)^2 \qquad (0 < x < a) \tag{4.26}$$

Solving the equation (4.26), the function governing the deformation of the clamped-clamped beam due to thermal compressive force F_T is determined as

$$z_T(x) = \frac{F_T h}{8aEI_y + k_\theta a^2} x(x-a)^2 \tag{4.27}$$

The thermally deformed clamped-clamped beam demonstrates two extremum points along its length at $x = \pm x_m$, marked by corresponding numbers 1 and 2 in Figure 4.14.b. Differentiation of equation (4.27) with respect to x gives $x_m = a/3$ which on the contrary to equation (4.14) which gave the location of the extremum point for pressure loading case is solely dependent on the clamped-clamped beam's geometry and does not relate to thermal loading ΔT or the rotational spring k_θ.

The compressive thermal force F_T which deforms the clamped-clamped beam originates from the difference between the thermal strains of the beam and the substrate to which the beam is anchored. This can be generalized for the multifunctional membrane from which the beam is selected. If α_m and α_s represent the CTEs of the beam and the substrate materials, respectively, F_T can be expressed as

$$F_T \propto EA(\alpha_m \Delta T_M - \alpha_s \Delta T_{SC-Si}) \tag{4.28}$$

where ΔT_M and ΔT_{SC-Si} are the temperature changes that the beam (or membrane) and the substrate experience and $A = tw$ is the cross section area of the beam. In an IC engine, as shown in thermal modeling section, ΔT_{SC-Si} is much smaller than ΔT_M (Figure 4.8). In contrast, in a steady state thermal analysis ΔT_{SC-Si} and ΔT_M are the same. So, different design guidelines are required for transient and steady state thermal conditions.

To expand the deformation of the beam model to the case of multifunctional membrane, function $\tilde{z}_T(y)$ is introduced into the thermal response equation. $\tilde{z}_T(y)$ is selected similar to $\tilde{z}_P(y)$ proposed in equation (4.19). Based on equation (4.3), the thermal response of the membrane is given by

$$z_T(x,y) = \frac{\xi_T E t_M w(\alpha_m \Delta T_M - \alpha_s \Delta T_{SC-Si})h}{8aEI_y + k_\theta a^2} x(x-a)^2 \left(\frac{y^2}{b^2} - 1\right)^2 \tag{4.29}$$

Substituting for I_y from equation (4.5) and recalling that $E^* = E \times w$, equation (4.29) is rewritten as

$$z_T(x,y) = \bar{\xi}_T(\alpha_m \Delta T_M - \alpha_s \Delta T_{SC-Si}) x(x-a)^2 \left(\frac{y^2}{b^2} - 1\right)^2 \tag{4.30}$$

where

$$\bar{\xi}_T = \frac{\xi_T t_M h}{2a{t_M}^3/3 + k_\theta a^2/E^*} \tag{4.31}$$

Similar to the method used in the previous section for the calculation of the modification factor ξ_P, $\bar{\xi}_T$ is numerically calculated by

$$\bar{\xi}_T = \frac{27}{4}\frac{z_{T,FEM}(a/3\,,0)}{(\alpha_m \Delta T_M - \alpha_s \Delta T_{SC-Si})a^3} \tag{4.32}$$

where $z_{T,FEM}(a/3\,,0)$ corresponds to the displacement predicted by the FE simulation at $(x = a/3\,, y = 0)$, for a given $(\alpha_m \Delta T_M - \alpha_s \Delta T_{SC-Si})$ value (more details on FE code in appendix B). As a numerical example, Figure 4.15 shows how $\bar{\xi}_T$ changes with W/t_M and h/t_M in an a-SiC membrane with $L/t_M = 37.5$. The modification factor $\bar{\xi}_T$ takes its highest value at $h/t_M \cong 1.2$. More

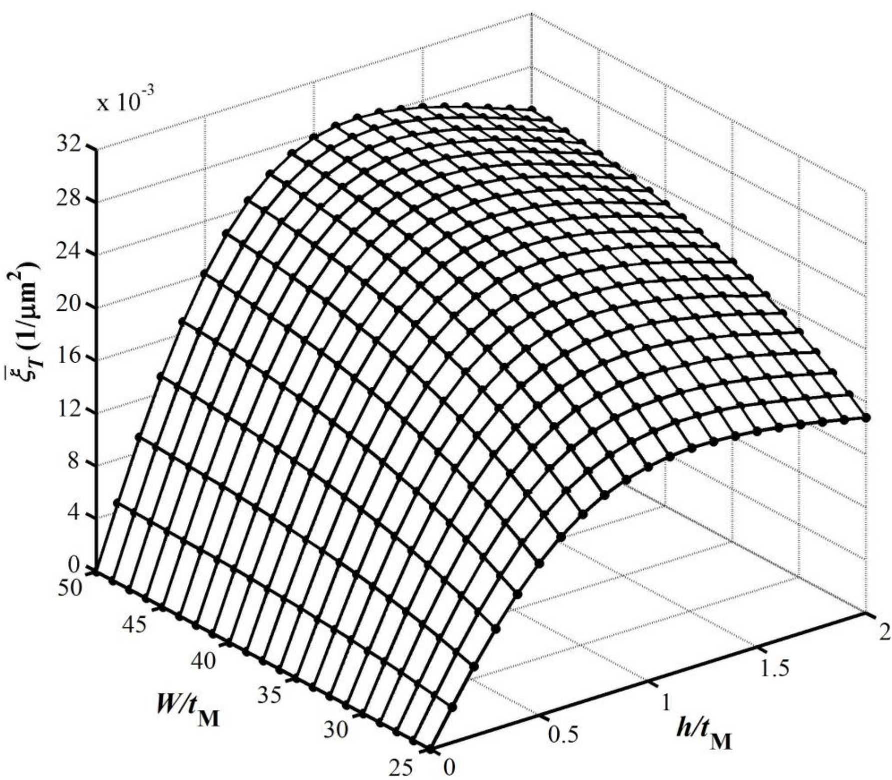

Figure 4.15. Variation of $\bar{\xi}_T$ with W/t_M and h/t_M in an a-SiC membrane with $L/t_M = 37.5$.

FE simulations show that this holds true for other dimensions and membrane-substrate materials. This suggests that for a given set of membrane dimensions, an optimized h/t_M ratio can be found which results in the highest thermal deformation of the multifunctional membrane.

Up to this point, the temperature dependence of the materials used in the fabrication of the MEMS sensor has not been taken into account. According to the data presented in Chapter 2, a temperature variation of 700 °C (which is comparable to $\Delta T_{M,1}$) can change the Young's modulus of SiC by as much as 2%. So, taking the Young's modulus as a temperature-independent material property will not bring about a major error to the response analysis of the sensor. However, the variation of other material properties such as CTE with similar temperature changes is far from negligible. To take this into account, equation (4.30) is first expressed in the differential form of

$$dz_T(x,y) = \bar{\xi}_T(\alpha_m dT_M - \alpha_s dT_{SC-Si})x(x-a)^2\left(\frac{y^2}{b^2}-1\right)^2 \tag{4.33}$$

where $dz_T(x,y)$ is the differential deformation of the membrane, dT_M is the temperature change the membrane experiences (from T_M to $T_M + dT_M$) and dT_{SC-Si} is the temperature change of the substrate (from T_{SC-Si} to $T_{SC-Si} + dT_{SC-Si}$) during the same period of time. If dT_M and dT_{SC-Si} are small enough, α_m and α_s can be assumed to remain constant during the temperature variation period. On the other hand, when the temperature changes are considerable, equation (4.30) is modified to

$$z_T(x,y) = \bar{\xi}_T(\bar{\alpha}_m \Delta T_M - \bar{\alpha}_s \Delta T_{SC-Si})x(x-a)^2\left(\frac{y^2}{b^2}-1\right)^2 \tag{4.34}$$

where $\bar{\alpha}_m$ and $\bar{\alpha}_s$ are CTEs averaged over the corresponding temperature variation ranges, i.e.

$$\bar{\alpha}_m = \frac{\int_{T_M}^{T_M+\Delta T_M} \alpha_m dT}{\Delta T_M}\ , \qquad \bar{\alpha}_s = \frac{\int_{T_{SC-Si}}^{T_{SC-Si}+\Delta T_{SC-Si}} \alpha_m dT}{\Delta T_{SC-Si}}\ . \tag{4.35}$$

In a harsh environment application associated with static (or steady state) thermal loading, all the components of the sensor have the same temperature. In this case, according to equation (4.34), maximizing the difference between the CTEs of the membrane and the substrate materials results in the highest achievable thermal deformation $z_T(x,y)$. Among the materials studied in Chapter 2, titanium (Ti) stands out as possessing the highest CTE over the temperature range of 300-1000 K. Accordingly, the combination of Ti membrane and Si substrate, in short Ti-Si system, would

potentially provide the largest thermal response of a MEMS sensor based on thermostatic effect. On the other hand, for a dynamic harsh environment application such as IC engine where different components of the sensor experience different temperatures (Figure 4.8), short thermal response time not the amplitude of the thermal response is the first priority. As argued in the previous section, the combination of SiC membrane and Si substrate, shortly SiC-Si system, could provide the shortest response time while maintaining an acceptable level of robustness throughout the loading cycle.

4.2.3 Combined pressure and temperature response

It was earlier assumed that the principle of superposition holds true and can be used in the analysis of the multifunctional membrane when subjected to pressure and temperature loading. So, when pressure and temperature loading coexist, the total deformation of the multifunctional membrane is expressed as

$$\begin{cases} z(x,y) = z_P(-x,y) - z_T(-x,y) & -a < x < 0\,, \quad -b < y < b \qquad (4.36) \\ z(x,y) = z_P(x,y) + z_T(-x,y) & 0 < x < a\,, \quad -b < y < b \qquad (4.37) \end{cases}$$

where z_P and z_T are given by equations (4.20) and (4.34), respectively, and a and b represent the half-length and half-width of the multifunctional membrane (Figure 4.9).

To validate the thermo-mechanical model of equations (4.36) and (4.37), Figure 4.16 compares the deformation profiles of two membrane-substrate systems, in their *xz*- and *yz*-planes, predicted by the thermo-mechanical model and by FE simulations. The first membrane-substrate system is a Ti-Si one with dimensions $L = W = 100$ µm and $h = t_M = 2$ µm, and the second one is a SiC-Si system with dimensions $L = W = 500$ µm and $h = t_M = 10$ µm. In both systems, the multifunctional membrane is subjected to $\Delta P = 2\ MPa$ and $\Delta T = 700\ °C$. The characteristic parameters extracted from the FE simulations and used in the semi-analytical model are $\xi_P = 0.66$, $k_z = 21.817$ µN/µm and $\bar{\xi}_T = 0.0092$ µm^{-2} for the Ti-Si system and $\xi_P = 0.66$, $k_z = 60.577$ µN/µm and $\bar{\xi}_T = 0.00037$ µm^{-2} for the SiC-Si system. The maximum difference between the displacements predicted by the two models is less than 3% which confirms the good agreement between the two approaches and validates the semi-analytical thermo- mechanical model. The main advantage of the semi-analytical model, however, is the reduced processing time it provides compared to FE simulations by ANSYS®. Such

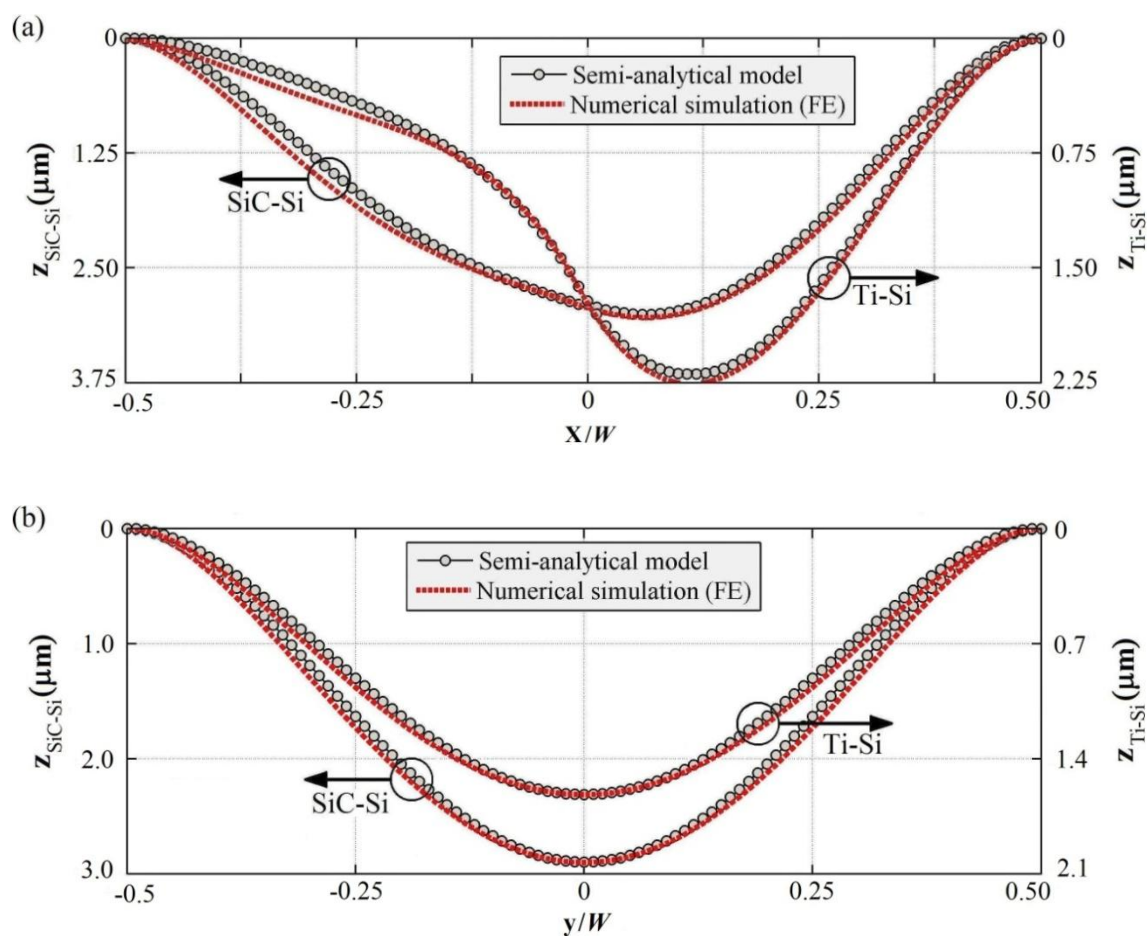

Figure 4.16. Deformation of the multifunctional membrane in (a) *xz*- plane and (b) *yz*-plane for SiC-Si and Ti-Si membrane-substrate systems predicted by the semi-analytical model (solid line with round symbol) and FE simulations (dotted red line).

an advantage facilitates the electrical modeling of the multifunctional MEMS sensor in the next section and also allows for quick optimization of the sensor design which will be discussed shortly.

As in Figure 3.10, the initial gaps between the multifunctional membrane and the bottom electrodes are designated G_1 and G_2. Since the multifunctional membrane is designed to work in non-contact mode of operation (i.e. at the maximum displacement the membrane would not touch the bottom electrodes), G_1 and G_2 need to be bigger than the maximum deflection of the membrane z_{max} to avoid any physical contact and/or pull-in to happen.

According to Figure 3.4, in a typical IC engine the maximum in-cylinder pressure and temperature occur almost simultaneously at the peak of the working stroke. So, the maximum deflection of a multifunctional membrane for IC engine application can easily be determined by putting the maximum pressure and temperature values (e.g. from Figure 3.4) in equations (4.36) and (4.37). Throughout this Thesis it is assumed that the pressure and temperature loading given in Figure 3.4 holds true for different engine speeds and loads. Generally speaking, assuming that the absolute maximum in cylinder pressure and temperature values are known, equations (4.36) and (4.37) are first used to determine z_{max}. If G_{clear} is the minimum clearance distance maintained between the top and bottom electrodes (Figure 3.10), G_1 and G_2 are then determined by

$$G_1 = G_2 = z_{max} + G_{clear} \tag{4.38}$$

In a flexible membrane with fixed boundary condition which is subjected to pressure difference, the maximum deflection of the membrane depends on its length- and width-to-thickness ratios [147]. That said, for a constant thickness, bigger in-plane dimensions result in a smaller maximum pressure associated with a given deflection. In the mechanical modeling section of this chapter, the linear beam theory was used in the derivation of equation (4.20). The application and validity of this theory is limited to the cases with small deflections. In this Thesis, small deflection refers to deflections which are smaller that the thickness of the deforming body (clamped-clamped beam, for example). Additionally, the numerical procedures developed for equations (4.18) and (4.21) have been used for small deflection cases. So, in this research, the length- and width-to-thickness ratios of the multifunctional membrane are selected in such a way that z_{max} is always smaller that t_M.

As argued earlier, to achieve the shortest thermal response time the membrane should be as thin as possible. Based on the design parameter ranges mentioned before, the ideal membrane thickness has been selected as 0.5 µm. Figure 4.17 shows how the maximum deflection of an a-SiC multifunctional membrane with $t_M = 0.5$ µm varies with its length and width. The pressure and temperature loading used in this figure are those given in Figure 3.4 at the peak of the working stroke. The results suggest that different combinations of length and width values (below and to the left of the $z_{max} = 0.5$ µm contour line in Figure 4.17) can satisfy the requirement of $z_{max} \leq t_M$. A sensitivity analysis (more details in Section 4.4) carried out on three example combinations of ($W = L = 25$ µm), ($W = 28$ µm and $L = 23$ µm), and ($W = 23$ µm and $L = 28$ µm) showed no noticeable difference between the results. So, $W = L = 25$ µm is selected for the in-plane dimensions of the membrane.

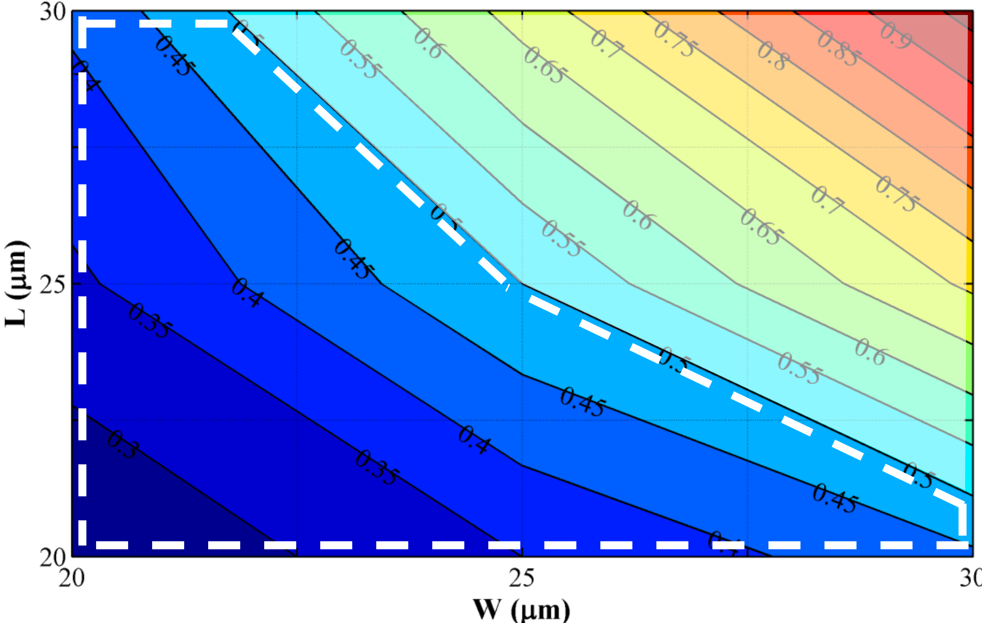

Figure 4.17. Variation of maximum deflection of a 0.5 µm thick a-SiC membrane with length L and width W when subjected to peak in-cylinder pressure and temperature. The region at which the maximum deflection is smaller than the thickness of membrane is contained within dotted line.

To measure the capacitive outputs of the sensor, a voltage difference between the membrane and the bottom electrodes is required. FE simulations show that for $W = L = 25$ µm and a hypothetical measurement voltage difference of 0.1 V, a minimum clearance of $G_{clear} = 0.05$ µm between the membrane and the bottom electrodes is enough to avoid any pull-in (or collapse) due to electrostatic attraction. If a bigger voltage difference is needed for the measurements, then a larger G_{clear} is also needed to be advised of in the design of the multifunctional sensor. A summary of the results and findings of the mechanical modeling section are given in the following. They supplement the ones presented at the end of the thermal modeling section.

- Multifunctional membrane width: $W = 25$ µm,
- Multifunctional membrane length: $L = 25$ µm,
- Multifunctional membrane step height: $h = 1.2 \times t_M = 0.6$ µm,
- Gap between the membrane and the left bottom electrode: $G_1 = 0.55$ µm,
- Gap between the membrane and the right bottom electrode: $G_2 = 0.55$ µm.

4.3 Electrical modeling

In this section, the capacitive output of the multifunctional MEMS sensor for different pressure and temperature loading is predicted and analyzed. According to the results rendered in the thermal modeling section (Figure 4.8 in particular), it is reasonable to assume that during the working cycle of the IC engine, the temperature of the substrate of the MEMS sensor, T_{SC-Si}, remains almost constant. Substituting $\Delta T_{SC-Si} = 0$ in equation (4.34) and its following equations, the modified model is used in this section to first calculate the three-dimensional deformation of the membrane $z(x, y)$ and then determine the capacitive outputs C_1 and C_2 by

$$C_1(P,T) = \int \frac{\varepsilon dxdy}{G_1 - |z(x,y)|} = \int \frac{\varepsilon dxdy}{G_1 - |z_P(-x,y) - z_T(-x,y)|} \qquad (-a < x < 0)$$

$$C_2(P,T) = \int \frac{\varepsilon dxdy}{G_2 - |z(x,y)|} = \int \frac{\varepsilon dxdy}{G_2 - |z_P(x,y) + z_T(x,y)|} \qquad (0 < x < a) \tag{4.39}$$

where z_P and z_T are given by equations (4.20) and (4.34), respectively. The optimized dimensions of the sensor determined in the thermal and mechanical modeling sections are used in the calculation of C_1 and C_2 from equation (4.39). Due to relatively complex shape of the $z(x, y)$ function, the integrations in equations (4.39) are carried out numerically.

Alternatively, C_1 and C_2 can be directly calculated by the FE simulations using ANSYS®. For that, the multiphysics module and ESSOLV solver are used for the analysis of the coupled thermomechanical-electrical model. In the multiphysics analysis, the solid model is first created and the material properties are defined in the form of temperature-dependent tables. The dielectric between the membrane and the bottom electrodes is assumed to be vacuum with the permittivity $\varepsilon_0 = 8.85 \times 10^{-12}$ F/m. Next, the solid model is meshed with 20-node brick element SOLID122. In a coupled multiphysics analysis, a pair of compatible electrical and structural elements is required in order to minimize the need for remeshing while switching between the physics. The ideal companion to the electrical element SOLID122 is the 20-node structural element SOLID186. For the loading cases which involve severe distortion of the dielectric volume elements, the mesh-morphing option is turned on to allow the software to remesh the model whenever needed during its iterative runs. The remeshing is specifically required when the membrane deflection is at its maximum and the gaps between the membrane and the bottom electrodes are at their lowest values.

4.3.1 Fringing effect

When two parallel plates form a capacitor, the electric field between the plates does not end abruptly at the edge of the plates. There is some electric field extending outside the plates which carries electrical energy and should be taken into account when the capacitance is calculated. This effect is referred to as fringing effect and causes the real capacitance to be larger than what calculated by the analytical model, as for example by equations (4.39) above. Calculation of the capacitance by the FE software ANSYS® has the advantage of taking the fringing effect into account. However, this inclusion in turn drastically increases the processing time and the complexity of the model since a bigger dielectric volume with irregular edges needs to be meshed and analysed. When the voltage difference between the capacitor's two electrodes is small the electric field between them does not extend far beyond the electrodes' boundary. For the the multifunctional MEMS sensor designed in this Thesis, ignoring the fringing effect and limiting the analysis to the boundary of the electrodes (as implied by equation (4.39) for example) is assumed to not bring about a major error in the results. Supports for this assumption are provided in appendix C where the effect of fringing effect on the capacitive output of a simple membrane-based pressure sensor is investigated by FE simulations.

4.3.2 Connecting multiple sensors in parallel

To get a bigger capacitive output from MEMS sensors, it is a common practice to connect multiple sensors in parallel [1]. Figure 4.18 schematically shows an array of $M \times N$ multifunctional MEMS sensors connected in parallel. The capacitive outputs C_1 and C_2 in this figure are $M \times N$ times those of the single MEMS sensor shown in Figure 3.10. In the connected configuration, the multifunctional membrane forms the common top electrode of all the connected units while the bottom individual electrodes are connected in series to form two large bottom electrodes. The connecting of multiple MEMS sensors in parallel would increase the surface area and the footprint of the sensor accordingly. It was assumed earleir that the electronic part of the sensor can meaningfully measure a minimum capacitance change of 1 fF. This will be used later in the determination of the number of the sensors required to be arrayed.

As argued in the thermal modeling section, for the multifunctional membrane to exhibit a good thermal performance it is critical to minimize its thermal lost into the substrate Q_1 (Figure 4.1). To do so, the contact area between the membrane and its underneath insulating layer should be minimized. This requirement is met with the custom fabrication process flow proposed in appendix A for the arrayed multifunctional MEMS sensor.

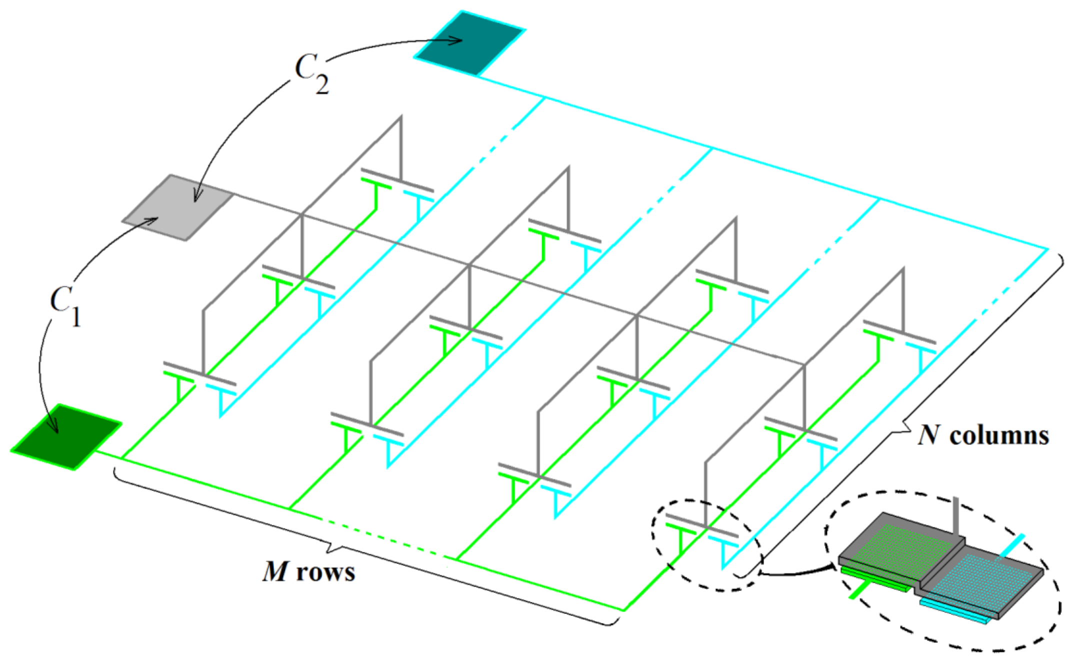

Figure 4.18. Several multifunctional MEMS sensors arrayed in parallel to provide bigger outputs.

4.3.3 Capacitive output

In this section, equation 4.39 is used for the calculation of the capacitive outputs of the multifunctional MEMS sensor. The dimensions and specifications of the multifunctional MEMS sensor studied in this section include $t_M = 0.5$ µm, $t_i = 5$ µm, $t_S = 1050$ µm, $L = W = 25$ µm, $G_1 = G_2 = 0.55$ µm, $h = 0.6$ µm and the number of individual sensor arrayed in parallel $= M \times N$ (yet to be determined in accordance with the assumption of a minimum capacitance change of 1 fF detectable by sensor electronics). The temperature dependence of the sensor material properties discussed in Chapter 2 is taken into account in this section. Moreover, the fringing effect as discussed in Section 4.3.1 is ignored in the numerical calculations. Furthermore, for the in-cylinder pressure and temperature loading of the sensor, the data from Figure 3.4 is used. The first results are presented in Figure 4.19 where the capacitive outputs C_1 and C_2 predicted by the semi-analytical model and the FE simulation (see appendix B for the FE code) are compared. The difference between the results of the two approaches, averaged over the entire pressure and temperature ranges, is about 2.3 % for C_1 and 1.5 % for C_2. The capacitance units of fF (10^{-15} Farad) or pF (10^{-12} Farad) deployed in this figure are associated with cases involving one single MEMS sensor or one thousand arrayed in parallel.

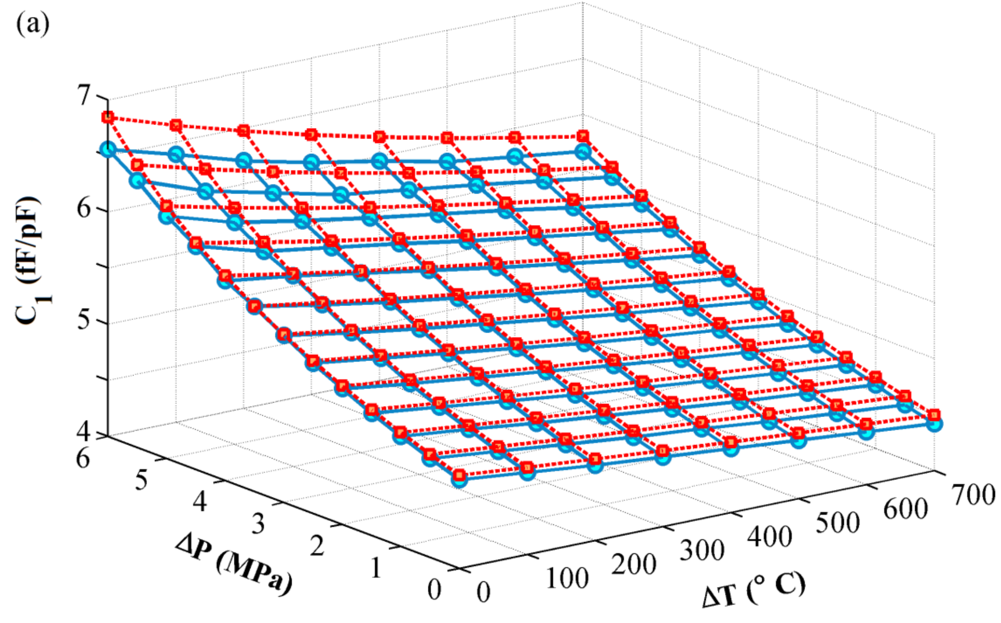

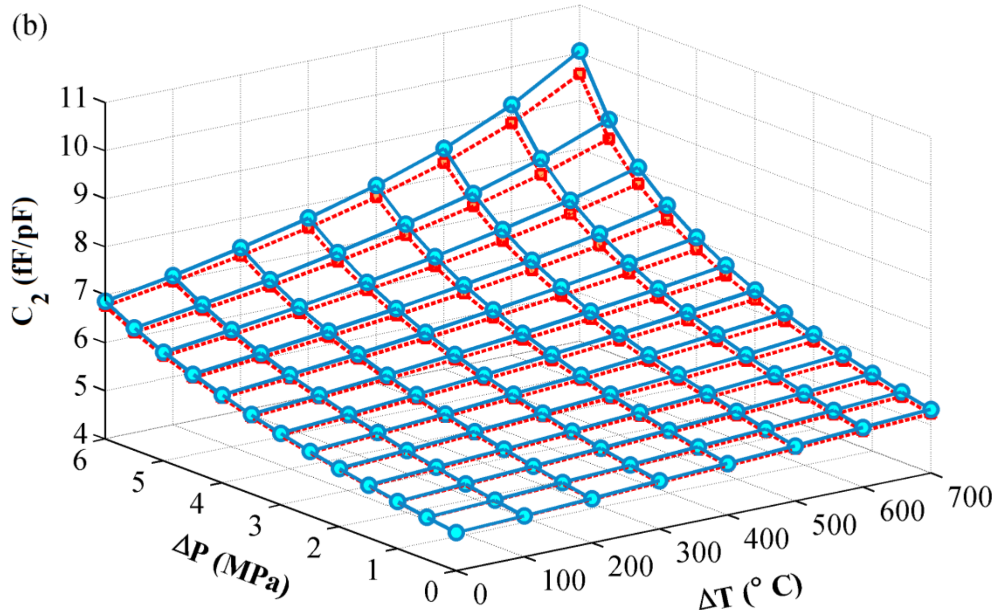

Figure 4.19. (a) C_1 and (b) C_2 predicted by the semi-analytical model (red dotted line) and FE simulation (blue solid line) for the SiC-Si MEMS sensor with dimensions: $L = W = 25$ μm, $h = 0.6$ μm, $t = 0.5$ μm, and $G_1 = G_2 = 0.55$ μm.

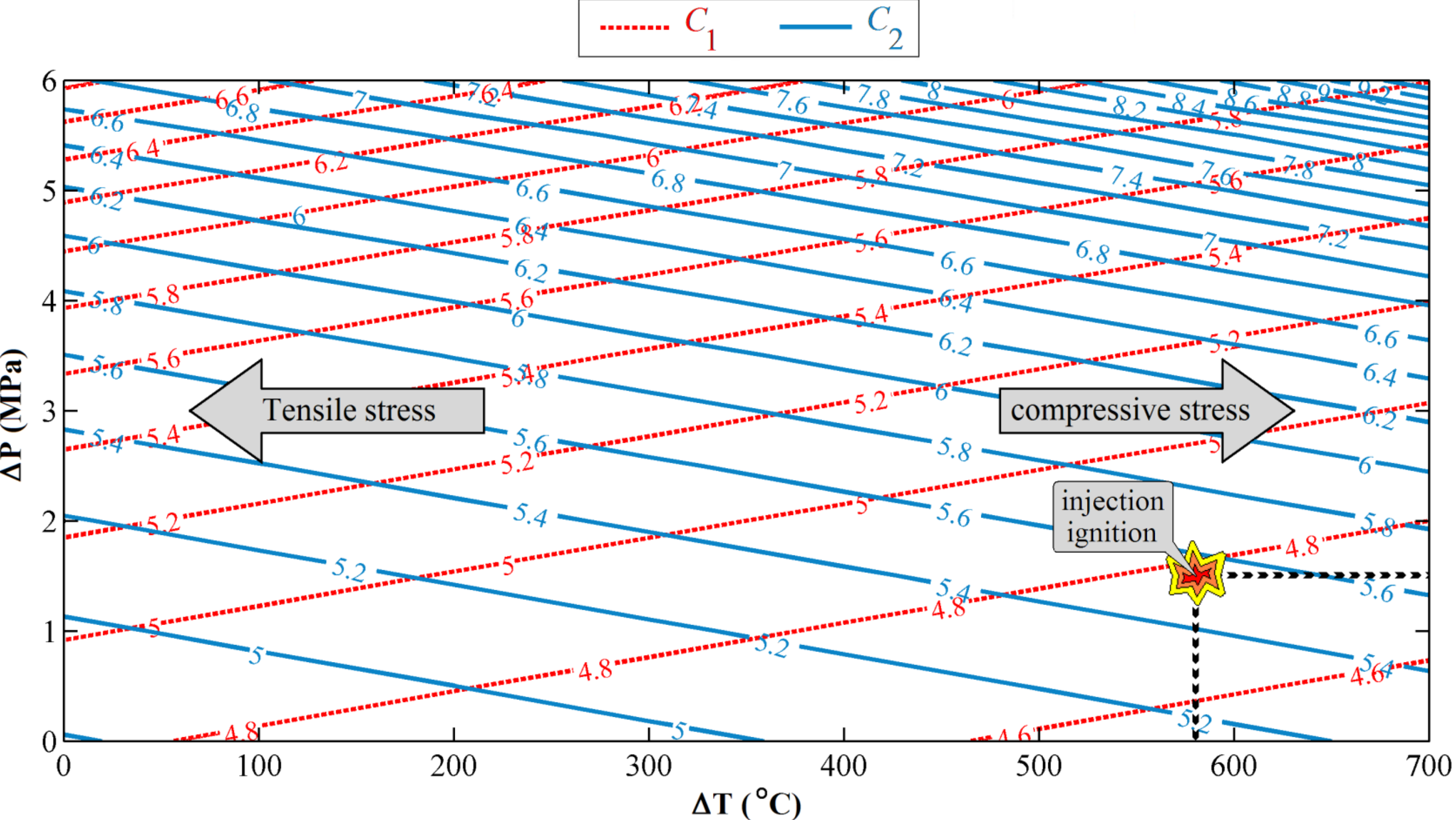

Figure 4.20. Characteristic capacitive output plot for the SiC-Si MEMS sensor with dimensions: $L = W = 25$ µm, $h = 0.6$ µm, $t = 0.5$ µm, and $G_1 = G_2 = 0.55$ µm, calculated by the semi-analytical model. in equation (4.39).

Figure 4.20 combines the results of the semi-analytical model for C_1 and C_2 and provides a comprehensive characteristic plot for the interpretation of the outputs of the sensor (compare with the one shown in Figure 3.11). Similar to Figure 4.19, the capacitance curves in this figure take either fF or pF units depending on whether a single MEMS sensor or one thousand of arrayed sensors are considered. The 0.2 fF (or 0.2 pF for $M \times N = 1000$ devices arrayed) pitch distance between the equal capacitance lines in this figure is tentatively selected for better visualization.

4.3.4 In-cylinder measurement

Figures 4.21 and 4.22 show the capacitive outputs C_1 and C_2 of the MEMS sensor subjected to the in-cylinder pressure and temperature loading given in Figure 3.4. Similar to Figures 4.19 and 4.20, C_1 and C_2 can take fF or pF units depending on the number of sensors connected in parallel (1 or 1000). If the electronics part requires even larger output signals, more sensing units can be arrayed in a similar manner. The in-cylinder pressure and temperature data are also shown in Figures 4.21 and 4.22. Following the measurement of C_1 and C_2 by the electronics, the characteristic plot of Figure 4.20 (calibrated for the subject MEMS device and including the effect of residual stresses) is used for the determination of the in-cylinder pressure and temperature values (inputs) which have given rise to C_1 and C_2 capacitances (outputs).

4.4 Sensitivity analysis

The sensitivity of a sensor is the slope of the output-versus-input characteristic curve. In the case of the multifunctional MEMS sensor designed in this Thesis, the outputs of the sensor are two capacitances C_1 and C_2 and the inputs are pressure and temperature variations. As shown in Figure 4.19, the capacitive outputs are not linear functions of the pressure and temperature variations. So, here the sensitivity should be looked at as a local parameter varying over the pressure and temperature working ranges of the sensor. In this work, the multifunctional MEMS sensor sensitivity to pressure and temperature are defined as

$$S_P = 0.5\left[\frac{\partial C_1(P,T)}{\partial P} + \frac{\partial C_2(P,T)}{\partial P}\right]$$

$$S_T = 0.5\left[\frac{\partial C_1(P,T)}{\partial T} + \frac{\partial C_2(P,T)}{\partial T}\right] \tag{4.40}$$

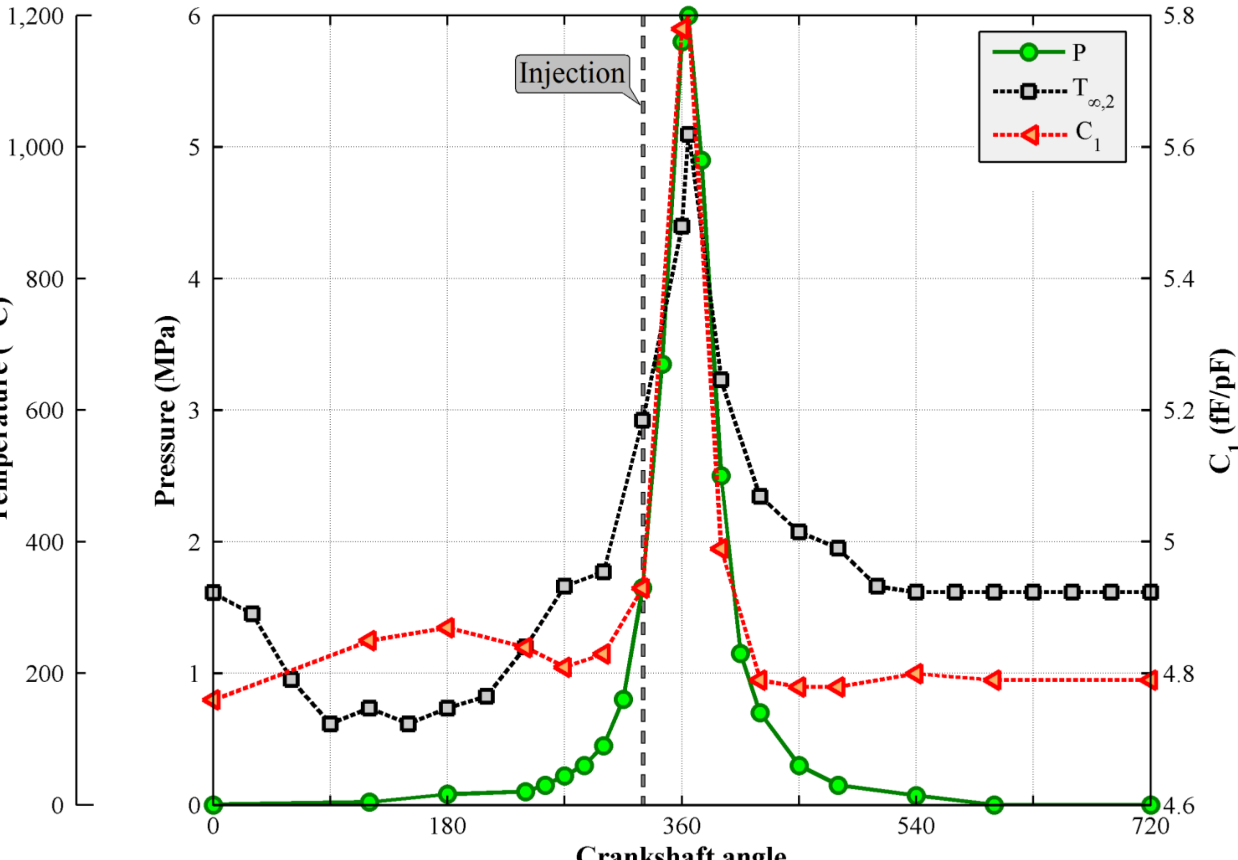

Figure 4.21. Capacitive output C_1 of the multifunctional MEMS sensor subjected to in-cylinder pressure P and temperature $T_{\infty,2}$; dimensions of a single MEMS sensor are: $L = W = 25$ µm, $h = 0.6$ µm, $t = 0.5$ µm, and $G_1 = G_2 = 0.55$ µm.

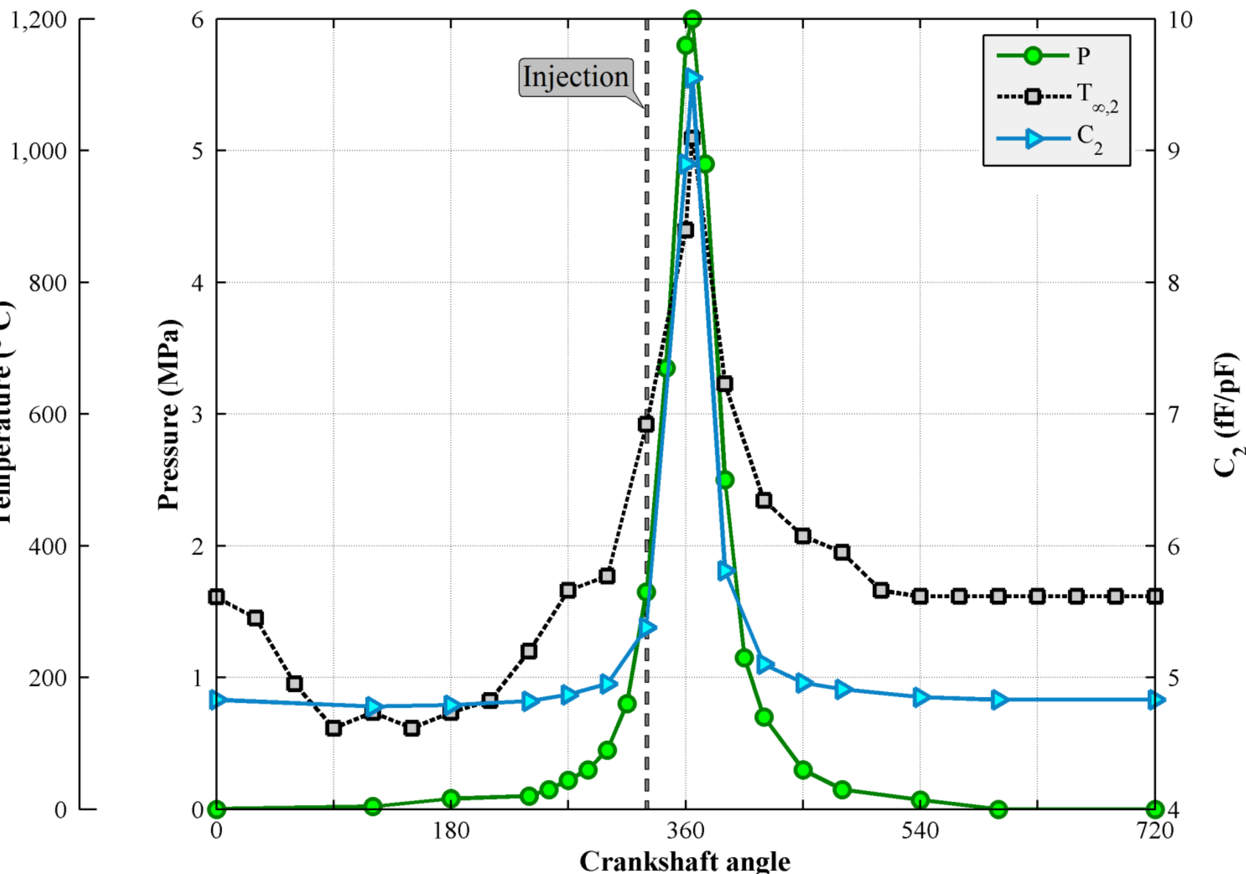

Figure 4.22. Capacitive output C_2 of the multifunctional MEMS sensor subjected to in-cylinder pressure P and temperature $T_{\infty,2}$; dimensions of a single MEMS sensor are: $L = W = 25$ µm, $h = 0.6$ µm, $t = 0.5$ µm, and $G_1 = G_2 = 0.55$ µm.

Based on equation (4.40), Figures 4.23 presents the results of the sensitivity analysis of a single multifunctional MEMS sensor with dimensions $L = W = 25$ μm, $h = 0.6$ μm, $t = 0.5$ μm, and

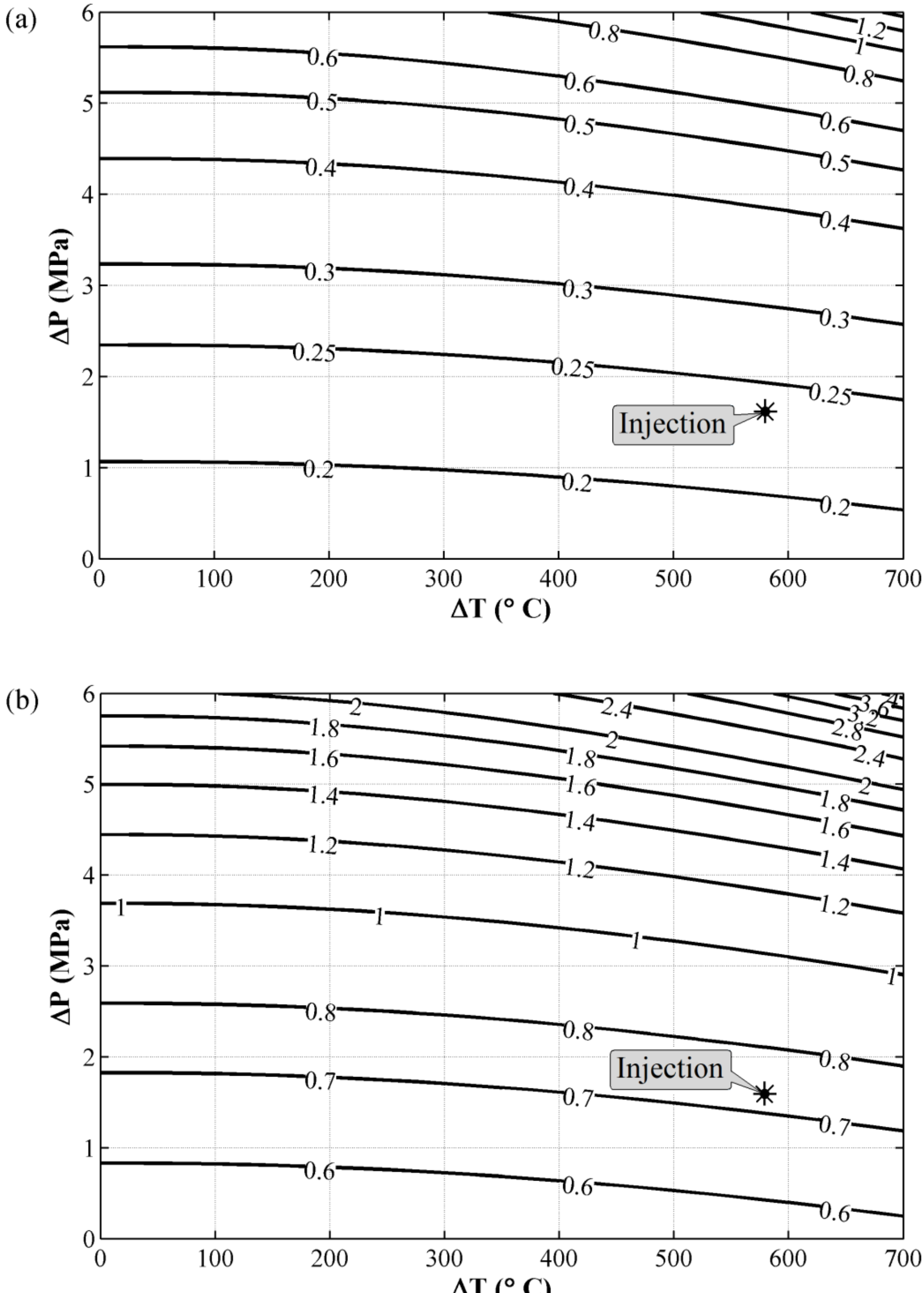

Figure 4.23. (a) S_P in aF/KPa, and (b) S_T in aF/°C for a single multifunctional MEMS sensor.

$G_1 = G_2 = 0.55$ µm. At the time of injection, S_P and S_T are calculated around 0.24 aF/KPa and 0.73 aF/°C, respectively (aF is 10^{-18} Farad). At the height of the working stroke when maximum in-cylinder pressure and temperature coexist (Figure 3.4), S_P and S_T exhibit their maximum values 1.42 aF/KPa and 4.1 aF/°C, respectively. The average values of S_P and S_T over the entire pressure and temperature working range of the sensor are calculated as 0.37 aF/KPa and 1.1 aF/°C, respectively.

Based on the results in Figure 4.23, Figure 4.24 shows the sensitivities to pressure and temperature a multifunctional MEMS sensor would demonstrate when subjected to in-cylinder pressure and temperature loading of Figure 3.4.

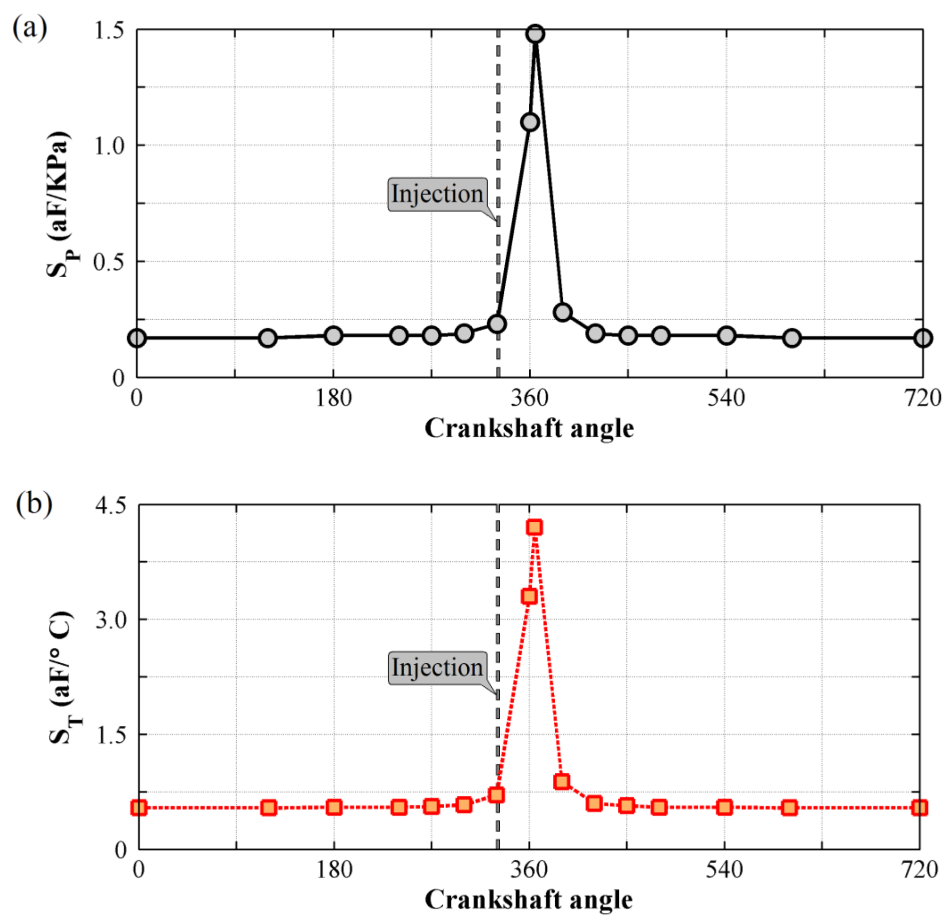

Figure 4.24. Sensitivities to (a) pressure and (b) temperature of a SiC-Si multifunctional MEMS sensor when subjected to in-cylinder pressure and temperature loading; The dimensions of the sensor are: $L = W = 25$ µm, $h = 0.6$ µm, $t = 0.5$ µm, and $G_1 = G_2 = 0.55$ µm.

Comparison between the minimum detectable capacitance change of 1 fF (assumed for the sensor electronics) and the sensitivity values presented in Figure 4.24 reiterates the need for connecting several sensors to achieve an acceptable minimum pressure and temperature detecting limit.

Table 4.1 summarizes the results and shows the effect of arraying multiple MEMS sensors, with the number of devices $M \times N$ varying between 1 and 4200. For each $M \times N$ number, the approximate sensor area (calculated based on the optimized dimensions and the fabrication process proposed in appendix A), the sensitivities to pressure and temperature, and the minimum measurable pressure and temperature at the time of injection and at the height of the working stroke are calculated and presented. The dimensions of the MEMS sensor studied in Table 4.1 are $L = W = 25$ µm, $h = 0.6$ µm, $t = 0.5$ µm, $G_1 = G_2 = 0.55$ µm, and $L_E = 150$ µm (Figures 3.10 and 4.1).

Table 4.1. Working characteristics of different configurations of multifunctional MEMS sensor.

Number of MEMS sensors connected ($M \times N$)	1	1000	2000	4200
Estimated sensor chip area (mm^2)	0.1	1.4	2.4	4.5
S_P at the time of injection (fF/KPa)	2.4×10^{-4}	0.24	0.48	1.01
S_P at the height of working stroke (fF/KPa)	1.42×10^{-3}	1.42	2.84	5.96
S_P average (fF/KPa)	3.7×10^{-4}	0.37	0.74	1.55
S_T at the time of injection (fF/°C)	7.3×10^{-4}	0.73	1.46	3.07
S_T at the height of working stroke (fF/°C)	4.1×10^{-3}	4.1	8.2	17.22
S_T average (fF/°C)	1.1×10^{-3}	1.1	2.2	4.62
ΔP_{min} § at the time of injection (KPa)	4167	4.17	2.08	0.99
ΔP_{min} at the height of working stroke (KPa)	704	0.7	0.35	0.17
ΔT_{min} ₪ at the time of injection (°C)	1369	1.37	0.68	0.33
ΔT_{min} at the height of working stroke (°C)	243.9	0.24	0.12	0.06

§ minimum measurable pressure variation

₪ minimum measurable temperature variation

The average sensitivity to temperature of 1.1 fF/°C calculated for the multifunctional MEMS sensor configuration with $M \times N = 1000$ (with vacuum dielectric between the electrodes) is comparable to the 7 fF/°C reported in literature for a multilayer MEMS temperature sensor with an area of 1 mm^2 and a 0.45 μm thick SiO_2/Si_3N_4 dielectric layer (relative permittivity ε_r of SiO_2 is 3.9 and that of Si_3N_4 is 7.5) [148]. The reported sensor has been designed and tested for static temperature measurement over the temperature range of -70 to 100 °C. Recently, a similar multilayer capacitive MEMS temperature sensor with a chip area of 4 mm^2 and a 1 μm thick SiO_2/Si_3N_4 dielectric layer has been reported in [149]. Between room temperature and 600 °C, the reported device has achieved an average sensitivity to temperature of 5 fF/°C which (regarding the use of high ε_r dielectric) is comparable to what the multifunctional MEMS sensor with $M \times N = 1000$ configuration and 1.4 mm^2 chip area delivers (Table 4.1).

For the average sensitivity to pressure, the 1.55 fF/KPa calculated for the multifunctional MEMS sensor configuration with $M \times N = 4200$ (4.5 mm^2 chip area) is comparable with some recent harsh environment MEMS pressure sensors reported in literature, namely: 0.91 fF/KPa ($M \times N = 128$, 2 mm^2 chip area) [77], 1.3 fF/KPa (SiC membrane and substrate, $M \times N = 130$, 20 mm^2 chip area) [1], and 0.61 fF/KPa (SiC membrane and Si substrate, $M \times N = 260$, chip area not reported) [84].

In summary, the designed MEMS sensor has the potential to deliver sensitivities to pressure and temperature comparable with the recent research MEMS sensor reported in literature. On top of this, it promises short thermal response times, which makes it the ideal design for such dynamic harsh environment applications as IC engine.

4.5 Multifunctional sensor design guideline

Based on the modeling and analysis work presented in this chapter, a design guideline for the customization and optimization of the multifunctional sensor for different applications can be established. To do so, the first step will be the determination of sensor's operational requirements based on the specific application. Next, the out-of-plane dimensions of the sensor, i.e. the thicknesses of its different components, will be optimized to achieve the required thermal response. This is then followed by the optimization of the in-plane dimensions of the sensor (mainly lengths and widths of the membrane) to achieve the required mechanical response. Finally, the configuration of the sensor will optimized (based on the outputs of thermal and mechanical optimization steps) in such a way that the required elelctrical specifications are met.

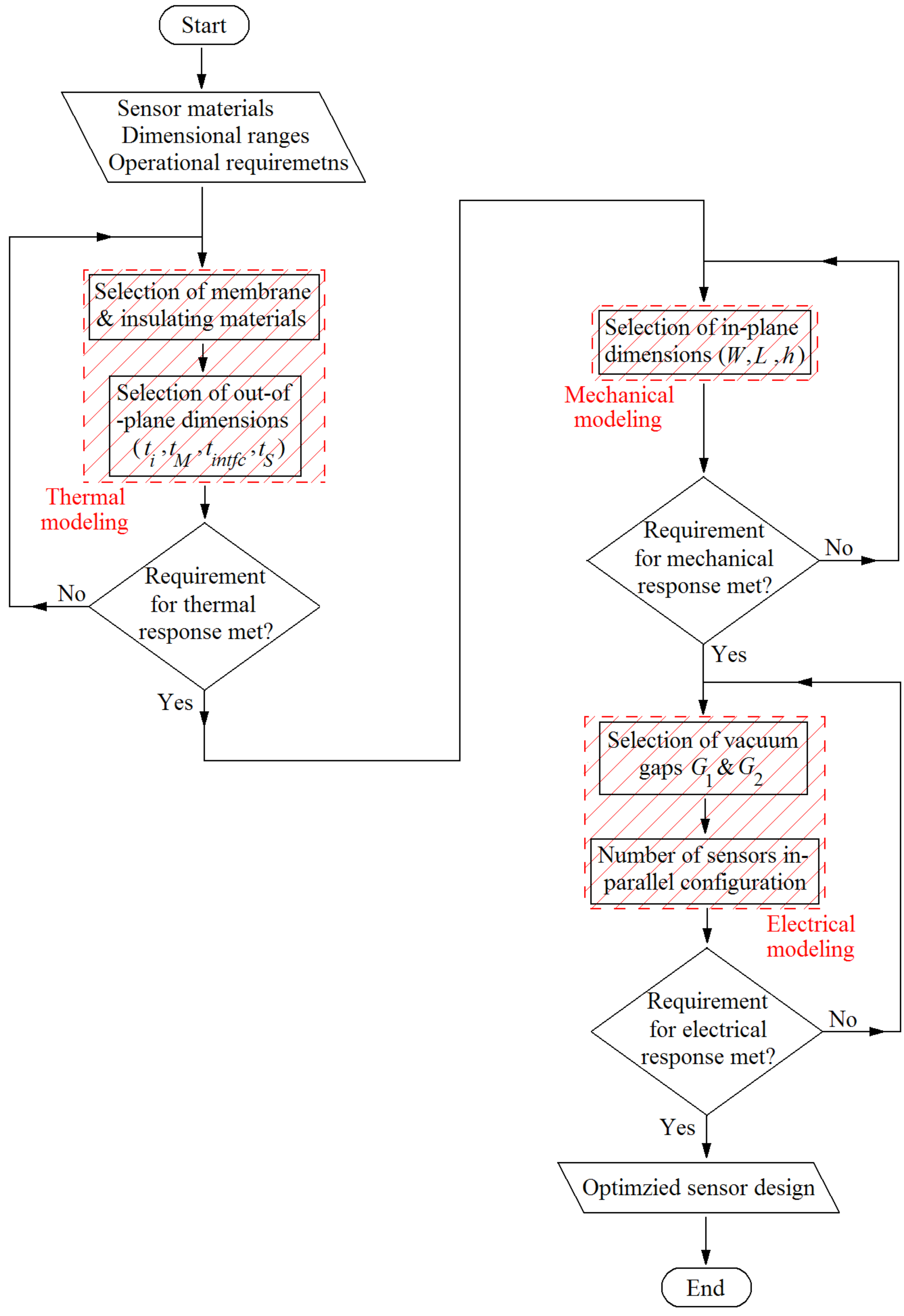

Figure 4.25. A step-by-step design guideline for multifunctional MEMS sensor (for information on geometrical parameters refer to Figure 4.1).

Figure 4.25 presents the design guidline in the form of a flow chart whose inputs are sensor'structural smaterials (in accordance with section 2.1.2), dimensions, and operation requiremetns. The output of the flow chart is the optimized disegn of the sensor which meets the operation requirements.

4.6 Effect of fabrication and deviations from design parameters

4.6.1 Residual stress in thin films

Microfabrication processes often introduce residual stresses to thin film structures. The residual stress originates mostly from the thermal mismatch between the deposited thin film and the substrate over which the thin film is deposited. The residual stress in as-deposited thin films is a major issue and can cause severe distortion or cracking in the thin film. To alleviate the residual stress in thin films, deposition optimization and post fabrication annealing are widely used. Even with such measures, a portion of the original residual stress, which still can be in the order of hundreds of mega Pascal, remains in the thin film [150, 151].

In a MEMS sensor, the residual stress manifests itself in the form of an initial curvature. Inspired by its thermal origin, the effect of the residual stress in a thin film can be assimilated by applying an initial temperature change ΔT_{init} to the model. Based on the direction of the residual stress being tensile or compressive, ΔT_{init} may take negative or positive values, respectively. For the case of the multifunctional membrane investigated in this chapter, the effect of the fabrication-induced residual stress can similarly be included in the modeling by modifying the temperature variation the sensor undergoes to include the effect of ΔT_{init}. This can be approximately incorporated into the characteristics plot of Figure 4.20, for example, by initially shifting the plots along the temperature-axis to the left (tensile residual stress) or right (compressive residual stress). According to Figure 4.23, a shift to the left (corresponding to a tensile residual stress in the multifunctional membrane layer) slightly increases the sensitivities of the sensor to pressure and temperature.

4.6.2 Deviation of dimensions from design parameters

The modeling sections in this chapter show that the performance of the multifunctional MEMS sensor greatly depends on its dimensions and material properties. Considering the uncertainties and common errors associated with microfabrication processes, achieving the ideal dimensions determined by the theoretical modeling or reproducing the material properties reported in literature is a formidable task,

if not impossible. In this section, the effects of deviations from ideal design parameters (both dimensions and material properties) on the sensor expected performance are briefly discussed.

Variation of in-plane dimensions

Among the dimensions introduced in Figure 4.1, the length L and the width W of the membrane play a major role in the mechanical response of the multifunctional membrane to pressure and temperature variations. Smaller than designed L and W result in increased extensional spring constant k_z. According to equation (4.20), this brings about a smaller pressure-induced deformation of the membrane than expected, which in turn negatively affects the sensor pressure sensitivity. From a thermal perspective, a smaller W gives rise to a smaller amplitude modification factor $\bar{\xi}_T$ (Figure 4.15) which undesirably reduces the sensor thermal sensitivity. Since the realization of the cavity under the multifunctional membrane is by DIRE process (refer to proposed fabrication process in appendix A), it is critical to take into account and foresee such side effects as undercut which may cause the final in-plane dimensions differ from the ideal design values. For the other important in-plane dimension, the width of the bonding interface L_E, it was shown earlier that its variation does not noticeably affect the sensor thermal performance. Further FE simulations show that such a variation does not affect the sensor mechanical performance as well.

Variation of out-of-plane dimensions

The most important out-of-plane dimensions of the sensor are the step height h (Figure 3.6) and the thickness of the multifunctional membrane t_M (Figure 4.1). While the former one only affects the sensor's mechanical response, the latter one influences both thermal and mechanical responses. As discussed in Figure 4.12, increasing the step height while keeping the other dimensions of the membrane unchanged increases the extensional spring constant k_z. On the other hand, the effect of an increased step height on the sensor's response to temperature variation is more complex as there is an optimum step height-to-thickness ratio which results in the highest $\bar{\xi}_T$ and thus maximizes the thermal sensitivity of the device. As suggested in the fabrication process flow in appendix A, the realization of the step feature in the multifunctional membrane is the result of the fabrication step "RIE etching of sacrificial SiO_2 layer". The RIE process is relatively slow and easy to control (by controlling such working parameters of the RIE equipment as ICP power, plasma power, chamber pressure, etc.).

The effect of the multifunctional membrane thickness t_M on the sensor's thermal performance was studied in Section 4.1. As shown in Figure 4.4, t_M significantly affects how closely the membrane

temperature $T_{M,1}$ follows the temperature of the in-cylinder gaseous content $T_{\infty,2}$. In general, the thinner the membrane, the better the match between $T_{M,1}$ and $T_{\infty,2}$ would be. On the other hand, a thinner membrane layer means a bigger deflection under pressure. This adversely affects the sensor's mechanical performance by requiring a larger number of smaller sensor cells to be arrayed in parallel to provide an acceptable capacitive output. The deposition of the a-SiC membrane layer is usually carried out by LPCVD or PECVD techniques. These processes are inherently slow and allow excellent control, with the possibility of *in situ* real time monitoring, of the deposition thickness.

Deviation of the step sidewall angle

As mentioned above, the step feature in the multifunctional membrane is the result of an RIE etching process on SiO_2 sacrificial layer. The resulting sidewall angle from an RIE process is usually controlled by manipulating its working parameters [152-154]. The ideal outcome of RIE process is vertical sidewalls; but, there might be deviations in the form of sidewalls with $\theta \neq 90$ (Figure 3.6). FE simulations show that such a deviation in sidewall angle increases k_z and k_θ, thus negatively affects the membrane sensitivity.

Variation of material properties

In Figure 4.5, the effect of the multifunctional membrane material (a-SiC versus poly-SiC) on its thermal performance was investigated. Proper thermal performance of the multifunctional membrane relies on minimizing the thermal communication between its over-the-cavity and off-the-cavity parts. Moreover, the deformation of the membrane due to in-cylinder conditions greatly depends on its elastic properties. A smaller than expected Young's modulus, for example, brings about a bigger displacement of the membrane which may results in the membrane contacting the bottom electrodes during the sensor operation. To avoid such issues, it is critical to get material properties as close to design parameters as possible. To achieve this, the fabrication process needs to be appropriately monitored and calibrated. As will be listed in the future work section in Chapter 6, the calibration and tuning of the various fabrication processes required for the fabrication of the multifunctional MEMS sensor forms a big portion of the future optimization plan to achieve the desired sensor performance.

Chapter 5
Experiment and Result

In this chapter, the experimental procedures and their results for some fabricated MEMS devices (including test devices and prototypes) are presented. The fabricated devices are categorized into two main groups. The first group includes test devices intended for material characterization of MEMS structural layers. The second group involves prototypes designed and fabricated for the evaluation (both qualitatively and quantitatively) of the thermal response of the proposed multifunctional MEMS sensor. The polysilicon multi user foundry process PolyMUMPs® [155] is used for the fabrication of all the reported devices. The visual characterizations of the fabricated MEMS devices using optical microscope, scanning electron microscope (SEM) and optical profilometer are also reported in this chapter. Finally, the high temperature experiments setup and results are presented.

5.1 PolyMUMPs® microfabrication process

All the MEMS devices reported in this chapter are fabricated using the PolyMUMPs® foundry process, facilitated by the Canadian Microelectronic Corporation (CMC). The PolyMUMPs® foundry process begins with a 6-inch silicon wafer on top of which a 0.6 µm thick Si_3N_4 (the stoichiometric ratio may vary) film is deposited as an electrical isolating layer. The first poly-Si layer (design name *Poly0*, thickness 0.5 µm) is then selectively deposited and patterned to form the bottom electrode (if needed). This is followed by the deposition and patterning of the first SiO_2 layer (design name *Oxide1*, thickness 2 µm), second poly-Si layer (design name *Poly1*, thickness 2 µm), second SiO_2 layer (design name *Oxide2*, thickness 0.75 µm), third poly-Si layer (design name *Poly2*, thickness 1.5 µm), and finally the gold layer (design name *gold*, thickness 0.5 µm). For all the mentioned layers but gold the patterning and creation of features are implemented by RIE process. For the gold layer, however, the patterning is done through liftoff process. After all the deposition and patterning steps are done, buffered hydrofluoric acid (BHF) is used to etch the sacrificial SiO_2 layers away. This is followed by supercritical CO2 drying to avoid stiction of the released MEMS devices to the substrate. A comprehensive description of the PolyMUMPs foundry process along with its design manual can be found at [155]. A schematic of PolyMUMPs® process flow is provided in appendix A. All the fabricated devices have been designed using the CoventorWare® MEMS design software [156]. The build-in libraries for material properties and the PolyMUMPs standard process flow have been used during the designs. Appendix D shows the layouts of the designed 5×5 mm^2 PolyMUMPs chips.

5.2 Fabricated devices and results

5.2.1 Test devices for material characterization

The fabricate devices presented in this section are those used for material characterization, specifically for the determination of the fabricated induced residual stresses. They include 1) Vernier gauges which are used for the measurement of residual stress of *Poly1* and *Poly2* polysilicon structural layers, and 2) gold-polysilicon bimaterial cantilevers for the measurement of residual stress of the *gold* layer. Figure 5.1 provides the SEM photo of the latter one.

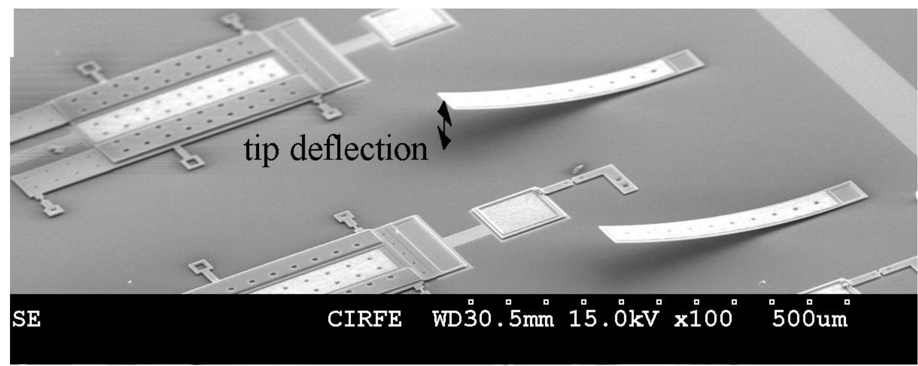

Figure 5.1. Bimaterial microcantilevers fabricated using the PolyMUMPs® foundry process and used in this work for material characterization.

The Vernier gauge device is fabricated based upon the work published by Lin et al. [157]. In the design of the device, the fixed markers (anchored to the substrate) and the unfixed ones (attached to the end of the indicator beam) are aligned. The fixed markers are spaced 0.25 μm (called offset value) further apart from the unfixed markers. Upon releasing with BFH, the residual stress in the structural material results in a displacement of the unfixed markers with respect to the fixed ones. Since the tooth gap on the unfixed markers is smaller than that on the fixed one, some teeth become closer to being aligned due to residual stress in the indicator beam. If the tip of the indicator beam moves to the left, the residual stress is tensile and vice versa.

By finding the number of the corresponding teeth in alignment, the relative displacement of the indicator beam can be calculated by multiplying the aligned tooth number minus one by the offset value. From this displacement the residual strain in the indicator beam is then determined (details of

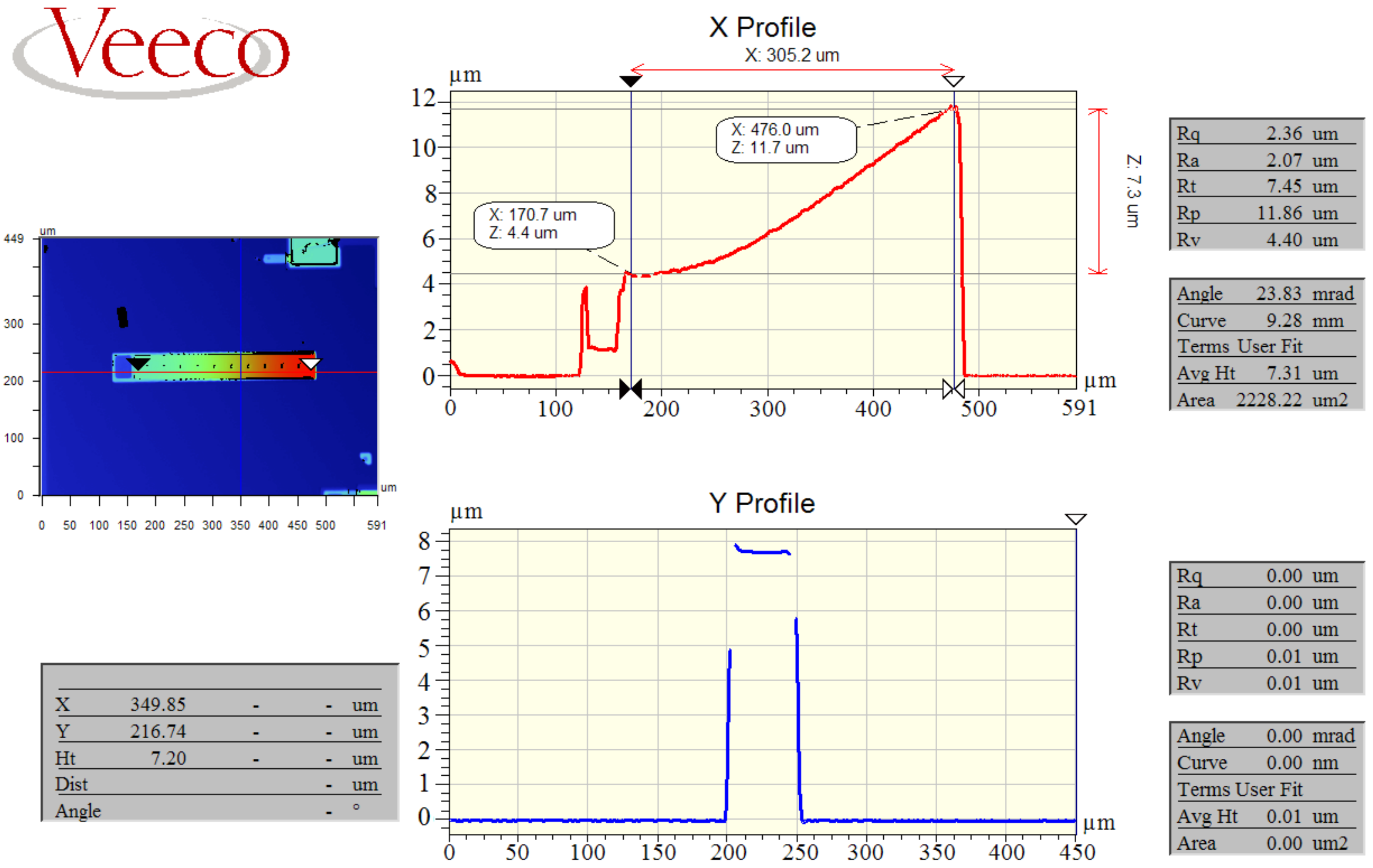

Figure 5.2. Optical profile of a gold-polysilicon bimaterial microcantilever.

calculation given at [157]). Finally, using the Young's modulus of the structural layer in which the Vernier gauge is realized, the residual stress of the layer can be determined. In line with the published data for the PolyMUMPs® structural layers [158], the following Young's moduli are used here: 165 GPa for *Polyl* layer, 165 GPa for *Poly2* layer, and 78 GPa for *gold* layer. Using these values, the residual stresses of the *poly1* and *poly2* layers are measured to be about 7 MPa and 6 MPa, respectively. The measured residual stresses are all compressive.

The above measured residual stress for *poly2* layer is now used for the determination of the residual stress of the gold layer. For this purpose, the gold-polysilicon bimaterial microcantilever is characterised under a WYKO NT1100 optical profiler and its tip deflection (or alternatively its curvature) is measured. For example, Figure 5.2 shows the optical profile of one of the tested bimaterial microcantilevers. The residual stress of the *poly2* base layer, the elastic moduli of the *poly2* and *gold* layers, and the nominal design dimensions of the microcantilevers (length, width, and thicknesses of their constituent layers) are fed into the FE program which predicts the microcantilever's tip deflection for various *gold* residual stress numbers. By comparing the results of FE simulations with the measurements from the optical profiler, the average residual stress of the gold layer is measured to be around 19 MPa.

5.2.2 First prototype

The first prototypes are clamped-clamped beams which are fabricated in polysilicon only and gold-polysilicon configurations (Figure 5.3). They are used for qualitative verification of the thermal response mechanism of the multifunctional membrane (Figure 3.8). The height of the step feature in Figure 5.3, *h,* measures about 2.75 μm. So, the step height-to-thickness ratio of the beam is about 1.4. In this section, the polysilicon beam (the right one in Figure 5.3) is investigated. Due to residual stress in *poly1* and *poly2* layers, the as-fabricated clamped-clamped beam is initially deformed in such a way that resembles a negative temperature variation being applied to it (Figure 5.4). Next, the beam is heated up by Joule heating. An Agilent triple output DC power supply is used to generate the DC signal with a peak-to-peak voltage, V_{PP}, between 0 and 6 V. The profile of the heated beam at $V_{PP} = 3$ (v) and $V_{PP} = 5$ (v) are also shown in Figure 5.4. This figure shows the thermal response mechanism which was proposed and analyzed in Chapters 3 and 4.

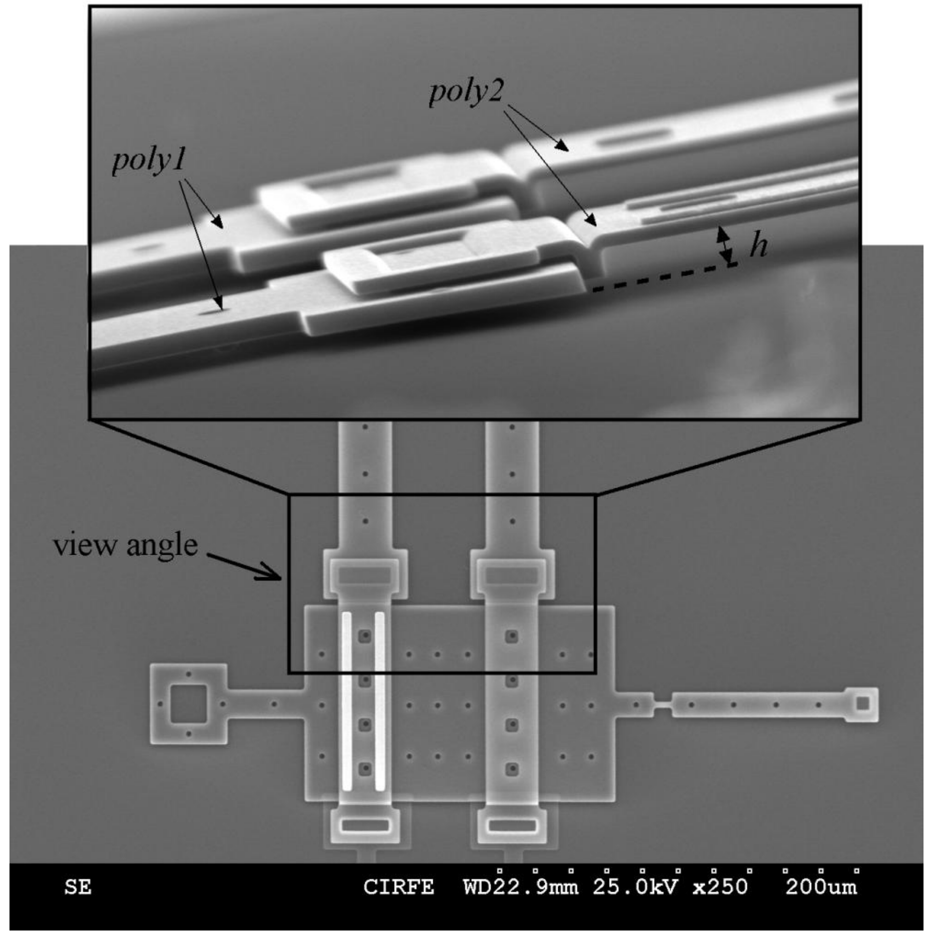

Figure 5.3. Clamped-clamped beams fabricated in polysilicon (right) and gold-polysilicon (left) configurations. The inset on top provides a closer isometric look at step feature.

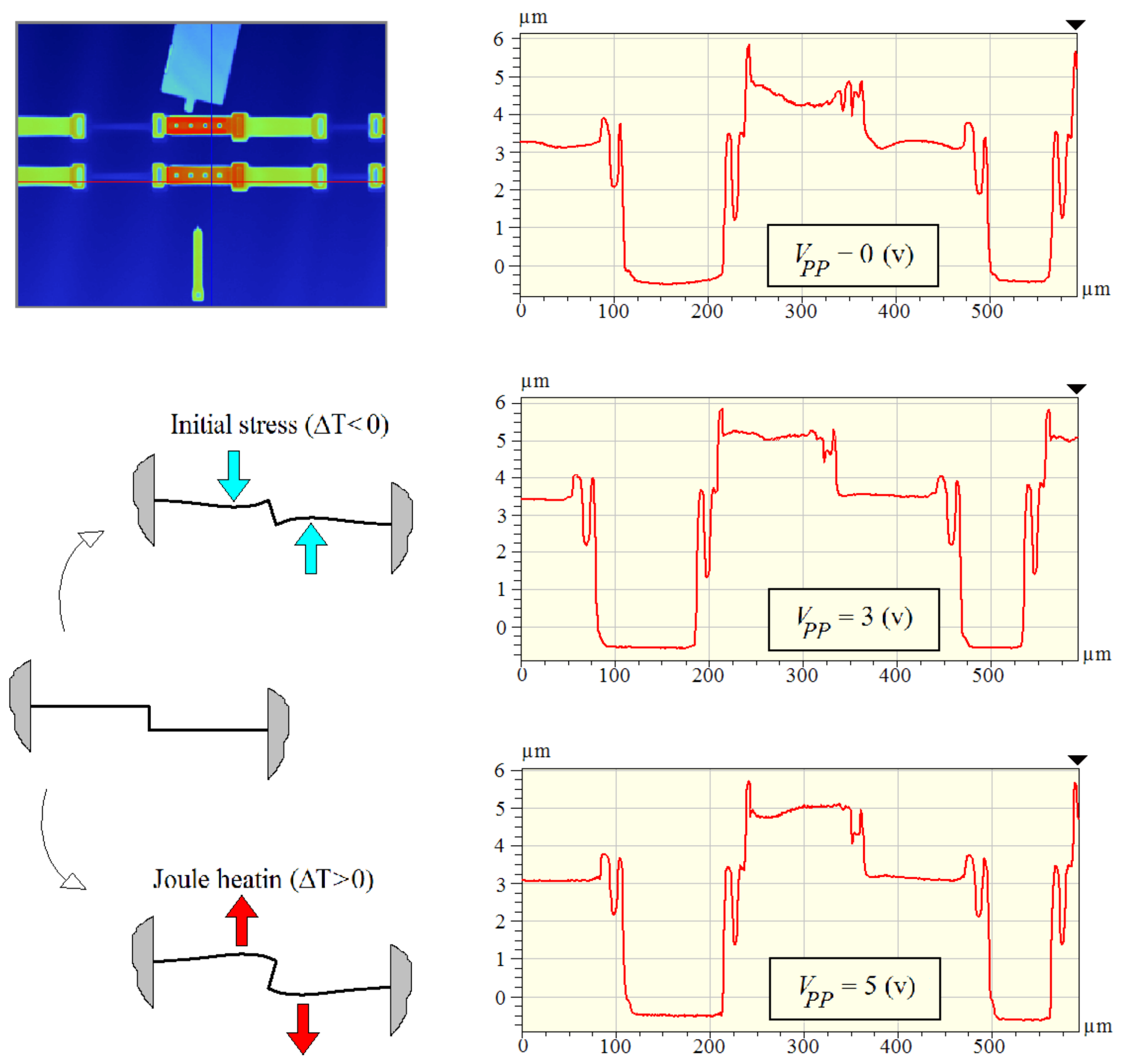

Figure 5.4. Deformation of a clamped-clamped beam (top) with increased temperature due to Joule heating (right); On the bottom left, the deformation patterns are schematically identified.

5.2.3 Second prototype

The second series of MEMS prototypes are designed and fabricated to quantitatively test the thermal response of the multifunctional membrane. One of the fabricated prototypes is shown in Figure 5.5.a. Mandated by the PolyMUMPs process flow, arrays of etch holes are added to the membrane for the sacrificial layer(s) under the membrane be etched away. These etch holes help in realizing a thin

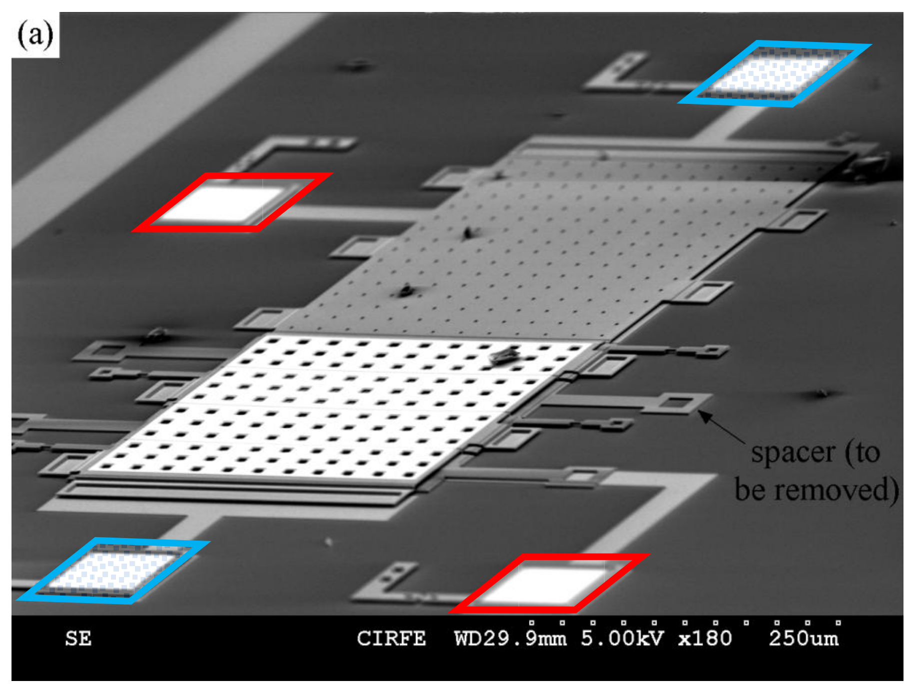

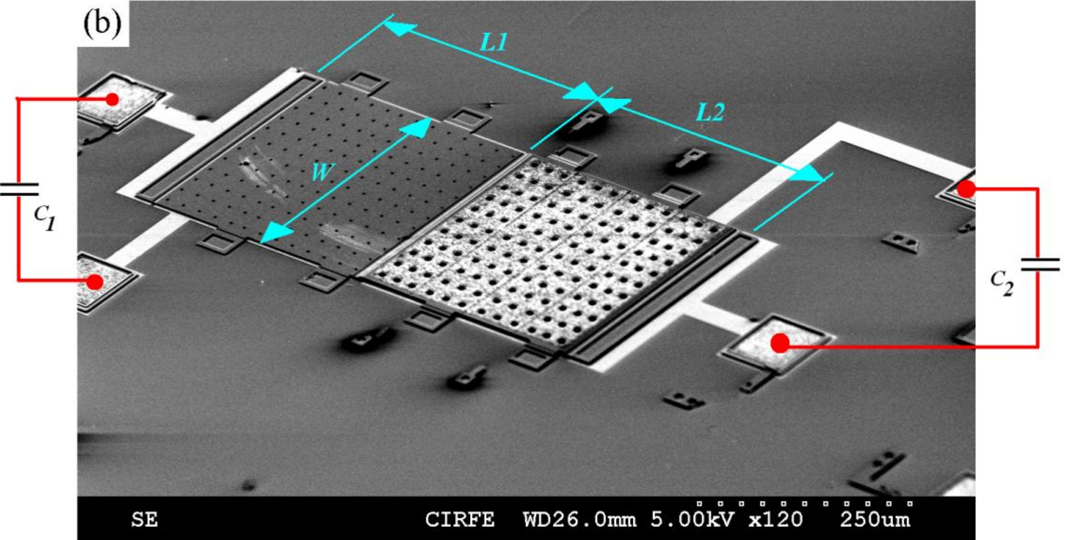

Figure 5.5. Multifunctional membrane (a) before and (b) after the spacers are removed. The membrane is connected to two pads (blue). The bottom electrodes are connected to the other two pads (red). Capacitances C_1 and C_2 are formed between the membrane and the bottom electrodes.

membrane suspended over bottom electrodes (resembling the multifunctional membrane shown in Figure 3.10). On the negative side, these holes remove the pressure responding function of the membrane (as no pressure difference between the two sides can build up). In the as-fabricated device shown in Figure 5.5.a, the *Poly1* layer is used for temporary spacer(s) that provide the additional height needed for the realization of the step feature. To prepare the device for high temperature experiments, these spacers are broken and removed manually under a Cascade Microtech M-150 probe station equipped with 2.4 µm tungsten tips. Figure 5.5.b shows the device after the spacers are removed (the broken anchors of the spacers left on the chip can be seen in this figure). The device is now ready for high temperature experiment.

Test setup

Figure 5.6 shows the test setup used for high temperature experiments. The setup is mounted on the stage of the probe station and includes an ULTRAMIC® ceramic heater from WATLOW (AlN, maximum temperature of 400 °C, integrated with a type K thermocouple) connected to a temperature controller. The ceramic heater is sandwiched between two insulating layers. A small 2×2 cm^2 window

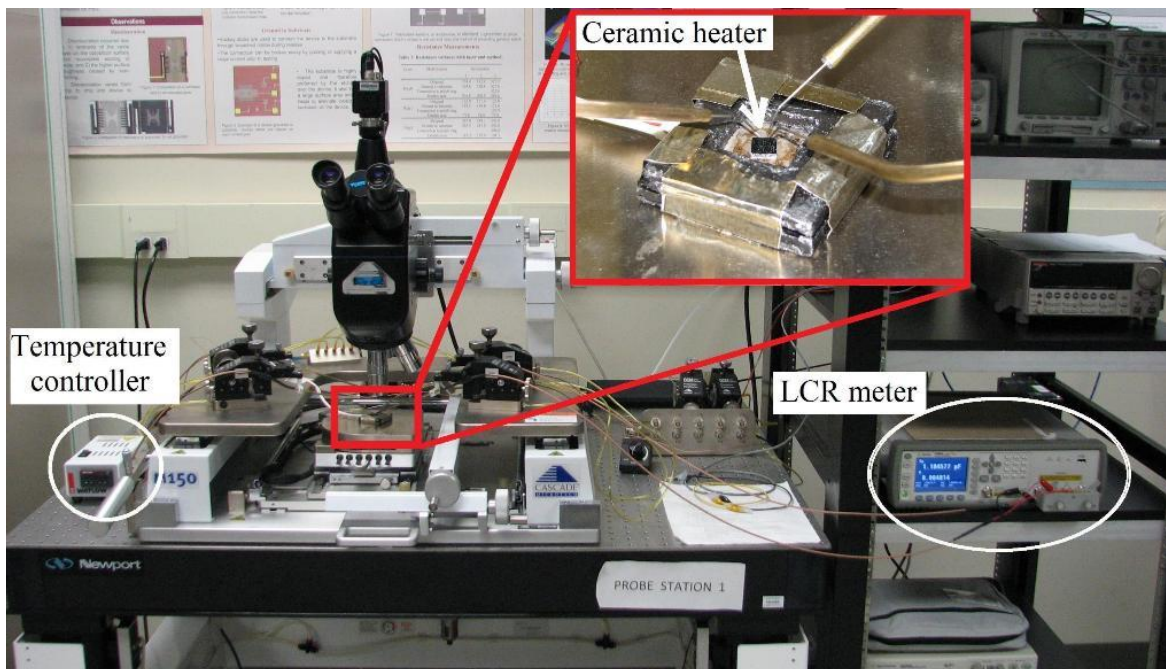

Figure 5.6. Test setup for capacitive temperature measurements.

is cut through the top insulating layer to provide access for the PolyMUMPs chip (measuring 5 by 5 mm) to be put directly on top of the ceramic heater (inset in Figure 5.6). The prototype devices are situated on the PolyMUMPs chip. The measurements are carried out at 25 °C temperature steps between 25 °C and a maximum temperature of 125 °C (limited by the occurrence of snap-through buckling of the membrane afterwhich the device capacitive performance deviated from the expected one). The average fluctuation of the ceramic heater temperature around the set values is about ±0.5 °C for 25 °C, ±1.0 °C for 50 °C, and ±3.0 °C for set temperatures up to 125 °C.

Each device is connected to four gold-covered pads which are used for probing the device (Figure 5.5). Two of the pads are connected to the bottom electrodes located under the membrane. The other two pads are connected to the gold-polysilicon membrane. The two pairs of neighboring pads are used to measure the capacitive outputs C_1 and C_2 (Figure 5.5). The same two tungsten probes used for removing the spacer parts are used here for probing the device and for the electrical measurements. The probes are connected to AGILENT precision LCR-meter which is used for capacitance measurement.

A third probe is also used for grounding the PolyMUMPs chip's SC-Si substrate. This probe is directly connected to the ground port on the LCR-meter. During the experiments, the third probe keeps the SC-Si substrate discharged and reduces the corresponding parasitic capacitance. The measured capacitances before the substrate is discharged are in the range of a few Pf; however, after the third probe is used they drop to a few hundred fF which is comparable with the predictions of FE simulations.

Experimental results and comparison with FE simulation

Figure 5.7 presents the results of thermal loading tests on the the prototype device shown in Figure 5.5.b. The dimensions of the device include $G_1 = 1.25\ \mu m$ (gap between the membrane and the left bottom electrode), $G_2 = 4\ \mu m$ (gap between the membrane and the right bottom electrode), $h = 2.75\ \mu m$, $t_{M,left} = 2\ \mu m$ (thickness of the left half of the membrane which is in *poly1*), $t_{M,right} = 2\ \mu m$ (total thickness of the right half of the membrane comprising gold over *poly2* polysilicon), $W = 300\ \mu m$, $L_1 = 400\ \mu m$, and $L_2 = 350\ \mu m$. The results of FE simulations, using the design dimensions and including the initial stresses, are also shown in this figure (the FE code is provided in appendix B). In order to separate the effect of parasitic capacitances, the variation of C_1 and C_2 with temperature, instead of their absolute value, are presented in Figure 5.7.

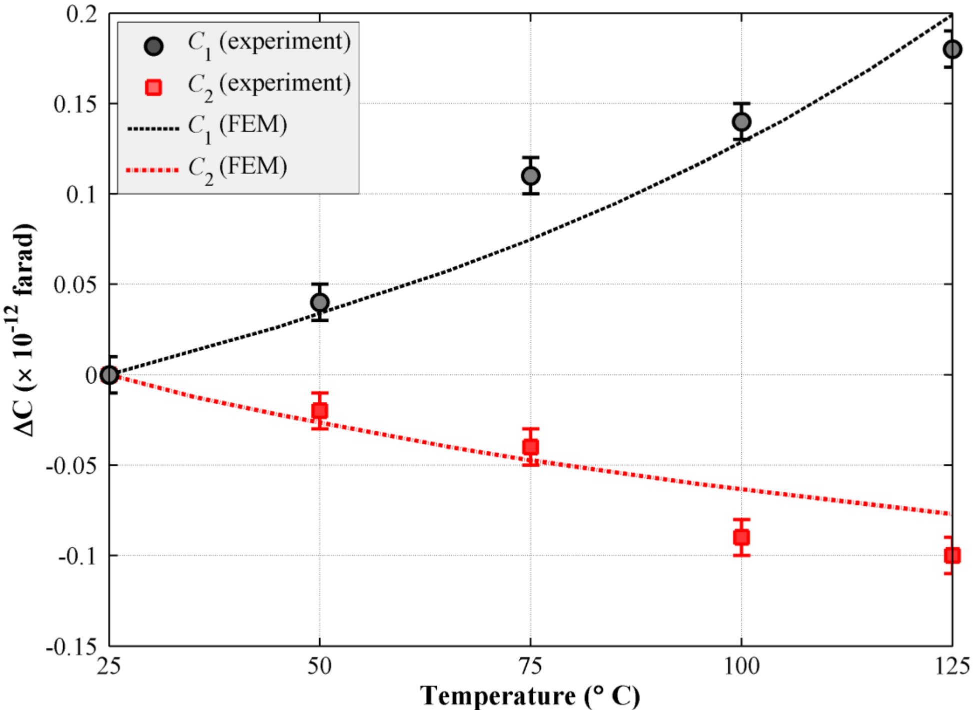

Figure 5.7. Capacitive outputs C_1 and C_2 of the device in Figure 5.5.b when temperature increases from 25 to 125 °C. The results of high temperature experiments as well as the predictions of FE simulations are shown. The slight difference between the results can be due to etch holes which are not included in the FE model.

As expected, C_1 increases with temperature which is due to a decreasing gap between the membrane and the left bottom electrode. On the contrary, C_2 exhibits a decreasing behavior with temperature which is due to an increasing gap between the membrane and the right bottom electrode. Figure 5.8 shows the X profiles of the membrane as its temperature changes from 25 to 125 °C. The thermal response of the membrane presented in this figure agrees with what the semi-analytical model in Chapter 4 has predicted. The area of the tested device in Figure 5.7 is around 0.23 mm^2. Yet, it delivers an average temperature sensitivity of about 1.4 fF/°C (equation 4.40). As mentioned earlier, the maximum temperature of the experiments were limited to 125 °C to avoid severe deformation of the membrane. It seems that such a limitation arises from the configuration of the anchors around the membrane (Figure 5.5). The configuration of the anchors is designed in such a way to provide access for the removal of *poly1* spacers. If this could be avoided, a higher maximum temperature might have

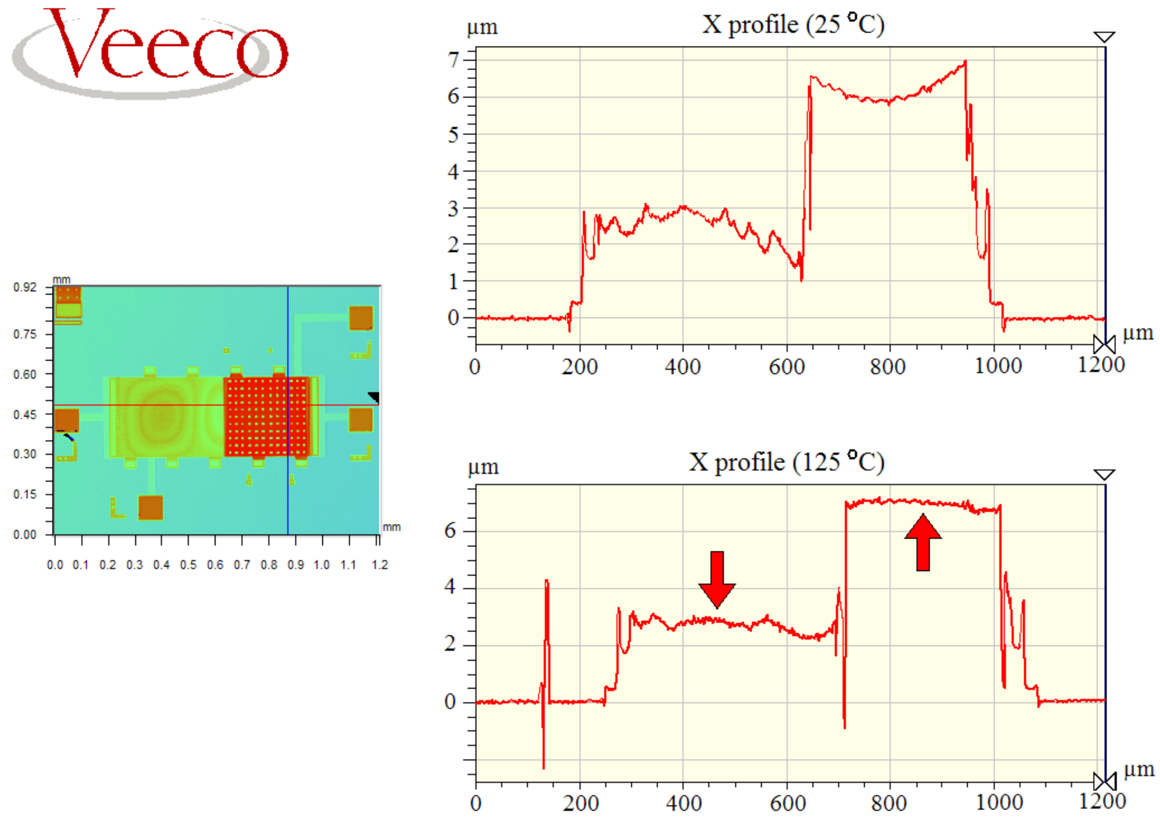

Figure 5.8. Profile of the tested membrane in Figure 4.7 at room temperature and 125 °C. The arrows in the bottom panel show the direction of thermally-induced deformation of the membrane.

been achievable (PolyMUMPs *gold* layer can tolerate temepratuers as high as 300 °C without showing any sign of plastic deformation).

Chapter 6
Concluding Remarks

6.1 Conclusion

In this work, a new multifunctional MEMS sensor for simultaneous measurement of pressure and temperature at harsh environments was developed. At the heart of the new sensor is a uniquely shaped non-planar membrane which is deposited over a stacking of insulating and conducting layers and anchored to a silicon substrate. The membrane sits above a sealed cavity and serves as the main sensing body whose response to pressure and temperature variation is an out-of-plane deformation. The membrane deformation is sensed and quantified into capacitive outputs by a pair of fixed electrodes situated under the membrane. The capacitive outputs of the sensor are analyzed using the numerical processing scheme proposed in Chapter 4 and the input pressure and temperature values are determined. The new sensor design was optimized for the harsh environment found inside the cylinder of a typical IC engine. It was shown numerically that the optimized sensor design can measure, with acceptable precision, the in-cylinder pressure and temperature variations during the compression stroke of the cylinder up to the point of combustion initiation.

6.2 Contributions of thesis

6.2.1 Development of a new membrane for simultaneous measurement of pressure and temperature at one location and a semi-analytical model for the analysis of its response

The main component of the new MEMS sensor described in Chapter 3 is a unique non-planar multifunctional membrane which reacts to pressure and temperature variations simultaneously. The membrane sits above a sealed cavity with reference pressure (vacuum) and deflects in response to pressure difference between its two sides. The pressure-induced deformation of the membrane manifests itself in the form of increases in the two capacitive outputs of the sensor. A semi-analytical model governing the pressure response of the membrane was developed in Section 4.2. When temperature changes, thermal mismatch between the multifunctional membrane and the substrate to which it is anchored induces thermal stresses which deform the multifunctional membrane. The thermal response of the membrane includes opposing out-of-plane deflections in its left and right halves separated by a step feature which provides an internal rotational mechanism. The temperature-

induced deformation of the membrane increases one of the capacitive outpus and decreases the other one. The thermo-mechanical response of the membrane was investigated in sections 4.2 and 4.3 and its governing semi-analytical equations were derived. In a combined loading case when both pressure and temperature vary, the membrane's response is predicted using the principle of superposition. Considering the small dimensions of the multifunctional membrane, it is reasonable to assume that during operation, the measurements will be carried out over a common small area or literally at one location.

6.2.2 Minimization of the effect of cross-sensitivity to temperature

The outputs of the developed multifunctional MEMS sensor are two capacitances which are coupled functions of pressure and temperature. By using the numerical processing scheme developed in Chapters 3 and 4, the effects of pressure and temperature on sensor's outputs are decoupled and their values are extracted. The processing scheme works based on the fact that for each pair of output capacitances there is only one corresponding pair of pressure and temperature values. The developed processing scheme has the potential of decoupling the effect of pressure and temperature and consequently could output temperature-independent pressure values. Analogously, it could deliver pressure-independent temperature measurements. As mentioned in Chapters 1 and 2, cross-sensitivity to undesired measurands is a ubiquitous problem in MEMS sensors. While some compensation techniques have been developed so far to address this concern, none of them provides a complete solution which can completely eliminate the undesired effects. This further highlights the importance of the proposed processing scheme.

6.2.3 Improved thermal response time

A short response time is the key to real-time monitoring of in-cylinder processes in an IC engine. Fast measurement provides indispensable information to the engine management unit and helps reduce the fuel consumption and emissions of an engine. As discussed in Chapter 3, based on the specifications of a typical IC engine, a sensor for in-cylinder operation has between 4 and 45 ms (based on engine speed) to undergo a temperature change of about 450 °C (during the compression stroke and up to the point of injection). The thermal modeling section in Chapter 4 demonstrated that such a short response time can only be realized using a thin film membrane along with optimized boundary conditions.

During optimization, meaningful dimensional ranges were selected for different components of the sensor (in line with available resources and fabrication processes). Following numerical analyses, the optimum configuration of the MEMS sensor for IC engine application was determined, which includes: 1) multifunctional membrane fabricated in amorphous silicon carbide with a thickness of 0.5 μm, 2) silicon dioxide insulating layers between the multifunctional membrane and the silicon substrate with a total thickness of 5 μm, and 3) single-crystal silicon substrate with a total thickness of 1.05 mm (corresponding to two bonded silicon substrates, each with the standard thickness of 0.525 mm). The other important dimensions of the sensor were determined and summarized in Sections 4.1 to 4.3 of this Thesis.

6.2.4 Small footprint

To achieve high sensitivities to pressure and temperature, the idea of using an array of MEMS sensors connected in parallel over a common substrate was followed in this Thesis. The optimized sensor configuration designed in Chapter 4 includes 4200 MEMS sensor connected in parallel, each measuring 25×25 μm^2 in area, and provides an average sensitivity to pressure of about 1.5 fF/KPa and an average sensitivity to temperature of about 4.62 fF/°C. The total surface area of the sensor chip is approximately 4.5 mm^2.

6.3 Proposed future work

Some potential extensions to the presented research work are presented in this section. They are categorized in three main groups as follows:

6.3.1 Modeling and Optimization

- *Investigating different shapes and geometries*:

  In this research, rectangular multifunctional membranes with a step feature at half-lenght were considered. An extension to this can take into account other membrane shapes and geometries.

- *Optimization for new applications:*

  The IC-engine considered in this research was one of many industrial applications requiring simultaneous measurement of pressure and temperature. The optimization carried out in Chapter 4 was geared toward minimizing the sensor's thermal response time for such application. An extension to this can be to use this optimization process for other promising applications such as Tire-Pressure-Monitoring-Systems (TPMS). This can be achieved, for

example, by extracting dimensionless design parameters that generalize the developed model to fit different applications/configurations.

- *Stress analysis:*

  Due to the severe nature of the in-cylinder environment, the new sensor will be exposed to high cyclic thermal and mechanical stresses. These stresses partially originate from the thermal mismatch among the different components of the sensor, pressure loading over the membrane, the wafer bonding process used for the fabrication of the device, etc. The operation at high temperatures further complexes the situation by weakening the strength of the materials used in the sensor. This needs a thorough stress analysis of the sensor to assure its long-term operation. One important factor of such an analysis is to know the temperature-dependent mechanical properties (such as yield strength) of the various materials used in the fabrication of the sensor. For materials such as silicon carbide, this is still an ongoing field of research.

- *Detailed investigation of the effect of initial stresses:*

  In Section 4.5, the effect of fabrication-induced initial stresses on the performance of multifunctional membrane was touched upon briefly. A more elaborated analysis of these stresses and their effect on sensor performance can be an extension to this work. In addition, the effect of these stresses on correction factors introduced into the analytical model can be investigated in more detail.

6.3.2 Fabrication and packaging

- *Custom fabrication of the complete sensor with capacitive readout:*

  The prototypes tested in this Thesis were fabricated using a multi-user foundry process. They were used to verify the thermal response mechanism designed in Chapter 4. The next prototype will need to show full functionality and respond to both pressure and temperature loading. A customized process flow (appendix A) will be used for its fabrication. The new sensor will be essentially similar to the one portrayed in Figure 3.12, including a vacuum sealed cavity under the membrane. The performance of the new sensor will need to be characterized accordingly, using the new test setup proposed in Section 6.3.3. The characterization may also include real time tests in engine condition, reliability and endurance, and hermeticity of the sealed cavity over time, to name a few.

- *Onboard electronics:*

  The capacitance measurements reported in this Thesis were performed using a precision LCR-meter. For commercial applications, customized electronics for signal processing should be developed. The electronics need to survive the relatively high temperature of the silicon substrate of the new sensor as well as electromagnetic interference common in IC-engines. Other aspects such as metallization and wire-bonding to the package will also need to be addressed.

- *Fabrication of a generation prototype with optical readout:*

  As set among the objectives of this Thesis, the sensor is designed in such a way that its measurements can be carried out optically, instead of electronically. Fabry-Perot optical interrogation has been successfully implemented in many harsh environment MEMS sensors. So, among the future extensions of this research is the fabrication of a new generation of the sensor that can be interrogated using an optical readout system.

- *Design of application-specific sensor packaging:*

  The thermal loading experiments presented in this Thesis have been carried out on unpackaged chips with tungsten tips used for probing. However, for more realistic tests at which both pressure and temperature loading coexist, specific packaging is required.

6.3.3 Experiments and test setups

- *New test setups:*

  The thermal loading experiments reported in this Thesis were carried out in ideal laboratory conditions and under a probe station. For the next generation devices, specific high pressure high temperature (HPHT) chambers would need to be developed for static tests. Dynamic tests (resembling the in-cylinder processes of an IC-engine) would likely be performed using test engines.

Appendix A
Fabrication process flow

A1. Custom fabrication process for the fabrication of multifunctional MEMS sensor

In this section, a custom designed fabrication process flow for the fabrication of the multifunctional MEMS sensor is proposed. The process starts from 4-inch SC-Si wafer and includes several deposition/patterning steps. The description of each process step is provided below.

Process Flow

(a) The process starts from a 4-inch SC-Si wafer on top of which about 5 µm SiO_2 is deposited. Next, RIE process is used to remove about 0.5 µm of the SiO_2 at selected location. This will later gives rise to the step feature when the following layers are deposited.

(b) About 0.5 µm of poly-Si is deposited (PECVD) and RIE patterned to form the bottom electrdes. During this step, etch holes are also created using the same RIE process that used to pattern the bottom electrodes.

(c) The second SiO_2 layer, with a thickness of 0.55 µm, is deposited (PECVD or LPCVD). This layer is later etched awayd using BHF. This would leave behind a gap between the multifunctional membrane and the bottom electrdes.

(d) The multifunctional membrane leyer (a-SiC) is deposited (PECVD or LPCVD) with a thickness of 0.5 µm. The deposition is supposed to be conformal so that the step feature transfers to the recently deposited thin film.

(e) DRIE process is used to etch a cavity on the bottom side of the chip. The DRIE process goes all the way through the SC-Si substrate and ends at the SiO_2 layer.

(f) Wet BHF etching is used to etch away the first SiO_2 layer. The process continues by etching the second sacrificial SiO_2 layer through the etch holes. At the end of this process the bottom electrodes are completely released; however, the multifunctional membrane is left connected to and supported by small SiO_2 posts which, from a mechanical perspective, divide the membrane layer into several smaller membranes (each with the optimized dimensions reported in this Thesis).

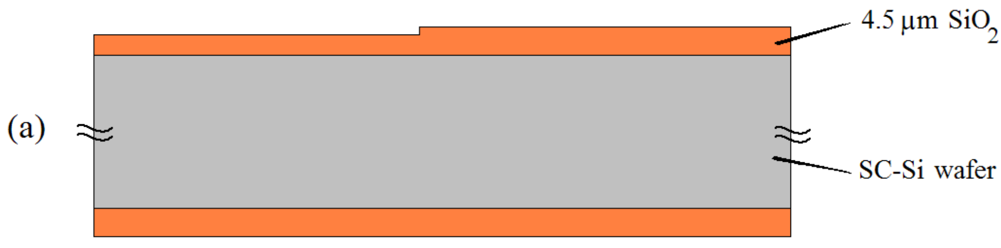

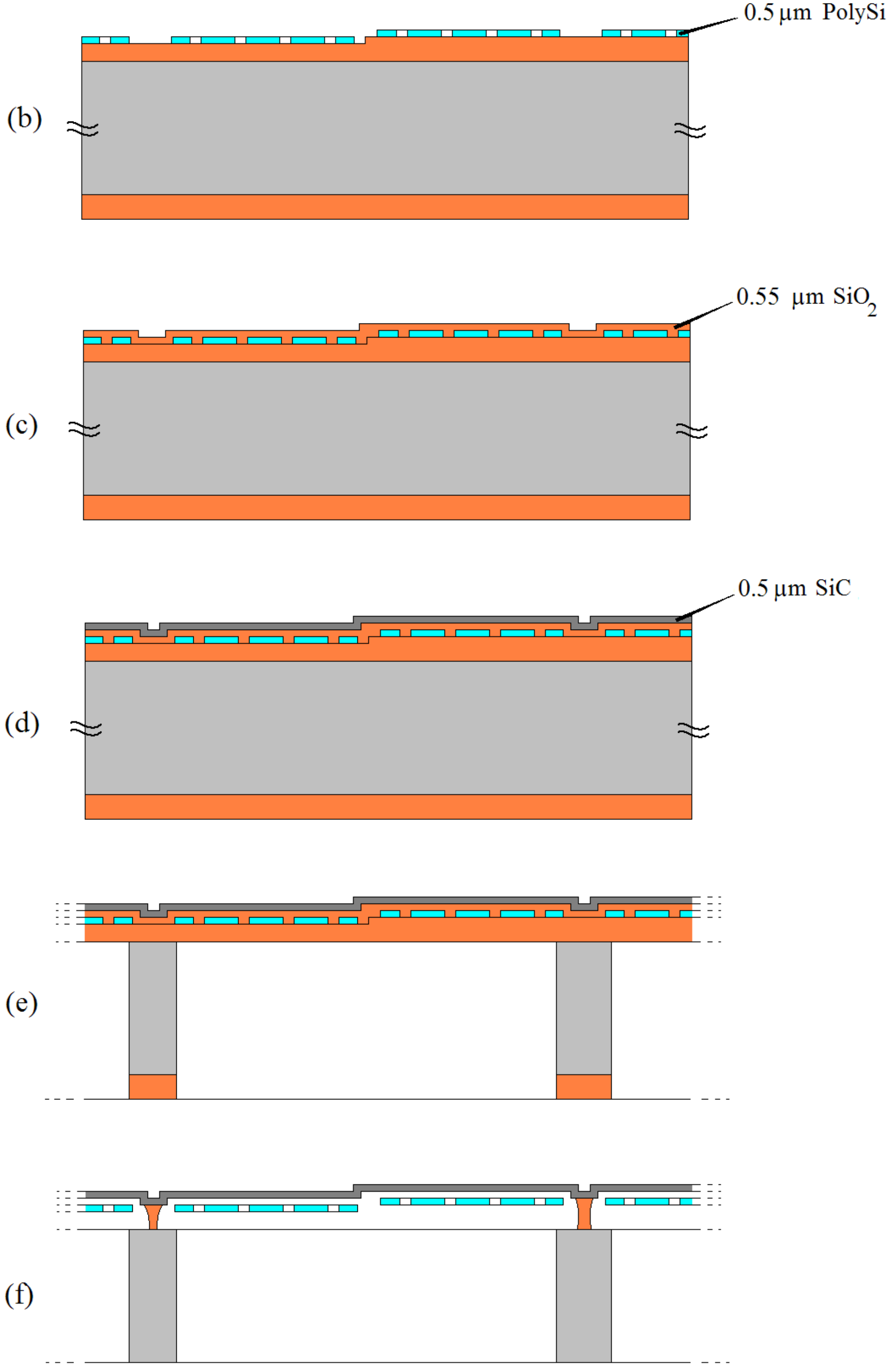
0.5 µm PolySi
(b)
0.55 µm SiO2
(c)
0.5 µm SiC
(d)
(e)
(f)

A second SC-Si wafer is used for wafer bonding (SiO2-SiO2 interface) and the bonded wafers are cut into smaller chips. Each of these chips can carry hundreds or thousands of sensing cells connected in parallel. Finally, an RIE process is carried out over the SiC top surface to open up access ports (on the chip corners) to the bottom elelctrodes. In the following, aschematic of the final chip is shown.

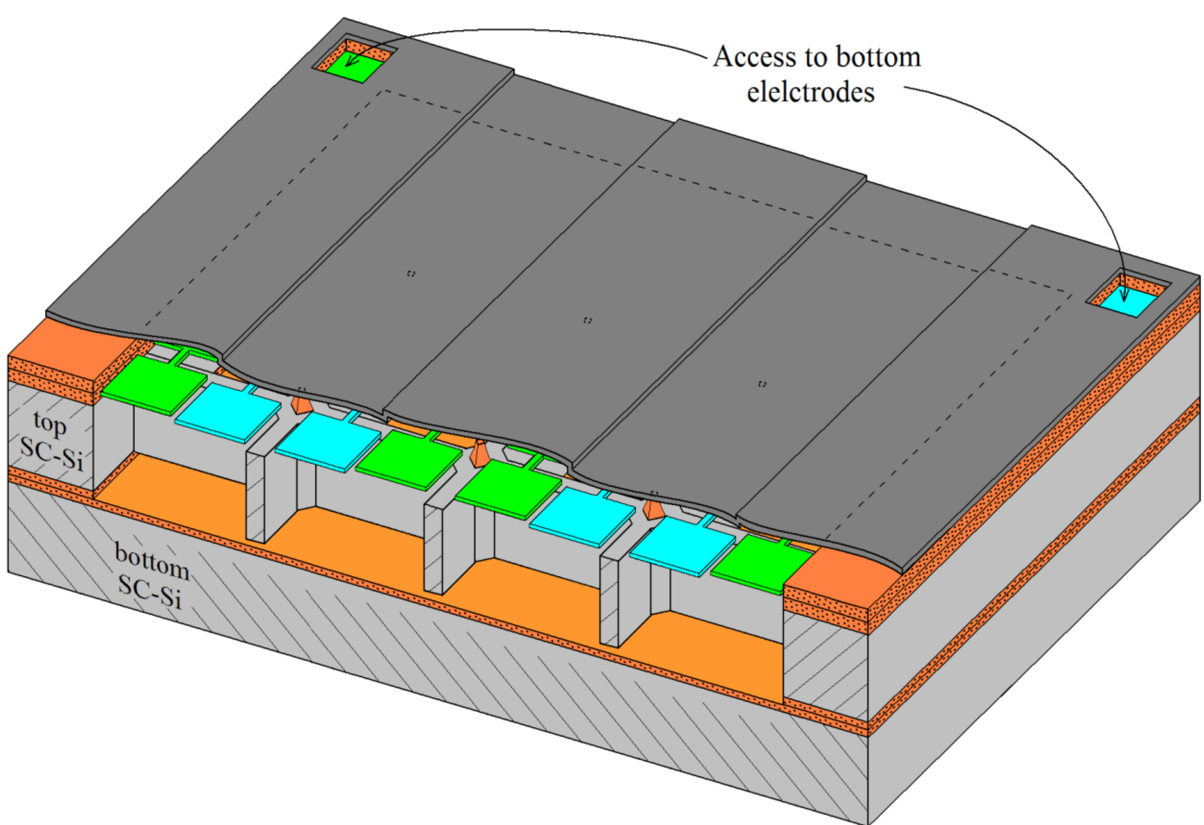

A2. PolyMUMPs® foundry process begins with a 6-inch silicon wafer on top of which a Si_3N_4 film is deposited as an electrical isolating layer. (a) The first poly-Si layer is then deposited and patterned to form the bottom electrode. This is followed by (b) the deposition and patterning of the first SiO_2 layer, and (c) second poly-Si layer and second SiO_2 layer. Next, (d) the third poly-Si layer is deposited and patterned. (e) The gold layer is next deposited. After all the deposition and patterning steps are done, buffered hydrofluoric acid (BHF) is used to etch the sacrificial SiO_2 layers away and release the device (f).

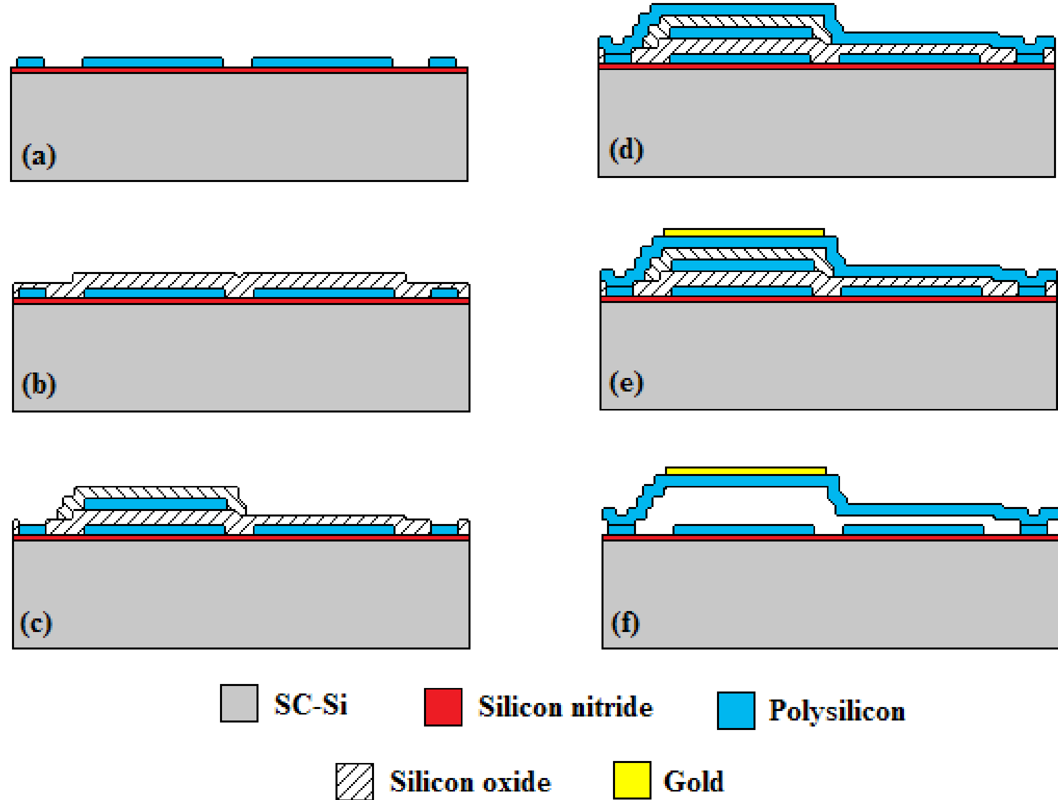

Appendix B

ANSYS ® APDL codes

B1. This ANSYS APDL code is used for the thermal modeling of the multifunctional MESM sensor presented in Section 4.1 of this Thesis.

```
!!!!!!!!!!!!
! START !
!!!!!!!!!!!!
   FINISH
   /CONFIG,NRES,1000000
   /clear
   ! Configuration 1 (Si-Si interface)
   ! Mounting scenario 1 or 2
   /TITLE, transient thermal analysis
   /FILNAME,TransThermal,0
   /PREP7
   BTOL, 1E-7
   Num_loop = 10              ! Number of cylinder cycles for the simulations
   !!!!!!!!!!!!!!!!!!!!!!!!!!!!!!!!!! Dimensions and specs !!!!!!!!!!!!!!!!!!!!!!!!!!!!!!!!!
   ts1     = 525e-6           ! Thickness of top Si chip (with cavity)
   ts2     = 525e-6           ! Thickness of bottom Si chip (bonding wafer)
   tox1    = 2.5e-6           ! Thickness of 1st top oxide
   tox2    = 2.5e-6           ! Thickness of 2nd top oxide
   toxbond = 3e-6             ! Thickness of bonding interface oxide(s)
   tfilm   = 0.5e-6           ! Thickness of top film (SiC) (tfilm should be 2-5 um)
   Lcav    = 1000e-6          ! Cavity length
   margin  = 150e-6           ! the same as LE in thesis
   Ls      = Lcav+2*margin    ! Length of Si chip
   ESR = 1                    ! Engine Speed Ratio to 700 rpm

   ET,1,Solid70               ! Silicon chip
   ET,2,Solid70               ! SiOx
   ET,3,Solid70               ! SiC
   !!!!!!!!!!!!!!!!!!!!!!!!!!!!!!!!!!! Creating the model !!!!!!!!!!!!!!!!!!!!!!!!!!!!!!!!!!
   RECTNG,0 ,Ls/2   ,0   ,Ls/2             ! Remove" /2" for full model
   RECTNG,0 ,Lcav/2 ,0 ,Lcav/2             ! Remove" /2" for full model
   ASBA,1,2
   NUMCMP,ALL
   ASEL, S, LOC, Z, 0
```

```
VEXT,ALL, , ,0,0,tox1,,,,
ASEL, S, LOC, Z, 0
VEXT,ALL, , ,0,0,-tox2,,,,
ASEL, S, LOC, Z, -tox2
VEXT,ALL, , ,0,0,-ts1,,,,
ASEL, S, LOC, Z, -tox2-ts1
VEXT,ALL, , ,0,0,-toxbond,,,,
Block,0 ,Ls/2,0,Ls/2,tox1,tox1+tfilm                         ! Remove" /2" for full
Block,0 ,Ls/2,0,Ls/2,-tox2-toxbond-ts1,-tox2-toxbond-ts1-ts2 ! Remove" /2" for full
/VIEW, 1 , 0.3 , -0.9 , 0.4
/ANG, 1 , -41
/REPLO
ALLSEL,ALL
vglue,all
NUMCMP, VOLU
ALLSEL,ALL
Vsel,S, VOLU, ,3                                             ! Pick volume # 3 for Si
Vsel,A, VOLU, ,6                                             ! Pick volume # 6 for Si
vatt,1,,1
Vsel,S, VOLU, ,1                                             ! Pick volume # 1 for SiO2
Vsel,A, VOLU, ,2                                             ! Pick volume # 2 for SiO2
Vsel,A, VOLU, ,4                                             ! Pick volume # 4 for SiO2
vatt,2,,2
Vsel,S, VOLU, ,5                                             ! Pick volume # 5 for SiC
vatt,3,,3
ALLSEL,ALL
!!!!!!!!!!!!!!!!!!!!!!!!!!!!!!!!!!! Material properties !!!!!!!!!!!!!!!!!!!!!!!!!!!!!!!!!!!
!!!!!!!!!  material #1 – SC-Si substrate  !!!!!!!!!!!
MPTEMP,1,300
MPTEMP,2,400
MPTEMP,3,500
MPTEMP,4,600
MPTEMP,5,700
MPTEMP,6,800
MPTEMP,7,900
MPTEMP,8,1000
MPDATA,KXX,1,,148
MPDATA,KXX,1,,100
MPDATA,KXX,1,,74
MPDATA,KXX,1,,58
MPDATA,KXX,1,,47
MPDATA,KXX,1,,39
```

```
MPDATA,KXX,1,,34
MPDATA,KXX,1,,29
MPTEMP,1,300
MPTEMP,2,400
MPTEMP,3,500
MPTEMP,4,600
MPTEMP,5,700
MPTEMP,6,800
MPTEMP,7,900
MPTEMP,8,1000
MPDATA,C,1,,707
MPDATA,C,1,,794
MPDATA,C,1,,841
MPDATA,C,1,,871
MPDATA,C,1,,895
MPDATA,C,1,,912
MPDATA,C,1,,931
MPDATA,C,1,,946
MP,DENS, 1,2900          !  Density
!!!!!!!!!!!  material #2 - SiO2!!!!!!!!!!!!!
MPTEMP,,,,,,,,
MPTEMP,1,0
MPDATA,DENS,2,,2500
MPTEMP,,,,,,,,
MPTEMP,1,300
MPTEMP,2,400
MPTEMP,3,500
MPTEMP,4,600
MPTEMP,5,700
MPTEMP,6,800
MPTEMP,7,900
MPTEMP,8,1000
MPDATA,C,2,,744
MPDATA,C,2,,890
MPDATA,C,2,,1008
MPDATA,C,2,,1073
MPDATA,C,2,,1136
MPDATA,C,2,,1269
MPDATA,C,2,,1131
MPDATA,C,2,,1148
MPTEMP,,,,,,,,
MPTEMP,1,300
```

```
MPTEMP,2,378
MPTEMP,3,453
MPTEMP,4,528
MPTEMP,5,700
MPTEMP,6,850
MPTEMP,7,1000
MPDATA,KXX,2,,0.68
MPDATA,KXX,2,,0.60
MPDATA,KXX,2,,0.52
MPDATA,KXX,2,,0.47
MPDATA,KXX,2,,0.42
MPDATA,KXX,2,,0.36
MPDATA,KXX,2,,0.33
!!!!!!!!!!!  material #3 - SiC  !!!!!!!!!!!!
!!!!!! poly-SiC !!!!!!
!MPTEMP,,,,,,,
!MPTEMP,1,0
!MPDATA,DENS,3,,3290
!MPTEMP,,,,,,,
!MPTEMP,1,300
!MPTEMP,2,400
!MPTEMP,3,500
!MPTEMP,4,600
!MPTEMP,5,700
!MPTEMP,6,800
!MPTEMP,7,900
!MPTEMP,8,1000
!MPDATA,C,3,,680
!MPDATA,C,3,,825
!MPDATA,C,3,,955
!MPDATA,C,3,,1030
!MPDATA,C,3,,1045
!MPDATA,C,3,,1130
!MPDATA,C,3,,1175
!MPDATA,C,3,,1220
!MPTEMP,,,,,,,
!MPTEMP,1,316
!MPTEMP,2,500
!MPTEMP,3,600
!MPTEMP,4,1000
!MPDATA,KXX,3,,51
!MPDATA,KXX,3,,28
```

```
!MPDATA,KXX,3,,21
!MPDATA,KXX,3,,12
!!!!! amorphous-SiC !!!!!!
MPTEMP,,,,,,,
MPTEMP,1,0
MPDATA,DENS,3,,3290
MPTEMP,,,,,,,
MPTEMP,1,300
MPTEMP,2,400
MPTEMP,3,500
MPTEMP,4,600
MPTEMP,5,700
MPTEMP,6,800
MPTEMP,7,900
MPTEMP,8,1000
MPDATA,C,3,,680
MPDATA,C,3,,825
MPDATA,C,3,,955
MPDATA,C,3,,1030
MPDATA,C,3,,1045
MPDATA,C,3,,1130
MPDATA,C,3,,1175
MPDATA,C,3,,1220
MPTEMP,,,,,,,
MPTEMP,1,316
MPTEMP,2,500
MPTEMP,3,600
MPTEMP,4,1000
MPDATA,KXX,3,,1
MPDATA,KXX,3,,1
MPDATA,KXX,3,,1
MPDATA,KXX,3,,1
!!!!!!!!!!!!!!!!!!!!!!!!!!!!!!!!!!! Mesh the model !!!!!!!!!!!!!!!!!!!!!!!!!!!!!!!!!!!
ESIZE,tox1/2,0,
MSHAPE,1,3D
MSHKEY,0
VSEL, , , , 1
VMESH,ALL
ESIZE,tfilm/2,0,
MSHAPE,1,3D
MSHKEY,0
VSEL, , , , 5
```

```
VMESH,ALL
ESIZE,tox2/2,0,
MSHAPE,1,3D
MSHKEY,0
VSEL, , , , 2
VMESH,ALL
ESIZE,toxbond/2,0,
MSHAPE,1,3D
MSHKEY,0
VSEL, , , , 4
VMESH,ALL
ESIZE,ts1/20,0,
MSHAPE,1,3D
MSHKEY,0
VSEL, , , , 3
VMESH,ALL
ESIZE,ts2/20,0,
MSHAPE,1,3D
MSHKEY,0
VSEL, , , , 6
VMESH,ALL
ALLSEL,ALL
FINISH
!!!!!!!!!!!!!!!!!!!!!!!!!!!!!!!!!!!!!!!!!! Analysis type !!!!!!!!!!!!!!!!!!!!!!!!!!!!!!!!!!!!!!!!!!!
/SOLU
ANTYPE,TRANS
TRNOPT,FULL,                              ! Full solution method
!SOLCONTROL,ON
KBC,1                                     ! STEP "1" or ramp "0" B.C.
TIME,(0.1714/ESR)*Num_loop+0.0            ! Total teim step = 0.1714 second
AUTOTS,ON                                 ! Use automatic time stepping
DELTIM,0.002/ESR,0.002/ESR,0.01/ESR       ! Substep size, first substep 0.002 second, the rest
                                          ! Between 0.02 and 0.01 seconds.
!!!!!!!!!!!!!!!!!!!!!!!!!!!!!!!!!!!! Time-dependent loading !!!!!!!!!!!!!!!!!!!!!!!!!!!!!!!!!!!!
! Time-dependent Pressure loading in a Table Array
arraydim = Num_loop*21+1
*DIM,my_pressure,table,arraydim,1,1,TIME  ! Arraydim rows, One Column, function of time
*SET,my_pressure(0,1),0/ESR
*SET,my_pressure(1,0),0/ESR               ! Start time
*DO,counter,1,Num_loop,1
temp = 21*(counter-1)
*SET,my_pressure(2+temp,0),0.0286 /ESR  +(0.1714/ESR)*(counter-1)
```

```
*SET,my_pressure(3+temp,0),0.0429 /ESR  +(0.1714/ESR)*(counter-1)
*SET,my_pressure(4+temp,0),0.0571 /ESR  +(0.1714/ESR)*(counter-1)
*SET,my_pressure(5+temp,0),0.0607 /ESR  +(0.1714/ESR)*(counter-1)
*SET,my_pressure(6+temp,0),0.0643 /ESR  +(0.1714/ESR)*(counter-1)
*SET,my_pressure(7+temp,0),0.0678 /ESR  +(0.1714/ESR)*(counter-1)
*SET,my_pressure(8+temp,0),0.0714 /ESR  +(0.1714/ESR)*(counter-1)
*SET,my_pressure(9+temp,0),0.0750 /ESR  +(0.1714/ESR)*(counter-1)
*SET,my_pressure(10+temp,0),0.0786 /ESR +(0.1714/ESR)*(counter-1)
*SET,my_pressure(11+temp,0),0.0821 /ESR +(0.1714/ESR)*(counter-1)
*SET,my_pressure(12+temp,0),0.0857 /ESR +(0.1714/ESR)*(counter-1)
*SET,my_pressure(13+temp,0),0.0869 /ESR +(0.1714/ESR)*(counter-1)
*SET,my_pressure(14+temp,0),0.0893 /ESR +(0.1714/ESR)*(counter-1)
*SET,my_pressure(15+temp,0),0.0928 /ESR +(0.1714/ESR)*(counter-1)
*SET,my_pressure(16+temp,0),0.0964 /ESR +(0.1714/ESR)*(counter-1)
*SET,my_pressure(17+temp,0),0.1000 /ESR +(0.1714/ESR)*(counter-1)
*SET,my_pressure(18+temp,0),0.1071 /ESR +(0.1714/ESR)*(counter-1)
*SET,my_pressure(19+temp,0),0.1143 /ESR +(0.1714/ESR)*(counter-1)
*SET,my_pressure(20+temp,0),0.1286 /ESR +(0.1714/ESR)*(counter-1)
*SET,my_pressure(21+temp,0),0.1428 /ESR +(0.1714/ESR)*(counter-1)
*SET,my_pressure(22+temp,0),0.1714 /ESR +(0.1714/ESR)*(counter-1)
*ENDDO
*SET,my_pressure(1,1),0                    ! In-cylinder pressure at start (N/m^2)
*DO,counter,1,Num_loop,1
temp = 21*(counter-1)
*SET,my_pressure(2+temp,1) ,20000
*SET,my_pressure(3+temp,1) ,80000
*SET,my_pressure(4+temp,1) ,100000
*SET,my_pressure(5+temp,1) ,150000
*SET,my_pressure(6+temp,1) ,220000
*SET,my_pressure(7+temp,1) ,300000
*SET,my_pressure(8+temp,1) ,450000
*SET,my_pressure(9+temp,1) ,800000
*SET,my_pressure(10+temp,1),1650000
*SET,my_pressure(11+temp,1),3350000
*SET,my_pressure(12+temp,1),5800000
*SET,my_pressure(13+temp,1),6000000
*SET,my_pressure(14+temp,1),4900000
*SET,my_pressure(15+temp,1),2500000
*SET,my_pressure(16+temp,1),1150000
*SET,my_pressure(17+temp,1),700000
*SET,my_pressure(18+temp,1),300000
*SET,my_pressure(19+temp,1),150000
```

```
*SET,my_pressure(20+temp,1),70000
*SET,my_pressure(21+temp,1),0
*SET,my_pressure(22+temp,1),0
*ENDDO
/title, in-cylinder pressure versus time
*VPLOT,my_pressure(1,0),my_pressure(1,1)
/ui,copy,save,png,graph,color,norm,portrait,yes
! Time-dependent Heat flux in a Table Array
arraydim = Num_loop*25+1
*DIM,my_hflx,table,arraydim,1,1,TIME          ! Arraydim rows, One Column, function of time
*SET,my_hflx(0,1),0/ESR
*SET,my_hflx(1,0),0/ESR                        ! Start time (sec)
*DO,counter,1,Num_loop,1
temp = 25*(counter-1)
*SET,my_hflx(2+temp,0), 0.0071/ESR +(0.1714/ESR)*(counter-1)
*SET,my_hflx(3+temp,0), 0.0143/ESR +(0.1714/ESR)*(counter-1)
*SET,my_hflx(4+temp,0), 0.0214/ESR +(0.1714/ESR)*(counter-1)
*SET,my_hflx(5+temp,0), 0.0286/ESR +(0.1714/ESR)*(counter-1)
*SET,my_hflx(6+temp,0), 0.0357/ESR +(0.1714/ESR)*(counter-1)
*SET,my_hflx(7+temp,0), 0.0428/ESR +(0.1714/ESR)*(counter-1)
*SET,my_hflx(8+temp,0), 0.0500/ESR +(0.1714/ESR)*(counter-1)
*SET,my_hflx(9+temp,0), 0.0571/ESR +(0.1714/ESR)*(counter-1)
*SET,my_hflx(10+temp,0),0.0643/ESR +(0.1714/ESR)*(counter-1)
*SET,my_hflx(11+temp,0),0.0714/ESR +(0.1714/ESR)*(counter-1)
*SET,my_hflx(12+temp,0),0.0786/ESR +(0.1714/ESR)*(counter-1)
*SET,my_hflx(13+temp,0),0.0857/ESR +(0.1714/ESR)*(counter-1)
*SET,my_hflx(14+temp,0),0.0869/ESR +(0.1714/ESR)*(counter-1)
*SET,my_hflx(15+temp,0),0.0928/ESR +(0.1714/ESR)*(counter-1)
*SET,my_hflx(16+temp,0),0.1000/ESR +(0.1714/ESR)*(counter-1)
*SET,my_hflx(17+temp,0),0.1071/ESR +(0.1714/ESR)*(counter-1)
*SET,my_hflx(18+temp,0),0.1143/ESR +(0.1714/ESR)*(counter-1)
*SET,my_hflx(19+temp,0),0.1214/ESR +(0.1714/ESR)*(counter-1)
*SET,my_hflx(20+temp,0),0.1286/ESR +(0.1714/ESR)*(counter-1)
*SET,my_hflx(21+temp,0),0.1357/ESR +(0.1714/ESR)*(counter-1)
*SET,my_hflx(22+temp,0),0.1428/ESR +(0.1714/ESR)*(counter-1)
*SET,my_hflx(23+temp,0),0.1500/ESR +(0.1714/ESR)*(counter-1)
*SET,my_hflx(24+temp,0),0.1571/ESR +(0.1714/ESR)*(counter-1)
*SET,my_hflx(25+temp,0),0.1643/ESR +(0.1714/ESR)*(counter-1)
*SET,my_hflx(26+temp,0),0.1714/ESR +(0.1714/ESR)*(counter-1)
*ENDDO
*SET,my_hflx(1,1),25000                        ! Heat flux at start (W/m^2)
*DO,counter,1,Num_loop,1
```

```
temp = 25*(counter-1)
*SET,my_hflx(2+temp,1),0
*SET,my_hflx(3+temp,1),-50000
*SET,my_hflx(4+temp,1),-50000
*SET,my_hflx(5+temp,1),-50000
*SET,my_hflx(6+temp,1),-50000
*SET,my_hflx(7+temp,1),-50000
*SET,my_hflx(8+temp,1),-50000
*SET,my_hflx(9+temp,1),-25000
*SET,my_hflx(10+temp,1),25000
*SET,my_hflx(11+temp,1),50000
*SET,my_hflx(12+temp,1),500000
*SET,my_hflx(13+temp,1),2620000
*SET,my_hflx(14+temp,1),2770000
*SET,my_hflx(15+temp,1),320000
*SET,my_hflx(16+temp,1),125000
*SET,my_hflx(17+temp,1),75000
*SET,my_hflx(18+temp,1),50000
*SET,my_hflx(19+temp,1),25000
*SET,my_hflx(20+temp,1),25000
*SET,my_hflx(21+temp,1),25000
*SET,my_hflx(22+temp,1),25000
*SET,my_hflx(23+temp,1),25000
*SET,my_hflx(24+temp,1),25000
*SET,my_hflx(25+temp,1),25000
*SET,my_hflx(26+temp,1),25000
*ENDDO
/title, heat flux versus time
*VPLOT,my_hflx(1,0),my_hflx(1,1)
/ui,copy,save,png,graph,color,norm,portrait,yes
! Time-dependent coefficient of heat transfer (h) in a Table Array
arraydim = Num_loop*25+1
*DIM,my_h,table,arraydim,1,1,TIME            ! Arraydim rows, One Column, function of time
*SET,my_h(0,1),0/ESR
*SET,my_h(1,0),0/ESR                         ! Start time (sec)
*DO,counter,1,Num_loop,1
temp = 25*(counter-1)
*SET,my_h(2+temp,0), 0.0071/ESR +(0.1714/ESR)*(counter-1)
*SET,my_h(3+temp,0), 0.0143/ESR +(0.1714/ESR)*(counter-1)
*SET,my_h(4+temp,0), 0.0214/ESR +(0.1714/ESR)*(counter-1)
*SET,my_h(5+temp,0), 0.0286/ESR +(0.1714/ESR)*(counter-1)
*SET,my_h(6+temp,0), 0.0357/ESR +(0.1714/ESR)*(counter-1)
```

```
*SET,my_h(7+temp,0), 0.0428/ESR +(0.1714/ESR)*(counter-1)
*SET,my_h(8+temp,0), 0.0500/ESR +(0.1714/ESR)*(counter-1)
*SET,my_h(9+temp,0), 0.0571/ESR +(0.1714/ESR)*(counter-1)
*SET,my_h(10+temp,0),0.0643/ESR +(0.1714/ESR)*(counter-1)
*SET,my_h(11+temp,0),0.0714/ESR +(0.1714/ESR)*(counter-1)
*SET,my_h(12+temp,0),0.0786/ESR +(0.1714/ESR)*(counter-1)
*SET,my_h(13+temp,0),0.0857/ESR +(0.1714/ESR)*(counter-1)
*SET,my_h(14+temp,0),0.0869/ESR +(0.1714/ESR)*(counter-1)
*SET,my_h(15+temp,0),0.0928/ESR +(0.1714/ESR)*(counter-1)
*SET,my_h(16+temp,0),0.1000/ESR +(0.1714/ESR)*(counter-1)
*SET,my_h(17+temp,0),0.1071/ESR +(0.1714/ESR)*(counter-1)
*SET,my_h(18+temp,0),0.1143/ESR +(0.1714/ESR)*(counter-1)
*SET,my_h(19+temp,0),0.1214/ESR +(0.1714/ESR)*(counter-1)
*SET,my_h(20+temp,0),0.1286/ESR +(0.1714/ESR)*(counter-1)
*SET,my_h(21+temp,0),0.1357/ESR +(0.1714/ESR)*(counter-1)
*SET,my_h(22+temp,0),0.1428/ESR +(0.1714/ESR)*(counter-1)
*SET,my_h(23+temp,0),0.1500/ESR +(0.1714/ESR)*(counter-1)
*SET,my_h(24+temp,0),0.1571/ESR +(0.1714/ESR)*(counter-1)
*SET,my_h(25+temp,0),0.1643/ESR +(0.1714/ESR)*(counter-1)
*SET,my_h(26+temp,0),0.1714/ESR +(0.1714/ESR)*(counter-1)
*ENDDO
*SET,my_h(1,1),205                          ! Coefficient of heat transfer (W/m^2)
*DO,counter,1,Num_loop,1
temp = 25*(counter-1)
*SET,my_h(2+temp,1),210
*SET,my_h(3+temp,1),220
*SET,my_h(4+temp,1),230
*SET,my_h(5+temp,1),240
*SET,my_h(6+temp,1),250
*SET,my_h(7+temp,1),260
*SET,my_h(8+temp,1),270
*SET,my_h(9+temp,1),330
*SET,my_h(10+temp,1),430
*SET,my_h(11+temp,1),690
*SET,my_h(12+temp,1),1470
*SET,my_h(13+temp,1),3300
*SET,my_h(14+temp,1),1730
*SET,my_h(15+temp,1),790
*SET,my_h(16+temp,1),480
*SET,my_h(17+temp,1),380
*SET,my_h(18+temp,1),300
*SET,my_h(19+temp,1),203
```

```
*SET,my_h(20+temp,1),203
*SET,my_h(21+temp,1),203
*SET,my_h(22+temp,1),203
*SET,my_h(23+temp,1),203
*SET,my_h(24+temp,1),203
*SET,my_h(25+temp,1),203
*SET,my_h(26+temp,1),203
*ENDDO
/title, coefficient of heat transfer versus time
*VPLOT,my_h(1,0),my_h(1,1)
/ui,copy,save,png,graph,color,norm,portrait,yes
! Time-dependent in-cylinder air temperature (my_bulk) in a Table Array
arraydim = Num_loop*25+1
*DIM,my_bulk,table,arraydim,1,1,TIME         ! Arraydim rows, One Column, function of time
*SET,my_bulk(0,1),0/ESR
*SET,my_bulk(1,0),0/ESR                       ! Start time
*DO,counter,1,Num_loop,1
temp = 25*(counter-1)
*SET,my_bulk(2+temp,0), 0.0071/ESR +(0.1714/ESR)*(counter-1)
*SET,my_bulk(3+temp,0), 0.0143/ESR +(0.1714/ESR)*(counter-1)
*SET,my_bulk(4+temp,0), 0.0214/ESR +(0.1714/ESR)*(counter-1)
*SET,my_bulk(5+temp,0), 0.0286/ESR +(0.1714/ESR)*(counter-1)
*SET,my_bulk(6+temp,0), 0.0357/ESR +(0.1714/ESR)*(counter-1)
*SET,my_bulk(7+temp,0), 0.0428/ESR +(0.1714/ESR)*(counter-1)
*SET,my_bulk(8+temp,0), 0.0500/ESR +(0.1714/ESR)*(counter-1)
*SET,my_bulk(9+temp,0), 0.0571/ESR +(0.1714/ESR)*(counter-1)
*SET,my_bulk(10+temp,0),0.0643/ESR +(0.1714/ESR)*(counter-1)
*SET,my_bulk(11+temp,0),0.0714/ESR +(0.1714/ESR)*(counter-1)
*SET,my_bulk(12+temp,0),0.0786/ESR +(0.1714/ESR)*(counter-1)
*SET,my_bulk(13+temp,0),0.0857/ESR +(0.1714/ESR)*(counter-1)
*SET,my_bulk(14+temp,0),0.0869/ESR +(0.1714/ESR)*(counter-1)
*SET,my_bulk(15+temp,0),0.0928/ESR +(0.1714/ESR)*(counter-1)
*SET,my_bulk(16+temp,0),0.1000/ESR +(0.1714/ESR)*(counter-1)
*SET,my_bulk(17+temp,0),0.1071/ESR +(0.1714/ESR)*(counter-1)
*SET,my_bulk(18+temp,0),0.1143/ESR +(0.1714/ESR)*(counter-1)
*SET,my_bulk(19+temp,0),0.1214/ESR +(0.1714/ESR)*(counter-1)
*SET,my_bulk(20+temp,0),0.1286/ESR +(0.1714/ESR)*(counter-1)
*SET,my_bulk(21+temp,0),0.1357/ESR +(0.1714/ESR)*(counter-1)
*SET,my_bulk(22+temp,0),0.1428/ESR +(0.1714/ESR)*(counter-1)
*SET,my_bulk(23+temp,0),0.1500/ESR +(0.1714/ESR)*(counter-1)
*SET,my_bulk(24+temp,0),0.1571/ESR +(0.1714/ESR)*(counter-1)
*SET,my_bulk(25+temp,0),0.1643/ESR +(0.1714/ESR)*(counter-1)
```

```
*SET,my_bulk(26+temp,0),0.1714/ESR +(0.1714/ESR)*(counter-1)
*ENDDO
*SET,my_bulk(1,1),322                                ! Bulk temperature at start (C)
*DO,counter,1,Num_loop,1
temp = 25*(counter-1)
*SET,my_bulk(2+temp,1),290
*SET,my_bulk(3+temp,1),190
*SET,my_bulk(4+temp,1),123
*SET,my_bulk(5+temp,1),147
*SET,my_bulk(6+temp,1),123
*SET,my_bulk(7+temp,1),147
*SET,my_bulk(8+temp,1),165
*SET,my_bulk(9+temp,1),240
*SET,my_bulk(10+temp,1),332
*SET,my_bulk(11+temp,1),354
*SET,my_bulk(12+temp,1),584
*SET,my_bulk(13+temp,1),879
*SET,my_bulk(14+temp,1),1019
*SET,my_bulk(15+temp,1),646
*SET,my_bulk(16+temp,1),469
*SET,my_bulk(17+temp,1),415
*SET,my_bulk(18+temp,1),390
*SET,my_bulk(19+temp,1),332
*SET,my_bulk(20+temp,1),332
*SET,my_bulk(21+temp,1),332
*SET,my_bulk(22+temp,1),332
*SET,my_bulk(23+temp,1),332
*SET,my_bulk(24+temp,1),332
*SET,my_bulk(25+temp,1),332
*SET,my_bulk(26+temp,1),332
*ENDDO
/title, in-cylinder air temperature versus time
*VPLOT,my_bulk(1,0),my_bulk(1,1)
/ui,copy,save,png,graph,color,norm,portrait,yes
! Important times in a Table Array
arraydim = Num_loop*8
*DIM,myTSRES,array,arraydim          ! Dimension a numerical Array, arraydim rows, 1 column
*DO,counter,1,Num_loop,1
temp = 8*(counter-1)
*SET,myTSRES(1+temp), 0.02/ESR +(0.1714/ESR)*(counter-1)
*SET,myTSRES(2+temp), 0.04/ESR +(0.1714/ESR)*(counter-1)
*SET,myTSRES(3+temp), 0.06/ESR +(0.1714/ESR)*(counter-1)
```

```
*SET,myTSRES(4+temp), 0.08/ESR +(0.1714/ESR)*(counter-1)
*SET,myTSRES(5+temp), 0.10/ESR +(0.1714/ESR)*(counter-1)
*SET,myTSRES(6+temp), 0.12/ESR +(0.1714/ESR)*(counter-1)
*SET,myTSRES(7+temp), 0.14/ESR +(0.1714/ESR)*(counter-1)
*SET,myTSRES(8+temp), 0.16/ESR +(0.1714/ESR)*(counter-1)
*ENDDO
!!!!!!!!!!!!!!!!!!!!!!!!!!!!!!!!!!!!!! B.C. and solve options !!!!!!!!!!!!!!!!!!!!!!!!!!!!!!!!!!!!!!!
TSRES,%myTSRES%                 ! Force transient solve to include these times
OUTRES,ERASE
OUTRES,ALL,ALL                  ! Save all results for all substeps
EQSLV,SPARSE                    ! Choose sparse solver for small example
Tbulk = 200                     ! Reference temperature
tunif = 200                     ! Force uniform starting temperature equal to Tbulk
ASEL, S, LOC, Z, -tox2-toxbond-ts1-ts2
DA,ALL,TEMP,Tbulk               ! Reference temperature applied to the bottom
                                ! surface of the SC-Si chip
ALLSEL,ALL
ASEL, S, LOC, Z, tox1+tfilm
 SFA,ALL,1,CONV,%my_h%,%my_bulk%
!SFA,ALL,1,HFLUX,%my_hflx%,%my_bulk%
ALLSEL,ALL
SOLVE
FINISH
!!!!!!!!!!!!!!!!!!!!!!!!!!!!!!!!!!!!!! Post-processing  !!!!!!!!!!!!!!!!!!!!!!!!!!!!!!!!!!!!!!!
ASEL, S, LOC, Z, tox1+tfilm
NSLA,S,1
NSEL, R, LOC, X, 0, Lcav/4
NSEL, R, LOC, Y, 0, Lcav/4
*GET,SiC_top_on_cav,NODE,,NUM,MAX
ALLSEL, ALL
ASEL, S, LOC, Z, tox1+tfilm
NSLA,S,1
NSEL, R, LOC, X, Ls/2-margin/2, Ls/2
NSEL, R, LOC, Y, Ls/2-margin/2, Ls/2
*GET,SiC_top_off_cav,NODE,,NUM,MAX
ALLSEL, ALL
ASEL, S, LOC, Z, tox1
NSLA,S,1
NSEL, R, LOC, X, 0, Lcav/4
NSEL, R, LOC, Y, 0, Lcav/4
*GET,SiC_bot_on_cav,NODE,,NUM,MAX
ALLSEL, ALL
```

```
ASEL, S, LOC, Z, tox1
NSLA,S,1
NSEL, R, LOC, X, Ls/2-margin/2, Ls/2
NSEL, R, LOC, Y, Ls/2-margin/2, Ls/2
*GET,SiC_bot_off_cav__SiOx,NODE,,NUM,MAX
ALLSEL, ALL
ASEL, S, LOC, Z, 0
NSLA,S,1
NSEL, R, LOC, X, Ls/2-margin/2, Ls/2
NSEL, R, LOC, Y, Ls/2-margin/2, Ls/2
*GET,SiOx__SiOx,NODE,,NUM,MAX
ALLSEL, ALL
ASEL, S, LOC, Z, -tox2
NSLA,S,1
NSEL, R, LOC, X, Ls/2-margin/2, Ls/2
NSEL, R, LOC, Y, Ls/2-margin/2, Ls/2
*GET,SiOx__Si,NODE,,NUM,MAX
ALLSEL, ALL
ASEL, S, LOC, Z, -tox2-ts1
NSLA,S,1
NSEL, R, LOC, X, Ls/2-margin/2, Ls/2
NSEL, R, LOC, Y, Ls/2-margin/2, Ls/2
*GET,mid_ox_top,NODE,,NUM,MAX
ALLSEL, ALL
ASEL, S, LOC, Z, -tox2-ts1-toxbond
NSLA,S,1
NSEL, R, LOC, X, Ls/2-margin/2, Ls/2
NSEL, R, LOC, Y, Ls/2-margin/2, Ls/2
*GET,mid_ox_bot,NODE,,NUM,MAX
ALLSEL, ALL
ASEL, S, LOC, Z, -tox2-ts1-toxbond-ts2
NSLA,S,1
*GET,Si_bot,NODE,,NUM,MAX
ALLSEL, ALL
/POST26                          ! Enter time history
FILE,'TransThermal', ,
NSOL,2,SiC_top_on_cav            ,TEMP,,SiC_top_on_cav
NSOL,3,SiC_bot_on_cav            ,TEMP,,SiC_bot_on_cav
NSOL,4,SiC_top_off_cav           ,TEMP,,SiC_top_off_cav
NSOL,5,SiC_bot_off_cav__SiOx     ,TEMP,,SiC_bot_off_cav__SiOx
NSOL,6,SiOx__SiOx                ,TEMP,,SiOx__SiOx
NSOL,7,SiOx__Si                  ,TEMP,,SiOx__Si
```

```
   NSOL,8,mid_ox_top                 ,TEMP,,mid_ox_top
   NSOL,9,mid_ox_bot                 ,TEMP,,mid_ox_bot
   NSOL,10,Si_bot                    ,TEMP,,Si_bot
   STORE,MERGE                       ! Stores the data
   PRVAR,2,4
   PLVAR,2,4
   !!!!!!!!!!!!!!!!!!!!!!!!!!!!!!!!!!!!!!! Making animation of loading  !!!!!!!!!!!!!!!!!!!!!!!!!!!!!!!!!!!!!!!!!!
   PLNS,TEMP,
   ANTIME,200,0.1, ,1,0,0,0
!!!!!!!!!
! END !
!!!!!!!!!
```

B2. This ANSYS APDL code is used for the extraction of extensional spring constant k_z and amplitude modification factor ξ_P as discussed in Section 4.2 of this Thesis.

```
!!!!!!!!!!!!
! START !
!!!!!!!!!!!!
   FINISH
   /CLEAR
   /prep7, pressure sensor
   !!!!!!!!!!!!!!!!!!!!!!!!!!!!!!!!!!!!!!! Dimensions and specs !!!!!!!!!!!!!!!!!!!!!!!!!!!!!!!!!!!!!
   P0   = 6.0                    ! Characterization pressure change in MPa
   !T0 = 700                     ! Characterization temperature change in degree C
   t     = 0.5
   HalfLmin  = 12.5              ! L/2 (half-lenght of membrane) range
   HalflLmax = 25
   HalfLstep  = 0.5
   HalfWmin  = 12.5              ! W/2 (half-width of membrane) range
   HalflWmax = 25
   HalfWstep  = 0.5
   hmax  = 0.5*t                 ! Step heigth
   hmin  = 1.0*t
   hstep  = 0.5*t
   lcountermax  = 1 + (HalflLmax-HalfLmin)/HalfLstep
   wcountermax = 1 + (HalflWmax-HalfWmin)/HalfWstep
   hcountermax  = 1 + (hmax-hmin)/hstep
   *CREATE,ansuitmp
```

```
*DO,bcounter,1,lcountermax,1
*DO,wcounter,1,lcountermax,1
*DO,hcounter,1,hcountermax,1
b = (bcounter-1)*HalfLstep + HalfLmin
a = (wcounter-1)*HalfWstep + HalfWmin
h = (hcounter-1)*hstep + hmin
L1 = a-t/2
L2 = a-t/2
W  = 2*b
P0   = 6.0                        ! Characterization pressure change in MPa
!T0 = 700                         ! Characterization temperature change in degree C
t      = 0.5
PARSAV
FINISH
/CLEAR
PARRES
/PREP7
!!!!!!!!!!!!!!!!!!!!!!!!!!!!!!!!!!! Creating the model !!!!!!!!!!!!!!!!!!!!!!!!!!!!!!!!!!!
K,1, 0         , 0 , 0
K,2, L1/2      , 0 , 0
K,3, L1        , 0 , 0
K,4, L1        , 0 , -1*h
K,5, L1+t/2    , 0 , -1*h
K,6, L1+L2/2+t , 0 , -1*h
K,7, L1+L2+t   , 0 , -1*h
K,8, L1+L2+t   , 0 , -1*h+t
K,9, L1+t      , 0 , -1*h+t
K,10, L1+t     , 0 , t
K,11, 0        , 0 , t
K,12, 0        , 10+1.0*W , 0
K,13, L1/2     , 10+1.0*W , 0
K,14, L1+t/2   , 10+1.0*W , 0
K,15, L1+t+L2/2 , 10+1.0*W , 0
K,16, L1+t+L2  , 10+1.0*W , 0
K,17, L1+t+L2  , 10+1.0*W , t
K,18, 0        , 10+1.0*W , t
L,1,2
L,2,3
L,3,4
L,4,5
L,5,6
L,6,7
```

```
L,7,8
L,8,9
L,9,10
L,10,11
L,11,1
LSEL,S, , ,ALL
CM,lineset1,LINE
AL,lineset1
L,12,13
L,13,14
L,14,15
L,15,16
L,16,17
L,17,18
L,18,12
LSEL,S, , ,ALL
LSEL,U, , ,lineset1
CM,lineset2,LINE
AL,lineset2
ALLSEL,ALL
VEXT,1, , ,0,W/2,0, , , ,
VEXT,1, , ,0,-W/2,0, , , ,
VADD,1,2,
VEXT,2, , ,0,W/2,0, , , ,
VEXT,2, , ,0,-W/2,0, , , ,
VADD,1,2,
NUMCMP,ALL
/VIEW,1,,-1
 /ANG,1
 /REP,FAST
 /USER,  1
 /VIEW,  1,  0.406464471114    , -0.797163891073    ,  0.446448613494
 /ANG,   1,  -41.3059175820
 /REPLO
 /AUTO,1
 /REP,FAST
!!!!!!!!!!!!!!!!!!!!!!!!!!!!!!!! Element type and meshing the model !!!!!!!!!!!!!!!!!!!!!!!!!!!!!!!!
ET,1,186                          ! Structural-thermal element
mp,ex,  1,4.10e5                  ! Elastic modulus (SiC)
mp,nuxy,1,0.22                    ! Poisson’s ratio (SiC)
mp,ALPX,1,4.4e-6                  ! Temperature-averaged CTE (SiC)
ESIZE,t                           ! Sets element size to 5 unit
```

```
MSHAPE,1,3D
MSHKEY,0
VMESH,ALL
!!!!!!!!!!!!!!!!!!!!!!!!!!!!!!!!!!!!!!!!!!!!!!! B.C. and loading !!!!!!!!!!!!!!!!!!!!!!!!!!!!!!!!!!!!!!!!!!!!
ASEL,S, , ,10
ASEL,A, , ,12
ASEL,A, , ,22
ASEL,A, , ,24
ASEL,A, , ,31
ASEL,A, , ,39
SFA,ALL,1,PRES,P0                    ! Pressure loading over the membrane
ALLSEL, ALL
ASEL,S, , ,2
ASEL,A, , ,14
ASEL,A, , ,9
ASEL,A, , ,21
ASEL,A, , ,13
ASEL,A, , ,25
ASEL,A, , ,1
ASEL,A, , ,30
ASEL,A, , ,33
ASEL,A, , ,38
ASEL,A, , ,32
ASEL,A, , ,40
DA,ALL,ALL,0
ALLSEL, ALL
ALLSEL,ALL
FINISH
!!!!!!!!!!!!!!!!!!!!!!!!!!!!!!!! Solution and Determination of k_z and ξ_P  !!!!!!!!!!!!!!!!!!!!!!!!!!!!!!!!
/SOL
ANTYPE,0
SOLVE
FINISH
/POST1
/DSCALE,ALL,AUTO
/EFACET,1
PLNSOL, U,Z, 2,1.0
NSEL, S, LOC, X, L1/2
NSEL, R, LOC, Y, 0
NSEL, R, LOC, Z, 0
*GET,NAstep,NODE,,NUM,MAX
*GET,ZAstep,NODE,NAstep,U,Z
```

```
ALLSEL, ALL
NSEL, S, LOC, X, L1+t/2
NSEL, R, LOC, Y, 0
NSEL, R, LOC, Z, -1*h
*GET,NBstep,NODE,,NUM,MAX
*GET,ZBstep,NODE,NBstep,U,Z
ALLSEL, ALL
NSEL, S, LOC, X, L1+L2/2+t
NSEL, R, LOC, Y, 0
NSEL, R, LOC, Z, -1*h
*GET,NCstep,NODE,,NUM,MAX
*GET,ZCstep,NODE,NCstep,U,Z
ALLSEL, ALL
etta = (2*ZBstep)/(ZAstep+ZCstep)
NSEL, S, LOC, X, L1/2
NSEL, R, LOC, Y, 10+1.0*W
NSEL, R, LOC, Z, 0
*GET,NAnonstep,NODE,,NUM,MAX
*GET,ZAnonstep,NODE,NAnonstep,U,Z
ALLSEL, ALL
NSEL, S, LOC, X, L1+t/2
NSEL, R, LOC, Y, 10+1.0*W
NSEL, R, LOC, Z, 0
*GET,NBnonstep,NODE,,NUM,MAX
*GET,ZBnonstep,NODE,NBnonstep,U,Z
ALLSEL, ALL
NSEL, S, LOC, X, L1+t+L2/2
NSEL, R, LOC, Y, 10+1.0*W
NSEL, R, LOC, Z, 0
*GET,NCnonstep,NODE,,NUM,MAX
*GET,ZCnonstep,NODE,NCnonstep,U,Z
ALLSEL, ALL
ettacorrec = (2*ZBnonstep)/(ZAnonstep+ZCnonstep)
corrfactor = 1.777777777/ettacorrec
ettanew = etta*corrfactor
kz = 32*410000*(t*t*t)/(a*a*a)*((1/ettanew)-(9/16))
Z_P_Theory = (a*a*a*a)*(P0/(2*410000*(t*t*t)))*(1-1/(1+((2*410000*(t*t*t))/( kz*(a*a)))))
ξP  = -1*ZBstep/Z_P_Theory                        ! Correction factor for amplitude of deflection
/OUTPUT,30AUG2012P, , ,APPEND                     ! Saves the results under the given name
*VWRITE,b,a,h,t,kz, ξP , , , ,                    ! Writes in order W/2 - L/2 - h - t - kz - ξP
(F8.3,' ',F8.3,' ',F8.3,' ',F8.3,' ',F15.8,' ',F15.8)
/OUTPUT
```

```
   *ENDDO
   *ENDDO
   *ENDDO
   *END
   /INPUT,ansuitmp
!!!!!!!!!
! END !
!!!!!!!!!
```

B3. This ANSYS APDL code is used for the determination of amplitude modification factor $\bar{\xi}_T$ as discussed in Section 4.2 of this Thesis.

```
!!!!!!!!!!!!
! START !
!!!!!!!!!!!!
   FINISH
   /CLEAR
   /prep7, pressure sensor
   !!!!!!!!!!!!!!!!!!!!!!!!!!!!!!!!!!! Dimensions and specs !!!!!!!!!!!!!!!!!!!!!!!!!!!!!!!!!!!
   !P0   = 6.0                  ! Characterization pressure change in MPa
   T0 = 700                     ! Characterization temperature change in degree C
   t     = 0.5
   HalfLmin  = 12.5             ! L/2 (half-lenght of membrane) range
   HalflLmax = 25
   HalfLstep  = 0.5
   HalfWmin  = 12.5             ! W/2 (half-width of membrane) range
   HalflWmax = 25
   HalfWstep  = 0.5
   hmax  = 0.0*t                ! Step heigth
   hmin  = 2.0*t
   hstep  = 0.5*t
   lcountermax   = 1 + (HalfLmax-HalfLmin)/HalfLstep
   wcountermax = 1 + (HalfWmax-HalfWmin)/HalfWstep
   hcountermax  = 1 + (hmax-hmin)/hstep
   *CREATE,ansuitmp
   *DO,lcounter,1,lcountermax,1
   *DO,wcounter,1,wcountermax,1
```

```
*DO,hcounter,1,hcountermax,1
!P0   = 6.0                              ! Characterization pressure change in MPa
T0 = 700                                 ! Characterization temperature change in degree C
t = 0.5
b = (lcounter-1)*HalfLstep + HalfLmin
a = (wcounter-1)*HalfWstep + HalfWmin
h = (hcounter-1)*hstep + hmin
L1 = a-t/2
L2 = a-t/2
W  = 2*b
PARSAV
FINISH
/CLEAR
PARRES
/PREP7
!!!!!!!!!!!!!!!!!!!!!!!!!!!!!!!!!!!!! Creating the model !!!!!!!!!!!!!!!!!!!!!!!!!!!!!!!!!!!!
K,1, 0             , 0 , 0
K,2, 2*L1/3+t/3    , 0 , 0
K,3, L1            , 0 , 0
K,4, L1            , 0 , -1*h
K,5, L1+t/2        , 0 , -1*h
K,6, L1+L2/3+2*t/3 , 0 , -1*h
K,7, L1+L2+t       , 0 , -1*h
K,8, L1+L2+t       , 0 , -1*h+t
K,9, L1+t          , 0 , -1*h+t
K,10, L1+t         , 0 , t
K,11, 0            , 0 , t
L,1,2
L,2,3
L,3,4
L,4,5
L,5,6
L,6,7
L,7,8
L,8,9
L,9,10
L,10,11
L,11,1
LSEL,S, , ,ALL
CM,lineset1,LINE
AL,lineset1
ALLSEL,ALL
```

```
VEXT,1, , ,0,W/2,0, , , ,
VEXT,1, , ,0,-W/2,0, , , ,
VADD,1,2,
 /VIEW,1,,-1
 /ANG,1
 /REP,FAST
 /USER,  1
 /VIEW,  1,  0.406464471114    , -0.797163891073    ,  0.446448613494
 /ANG,   1,  -41.3059175820
 /REPLO
 /AUTO,1
 /REP,FAST
!!!!!!!!!!!!!!!!!!!!!!!!!!!!!!!!! Element type and meshing the model !!!!!!!!!!!!!!!!!!!!!!!!!!!!!!!!!
ET,1,186                        ! Structural-thermal element
mp,ex,  1,4.10e5                ! Elastic modulus (SiC)
mp,nuxy,1,0.22                  ! Poisson’s ratio (SiC)
mp,ALPX,1,4.4e-6                ! Temperature-averaged CTE (SiC)
ESIZE,t                         ! Sets element size to 5 unit
MSHAPE,1,3D
MSHKEY,0
VMESH,ALL
!!!!!!!!!!!!!!!!!!!!!!!!!!!!!!!!!!!!!!!!!!!!!!!!!!!! B.C. and loading !!!!!!!!!!!!!!!!!!!!!!!!!!!!!!!!!!!!!!!!!!!!!!
ASEL,S, , ,2
ASEL,A, , ,14
ASEL,A, , ,9
ASEL,A, , ,21
ASEL,A, , ,13
ASEL,A, , ,25
DA,ALL,ALL,0
ALLSEL, ALL
NSEL,S, , ,ALL                  ! Thermal loading for SOLID186 element
BF,ALL,TEMP,T0                  ! Thermal loading for SOLID186 element
FINISH
!!!!!!!!!!!!!!!!!!!!!!!!!!!!!!!! Solution and Determination of ξ̄_T !!!!!!!!!!!!!!!!!!!!!!!!!!!!!!!!
/SOL
ANTYPE,0
SOLVE
FINISH
/POST1
/DSCALE,ALL,AUTO
/EFACET,1
PLNSOL, U,Z, 2,1.0
```

```
NSEL, S, LOC, X, (L1+t+L2)/3                ! Get the maximum deflection
NSEL, R, LOC, Y, 0
NSEL, R, LOC, Z, 0
*GET,NAstep,NODE,,NUM,MAX
*GET,ZAstep,NODE,NAstep,U,Z
ALLSEL, ALL
NSEL, S, LOC, X, 2*(L1+t+L2)/3              ! Get the minimum deflection
NSEL, R, LOC, Y, 0
NSEL, R, LOC, Z, -1*h
*GET,NBstep,NODE,,NUM,MAX
*GET,ZBstep,NODE,NBstep,U,Z
ALLSEL, ALL
ZTFEM = (ZAstep-ZBstep)/2             ! "-" is used to account for max+abs(min)
denominator = (4.4e-6)*(700)*((L1+L2+t)*(L1+L2+t)*(L1+L2+t))/54
ξ̄T = ZTFEM/denominator                ! Correction factor for amplitude of deflection
/OUTPUT,30AUG2012T, , ,APPEND         ! Saves the results under the given name
*VWRITE,b,a,h,t,NAstep,ZAstep,NBstep,ZBstep,ZTFEM, ξ̄T, , , ,
(F8.4,' ',F8.4,' ',F8.4,' ',F8.4,' ',F10.3,' ',F10.5,' ',F10.3,' ',F10.5,' ',F10.5,' ',F15.8)
/OUTPUT
*ENDDO
*ENDDO
*ENDDO
*END
/INPUT,ansuitmp
!!!!!!!!!
! END !
!!!!!!!!!
```

B4. This ANSYS APDL code is used for calculation of capacitive outputs C_1 and C_2 reported in Sections 4.3.

```
!!!!!!!!!!!!
! START !
!!!!!!!!!!!!
FINISH
/CLEAR
/prep7, pressure sensor
```

```
!!!!!!!!!!!!!!!!!!!!!!!!!!!!!!!!!!! Dimensions and specs !!!!!!!!!!!!!!!!!!!!!!!!!!!!!!!!!!!
Pmin  = 0.0                     ! Minimum presure difference (MPa)
Pmax  = 6.0                     ! Maximum presure difference (MPa)
Pstep = 0.5                     ! Presure difference step    (MPa)
Tmin  = 000                     ! Minimum temperature difference in degree C
Tmax  = 700                     ! Maximum temperature difference in degree C
Tstep = 100                     ! Temperature difference step in degree C
Pcountermax = 1 + (Pmax-Pmin)/Pstep
Tcountermax = 1 + (Tmax-Tmin)/Tstep
vltg = 0.1                      ! Readout voltage (v) for capacitance extraction
a = 12.5                        ! Half length of membrane
b = 12.5                        ! Half width of membrane
t = 0.5                         ! Thickness of membrane
h = 0.6                         ! Step height of membrane
margin = 1                      ! Margin for the inclusion of fringing effect
L1 = a
L2 = a
L=L1+L2+t
W = 2*b
L_elec_left   = L1-h            ! Length of the left electrode
L_elec_right = L2-h             ! Length of the rigth electrode
W_elec        = W               ! Width of the electrodes
t_elec        = t               ! Thickness of the electrodes
G2            = 0.55            ! Gap between the rigth elec and membrane
G1            = G2              ! Gap between the left elec and membrane
*CREATE,ansuitmp
*DO,Pcounter,1,Pcountermax,1      ! Do for Pcounter from 1 to Pcountermax in steps of 1
*DO,Tcounter,1,Tcountermax,1      ! Do for Tcounter from 1 to Tcountermax in steps of 1
P0 = (Pcounter-1)*Pstep + Pmin
T0 = (Tcounter-1)*Tstep + Tmin
vltg = 0.1                      ! Readout voltage (v) for capacitance extraction
a = 12.5                        ! Half length of membrane
b = 12.5                        ! Half width of membrane
t = 0.5                         ! Thickness of membrane
h = 0.6                         ! Step height of membrane
margin = 1                      ! Margin for the inclusion of fringing effect
L1 = a
L2 = a
L=L1+L2+t
W = 2*b
L_elec_left   = L1-h            ! Length of the left electrode
L_elec_right = L2-h             ! Length of the rigth electrode
```

```
W_elec        = W                      ! Width of the electrodes
t_elec         = t                      ! Thickness of the electrodes
G2              = 0.55                  ! Gap between the rigth elec and membrane
G1              = G2                    ! Gap between the left elec and membrane
PARSAV
FINISH
/CLEAR
PARRES
/PREP7
!!!!!!!!!!!!!!!!!!!!!!!!!!!!!!!!!!!!!!!! Element type !!!!!!!!!!!!!!!!!!!!!!!!!!!!!!!!!!!!!!!!
et,1,122                                ! Element for electrodes
et,2,122                                ! Elelent for air left
et,3,122                                ! Element for membrane
et,4,122                                ! Elelent for air right
emunit,epzro,8.854e-6                   ! Free-space permittivity,uMKSV units
mp,perx,2,1                             ! Relative permittivity for air left
mp,perx,4,1                             ! Relative permittivity for air right
!!!!!!!!!!!!!!!!!!!!!!!!!!!!!!!!!!!!!! Creating the model !!!!!!!!!!!!!!!!!!!!!!!!!!!!!!!!!!!!!!
block, 0              , L_elec_left , 0 , W      , 0            , t
block, L_elec_left    , L1          , 0 , W      , 0            , t
block, L1             , L1+t        , 0 , W      , -h           , t
block, L1+t           , L1+t+h      , 0 , W      , -h           , -h+t
block, L1+t+h         , L1+L2+t     , 0 , W      , -h           , -h+t
block, 0              , L_elec_left , 0 , W_elec , -G1          , -G1-t_elec
block, L-L_elec_right , L           , 0 , W_elec , -G2-h        , -G2-h-t_elec
block, 0              , L_elec_left , 0 , W_elec , -G1-t_elec   , t
block, L-L_elec_right , L           , 0 , W_elec , -h-G2-t_elec , -h+t
vovlap,all
VGLUE,1,15,13,11,12
NUMCMP, VOLU
/VIEW,1,,-1
/ANG,1
/REP,FAST
/USER,  1
/VIEW,  1,  0.477569319649    , -0.738322971230    ,  0.476242307113
/ANG,   1,  -45.9095609383
/REPLO
!!!!!!!!!!!!!!!!!!!!!!!!!!!!!!!!! Volume attributes and components !!!!!!!!!!!!!!!!!!!!!!!!!!!!!!!!
vsel,s, volu, ,2                ! Pick left electrode
vsel,a, volu, ,3                ! Pick right electrode
Vatt,1,,1                       ! Assign material#1 (Si) to the picked volume(s)
ALLSEL,ALL
```

```
vsel,s, volu, ,4                ! Pick air left
cm,airleft,volu                 ! Group air volume into component "airleft"
Vatt,2,,2                       ! Assign material#2 (air) to the picked volume(s)
ALLSEL,ALL
Vsel,s,volu,,1                  ! Pick membrane component
Vsel,A,volu,,5
Vsel,A,volu,,6
Vsel,A,volu,,7
Vsel,A,volu,,9
vatt,3,,3                       ! Assign material#3 (SiC) to the picked volume(s)
ALLSEL,ALL
vsel,s, volu, ,8                ! Pick air right
cm,airright,volu                ! Group air volume into component "airright"
Vatt,4,,4                       ! Assign material#4 (air) to the picked volume(s)
ALLSEL,ALL
VSEL,S, , , 1                   ! Group top surface of membrane for pressure loading
VSEL,A, , , 5
VSEL,A, , , 9
ASLV,S
ASEL, R, LOC, Z, t
cm,mmbrn_top_1,AREA
ALLSEL,ALL
VSEL,S, , , 9
ASLV,S
ASEL, R, LOC, X, L1+t
ASEL, R, LOC, Z, t-h/2
cm,mmbrn_top_2,AREA
ALLSEL,ALL
VSEL,S, , , 6
VSEL,A, , , 7
ASLV,S
ASEL, R, LOC, Z, t-h
cm,mmbrn_top_3,AREA
ALLSEL,ALL
CMGRP, mmbrn_top, mmbrn_top_1, mmbrn_top_2, mmbrn_top_3
VSEL,S, , , 1                        ! Group the perimeter of membrane for fixed BC
VSEL,A, , , 5
VSEL,A, , , 6
VSEL,A, , , 7
VSEL,A, , , 9
ASLV,S
ASEL, R, LOC, X, 0
```

```
cm,perim_1,AREA
VSEL,S, , , 1
VSEL,A, , , 5
VSEL,A, , , 6
VSEL,A, , , 7
VSEL,A, , , 9
ASLV,S
ASEL, R, LOC, X, L
cm,perim_2,AREA
VSEL,S, , , 1
VSEL,A, , , 5
VSEL,A, , , 6
VSEL,A, , , 7
VSEL,A, , , 9
ASLV,S
ASEL, R, LOC, Y, 0
cm,perim_3,AREA
VSEL,S, , , 1
VSEL,A, , , 5
VSEL,A, , , 6
VSEL,A, , , 7
VSEL,A, , , 9
ASLV,S
ASEL, R, LOC, Y, W
cm,perim_4,AREA
CMGRP, mmbrn_perim, perim_1, perim_2, perim_3, perim_4
ALLSEL,ALL
!!!!!!!!!!!!!!!!!!!!!!!!!!!!!!!!! Line division and meshing !!!!!!!!!!!!!!!!!!!!!!!!!!!!!!!!
ASEL,S, , , 1
ASEL,A, , , 2
ASEL,A, , , 31
ASEL,A, , , 32
ASEL,A, , , 37
ASEL,A, , , 38
ASEL,A, , , 67
ASEL,A, , , 68
LSLA,S
LESIZE,all, , ,50, , , , ,1
ALLSEL,ALL
LSEL, R, LOC, X, 0
LSEL, R, LOC, Y, 0
LESIZE,all, , ,1, , , , ,1
```

```
ALLSEL,ALL
LSEL, R, LOC, X, L_elec_left
LSEL, R, LOC, Y, 0
LESIZE,all, , ,1, , , , ,1
ALLSEL,ALL
LSEL, R, LOC, X, 0
LSEL, R, LOC, Y, W
LESIZE,all, , ,1, , , , ,1
ALLSEL,ALL
LSEL, R, LOC, X, L_elec_left
LSEL, R, LOC, Y, W
LESIZE,all, , ,1, , , , ,1
ALLSEL,ALL
LSEL, R, LOC, X, L-L_elec_right
LSEL, R, LOC, Y, 0
LESIZE,all, , ,1, , , , ,1
ALLSEL,ALL
LSEL, R, LOC, X, L
LSEL, R, LOC, Y, 0
LESIZE,all, , ,1, , , , ,1
ALLSEL,ALL
LSEL, R, LOC, X, L-L_elec_right
LSEL, R, LOC, Y, W
LESIZE,all, , ,1, , , , ,1
ALLSEL,ALL
LSEL, R, LOC, X, L
LSEL, R, LOC, Y, W
LESIZE,all, , ,1, , , , ,1
ALLSEL,ALL
MSHAPE,0,3D
MSHKEY,1
VSEL, , , ,      2
Vmesh,all
VSEL, , , ,      3
Vmesh,all
VSEL, , , ,      4
Vmesh,all
VSEL, , , ,      8
Vmesh,all
VSEL, , , ,      1
Vmesh,all
VSEL, , , ,      7
```

```
Vmesh,all
MSHAPE,1,3D
MSHKEY,0
VSEL, , , ,      5
Vmesh,all
VSEL, , , ,      6
Vmesh,all
VSEL, , , ,      9
Vmesh,all
ALLSEL,ALL
!!!!!!!!!!!!!!!!!!!!!!!!!!!!!!! Applying electrical load (voltage) !!!!!!!!!!!!!!!!!!!!!!!!!!!!!!!
VSEL, , , ,      1                ! Select membrane
ASLV,S
ASEL, R, LOC, Z, 0
da,all,volt,vltg                  ! Apply voltage to the bottom surface of membrane left
ALLSEL,ALL
VSEL, , , ,      7                ! Select membrane
ASLV,S
ASEL, R, LOC, Z, -h
da,all,volt,vltg                  ! Apply voltage to the bottom surface of membrane right
ALLSEL,ALL
VSEL, , , ,      2                ! Select left electrode
ASLV,S
ASEL, R, LOC, Z, -G1
da,all,volt,0                     ! Ground the top surface of the left electrode
ALLSEL,ALL
VSEL, , , ,      3                      ! Select right electrode
ASLV,S
ASEL, R, LOC, Z, -h-G2
da,all,volt,0                           ! Ground the top surface of the left electrode
ALLSEL,ALL
!!!!!!!!!!!!!!!!!!!!!!!!!!!!!!! Electrostaic physics !!!!!!!!!!!!!!!!!!!!!!!!!!!!!!!
et,1,0                            ! Set electrodes to null element type
et,2,122                          ! Elelent for air left
et,3,0                            ! Set membrane to null element type
et,4,122                          ! Elelent for air right
physics,write,ELECTROS            ! Write electrostatic physics file for air
physics,clear                     ! Clear Physics
!!!!!!!!!!!!!!!!!!!!!!!!!!!!!!! Structural physics !!!!!!!!!!!!!!!!!!!!!!!!!!!!!!!
et,1,186                          ! Define electrodes element type
et,2,0                            ! Set air left to null element type
et,3,186                          ! Define membrane element type
```

```
et,4,0                          ! Set air right to null element type
mp,ex,   1, 1.65e5              ! Elastic modulus (Si)
mp,nuxy, 1, 0.22                ! Poisson's ratio (Si)
mp,ALPX, 1, 0                   ! CTE (Si); Corresponding to ΔT_{SC-Si} = 0 (refer to sention 4.1)
mp,ex,   3, 4.10e5              ! Elastic modulus (SiC)
mp,nuxy, 3, 0.22                ! Poisson's ratio (SiC)
mp,ALPX, 3, 4.4e-6              ! Temperature-averaged CTE (SiC); averaged over 300-1000 K
ASEL,S, , , mmbrn_perim,        ! BC: fix the perimeter of the membrane
DA,ALL,ALL,0
ALLSEL,ALL
VSEL, , , ,      2              ! BC: fix the bottom of electrodes
ASLV,S
ASEL,R, LOC, Z, -G1-t_elec
DA,ALL,ALL,0
VSEL, , , ,      3
ASLV,S
ASEL,R, LOC, Z, -h-G2-t_elec
DA,ALL,ALL,0
ALLSEL,ALL
ASEL,S, , , mmbrn_top,          ! Loading: apply pressure over the membrane
SFA,ALL,1,PRES,P0
ALLSEL,ALL
NSEL,S, , ,ALL                  ! Loading: apply uniform temperature
BF,ALL,TEMP,T0                  ! Loading: apply uniform temperature
ALLSEL,ALL
finish
physics,write,STRUCTURE            ! Write structural physics file
!!!!!!!!!!!!!!!!!!!!!!!!!!!!!!!! Multiphysics solution and post-processing!!!!!!!!!!!!!!!!!!!!!!!!!!!!!!!
ESSOLV,'ELECTROS','STRUCTURE',3,0,'airright',,,,20
finish
physics,read,ELECTROS                          ! Read electrostatic physics file
finish
ALLSEL,ALL
VSEL,S, , , 1
VSEL,A, , , 2
VSEL,A, , , 4
ALLSEL,BELOW,VOLU
/post1
SET,LAST
ETABLE,Sene1,SENE,
SSUM
*GET, W1 , SSUM ,      , ITEM , Sene1
```

```
*SET,C1 , (W1*2)/((vltg-0)**2)                ! Calculate capacitance in E-12 Farad (pF)
ALLSEL,ALL
VSEL,S, , , 3
VSEL,A, , , 7
VSEL,A, , , 8
ALLSEL,BELOW,VOLU
/post1
SET,LAST
ETABLE,Sene2,SENE,
SSUM
*GET,W2,SSUM, ,ITEM,Sene2
*SET,C2 , (W2*2)/((vltg-0)**2)                ! Calculate capacitance in E-12 Farad (pF)
/OUTPUT,30AUG2012PTSiCSi, , ,APPEND           ! Saves the results
*VWRITE,L,W,h,t,G1,G2,P0,T0,C1,C2, , , ,
(F8.2,' ',F8.2,' ',F8.2,' ',F8.2,' ',F8.2,' ',F8.2,'   ',F8.2,'   ',F8.2,'   ',F10.5,'    ',F10.5)
/OUTPUT
*ENDDO
*ENDDO
*END
/INPUT,ansuitmp
physics,read,STRUCTURE                        ! Read structural physics for plotting the results
FINISH
/post1
SET,LAST
/DSCALE,ALL,1.0
/EFACET,1
PLNSOL, U,Z, 0,1.0
!!!!!!!!!
! END !
!!!!!!!!!
```

Appendix C
Fringing effect in parallel plate capacitors

In electrical modeling section in Chapter 4, it was assumed that the fringing effect in the designed multifunctional sensor can be ignored without bringing about a major error to the resutsl. This appendix sheds more light on the issue and numerically investigating the validity of such an assumption. Figure C.1 schematically shows a capacitive MEMS pressure sensor comprising two parallel square membranes measuring 100×100 μm^2 with a 3 μm vacuum gap between them. The Edges of the elelctrodes are fixed and a pressure difference ΔP is applied on the top elelctrode. The material properties of SiC are used for the top plate and it deflects under the pressure difference ΔP.

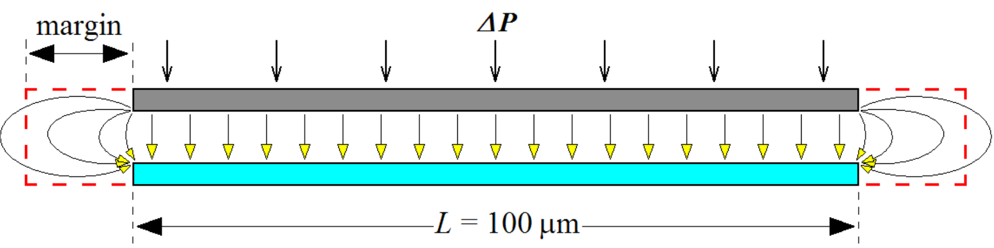

Figure C.1 A capacitive MEMS pressure sensorunder pressure loading ΔP.

A reduced edition of the FE code given in appendix B, Section B4, is used for the calculation of the capacitance between the two plates. The voltage difference between the two plates is set to 0.1 (v). The FE results are calculated for two different scenarios, one without including the fringing effect (margin = 0 in Figure C.1), and the other one including the fringing effect (margin varying between 0 and 10 μm). The ratios of the two results are shown in Figure C.2 for different values of "margin" and ΔP. These results show that the maximum difference between the results with and without the fringing effect is about 8% and it decreases when the gap between the two electrodes decreases by pressure loading. Though these results are calculated for a simple capacitive MEMS pressure sensor, but they can be easily extended for other similar devices with altered geometries. As a result, it is expected that ignoring the fringing effect in the modeling of the multifunctional MEMS sensor (as carried out in Chapter 4) would bring about a comparable average error of 5% in the prediction of the sensor capacitive outputs C_1 and C_2.

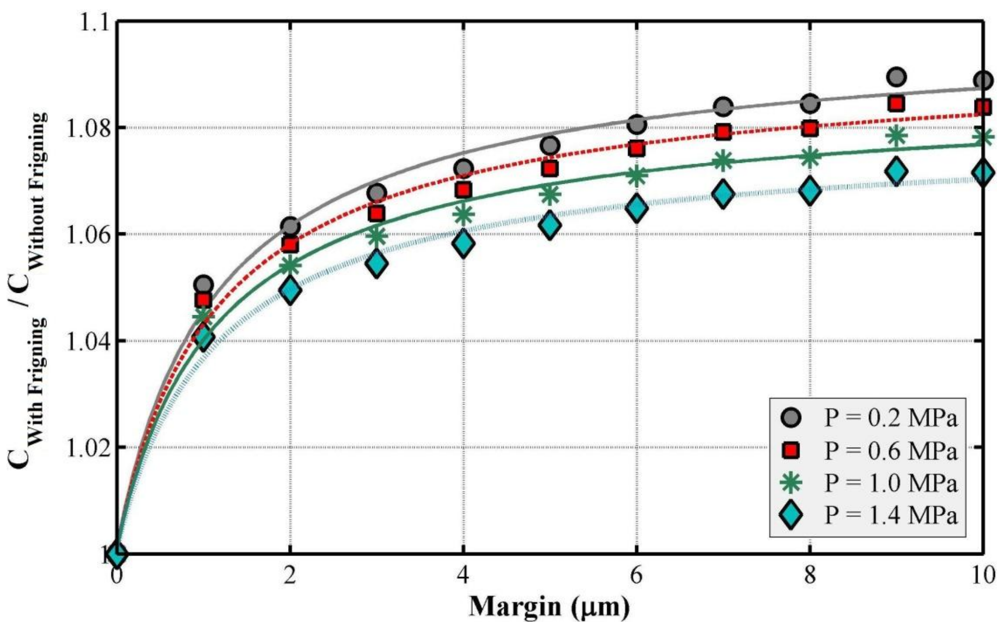

Figure C.2 The capacitive output of the sensor in Figure C.1 versus different values of “margin” and pressure loading ΔP.

Appendix D
Layouts of PolyMUMPs chips

D1. PolyMUMPs chip #1

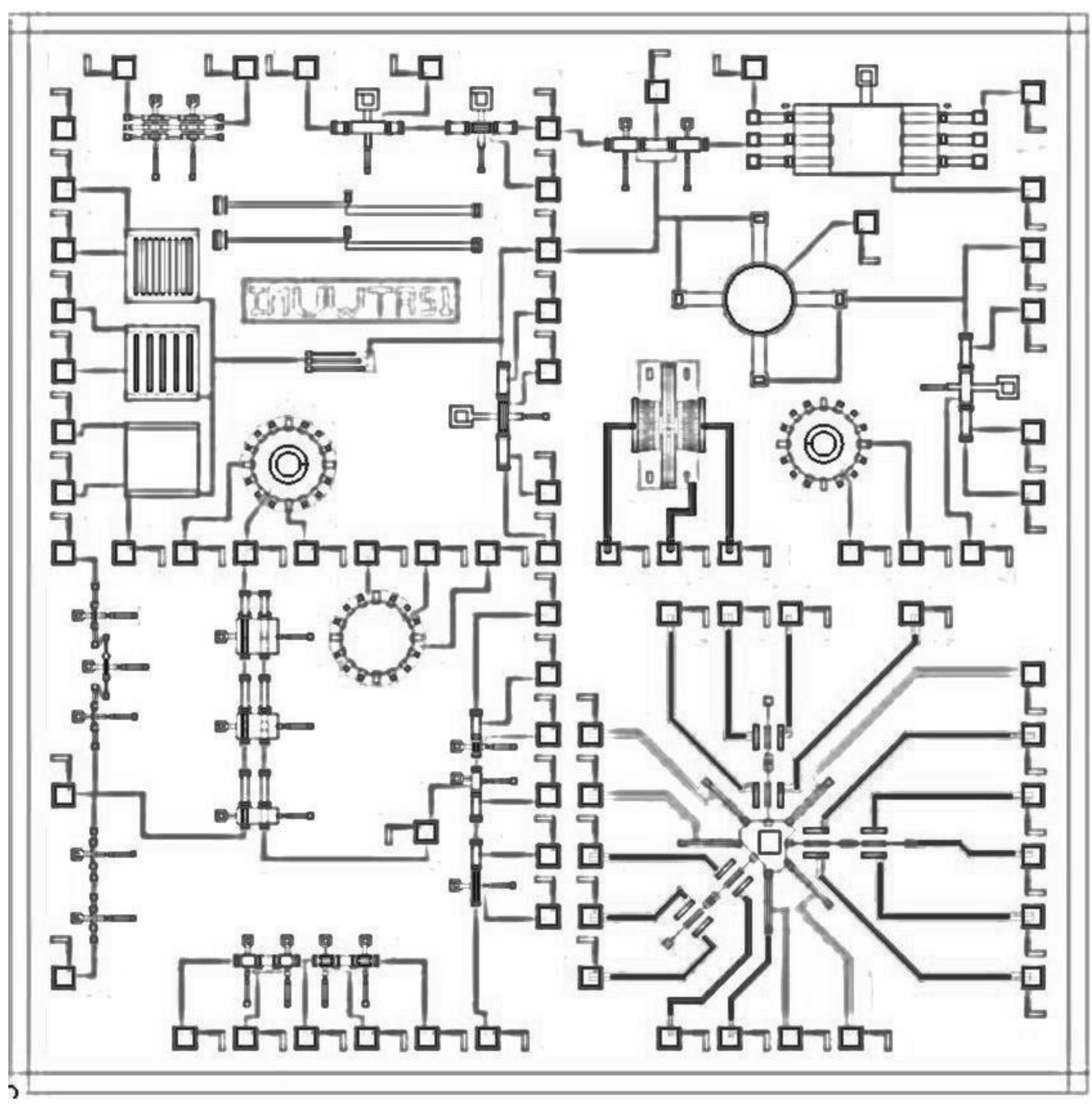

D2. PolyMUMPs chip #2

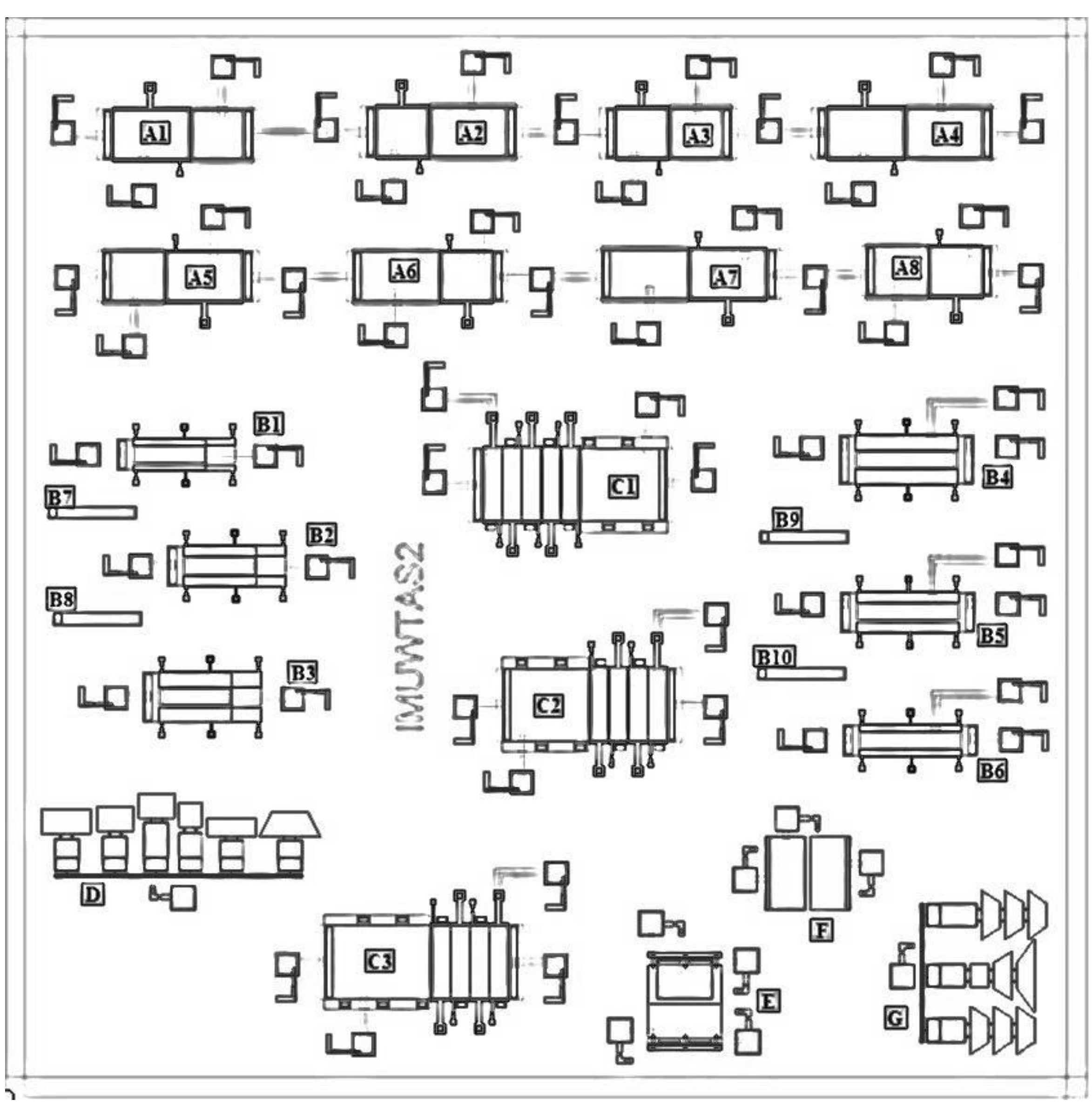

Copyright Permissions

In the preparation of this Thesis, copyrighted material in the form of two figures have been used. These include Figures 2.10 and 2.11. In the following, photos of the letters of copyright permission issued for these figures are presented. Also, Figure 2.9 is taken from reference [113] whose distribution/availability statement reads **Approved for public release; distribution unlimited**.

- Copyright permission for Figure 2.10 (issued by Elsevier):

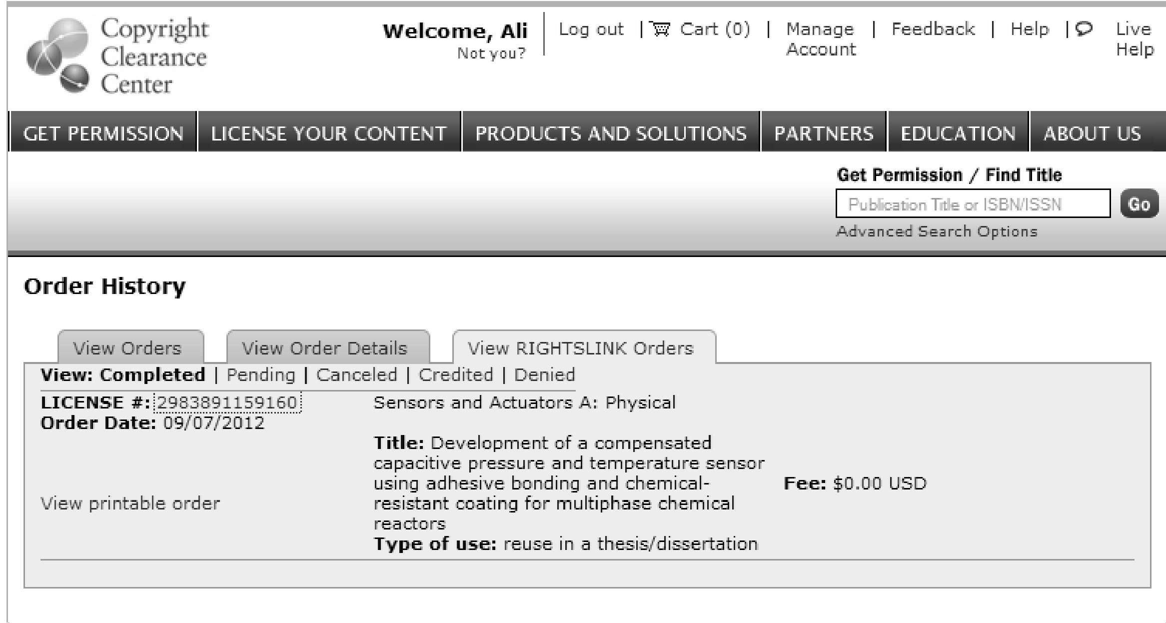

Order History

View Orders | View Order Details | View RIGHTSLINK Orders

View: Completed | Pending | Canceled | Credited | Denied

LICENSE #: 2983891159160
Order Date: 09/07/2012

View printable order

Sensors and Actuators A: Physical

Title: Development of a compensated capacitive pressure and temperature sensor using adhesive bonding and chemical-resistant coating for multiphase chemical reactors
Type of use: reuse in a thesis/dissertation

Fee: $0.00 USD

To view this email as a web page, go here.

Do Not Reply Directly to This Email

To ensure that you continue to receive our emails,
please add rightslink@marketing.copyright.com to your address book.

RightsLink

Thank You For Your Order!

Dear Mr. Ali Najafi Sohi,

Thank you for placing your order through Copyright Clearance Center's RightsLink service. Elsevier has partnered with RightsLink to license its content. This notice is a confirmation that your order was successful.

Your order details and publisher terms and conditions are available by clicking the link below:
http://s100.copyright.com/CustomerAdmin/PLF.jsp?lID=2012090_1347061327160

Order Details
Licensee: Ali Najafi Sohi
License Date: Sep 7, 2012
License Number: 2983891159160
Publication: Sensors and Actuators A: Physical
Title: Development of a compensated capacitive pressure and temperature sensor using adhesive bonding and chemical-resistant coating for multiphase chemical reactors
Type Of Use: reuse in a thesis/dissertation
Total: 0.00 USD

To access your account, please visit https://myaccount.copyright.com.

Please note: Online payments are charged immediately after order confirmation; invoices are issued daily and are payable immediately upon receipt.

To ensure we are continuously improving our services, please take a moment to complete our customer satisfaction survey.

B.1:v4.2

+1-877-622-5543 / Tel: +1-978-646-2777
customercare@copyright.com
http://www.copyright.com

This email was sent to: **sohi@uwaterloo.ca**

Please visit Copyright Clearance Center for more information.

This email was sent by Copyright Clearance Center
222 Rosewood Drive Danvers, MA 01923 USA

- Copyright permission for Figure 2.11 (issued by SPIE):

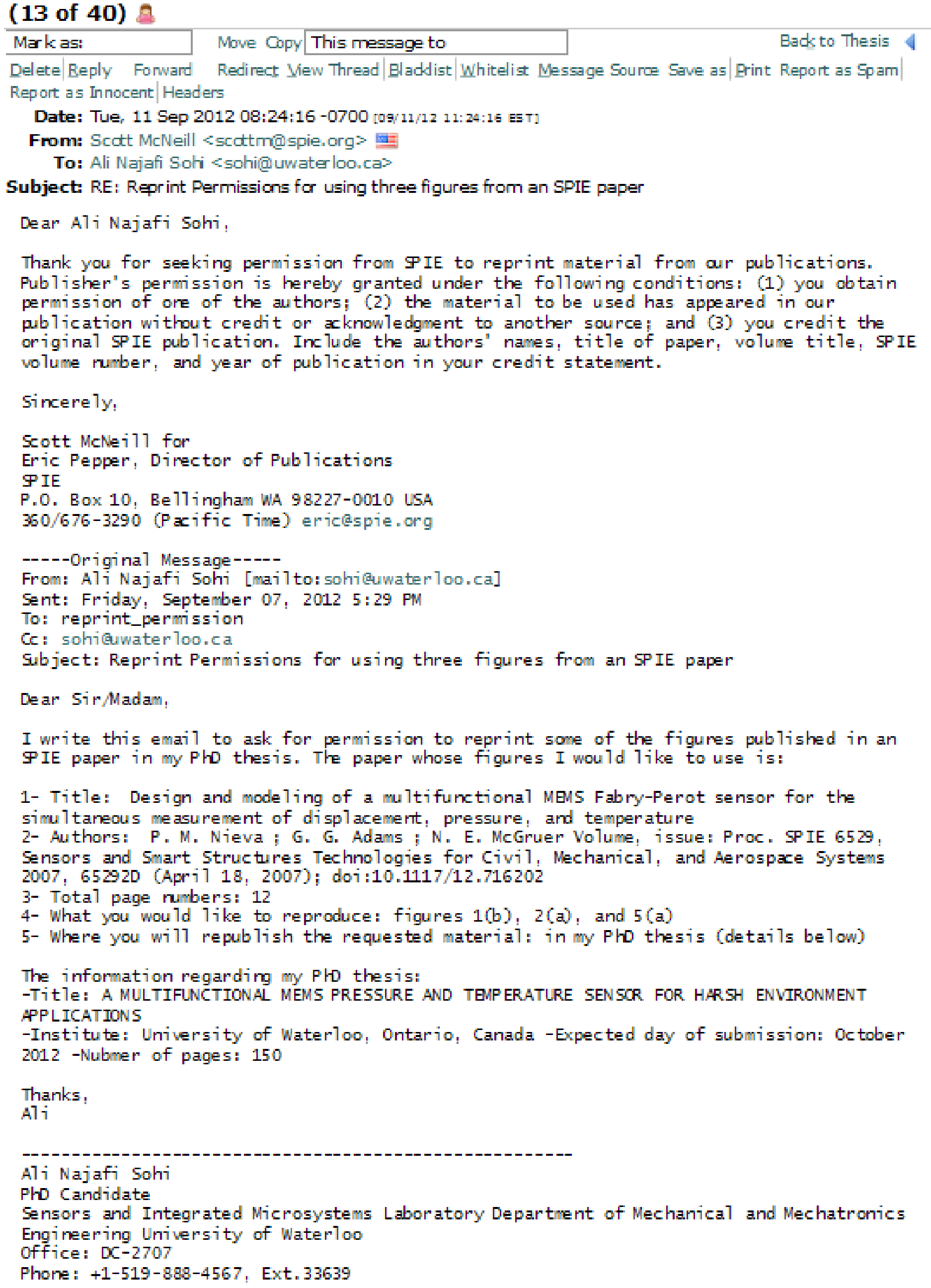

Thesis: RE: Reprint Permissions for using three figures from an SPIE paper (13 of 40)

Mark as: Move Copy This message to Back to Thesis

Delete | Reply Forward Redirect View Thread | Blacklist | Whitelist Message Source Save as | Print Report as Spam | Report as Innocent | Headers

Date: Tue, 11 Sep 2012 08:24:16 -0700 [09/11/12 11:24:16 EST]
From: Scott McNeill <scottm@spie.org>
To: Ali Najafi Sohi <sohi@uwaterloo.ca>
Subject: RE: Reprint Permissions for using three figures from an SPIE paper

Dear Ali Najafi Sohi,

Thank you for seeking permission from SPIE to reprint material from our publications. Publisher's permission is hereby granted under the following conditions: (1) you obtain permission of one of the authors; (2) the material to be used has appeared in our publication without credit or acknowledgment to another source; and (3) you credit the original SPIE publication. Include the authors' names, title of paper, volume title, SPIE volume number, and year of publication in your credit statement.

Sincerely,

Scott McNeill for
Eric Pepper, Director of Publications
SPIE
P.O. Box 10, Bellingham WA 98227-0010 USA
360/676-3290 (Pacific Time) eric@spie.org

-----Original Message-----
From: Ali Najafi Sohi [mailto:sohi@uwaterloo.ca]
Sent: Friday, September 07, 2012 5:29 PM
To: reprint_permission
Cc: sohi@uwaterloo.ca
Subject: Reprint Permissions for using three figures from an SPIE paper

Dear Sir/Madam,

I write this email to ask for permission to reprint some of the figures published in an SPIE paper in my PhD thesis. The paper whose figures I would like to use is:

1- Title: Design and modeling of a multifunctional MEMS Fabry-Perot sensor for the simultaneous measurement of displacement, pressure, and temperature
2- Authors: P. M. Nieva ; G. G. Adams ; N. E. McGruer Volume, issue: Proc. SPIE 6529, Sensors and Smart Structures Technologies for Civil, Mechanical, and Aerospace Systems 2007, 65292D (April 18, 2007); doi:10.1117/12.716202
3- Total page numbers: 12
4- What you would like to reproduce: figures 1(b), 2(a), and 5(a)
5- Where you will republish the requested material: in my PhD thesis (details below)

The information regarding my PhD thesis:
-Title: A MULTIFUNCTIONAL MEMS PRESSURE AND TEMPERATURE SENSOR FOR HARSH ENVIRONMENT APPLICATIONS
-Institute: University of Waterloo, Ontario, Canada -Expected day of submission: October 2012 -Nubmer of pages: 150

Thanks,
Ali

Ali Najafi Sohi
PhD Candidate
Sensors and Integrated Microsystems Laboratory Department of Mechanical and Mechatronics Engineering University of Waterloo
Office: DC-2707
Phone: +1-519-888-4567, Ext.33639

Bibliography

[1] CHEN, L. and MEHREGANY, M., 2008. A silicon carbide capacitive pressure sensor for in-cylinder pressure measurement. *Sensors and Actuators A: Physical*, **145-146**, pp. 2-8.

[2] http://www.kistler.com/mediaaccess/000-574e-09.08.pdf

[3] MEHREGANY, M., ZORMAN, C.A., RAJAN, N. and WU, C.H., 1998. Silicon carbide MEMS for harsh environments. *Proceedings of the IEEE*, **86**, pp. 1594-1610.

[4] FAHRNER, W.R., JOB, R. and WEMER, M., 2001. Sensors and smart electronics in harsh environment applications. *Microsystem Technologies*, **7**, pp. 138-144.

[5] KROETZ, G.H., EICKHOFF, M. H. and MOELLER, H., 1999. Silicon compatible materials for harsh environment sensors. *Sensors and Actuators A: Physical*, **74**, pp. 182–189.

[6] TURNER, R.C., FUIERER, P.A., NEWNHAM, R.E. and SHROUT, T.R., 1994. Materials for high temperature acoustic and vibration sensors: A review. *Applied Acoustic*, **41**, pp. 299-324.

[7] KHOSHMANA, J.M. and KORDESCH, M.E., 2005. Optical characterization of sputtered amorphous aluminum nitride thin films by spectroscopic ellipsometry. *Journal of Non-Crystalline Solids*, **351**, pp. 3334–3340.

[8] SANCHEZ, G., WUA, A., TRISTANT, P., TIXIER, C., SOULESTIN, B., DESMAISON, J. and BOLOGNA ALLES, A., 2008. Polycrystalline AlN films with preferential orientation by plasma enhanced chemical vapor deposition. *Thin Solid Films*, **516**, pp. 4868–4875.

[9] IRIARTE, G.F., 2003. Surface acoustic wave propagation characteristics of aluminum nitride thin films grown on polycrystalline diamond. *Journal of Applied Physics*, **93**, pp. 9604-9609.

[10] MIYANAGA, M., MIZUHARA, N., FUJIWARA, S., SHIMAZU, M., NAKAHATA, H. and KAWASE, T., 2006. Single crystal growth of AlN by sublimation method. *SEI Technical Review*, **63**, pp. 22-26.

[11] CHEMEKOVA, T.Y., AVDEEV, O.V., BARASH, I.S., MOKHOV, E.N., NAGALYUK, S.S., ROENKOV, A.D., SEGAL, A.S., MAKAROV, Y.N., RAMM, M.G., DAVIS, G., HUMINIC, G. and HELAVA, H., 2008. Sublimation growth of 2-inch diameter bulk AlN crystals. *Physica Status Solidi C*, **5**, pp. 1612-1614.

[12] CLELAND, A.N., POPHRISTIC, M. and FERGUSON, I., 2001. Single-crystal aluminum nitride nanomechanical resonators. *Applied Physics Letters*, **79**, pp. 2070-2072.

[13] TILAK, V., BATONI, P., JIANG, J. and KNOBLOCH, A., 2007. Measurement of piezoelectric coefficient of gallium nitride using metal-insulator-semiconductor capacitors. *Applied Physics Letters*, **90**, p. 043508.

[14] ZIMMERMANN, T., NEUBURGER, M., BENKART, P., HERNÁNDEZ-GUILLÉN, F.J., PIETZKA, C., KUNZE, M., DAUMILLER, I., DADGAR, A., KROST, A. and KOHN, E., 2006. Piezoelectric GaN sensor structures. *IEEE Electron Device Letters*, **27(5)**, pp. 309 – 312.

[15] LORENZ, K., WAHL, U., ALVES, E., NOGALES, E., DALMASSO, S., MARTIN R, W., O'DONNELL, K.P., WOJDAK, M., BRAUD, A., MONTEIRO, T., WOJTOWICZ, T., RUTERANA, P., RUFFENACH, S. and BRIOT, O., 2006. High temperature annealing of rare earth implanted GaN films: Structural and optical properties. *Optical Materials*, **28**, pp. 750-758.

[16] WEI, L., KUO, P.K., THOMAS, R.L., ANTHONY, T.R. and BANHOLZER, W.F., 1993. Thermal conductivity of isotopically modified Single crystal diamond. *Physical Review Letters*, **70**, pp. 3764-3767.

[17] BELAY, K., ETZEL, Z., ONN, D.G. and ANTHONY, T.R., 1996. The thermal conductivity of polycrystalline diamond films: Effects of isotope content. *Journal of Applied Physics*, **79**, pp. 8336-8340.

[18] KOHN, E., 2007. Harsh environments Materials. In: Y.B. GIANCHANDANI, O. TABATA and H. ZAPPE, eds, *Comprehensive microsystems*. Elsevier.

[19] JOHN, P., POLWART, N., TROUPE, C.E. and WILSON, J.I.B., 2002. The oxidation of (100) textured diamond. *Diamond and related materials*, **11**, pp. 861-866.

[20] NEUDECK, P.G., GARVERICK, S.L., SPRY, D.J., CHEN, L.Y., BEHEIM, G.M., KRASOWSKI, M.J. and MEHREGANY, M., 2009. Extreme temperature 6H-SiC JFET integrated circuit technology. *Physica Status Solidi A*, **206**, pp. 2329-2345.

[21] FU, X.A., DUNNING, J.L., ZORMAN, C.A. and MEHREGANY, M., 2005. Polycrystalline 3C-SiC thin films deposited by dual precursor LPCVD for MEMS applications. *Sensors and actuators A: Physical*, **119**, pp. 169-176.

[22] ZHE, C.F. and ZHAO, J.H., 2003. *Silicon Carbide: Materials, Processing & Devices*. CRC Press.

[23] http://www.nsc.co.jp/CGI/news/whatsnew_detail.cgi?section=11&seq=00021103 [October/1, 2012].

[24] MEHREGANY, M. and ZORMAN, C.A., 1999. SiC MEMS: opportunities and challenges for applications in harsh environments. *Thin Solid Films*, **355-356**, pp. 518-524.

[25] FUJITA, S., MAEDA, K. and HYODO, S., 1987. Dislocation glide motion in 6H SiC single crystals subjected to high temperature deformation. *Philosophical Magazine A*, **55**, pp. 203-215.

[26] YONENAGA, I., KOIZUMI, H., OHNO, Y. and TAISHI, T., 2008. High-temperature strength and dislocation mobility in the wide band-gap ZnO: Comparison with various semiconductors. *Journal of Applied Physics*, **103**, p. 093502.

[27] LIEW, L.A., SARAVANAN, R.A., BRIGHT, V.M., DUNN, M.L., DAILY, J.W. and RAJ, R., 2003. Processing and characterization of silicon carbon-nitride ceramics: application of electrical properties towards MEMS thermal actuators. *Sensors and Actuators A: Physical*, **103**, pp. 171-181.

[28] MALLIKARJUNANA, A., JOHNSONA, A.D., MATZA, L., VRTISA, R.N., DERECSKEI-KOVACSA, A., JIANGA, X. and XIAOB, M., 2012. Silicon precursor development for advanced dielectric barriers for VLSI technology. *Microelectronic Engineering*, **92**, pp. 83-85.

[29] CHUNG, G.S., 2007. Characteristics of SiCN microstructures for harsh environment and high-power MEMS applications. *Microelectronics Journal*, **38**, pp. 888-893.

[30] DING, C., HUANG, X., GREGORI, G., PARKER, G.E.R., RAO, M.P., CLARKE, D.R. and MACDONALD, N.C., 2005. Development of bulk-titanium-based mems RF switch for harsh environment applications. *Proceedings of IMECE, Orlando, Florida*, November 5-11, 2005.

[31] LLOYD SPETZ, A, UNÉUS, L., SVENNINGSTORP, H., TOBIAS, P., EKEDAHL, L.G., LARSSON, O., GÖRAS, A., SAVAGE, S., HARRIS, C., MÅRTENSSON, P., WIGREN, R., SALOMONSSON, P., HÄGGENDAHL, B., LJUNG, P., MATTSSON, M. and LUNDSTRÖM, I., 2001. SiC based field effect gas sensors for industrial applications. *Physica Status Solidi A*, **185**, pp. 15-25.

[32] KRIZ, J., GOTTFRIED, K., SCHOLZ, T., KAUFMANN, C. and GEBNER, T., 1997. Ohmic contacts to n-type polycrystalline SiC for high-temperature micromechanical applications. *Materials Science and Engineering: B*, **46**, pp. 180-185.

[33] NEUDECK, P.G., 2006. Silicon carbide technology, In: W.K. Chen, ed, *The VLSI Handbook*, Second edn. CRC Press.

[34] CHUNG, G.S. and YOON, K.H., 2008. Ohmic contacts to single-crystalline 3C-SiC films for extreme environment MEMS applications. *Microelectronics Journal*, **39**, pp. 1408-1412.

[35] UMA, S., MCCONNELL, A.D., ASHEGHI, M., KURABAYASHI, K. and GOODSON, K.E., 2001. Temperature-dependent thermal conductivity of undoped polycrystalline silicon layers. *International Journal of Thermophysics*, **22**, pp. 605-616.

[36] GEISBERGER, A.A., SARKAR, N., ELLIS, M. and SKIDMORE, G.D., 2003. Electrothermal properties and modeling of polysilicon microthermal actuators. *Journal of Microelectromechanical Systems*, **12**, pp. 513-523.

[37] TADA, H., KUMPEL, A.E., LATHROP, R.E., SLANINA, J.B., NIEVA, P., ZAVRACKY, P., MIAOULIS, I.N. and WONG, P.Y., 2000. Thermal expansion coefficient of polycrystalline silicon and silicon dioxide thin films at high temperatures. *Journal of Applied Physics*, **87**, PP. 4189-4193.

[38] JANSEN, F., MACHONKIN, M.A., PALMIERI, N. and KUHMAN, D., 1987. Thermomechanical properties of amorphous silicon and nonstoichiometric silicon oxide films. *Journal of Applied Physics*, **62**, pp. 4732-4736.

[39] QUAY, R., 2008. *Gallium Nitride Electronics*, First edn. Springer.

[40] WANG, Z., ALANIZ, J.E., JANG, W., GARAY, J.E. and DAMES, C., 2011. "Thermal conductivity of nanocrystalline silicon: importance of grain size and frequency-dependent mean free paths. *Nano Letters*, **11(6)**, pp 2206-2213.

[41] PARFEN'EVA, L.S., ORLOVA, T.S., KARTENKO, N.F., SHARENKOVA, N.V., SMIRNOV, B.I., SMIRNOV, I.A., MISIOREK, H., JEZOWSKI, A., VARELA-FERIA, F.M., MARTINEZ-FERNANDEZ, J. and DE ARELLANO-LOPEZ, A.R., 2005. Thermal conductivity of the SiC/Si biomorphic composite, a new cellular ecoceramic. *Physics of the Solid State*, **47(7)**, pp. 1216-1220.

[42] JEONG, T., ZHU, J.G., MAO, S., PAN, T. and TANG, Y.J., 2012. Thermal Characterization of SiC Amorphous Thin Films. *International Journal of Thermophysics*, **33**, pp. 1000-1012.

[43] SCHAFFT, H.A., SUEHLE, J.S. and MIREL, P.G.A., 1989. Thermal conductivity measurements of thin-film silicon dioxide. *Proceedings of IEEE 1989 International Conference on Microelectronic Test Structures*, **2**, pp. 121-125.

[44] LEE, S.M. and CAHILL, D.G., 1997. Heat transport in thin dielectric films. *Journal of Applied Physics*, **81**, pp. 2590-2595.

[45] MOORE, J.P., WILLIAMS, R.K. and GRAVES, R.S., 1977. Thermal conductivity, electrical resistivity, and Seebeck coefficient of high purity chromium from 280 to 1000 K. *Journal of Applied Physics*, **48**, pp. 610-617.

[46] ERMOLAEV, B.I., 1974. Thermal conductivity and electrical conductivity of materials based on titanium and its alloys at temperatures from 20-80 to 1000 °K. *Metal Science and Heat Treatment*, **16**, pp. 1049-1051.

[47] HAYNES, W.M., 2012. *CRC Handbook of Chemistry and Physics*, 92nd edn. CRC Press.

[48] http://www.ioffe.ru/SVA/NSM/Semicond/ [October/1, 2012]

[49] JAIN, A. and GOODSON, K.E., 2008. Measurement of the thermal conductivity and heat capacity of freestanding shape memory thin films using the 3ω method. *Journal of Heat Transfer*, **130**, p. 102402.

[50] ABU EISHAH, S.I., HADDAD, Y., SOLIEMAN, A. and BAJBOUL, A., 2004. A new correlation for the specific heat of metals, metal oxides and metal fluorides as a function of temperature. *Latin American Applied Research*, **34**, pp. 257-265.

[51] WATANABE, H., YAMADA, N. and OKAJI, M., 2004. Linear thermal expansion coefficient of silicon from 293 to 1000 K. *International Journal of Thermophysics*, **25**, pp. 221-236.

[52] REEBER, R.R. and WANG, K., 1996. Thermal expansion and lattice parameters of group IV semiconductors. *Materials Chemistry and Physics*, **46**, pp. 259-264.

[53] SHINODA, T., SOGA, N., HANADA, T. and TANABE, S., 1997. Young's modulus of RF-sputtered amorphous thin films in the $Si0_2$-y_20_3 system at high temperature. *Thin Solid Films*, **293**, pp. 144-148.

[54] TOMENO, I., 1981. High temperature elastic moduli of Si3N4 ceramics. *Japanese Journal of Applied Physics*, **20**, pp. 1751-1752.

[55] HOLZWARTH, U. and STAMM, H., 2002. Mechanical and thermomechanical properties of commercially pure chromium and chromium alloys. *Journal of Nuclear Materials*, **300**, pp. 161-177.

[56] OKAJI, M., 1988. Absolute thermal expansion measurements of single-crystal silicon in the range 300-1300 K with an interferometric dilatometer. *International Journal of Thermophysics*, **9**, pp. 1101-1109; **Fisher, E.S. and Renken, C.J.,** 1964. Single-Crystal Elastic Moduli and the hcp → bcc Transformation in Ti, Zr, and Hf. *Physical Review*, **135**, pp. 482-494.

[57] LI, Z. and BRADT, R.C., 1986. Thermal expansion of the cubic (3C) polytype of SiC. *Journal of Materials Science*, **21**, pp. 4366-4368.

[58] FIGGE, S., KRÖNCKE, H., HOMMEL, D. and EPELBAUM, B.M., 2009. Temperature dependence of the thermal expansion of AlN. *Applied Physics Letters*, **94**, p. 101915.

[59] RODER, C., EINFELDT, S., FIGGE, S. and HOMMEL, D., 2005. Temperature dependence of the thermal expansion of GaN. *Physical Review B*, **72**, p. 085218.

[60] BRULS, R.J., HINTZEN, H.T., DE WITH, G., METSELAAR, R. and VAN MILTENBURG, J.C., 2001. The temperature dependence of the Gruneisen parameters of $MgSiN_2$, AlN and β-Si_3N_4. *Journal of Physics and Chemistry of Solids*, **62**, pp. 783-792.

[61] TOULOUKIAN, Y.S., KIRBY, R.K., TAYLOR, R.E. and DESAI, P.D., 1975. *Thermophysical properties of matter, thermal expansion, metallic elements and alloys*. New York: IFI/Plenum.

[62] GEYLING, F.T. and FORST, J.J., 1960. Semiconductor strain transducers. *Bell System Technical Journal*, **39**, pp. 705-731.

[63] SMITH, C.S., 1954. Piezoresistance effect in germanium and silicon. *Physical Review*, **94**, pp. 42-49.

[64] TUFTE, O.N., CHAPMAN, P.W. and LONG, D., 1962. Silicon diffused-element piezoresistive diaphragms. *Journal of Applied Physics*, **33**, pp. 3322-327.

[65] SAMAUN, S., WISE, K.D. and ANGELL, J.B., 1973. An IC piezoresistive pressure sensor for biomedical instrumentation. *IEEE Transactions on Biomedical Engineering*, **20**, pp. 101-109.

[66] CLARK, S. K. and WISE, K.D., 1979. Pressure sensitivity in anisotropically etched thin-diaphragm pressure sensors. *IEEE Transactions in Electron Devices*, **26**, pp. 1887-1895.

[67] PETERSEN, K., BROWN, J., VERMEULEN, T., BARTH, P., MALLON, J. and BRYZEK, J., 1990. Ultra-stable, high-temperature pressure sensors using silicon fusion boding. *Sensors and Actuators A: Physical*, **22(1-3)**, pp. 96-101.

[68] YULONG, Z., LIBO, Z. and ZHUANGDE, J., 2003. A novel high temperature pressure sensor on the basis of SOI layers. *Sensors and Actuators A: Physical*, **108**, pp. 108-111.

[69] SUSKI, J., MOSSER, V. and GOSS, J., 1989. Polysilicon SOI pressure sensor. *Sensors and Actuators*, **17**, pp. 405-414.

[70] CHUNG, G.S., KAWAHITO, S., ISHIDA, M., NAKAMURA, T. and SUZAKI, T., 1991. Temperature-independent pressure sensors using epitaxially stacked Si/$A1_2O_3$/Si structures. *Sensors and Actuators A: Physical*, **29**, pp. 107-115.

[71] STUCHEBNIKOV, V.M., 1991. SOS strain gauge sensors for force and pressure transducers. *Sensors and Actuators A: Physical*, **28**, pp. 207-213.

[72] REGGIANI, S., VALDINOCI, M., COLALONGO, L., RUDAN, M., BACCARANI, G., STRICKER, A.D., ILLIEN, F., FELBER, N., FICHTNER, W. and ZULLINO, L., 2002. Electron and hole mobility in silicon at large operating temperatures- Part I: Bulk mobility. *IEEE Transactions on Electron devices*, **49**, pp. 490-499.

[73] GUO, S., ERIKSEN, H., CHILDRESS, K., FINK, A. and HOFFMAN, M., 2009. High temperature smart-cut SOI pressure sensor. *Sensors and Actuators A: Physical*, **154**, pp. 255-260.

[74] YAMAMOTO, A., NAWACHI, N., TSUTSUMOTO, T. and TERAYAMA, A., 2005. Pressure sensor using p-type polycrystalline diamond piezoresistors. *Diamond and Related Materials*, **12**, pp. 657-660.

[75] WERNER, M.R. and FAHRNER, W.R., 2001. Review on materials, microsensors, systems, and devices for high-temperature and harsh-environment applications. *IEEE Transactions on Industrial Electronics*, **48**, pp. 249-257.

[76] CIMALLA, V., PEZOLDT, J. and AMBACHER, O., 2007. Group III nitride and SiC based MEMS and NEMS: materials properties, technology and applications. *Journal of Physics D: Applied Physics*, **40**, pp. 6386-6434.

[77] KASTEN, K., AMELUNG, J. and MOKWA, W., 2000. CMOS-compatible capacitive high temperature pressure sensors. *Sensors and Actuators A: Physical*, **85**, pp. 147-152.

[78] YOUNG, D.J., DU, J., ZORMAN, C.A. and KO, W.H., 2004. High-temperature single-crystal 3C-SiC capacitive pressure sensor. *IEEE Sensors*, **4(4)**, pp. 464-470.

[79] EATONY, W.P. and SMITH, J.H., 1997. Micromachined pressure sensors: Review and recent developments. *Smart Materials & Structures*, **6**, pp. 530-539.

[80] PATIL, A., FU, X., ANUPONGONGARCH, C., MEHREGANY, M. and GARVERICK, S., 2007. Characterization of silicon carbide differential amplifiers at high temperature. *Proceedings of the IEEE Compound Semiconductor IC Symposium, Portland, OR*, October, 2007, pp. 139-142.

[81] NEUDECK, P.G., BEHEIM, G.M. and SALUPO, C.S., 2000. 600 °C logic gates using silicon carbide JFETs. *Government Microcircuit Applications Conference Technical Digest, Anahiem, CA*, pp. 421-424.

[82] MOE, S.T., SCHJOLBERG-HENRIKSEN, K., WANG, D.T., LUND, E., NYSAETHER, J., FURUBERG, L., VISSER, M., FALLET, T. and BERNSTEIN, R.W., 2000. Capacitive differential pressure sensor for harsh environments. *Sensors and Actuators A: Physical*, **83**, pp. 30-33.

[83] KASTEN, K., KORDAS, N., KAPPERT, H. and MOKWA, W., 2002. Capacitive pressure sensor with monolithically integrated CMOS readout circuit for high temperature applications. *Sensors and Actuators A: Physical*, **97-98**, pp. 83-87.

[84] JIN, S., RAJGOPAL, S. and MEHREGANY, M., 2011. Silicon carbide pressure sensor for high temperature and high pressure applications: influence of substrate material on performance. *Proceedings of Transducers'11 conference, Beijing, China*, pp. 2026-2029.

[85] PULLIAM, W.J., RUSSLER, P.M., MLCAK, R., MURPHY, K.A. and KOZIKOWSKI, C.L., 2000. Micromachined, SiC fiber optic pressure sensors for high-temperature aerospace applications. *Proceedings of SPIE*, **4202**, pp. 21-30.

[86] PULLIAM, W.J., RUSSLER, P.M. and FIELDER, R.S., 2001. High-temperature high-bandwidth fiber optic MEMS pressure-sensor technology for turbine-engine component testing. *Proceedings of SPIE*, **4578**, pp. 229-238.

[87] RIZA, N., SHEIKH, M. and PEREZ, F., 2010. Hybrid wireless-wired optical sensor for extreme temperature measurement in next generation energy efficient gas turbines. *Journal of Engineering for Gas Turbines and Power*, **132**, p. 051601.

[88] ZHU, Y., COOPER, K.L., PICKRELL, G.R. and WANG, A., 2006. High-temperature fiber-tip pressure sensor. *IEEE Journal of Lightwave Technology*, **24**, pp. 861-869.

[89] CEYSSENS, F., DRIESEN, M. and PUERS, R., 2009. An optical absolute pressure sensor for high-temperature applications, fabricated directly on a fiber. *Journal of Micromechanics and Microengineering*, **19**, p. 115017.

[90] YI, J., LALLY, E., WANG, A. and XU, Y., 2011. Demonstration of an all-sapphire Fabry–Pérot cavity for pressure sensing. *IEEE Photonics Technology Letters*, **23**, pp. 9-11.

[91] SPIERING, V.L., BOUWSTRA, S., BURGERT, J.F. and ELWENSPOEK, M., 1993. Membranes fabricated with a deep single corrugation for package stress reduction and residual stress relief. *Journal of Micromechanics and Microengineering*, **3**, pp. 243-246.

[92] SCHEEPER, P., OLTHUIS, W. and BERGVELD, P., 1994. The design, fabrication, and testing of corrugated silicon nitride diaphragms. *Journal of Microelectromechanical Systems*, **3**, pp. 36-42.

[93] KRESSMANN, R., KLAIBER, M. and HESS, G., 2002. Silicon condenser microphones with corrugated silicon oxide/nitride electret membranes. *Sensors and Actuators A: Physical*, **100**, pp. 301-309.

[94] HAO, X.C., JIANG, Y.G., TAKAO, H., MAENAKA, K., FUJITA, T. and HIGUCHI, K., 2011. Zero temperature coefficient gas-sealed pressure sensor using mechanical temperature compensation. *Proceedings of Transducers'11conference, Beijing, China*, pp. 116-119.

[95] WILSON, J.S., 2004. *Sensor technology handbook*. Elsevier.

[96] GREGORY, O.J. and YOU, T., 2004. Integrated ceramic temperature sensors for harsh environments. *Proceedings of IEEE Sensors*, 2004, pp. 1165-1168.

[97] RAKOPOULOS, C.D. and MAVROPOULOS, G.C., 2008. Experimental evaluation of local instantaneous heat transfer characteristics in the combustion chamber of air-cooled direct injection diesel engine. *Energy*, **33**, pp. 1084-1099.

[98] TORREGROSA, A.J., BERMUDEZ, V., OLMEDA, P. and FYGUEROA, O., 2012. Experimental assessment for instantaneous temperature and heat flux measurements under Diesel motored engine conditions. *Energy Conversion and Management*, **54**, pp. 57-66.

[99] NAGAI, T., YAMAMOTO, K. and KOBAYASHI, I., 1982. SiC thin-film thermistor. *Journal of Physics E: Scientific Instruments*, **15**, pp. 520-524.

[100] NAGAI, T. and ITOH, M., 1990. SiC thin-film thermistors. *IEEE Transactions on Industry Applications*, **26**, pp. 1139-1143.

[101] KATSUKI, N., TAMAL, T., MORIWAKE, H., LEGARE, J. and YOSHIDA, S., 1996. Exhaust gas high temperature sensor for LEV/ULEV and OBD systems. *SAE Technical Papers*, **960336**.

[102] LOURENCO, M.J., SERRA, J.M., NUNES, M.R., VALLERA, A.M. and CASTRO, C.A., 1998. Thin-film characterization for high-temperature applications. *International Journal of Thermophysics*, **19**, pp. 1253-1265.

[103] MIYAKAWA, N., LEGNER, W., ZIEMANN, T., TELITSCHKIN, D., FECHT, H.J. and FRIEDBERGER, A., 2012. MEMS-based microthruster with integrated platinum thin film resistance temperature detector (RTD), heater meander and thermal insulation for operation up to 1000 °C. *Microsystem Technologies*, **18(7-8)**, pp. 1077-1087.

[104] FIREBAUGH, S.L., JENSEN, K.F. and SCHMIDT, M.A., 1998. Investigation of high-temperature degradation of platinum thin films with an in situ resistance measurement apparatus. *Journal of Microelectromechanical Systems*, **7**, pp. 128-135.

[105] SCHULZ, C. and SICK, V., 2005. Tracer-LIF diagnostics: quantitative measurement of fuel concentration, temperature and fuel/air ratio in practical combustion systems. *Progress in Energy and Combustion Science*, **31**, pp. 75-121.

[106] PETERSON, B., BAUM, E., BÖHM, B., SICK, V. and DREIZLER, A., 2012. High-speed PIV and LIF imaging of temperature stratification in an internal combustion engine. *Proceedings of the Combustion Institute*, **(In Press)**.

[107] EWART, P., WILLIAMS, R.B., LIM, E.P. and STONE, C.R., 2001. Comparison of in-cylinder coherent anti-Stokes-Raman scattering temperature measurements with predictions from an engine simulation. *International Journal of Engine Research*, **2**, pp. 149-162.

[108] SCHULZ, C., SICK, V. and WOLFRUM, J., 1996. Quantitative 2D single-shot imaging of no concentrations and temperatures in a transparent SI engine. *Proceedings of the Combustion Institute*, **26(2)**, pp. 2597-2604.

[109] CRUA, C., 2002. *Combustion Processes in a Diesel Engine,* The University of Brighton.

[110] RIZA, N.A. and SHEIKH, M., 2010. Silicon carbide-based extreme environment hybrid design temperature sensor using optical pyrometry and laser interferometry. *IEEE Sensors*, **10**, pp. 219-224.

[111] AZEVEDO, R.G., JONES, D.G., JOG, A.V., JAMSHIDI, B., MYERS, D.R., CHEN, L., FU, X.A., MEHREGANY, M., WIJESUNDARA, M.B.J. and PISANO, A.P., 2007. A SiC MEMS resonant strain sensor for harsh environment applications. *IEEE Sensors*, **7**, pp. 568-576.

[112] MYERS, D.R., CHENG, K.B., JAMSHIDI, B., AZEVEDO, R.G., SENESKY, D.G., CHEN, L., MEHREGANY, M., WIJESUNDARA, M.B.J. and PISANO, A.P., 2009. Silicon carbide resonant tuning fork for microsensing applications in high-temperature and high G-shock environments. *Journal of Micro/Nanolithography, MEMS, and MOEMS*, **8**, p. 021116.

[113] PISANO, P.A., 2009. Harsh environment wireless MEMS sensors for energy & power. *MTO (DARPA Microsystems Technology Office) Symposium*, *San Jose, CA,* 2-5 March, 2009.

[114] MOHAMMADI, A.R., GRAHAM, T.C.M., BENNINGTON, C.P.J. and CHIAO, M., 2010. Development of a compensated capacitive pressure and temperature sensor using adhesive bonding and chemical-resistant coating for multiphase chemical reactors. *Sensors and Actuators A: Physical*, **163**, pp. 471-480.

[115] MOHAMMADI, A.R., BENNINGTON, C.P.J. and CHIAO, M., 2011. Development of a combined piezoresistive pressure and temperature sensor using a chemical protective coating for Kraft pulp digester process monitoring. *Journal of Micromechanics and Microengineering*, **21**, p. 015009.

[116] MERTENS, J., FINOT, E., THUNDAT ,T., FABRE, A., NADAL, M.H., EYRAUD, V. and BOURILLOT, E., 2003. Effects of temperature and pressure on microcantilever resonance response. *Ultramicroscopy*, **97**, pp. 119-126.

[117] SANDBERG, R., SVENDSEN, W., MOLHAVE, K. and BOISEN, A., 2005. Temperature and pressure dependence of resonance in multi-layer microcantilevers. *Journal of Micromechanics and Microengineering*, **15**, pp. 1454-1458.

[118] NIEVA, P., ADAMS, G.G. and MCGRUER, N.E., 2007. Design and modeling of a multifunctional MEMS Fabry-Perot sensor for the simultaneous measurement of displacement, pressure and temperature. *Proceedings of SPIE*, **6529**, p. 65292D.

[119] WALTHER, D., LIN, L. and PISANO, A., 2007. Micro- and nano-technologies for automotive sensor research. *SAE Technical Paper*, **2007-01-1012**.

[120] TOTH, D., SHAW, T., WLODARCZYK, M. and CUMMINGS, C., 2011. Cylinder head gasket with integrated combustion pressure sensors for advanced engine controls. *SAE International Journal of Engines*, **4(1)**, pp. 1235-1246.

[121] SANLI, A., OZSEZEN, A.N., KILICASLAN, I. and CANAKCI, M., 2008. The influence of engine speed and load on the heat transfer between gases and in-cylinder walls at fired and motored conditions of an IDI diesel engine. *Applied Thermal Engineering*, **28**, pp. 1395-1404.

[122] RAKOPOULOS, C.D., GIAKOUMIS, E.G. and RAKOPOULOS, D.C., 2008. Study of the short-term cylinder wall temperature oscillations during transient operation of a turbocharged diesel engine with various insulation schemes. *International Journal of Engine Research*, **9**, pp. 177-193.

[123] CHANG, J., FILIPI, Z., ASSANIS, D., KUO, T-.W., NAJT, P. and RASK, R., 2005. Characterizing the thermal sensitivity of a gasoline homogeneous charge compression ignition engine with measurements of instantaneous wall temperature and heat flux. *International Journal of Engine Research*, **6**, pp. 289-309.

[124] www.aremco.com/wp-content/uploads/2010/11/A2_091.pdf [October/1, 2012]

[125] http://www.grc.nasa.gov/WWW/RT/2007/Inst-Cnt/20-RIS-okojie2.html [October/1, 2012]

[126] GURALP, O.A., 2008. *The effect of combustion chamber deposits on heat transfer and combustion in a homogeneous charge compression ignition engine*. The University of Michigan.

[127] BUTTSWORTH, D.R., STEVENS, R. and STONE, C.R., 2005. Eroding ribbon thermocouples: impulse response and transient heat flux analysis. *Measurement Science and Technology*, **16**, pp. 1487-1494.

[128] RAKOPOULOS, C.D. and MAVROPOULOS, G.C., 2000. Experimental instantaneous heat fluxes in the cylinder head and exhaust manifold of an air-cooled diesel engine. *Energy Conversion & Management*, **41**, pp. 1265-1281.

[129] RAKOPOULOS, C.D., RAKOPOULOS, D.C., MAVROPOULOS, G.C. and GIAKOUMIS, E.G., 2004. Experimental and theoretical study of the short term response temperature transients in the cylinder walls of a diesel engine at various operating conditions. *Applied Thermal Engineering*, **24**, pp. 679-702.

[130] RAKOPOULOS, C.D., MAVROPOULOS, G.C. and HOUNTALAS, D.T., 2000. Measurements and analysis of load and speed effects on the instantaneous wall heat fluxes in a direct injection air-cooled diesel engine. *International Journal of Energy Research*, **24**, pp. 587-604.

[131] DEMUYNCK, J., PAEPE, M.D., HUISSEUNE, H., SIERENS, R., VANCOILLIE, J. and VERHELST, S., 2011. Investigation of the influence of engine settings on the heat flux in a hydrogen- and methane-fueled spark ignition engine. *Applied Thermal Engineering*, **31**, pp. 1220-1228.

[132] KAMINSKI, C.F., ENGSTROM, J. and ALDEN, M., 1998. Quasi-instantaneous two-dimensional temperature measurements in a spark ignition engine using 2-line atomic fluorescence. *Proceedings of the Combustion Institute*, **27**, pp. 85-93.

[133] MAIGAARD, P., MAUSS, F. and KRAFT, M., 2003. Homogeneous charge compression ignition engine: a simulation study on the effects of inhomogeneities. *Journal of Engineering for Gas Turbines and Power*, **125**, pp. 466-471.

[134] SOYLU, S., 2005. Examination of combustion characteristics and phasing strategies of a natural gas HCCI engine. *Energy Conversion and Management*, **46**, pp. 101-119.

[135] SHEHATA, M.S., 2010. Cylinder pressure, performance parameters, heat release, specific heats ratio and duration of combustion for spark ignition engine. *Energy*, **35**, pp. 4710-4725.

[136] SJOBERG, M. and DEC, J.E., 2005. An investigation into lowest acceptable combustion temperatures for hydrocarbon fuels in HCCI engines. *Proceedings of the Combustion Institute*, **30**, pp. 2719-2726.

[137] LIU, D.X. and FENG, H.Q., 2006. In-cylinder temperature field measurement with laser shearing interferometry for spark ignition engines. *Optics and Lasers in Engineering*, **44**, 1258-1269.

[138] YAO, M., ZHENG, Z. and LIU, H., 2009. Progress and recent trends in homogeneous charge compression ignition (HCCI) engines. *Progress in Energy and Combustion Science*, **35**, pp. 398–437.

[139] TAYLOR, C.F., 1985. *Internal combustion engine in theory and practice: combustion, fuels, materials, design*. Second edn. The MIT Press.

[140] ACEVES, S.M., FLOWERS, D.L., MARTINEZ-FRIAS, J., SMITH, J.R., WESTBROOK, C.K., PITZ, W.J., DIBBLE, R., WRIGHT, J.F., AKINYEMI, W.C. and HESSEL, R.P., 2001. A

sequential fluid-mechanic chemical-kinetic model of propane HCCI combustion. *SAE Technical Paper*, **2001-01-1027**.

[141] ALHARBI, A., 2010. *High-speed high-resolution vector field measurements and analysis of boundary layer flows in an internal combustion engine*. The University of Michigan.

[142] OUDE NIJEWEME, D.J., KOK, J.B.W., STONE,C.R. and WYSZYNSKI, L., 2001. Unsteady in-cylinder heat transfer in a spark ignition engine: experiments and modeling. *Journal of Automobile Engineering*, **215**, pp. 747-760.

[143] KILLINGSWORTH, N.J., RAPP, V.H., FLOWERS, D.L., ACEVESA, S.M., CHEN, J-.Y. and DIBBLE, R., 2011. Increased efficiency in SI engine with air replaced by oxygen in argon mixture. *Proceedings of the Combustion Institute*, **33(2)**, pp. 3141-3149.

[144] NAGASHIMA, T., OKAMOTO, K. and RIBAUD, Y., 2005. Cycles and thermal system integration issues of ultra-micro gas turbines. *Micro Gas Turbines*, *Educational Notes RTO-EN-AVT-131, Neuilly-sur-Seine, France: RTO*, pp. 4.1-4.66.

[145] WANG, S.C., NAYAK, P.K., CHEN, Y.L., SUNG, J.C. and HUANG, J.L., 2012. Growth of single crystal silicon carbide by liquid phase epitaxy using samarium/cobalt as unique solvent. *Proceedings of the Institution of Mechanical Engineers, Part N: Journal of Nanoengineering and Nanosystems*, **226**, p. 75-79.

[146] ROARK, R.J., 1965. *Roark's Formulas for Stress and Strain*. 4th edn. McGraw-Hill.

[147] SENTURIA, S.D., 2000. *Microsystems Design*, Norwell, MA: Kluwer Academic Publisher.

[148] MA, H.Y., HUANG, Q.A., QIN, M. and LU, T., 2010. A micromachined silicon capacitive temperature sensor for wide temperature range applications. *Journal of Micromechanics and Microengineering*, **20**, p. 055036.

[149] SCOTT, S., SCUDERI, M. and PEROULIS, D., 2012. A 600°C wireless multimorph-based capacitive MEMS temperature sensor for component health monitoring. *IEEE 25th Internation Conference on MEMS, Paris, France*, pp. 496-499.

[150] CHOI, D., SHINAVSKI, R.J., STEFFIER, W.S. and SPEARING, S.M., 2005. Residual stress in thick low-pressure chemical-vapor deposited polycrystalline SiC coatings on Si substrates. *Journal of Applied Physics*, **97**, p. 074904.

[151] CHANG, R.C., CHEN, F.Y., CHUANG, C.T. and TUNG, Y.C., 2010. Residual stresses of sputtering titanium thin films at various substrate temperatures. *Journal of Nanoscience and Nanotechnology*, **10**, pp. 4562-4567.

[152] PANI, S.K., WONG, C.C., SUDHARSANAM, K., MHAISALKAR, S.G., LIM, V., MOHANRAJ, S. and RAMANA, P.V., 2004. Effect of process parameters on sidewall roughness in polymeric optical waveguides. *Thin Solid Films*, **462-463**, pp. 471-476.

[153] PONOTH, S.S., AGARWAL, N.T., PERSANS, P.D. and PLAWSKY, J.L., 2003. Fabrication of controlled sidewall angles in thin films using isotropic etches. *Journal of Vacuum Science and Technology B*, **21**, pp. 1240-1247.

[154] SUN, L. and SARANGAN, A., 2011. Fabrication of sloped sidewalls by inductively coupled plasma etching for silicon micro-optic structures. *Journal of Micro/Nanolithography, MEMS, and MOEMS*, **10**, p. 023006.

[155] PolyMUMPs® is the multiuser polysilicon fabrication process offered by the MEMSCAP company, more information available at http://www.memscap.com/products/mumps/polymumps. Reference materials available http://www.memscap.com/products/mumps/polymumps/reference-material [October/1, 2012].

[156] CoventorWare® is a MEMS design and simulation software offered by the Coventor company, more information available at http://www.coventor.com/products/coventorware/ [October/1, 2012].

[157] LIN, L., PISANO, A.P. and HOWE, R.T., 1997. A micro strain gauge with mechanical amplifier. *Journal of Microelectromechanical Systems*, **6**, pp. 313-321.

[158] PAMULA, V.K., JOG, A. and FAIR, R.B., 2001. Mechanical property measurement of thin-film gold using thermally actuated bimetallic cantilever beams. *Proceedings of the 2001 International Conference on Modeling and Simulation of Microsystems NANOTECH 2001*, pp. 410-413.